

THE UNIVERSITY OF HULL

Representing vegetation in experimental models of river systems.

being a Thesis submitted for the Degree of

PhD

in the University of Hull

by

Bas Bodewes, Msc

December 2020



Abstract

The physical behaviour of fluvial systems have been studied in detail and as have their representations of the impact and interaction between hydraulic and sedimentological features within these river systems. However, there is limited understanding of the interaction and impact of organic features like vegetation. Vegetation, in particular riparian vegetation on the banks and floodplains of rivers, is closely intertwined with river behaviour. Rivers can be growth enhancing, by deposition of nutrient rich sediments and the supply of water, or growth inhibiting during periods of low flow or erosive floods. Furthermore, vegetation itself influences the river system by, for example, increasing bank strength and flow resistance.

Vegetation is a living organism interacting with the fluvial system, and its behaviour is dynamic over time (both in terms of growth and decay). Vegetation not only strengthens itself and the substrate it grows in, but it also evolves over time and thrives differently over the seasons in a year. In systems that exhibit dynamic equilibrium this temporal variance of vegetation adjusts into the resulting river morphology and the vegetation itself follows the dynamics of the fluvial system as well. However, present-day predictions of climate change can significantly change river systems. Firstly, flood events may increase in magnitude and frequency; and secondly droughts may increase in length. Simultaneously, changes in temperature and rainfall will affect vegetation growth and decay and may change species types within a given area. These predicted effects will change the behaviour of systems over the next decades, a timescale that is significantly faster than most 'natural' changes in fluvial systems. Hence, it is essential to be able to model these fluvial systems and understand their changes over the next decades.

Physical modelling offers a solution to modelling these systems, and enables time to be compressed by reducing the scale of the river systems. In analogue physical models, surrogates are often used to represent vegetation in small-scale models. Surrogate vegetation enables modellers to incorporate vegetation density, growth and decay into models of fluvial environments since the surrogate vegetation represents the cohesive effect of plant roots, introducing the biotic forcing produced by vegetation in scaled physical models of hydraulic and

sediment behaviour. However, despite the rapid growth that can be achieved with surrogate vegetation, it still takes a significant time to representative vegetation in an experiment which has a significant financial cost.

This research consists of a number of different experiments that: (i) elucidate how different stages of surrogate vegetation (Alfalfa) affects bank stability and the dynamics of a braided river system; and (ii) demonstrate how chemical surrogates that have instantaneous effects on sediment cohesion can be used as an alternative to growing surrogate vegetation. These experiments are conducted across different scales, with small bank erosion experiments to determine erosion rates for different ages and densities of surrogate vegetation followed by larger scale braided river experiments to demonstrate how the dynamic behaviour of the system is dependent on threshold ages of vegetation. These experiments include the novel use of chemical surrogates such as xanthan gum and sodium alginate which can be used in different concentrations to represent the behaviour of surrogate vegetation in both controlled bank erosion experiments as in dynamic braided systems.

Finally, this research introduces a new method to control the cohesive strength of these chemical surrogates. This method enables experiments to mimic the growth and decay of surrogate vegetation without the need to alter the sediment itself, thereby maintaining the characteristic existing morphology of previous stages. Experiments demonstrate that the chemical surrogates can be used to simulate sequences of vegetation growth, simulating either seasonal or longer-term climate induced changes in vegetation impacts of fluvial systems. Therefore this method significantly extends analogue scale modelling of complex fluvial systems.

Contents

Abstract.....	2
Contents.....	4
List of figures.....	8
List of tables	15
1. Introduction; Representing vegetation in experimental models of river systems.....	16
2. Literature review.....	20
2.1. Fluvial systems	20
2.2. Morphological adjustment of fluvial systems.....	21
2.2.1. Dependent and Independent variables	21
2.2.2. Equilibrium channel form, bankfull and dominant discharge	21
2.2.3. Channel pattern classification	21
2.3. Bank stability.....	24
2.3.1. Fluvial erosion	24
2.3.2. Mass failure.....	26
2.4. Fluvial – vegetation interactions	29
2.4.1. Timescales of adjustment in braided rivers.....	32
2.5. The application of physical modelling to fluvial science.....	34
2.5.1. Scaling in physical models	35
2.5.2. The “unreasonable effectiveness” of scaled models.....	37
2.5.3. Braided river experiments	37
2.5.4. Vegetation in large scale physical experiments.....	55
2.5.5. Use of surrogate vegetation	56
2.5.6. Other surrogates	58
2.5.7. Extracellular polymeric substances (EPS)	59
3. Small scale experimental research on bank erosion	61
3.1. Introduction to bank erosion and cohesion in natural systems.....	61
3.1.1. Vegetation in physical experimental models.....	65
3.1.2. Introduction to polysaccharides	66
3.1.3. Use of small-scale experiments to understand large-scale processes	67
3.1.4. Outline of this chapter.....	68
3.2. Experimental methodology	69
3.2.1. Experimental set-up	70
3.2.2. Experimental Runs.....	71
3.2.3. Preparation of sediment blocks.....	73
3.2.4. Data processing	83
3.3. Results.....	89

3.3.1.	Normalized eroded area of bare blocks.....	89
3.3.2.	Normalized area of erosion blocks with surrogate vegetation	91
3.3.3.	Normalized area of blocks with chemical agents.....	95
3.3.4.	Variation and erosion rate for bare blocks	98
3.3.5.	Variation and erosion rate for blocks with surrogate vegetation	100
3.3.6.	Variation and erosion rate for blocks with chemical surrogates	102
3.3.7.	Normalized area of blocks with sodium alginate	105
3.3.8.	Erosion rates for blocks with sodium alginate	108
3.4.	Discussion.....	111
3.4.1.	Bare blocks	111
3.4.2.	Blocks with surrogate vegetation	112
3.4.3.	Blocks with chemical agents	114
3.4.4.	Can chemical agents replace surrogate vegetation?	116
3.4.5.	Temporal and spatial variations in erosion rates.....	121
3.4.6.	Husbandry of surrogate vegetation	123
3.4.7.	Effectiveness of image analysis	124
3.5.	Conclusions	125
4.	Controlling chemical cohesive agents in small scale fluvial experiments	126
4.1.	Introduction	126
4.1.1.	Description of the problem	126
4.2.	Methodology.....	127
4.2.1.	Settings and experimental runs.....	129
4.2.2.	Sediment and bed preparation.....	131
4.2.3.	Sodium bicarbonate preparation	132
4.2.4.	Sediment collection	132
4.2.5.	TLS processing	133
4.3.	Results.....	136
4.3.1.	Constant conditions.....	136
4.3.2.	Planform river, alternating conditions.....	141
4.3.3.	Planform river, surface adjustments	145
4.3.4.	Conductivity and other environmental parameters	150
4.4.	Discussion.....	151
4.4.1.	Sodium bicarbonate	151
4.4.2.	Application of sodium alginate	153
4.4.3.	Experimental considerations	155
4.5.	Conclusion.....	158

5. Erosion rates in experiments with braided rivers to understand the impact of Alfalfa vegetation	160
5.1. Introduction	160
5.2. Experimental methodology	162
5.2.1. Experimental set-up	162
5.2.2. Experimental settings	165
5.2.3. Data collection	168
5.2.4. Post processing	169
5.2.5. Analysis	171
5.3. Results	174
5.3.1. Sediment output	174
5.3.2. Area of change	175
5.3.3. Rates of erosion and deposition - probability density functions	177
5.3.4. Comparison between channel beds	177
5.3.5. Impact of vegetation on erosion/deposition rates	178
5.3.6. Impact of flood event scale on erosion/deposition rates	179
5.3.7. Combining flood events with vegetation	179
5.3.8. Impact of the evolution of vegetation	180
5.4. Discussion	182
5.4.1. Erosion and deposition rates	182
5.4.2. Higher median lateral erosion lengths	184
5.4.3. Differences between the channels	186
5.4.4. Differences in discharge	187
5.4.5. Surrogate vegetation	187
5.4.6. Surrogate vegetation age	189
5.5. Conclusions	190
6. Discussion	192
6.1. Scaling	192
6.1.1. Vegetation spatial scaling	195
6.1.2. Temporal scaling	195
6.1.3. Chemical scaling	200
6.2. Use of surrogates in physical models	201
6.2.1. Live vegetation surrogates	202
6.2.2. Chemical surrogates	206
6.2.3. Is there a best approach?	208
6.3. Limitations	212
6.3.1. Discharge	212

6.3.2.	Experimental basin width	212
6.3.3.	Boundary effects	214
6.3.4.	Temporal effects	215
6.4.	Impact of vegetation	216
7.	Conclusion.....	220
	References	222

List of figures

Figure 2.1: Classification diagrams for rivers of A) Schumm (1985), B) Alabyan and Chalov (1998) and C) Church (2006), modified from Church (2006).	23
Figure 2.2: Shields diagram indicating the beginning of motion over different grainsizes. θ indicates non-dimensional Shields parameter, $\theta = \tau_b \rho_s / \rho g D_{50}$, where τ_b = applied boundary shear stress, ρ_s = density of sediment, ρ = density of water, g = gravitational acceleration and D_{50} = median grain size, and D^* indicates non-dimensional grainsize, $D^* = D_{50} g v^2 \rho_s / \mu^2$, where v = kinematic viscosity of water. Diagram based on van Rijn (1993).....	26
Figure 2.3. Schematic overview of three types of mass failure events along river banks; A: Rotational failure; B: Planar failure; C: Cantilever failure. Thick arrow indicates the direction of failure. Image based on FISRWG, Chapter 7 (1998).	28
Figure 2.4: Overview of temporal-spatial diagrams that distinguish between different physical model types. A) Peakall et al.'s (1996) physical modelling overview; B) Schematic overview of implications on replication of prototype by increased time or space (Kleinhans et al., 2014) modified after Peakall et al. (1996); and C) Relative application of different approaches for physical modelling over different spatial and temporal scales, modified after Peakall et al. (1996).....	35
Figure 3.1: Bank failure mechanisms: (a) rotational; (b) planar; (c) cantilever; and (d) piping or sapping. From (Langendoen & Simon, 2008).	63
Figure 3.2: Overview of a range of root architecture types reworked from Pagès (2011) based classification of Cannon (1949).	64
Figure 3.3: Plan-view overview of fluvial geomorphic research with alfalfa from A) Tal and Paola (2010), B) Braudrick et al. (2009) and C) Bertoldi et al. (2015).....	65
Figure 3.4: Small scale experimental set-ups of A) Friedkin (1945) and B) van Dijk et al. (2013).	69
Figure 3.5: A) Overview of the experimental set-up during an active run (image taken from downstream position). B) Schematic planform overview of the experimental set-up, including removable mould for placement of each sample. *Experiments 19-27 have an input discharge of 479 L/hr.	70
Figure 3.6: Cumulative grainsize distribution for CHSP30, CH30 and Redhill110 sediments.....	74
Figure 3.7: A) Overview of set-up during the growth phase of alfalfa samples. B) Example GoPro time-lapse image during one run with high-density vegetation. Image highlights the difficulties with capturing the bank line due to the overlapping vegetation.	75
Figure 3.8: Schematic overview of the experimental procedure for polysaccharide sample preparation	79
Figure 3.9: Overview of smallest scale preliminary tests with sodium alginate (SA) and sodium bicarbonate (SB), A) start of experiment, B) after 20 hours. Petri dishes from left to right show a) 1 g kg ⁻¹ SA + 20 g L ⁻¹ SB, b) 1 g kg ⁻¹ SA + 10 g L ⁻¹ SB, c) 1 g kg ⁻¹ SA + tap water, d) sand + tap water.....	81
Figure 3.10: A) Experimental set-up of up-scaled preliminary test. B-D) Top-view experimental sample after B) 2 hours (10 g L ⁻¹), C) 4.5 hours (20 g L ⁻¹) and D) 8 hours (30 g L ⁻¹) in the experiment.	82
Figure 3.11 Schematic flow diagram of the image analysis processing using MATLAB®.....	85
Figure 3.12: Sequence (A – E) of morphological operations used in the image analysis process. A) initial thresholded black and white image following <code>im2bw</code> . B) image following application of <code>imcomplement</code> and <code>bwareaopen</code> . C) image following application of <code>imdilate</code> and <code>imerode</code> . D) image following application of <code>imcomplement</code> , <code>imfill</code> , <code>imcomplement</code> , <code>imfill</code> and <code>imcomplement</code> . E final image following application of <code>dilate</code> , <code>imfill</code> and <code>erode</code>	86

Figure 3.13: Block area selection. A) Original grayscale image, B) Schematization of lines that identify the final block area (C).87

Figure 3.14: Normalized block area (block area at each time step divided by the maximum area of each sample) against time for bare block experiments with coarse sand, fine sand and a bimodal mixture composed of 50:50 fine and coarse sand. Dots indicate measurements for each individual run at each time step. Lines represent average for each experiment.90

Figure 3.15: Overview of normalized block area over time for all experiments with vegetation. Seed density increases towards the right subplots, age of vegetation increases further down in the subplots.92

Figure 3.16: Selection of captured uprooted surrogate vegetation from the experimental runs, subdivided between samples that have grown for 7, 10 or 13 days.94

Figure 3.17: Overview of normalized sediment block area against time for all experiments with chemical agents. Xanthan gum in the left column, carrageenan in the right column. Concentration of chemical agent increases downward. Carrageenan samples show five sequential increments of concentration, the column of xanthan gum only four. Rows show the same concentration for different chemical agents.97

Figure 3.18: Average erosion rates ($\text{cm}^2 \text{min}^{-1}$) against time for bare sediment block experiments with coarse sand, fine sand and a 50:50 mixture. Individual dots indicate averages over all runs per experiments for each time step; lines indicate 2.5-minute moving average. Rapid erosion in the initial time step exceeds the range of this plot.98

Figure 3.19: Variance against mean normalized block area for bare experiments. Mean normalized block area is determined by the average block area at each time-step divided by the maximum average block area for each experiment. Modified standard error (mse) is shown as standard deviation divided by the difference of maximum and average area. Individual points indicate modified standard error per time step, per experiment; lines indicate a 5-sample (150 second) moving average of modified standard error.100

Figure 3.20: Overview of erosion rates for all sediment blocks with surrogate vegetation; seed density increases towards the right, growth duration increases further down the subplots. Points indicate average erosion rate per time step, lines indicate moving average over 5.5 minutes.101

Figure 3.21: Modified standard error in erosion rates for erosion blocks with low density surrogate vegetation (left) and for erosion blocks with high density vegetation (right).102

Figure 3.22: Overview of average erosion rates against time for all experiments with chemical surrogates. Left column shows all experiments with xanthan gum, right column shows all experiments with carrageenan. Concentration of chemical agents increases downward and matches horizontally. Lines indicate a 9-sample (270 second) moving average for each experiment.103

Figure 3.23: Modified standard error in erosion rates against mean normalized block area for blocks with chemical surrogates; 4 concentrations of xanthan gum on the left, 5 concentrations of carrageenan on the right. Dots indicate modified standard error per time-step, lines indicate 9-sample (270 second) moving average.104

Figure 3.24: Normalized block area against time for experiments with an increasing concentration of sodium alginate under tap water flow conditions. Dots indicate individual data points. Solid lines show averages over time per experiment.106

Figure 3.25: Normalized block area over time for experiments with an increasing concentration of sodium alginate under flow conditions with a low concentration of sodium bicarbonate. Dots indicate individual data points. Solid lines show averages over time per experiment.107

Figure 3.26: Normalized block area against time for experiments with an increasing concentration of sodium alginate under flow conditions with a high concentration of sodium

bicarbonate. Dots indicate individual data points. Solid lines show averages over time per experiment.....	108
Figure 3.27: Erosion rates averaged per time step for experiments with an increasing concentration of sodium alginate under tap water flow conditions. Dots indicate average erosion rate per time step. Solid lines show a 2.5 minutes moving average.	109
Figure 3.28: Erosion rates averaged per time step for experiments with an increasing concentration of sodium alginate under flow conditions with a low concentration sodium bicarbonate. Dots indicate average erosion rate per time step. Solid lines show a 5-point (2.5 minute) moving average.	110
Figure 3.29: Erosion rates averaged per time step for experiments with an increasing concentration of sodium alginate under flow conditions with a high concentration of sodium bicarbonate. Dots indicate average erosion rate per time step. Solid lines show a 5-point (2.5 minute) moving average.	111
Figure 3.30: Diagram for the threshold for motion of different grainsizes based on van Rijn (1993). Red line indicates the 458- μm sediment, blue line indicates the 190 μm sediment....	112
Figure 3.31: Half-life time (hr) for all runs with chemical agents (xanthan gum (blue), carrageenan (red) and sodium alginate (green)) against concentration (g kg^{-1}) of the chemical agent and half-life time (hr) for coarse sand runs with 0 g kg^{-1} of added chemical agent. Experiments that did not finish are excluded. Experiment 7 (Xanthan gum 1.000 g kg^{-1}) is of the chart, with half-life times over 1 hour.....	116
Figure 3.32: Schematic erosion steps of an alfalfa sprout (green) in the experimental set-up under simplified erosion. A) Unaffected sprout; B) Soil matrix is eroded from around some lateral roots which deflect with flow; C) Soil matrix is eroded from around the main tap root, which deflects with flow; D) Stem bends and fall into flow; E) Last roots lose matrix (break or pull out). Average flow direction indicated by blue arrow.	117
Figure 3.33: Average erosion rates against time for sediment blocks composed of bare coarse sand, blocks with xanthan gum and blocks with low-density surrogate vegetation.	118
Figure 3.34: A) Experimental run with surrogate vegetation. Some individual alfalfa sprouts are floating on the water while others are captured downstream by neighbouring alfalfa sprouts. B) Erosion block with chemical agent (Xanthan gum), being dried in situ for several days. C) Experimental run with chemical agent indicating spatial irregularity in erosion.	119
Figure 3.35: Example of two time-lapse images without (A) and with (B) a bar forming on the inside of the experimental set-up. Progress in block area is similar on both images.	122
Figure 3.36: Examples of bank erosion; A) Potential for undercutting of a grassy bank at Waiau river (NZ). B) Failure blocks resulting from cantilever failure of an undercut bank in a small braided river (Dingle Burn (NZ)). Pictures by Bas Bodewes (2020).	123
Figure 4.1: A) Schematic overview and dimensions of the experimental basin. B) Overview of initial set-up of a planform river experiment looking sideward in downstream direction. C) Schematic view of spacing of nails in the spreading device based on a quincunx pattern. D) Close up on movable end tanks at the downstream end of the stream table.	128
Figure 4.2: Initial post processing steps Faro X330 terrestrial laser scans for each scan, using Scene 6.2.5.7. Target-based registration uses a selection of 12 checkerboards located in and around the stream table. Target-based registration is done separately for each experiment (n = 1 to 9).....	133
Figure 4.3: Second set of post processing steps in Cloud Compare v.2.9.1 used to transform point clouds into a rasterized digital elevation model (DEM). This includes translation and removal of standing water and reflections.	134
Figure 4.4: Interpolation of missing values (NaNs) in rasterized digital elevation model (left) to a digital elevation model (DEM) without missing values (right). Missing values (-) were	

interpolated using neighbouring values (x) using a 4-step algorithm (colour coded) as indicated by the close up (bottom).....	135
Figure 4.5: Flowchart of creating detrended, difference and channel maps for the analysis of digital elevation models (DEM). All maps show experiment 1 after 3 periods of flow (t) and after 2 periods of flow (t-1).	136
Figure 4.6: Planform evolution against time (top to bottom) of experiments 1, 2 and 3 described by detrended digital elevation models. Coloured boxes indicate tap water flow (yellow) or 10 g L ⁻¹ sodium bicarbonate per litre tap water (magenta). Spatial units in centimetres, elevation in millimetres.	137
Figure 4.7: Subplot of different variables against time describing experiments 1, 2 and 3. Symbols and legends match all individual figures. A) Relative sediment output (Sed_{out}/Sed_{in}) over three consecutive periods. Dotted line ($y=1$) indicates equilibrium, observations above indicate deposition of sediment. B) Relative expansion of the planform channel belt area per period. C) Volumetric change per period; Negative values indicate net erosion, positive values indicate net deposition. D) Width to depth ratio at the end of each period, distinction between an upstream area (0.25 m – 0.65 m) and downstream area (0.65 m – 1.05 m).	139
Figure 4.8: Planform evolution over time (top to bottom) of experiments 4 and 5 described by detrended digital elevation models. Both experiments have an alternating fluid content of tap water (yellow box) and 10 g L ⁻¹ sodium bicarbonate per litre tap water (magenta box). Spatial units in centimetres, elevation in millimetres.	142
Figure 4.9: Subplot of different variables against time describing experiments 4 and 5. Symbols and legends match all individual figures. A) Relative sediment output (Sed_{out}/Sed_{in}) over three consecutive periods. Dotted line ($y=1$) indicates equilibrium, observations above indicate deposition of sediment. B) Relative expansion of the planform channel belt area per period. C) Volumetric change per period; Negative values indicate net erosion, positive values indicate net deposition. D) Width to depth ratio at the end of each period, distinction between an upstream area (25 cm - 65 cm) and downstream area (65 cm - 105 cm).	144
Figure 4.10: Planform evolution over time (left to right) of experiments 6, 7 and 8 described by detrended digital elevation models. Each experiment is captured in two rows, the top row shows the evolution under bare conditions, and the bottom row of each experiment show the evolution when a cohesive agent is added (sodium alginate spray for experiments 6 and 7 or 10-day old alfalfa vegetation for experiment 8). Coloured boxes indicate tap water flow (yellow) or 10 g L ⁻¹ sodium bicarbonate per litre tap water (magenta). Spatial units in centimetres, elevation in millimetres.	147
Figure 4.11: Subplot of different variables describing experiments 1, 6, 7 and 8 over time. Symbols and legends match all individual figures. A) Relative sediment output (Sed_{out}/Sed_{in}) over three consecutive periods. Dotted line ($y=1$) indicates equilibrium, observations above indicate deposition of sediment. B) Relative expansion of the planform channel belt area per period. C) Volumetric change per period; Negative values indicate net erosion, positive values indicate net deposition. D) Width to depth ratio at the end of each period, distinction between an upstream area (25 cm - 65 cm) and downstream area (65 cm - 105 cm).	148
Figure 4.12: Conductivity (mS) over time for A) experiments 2 and 3 and B) experiments 4 and 5. Open markers indicate tap water measurements, closed marker indicate sodium bicarbonate solution measurements.	151
Figure 4.13: Experiment 9; A) Overview spatial distribution sodium alginate at start of the experiment. Blue indicates initial channel, darker shades indicate 0.5 g kg ⁻¹ sodium alginate – sediment mixture. B) Experiment during the third period (100 – 150 minutes).	158
Figure 5.1: Alfalfa vegetation under high flow conditions in run 2, images highlight that most above surface biomass of alfalfa is located above the flood level.	162

Figure 5.2: Overview of the experimental flume with two parallel beds, initial channels and the sediment and water in- and output locations with dimensions. Insets for inlet (A), initial channel (B) and outlet (C). Flow direction from left to right.163

Figure 5.3: Selections of images of the experiments taken during events 11-14 of run 2. A) Close up of inlet and sediment feeder. B) Longitudinal view of bed 2, looking downstream from inlet. C) Downstream weir and water and sediment collection basin(s). D) Upstream view of both beds including cameras positioned 2.5 m above the bed on the ceiling, Faro scanning locations A and B are located directly above the central wall, 2.5 m above the bed and 4 m apart.165

Figure 5.4: Schematic overview of experimental runs with alternation of 1-hour long flood events. Blue bars indicate discharge ($L s^{-1}$), red bars indicate sediment input ($g s^{-1}$). Each event is separated by a 40-60 minute data collection interval which is extended to at least 14 hours (14 hours for runs on subsequent days, or more for weekends or vegetation growing periods) at vertical dotted lines that mark a day break. Vegetation is seeded between events separated by dashed green lines.166

Figure 5.5: Schematic overview of the vegetation experiment (run 2), including the spin-up interval, growing breaks, flood events and seeding of alfalfa seeds.167

Figure 5.6: Initial post processing steps for the Faro X330 terrestrial laser scans for each scan pair A-B, using Scene 6.2.5.7. Target based registration uses a selection of 8 spheres and 25 checkerboards located in and around the flume.169

Figure 5.7: Second set of post processing steps in CloudCompare v.2.9.1 that transforms pairs of point clouds into a rasterized digital elevation model (DEM). This include merging, translation and a removal of standing water and reflections.170

Figure 5.8: Interpolation of missing values (NaNs) in rasterized digital elevation model (top) towards a digital elevation model (DEM) without missing values (bottom). Missing values (-) are interpolated using neighbouring values (x) using a 3-step algorithm (colour coded) as indicated by close up (right).171

Figure 5.9: Post processing and pre-analysis steps to determine erosion rates using Matlab© 2017. Flowchart includes DEMs of difference and erosion maps (right) and flow accumulation maps using Topotoolbox 2 (Schwanghart & Scherler, 2014) (left).172

Figure 5.10: Overview and order of morphological operations used to clean classified erosion maps (Figure 5.9).173

Figure 5.11: Overview of sediment output, blue diamonds indicate a single event, red line indicates mean of each dataset. A) Sediment output (kg) for all large and small flood events split between bed 1 and bed 2. B) Sediment output (kg) for all bare and vegetated events split between large and small flood events. C) Net sediment output (kg) for all bare and vegetated events split between large and small flood events.175

Figure 5.12: Area of change (areal percentage of the bed with a change of elevation over 2 mm) for large (open diamonds) and small (closed diamonds) flood events in bed 1 (green) and bed 2 (blue) for A) run 1 and B) run 2. Green bars indicate duration of growing breaks, time on the top shows total duration of vegetation cover.176

Figure 5.13: Probability density of erosion (red) and deposition (blue) rates collected from all experiments. Vertical lines indicate median of the dataset.177

Figure 5.14: Probability density of erosion (left) and deposition (right) rates collected from all events in bed 1 (red) and bed 2 (blue). Vertical lines indicate median of each dataset.178

Figure 5.15: Probability density of erosion (left) and deposition (right) rates collected from all events in the non-vegetated experiment (red) and the vegetated experiment (blue). Vertical lines indicate median of each dataset.179

Figure 5.16: Probability density of erosion (left) and deposition (right) rates collected from all large flood events (red) and all small flood events (blue). Vertical lines indicate median of each dataset.179

Figure 5.17: Probability density of erosion (left) and deposition (right) rates collected from all large flood events (top) and small flood events (bottom) for the non-vegetated (red) and vegetated experiments (blue). Vertical lines indicate median of each dataset.....180

Figure 5.18: Median of erosion (red) and deposition (blue) rates for experiments with vegetation cover differentiated over days of vegetation cover before the event for large flood events (left) and small flood events (right). Lines indicate the mean of the bare experiments under further identical conditions.181

Figure 5.19: Four different approaches to quantify erosion rates, solid line indicates previous bank line, dashed line indicates new bank line. Crossed filling indicates area. A) Planform metrical erosion (bank top retreat), B) Planform areal erosion (spatial bank top retreat), C) Cross-sectional areal erosion, D) Lateral erosion length (horizontal length of section with reduced elevation), used in this research.183

Figure 5.20: Overview of lateral erosion and deposition lengths in different hypothetical cross-sections/ scenarios. Top part of each graph shows cross-section with current elevation (solid line) and previous elevation (dashed line). Bottom part of each graph shows the application of the threshold vertical elevation change to identify regions of erosion (red) and deposition (blue) along the cross-section. Points with vertical elevation changes with a magnitude less than the threshold are neither depositional nor erosional. Scenarios include A) a channel migrating laterally to the right. B) a channel migrating laterally to the right while also expanding, C) an incising channel and D) a complex terraced channel migrating to the right.184

Figure 5.21: Schematic plot in phase space of bank-migration scenarios showing the different phases of channel-bank interaction. n_{LB} and n_{RB} are the migration rates of the left and right banks, respectively (Eke et al., 2014).185

Figure 5.22: Overview of overall trends of lateral erosion and deposition in vegetated and non-vegetated experiments for A) all events, B) large flood events only and C) small flood events only. Overview of trends of lateral erosion and deposition in vegetated events over time for D) large flood events and E) small flood events.....188

Figure 6.1: Schematic overview of different types of physical models and their placement over spatial and temporal scale. Coloured fields indicate suggested location of the present experiments highlighted in orange (bare experiments). B_b are the bare braided experiments, S_b are the bare planform river experiments and F_b are the bare bank erosion experiments (concept after Peakall et al., 1996).194

Figure 6.2: Schematic conceptual overview of features to describing characteristics of hydrographs.....196

Figure 6.3: Schematic overview of three conceptual vegetation time scales indicating recovery, seasonal and life cycle. Combined (not shown), recovery and seasonality superimposed on a lifecycle it shows the conceptual strength of vegetation over time.....198

Figure 6.4: Schematic overview of different types of physical models and their placement over spatial and temporal scales. Coloured fields indicate suggestive location of the present experiments highlighted in orange (bare experiments) or green (experiments with surrogates). Uppercase B are the braided experiments, S are the planform experiments and F are the bank erosion experiments. Subscripts indicate bare settings (_b), vegetated settings (_v) or settings with surrogates (_c) (concept after Peakall et al., 1996).200

Figure 6.5: Schematic overview scaling choices of different used surrogates within the present sets of experiments.....200

Figure 6.6: Flow-diagram of choices and options when using two surrogates to represent vegetation in a physical model. Diagram of surrogate vegetation, based on Alfalfa, on the left, diagram of surrogate chemicals, based on Xanthan Gum, Carrageenan and Sodium Alginate, on the right.202

Figure 6.7: Conceptual spatial-mobility diagram with spatial scale of experiments against relative channel mobility; conceptual channel mobility described as channel movement relative to channel width ($ms^{-1}m^{-1}$). Shading indicates preference for surrogate vegetation (green) or chemical surrogates (pink). Uppercase letters indicate braided river experiments (B), planform river experiments (S) and bank erosion experiments (F).211

Figure 6.8: Examples of bank erosion; A) Potential for undercutting of a grassy bank at Waiau river (NZ). B) Result of an undercut bank as compact blocks of soil in a small braided river (Dingle Burn (NZ)). Pictures by the author (2020)217

Figure 6.9: Overview of different stages of vegetation succession in active braided systems in New Zealand. Colours in A highlight the different stages of succession occurring simultaneously in the channel belt of the Upper Waimakariri- grey = base sediment, yellows = mosses, light green = grasses, dark green = trees. B mosses at Steele Creek, C small herbaceous vegetation at Waimakariri river and D grasses at Hopkins river. Pictures by the author (2020).218

Figure 6.10: Map of bed 1 after the final event (14) of Run 2 that indicates the last event that erosion (> 2 mm) occurred for each cell. These types of maps can be used to capture the temporal evolution of the spatial distribution of the channels over the bed and linked to the potential age of vegetation.219

List of tables

Table 2.1: Overview of previous physical modelling studies of fluvial systems, indicating institution and author as well as geometrical dimensions of the physical model (Length, width, slope). Overview includes sediment size, discharge and sediment rate as well as duration of the experiment (when available).	39
Table 3.1: Overview of first set of experiments, experiments 1-18, with conditions, repetitions and characteristics.	72
Table 3.2: Overview of second set of experiments, experiments 19-27, with conditions, repetitions and characteristics.	80
Table 3.3: Vegetation root characteristics measured from photographs taken from uprooted surrogate vegetation (see examples in Figure 3.16).	95
Table 3.4: Normalized average erosion (-) (normalized by erosion of bare blocks composed of coarse sediment (exp. 1)) for all experiments of blocks with vegetation organized by seed density and vegetation growth duration.	113
Table 3.5: Normalized average erosion (-) (normalized by erosion of bare blocks composed of coarse sediment (exp. 1)) for all experiments of blocks with chemical agents organized by concentration and chemical agent (Xanthan gum, Carrageenan and sodium alginate).	114
Table 3.6: Normalized average erosion (-) (normalized by erosion from bare blocks with coarse sediment) for three experiments of blocks with xanthan gum and for three experiments with low-density alfalfa surrogate vegetation.	118
Table 4.1: Overview of planform river experiments. First column indicates initial bed content; sand refers to 458 μm sediment, sodium alginate refers to 0.5 g kg^{-1} premixed sodium alginate. The subsequent four periods show whether the experimental period runs with tap water or with bicarbonate solution. In experiments 6-8, conditions change mid-experiment, noted by the addition of sodium alginate spray or 10-day old vegetation. * This period is only 40 minutes long. ** This initial bed has sodium alginate mixed in in only the upstream 0.15 m and the outermost 0.10 m on each side.	130
Table 5.1: Key dimensional variables (length, width, sediment size, discharge and slope) for various experiments on braided rivers.	164
Table 6.1: Analogue braided river experiments placed in context by showing different Froude scaling factors based on sediment size.	193

1. Introduction; Representing vegetation in experimental models of river systems

Fluvial systems have been important over the centuries, either as a supply of water, as a method of transportation or a key corridor for ecology, which result in well developed research on rivers. Until recently, the behaviour of rivers was considered as relative constant, with changes in behaviour only forced due tectonics or changes of land cover and other anthropogenic influences. However, more recently, rivers also became subject of shorter-term climatic changes that predict rapid changes in precipitation and thus discharge regimes in fluvial systems. An increase in temperature is predicted to provide the possibility of higher and more frequent peak flows in conjunction with more prolonged periods of draught (IPCC, 2014). Whereas many individual or generic fluvial systems have been studied intensively in the past over a range of temporal and spatial scales, medium to long term changes have had only limited attention. Not short enough to impose immediate change, not long enough to impose a change in system behaviour. Within fluvial research, this is not a massive shortcoming, as expertise exist to upscale research of these systems over both time and space.

However, over the past decades it became common understanding that the behaviour or characteristic of fluvial systems is not only dominated by grain size, gradient and discharge (Church, 2006), but also heavily impacted by vegetation in these systems (Gurnell et al., 2016). Vegetation is understood to add a cohesive effect to the sediment, increase the roughness and flow resistance during higher flows and promote sediment trapping outside the main channels (Gurnell, 2014). Concurrently the strength and growth of this type of vegetation is subject of the flow regime itself. Not only does the fluvial system provide water and nutrients to allow vegetation to grow, it also can damage or even destroy or wash away vegetation during periods of higher flow. On top of that, on a larger spatial scale, fluvial systems stimulate seed distribution and plant growth when the hydrodynamic time scales align with the seasonal growth of species of vegetation (Garssen et al., 2014, 2015). As a result, the impact of this vegetation under

changing climatic conditions is unknown and as such a factor of uncertainty in the evolution of a fluvial system.

However, growth (and decay) of natural vegetation ranges from years to several decades, a period of time that overlaps with a range of climatic change effects that impact over periods of a few decades. As a result, both these impacts are expected to be closely related and as such critical in understanding the impact climate change has on fluvial systems. In particular as suggestive shifts in fluvial systems are often linked towards a change in vegetation (Kleinhans & van den Berg, 2011). This latter is highlighting a key concept introduced by Murray and Paola (1997), where the river width (and thus similarly river type) is dominated by the strength of the bank. In general this bank strength is increased by existing vegetation (e.g. Bankhead et al., 2016). However, so far common research techniques that require fieldwork and/or remote sensing techniques are limited monitor the impact of ongoing changes by medium term periods. Moreover, field data on vegetation is often hard to gather as in situ fieldwork often causes disturbances that interact with the fluvial system itself. Finally, an increased peak flow is often hard to capture, in particular as they have to potential to expand beyond previous boundaries.

Despite these barriers are relative hard and in particular time consuming to overcome within field campaigns, other approaches exist that can help understanding these impacts rapidly. Physical modelling has the potential to understand processes at larger temporal and spatial scale and thus explore different scenarios more thorough. However, in order to unlock this potential fully, an understanding is required on how to represent vegetation in physical models. Over the past decades small surrogate vegetation has been introduced in physical modelling (Gran & Paola, 2001). Whereas further research (Braudrick et al., 2009; Tal & Paola, 2007; van Dijk, van de Lageweg, et al., 2013) has continued to build upon this experiment, it often limited to increased cohesion to understand the impact of meandering systems, thereby abandoning an unknown potential for braided systems.

Part of this reasoning is linked to one of the current downsides of the use of surrogate vegetation. Surrogate vegetation significantly increases the length of experiments, as it needs to allow vegetation the time to sprout and develop. Obvious different techniques exist in seeding vegetation (Clarke, 2014) or placement of more full grown vegetation (Frostick et al., 2014), each technique comes with its own benefits and shortcomings. On top of that, the lack of a developed protocol for the use of surrogate vegetation, allows a wide range of methods to be specified for their unique physical experiment. As such physical modelling would benefit strongly from a structured method that ideally could overcome the main shortcoming of surrogate vegetation; time. A faster alternative would ideally allow an increased number of experimental repetitions, a wider range of alternatives or just a plain reduction in experimental costs; all contributing to more thorough and focused research.

As such, this research, aims to explore different surrogates for vegetation to understand their behaviour and how that could contribute to an improvement of physical models. After a broad overview on the current state of research on rivers and physical modelling (chapter 2), this research, with a selection of experiments, attempts to contribute to a better understanding of these surrogates. Hence, the most commonly used surrogate, alfalfa (*Medicago sativa*), is used to elucidate how different growing stages affect erosion rates and bank stability in small-scale experiments (chapter 3). Experience and knowledge gained from these experiments is then used to understand the impact of added vegetation on the evolution of a braided system under a variation of discharge regimes and sequential vegetation growth (chapter 5). Concurrently three types of chemical surrogates, often referred to as EPS in previous experimental research (Baynes et al., 2018; Malarkey et al., 2015; van de Lageweg et al., 2018), and known for their cohesive behaviour, were used in identical small-scale experiments to understand their impact on erosion rates and bank stability. These three chemical surrogates, xanthan gum, carrageenan and sodium alginate, are described in chapter 3 where they are compared to the experiments with alfalfa. Sodium alginate, one of these explored chemical surrogates, is subject to medium scale planform experiment (chapter 5). This experiment expanded further as it used a novel method

to alter the cohesive behaviour of the sodium alginate by adding sodium bicarbonate to the fluid in a small fluvial system (chapter 5) in an attempt to represent vegetation. Chapter 6 will bring this research together by giving a suggestive summary on how to represent vegetation in physical models, where to use different techniques and what to else to consider when dealing with natural vegetation. Chapter 6 will also reflect back on how vegetation changes the behaviour of fluvial systems.

2. Literature review

Rivers play an important role on Earth: their floods provide both fertile land around their margins as well as significant disruption and destruction (Marshak, 2008). In recent decades, the pressure on fluvial systems has increased across the planet due to human population, either directly or indirectly (e.g. Knighton, 1998). Over the past centuries, understanding on rivers and river systems has grown significantly, but rivers continue to evolve either by potential human or climatic forcings (Bendix & Stella, 2013). Although this already sets itself as a complex problem, the existence of vegetation in and along the riverbed and banks adds more complexity to understanding these systems (e.g. Tal et al., 2003; Thorne, 1990). As such, it is important to understand not only how water-sediment systems behave under both stable and shifting conditions but also how these systems behave in conjunction with vegetation. One of the key tools to understand and predict their behaviour is the modelling of coupled water-sediment-vegetation systems (e.g. Kleinhans, 2010a). As such, this thesis aims to improve our understanding of the behaviour of these systems while simultaneously aiming to improve the robustness and applicability of the physical modelling tools to represent vegetation in fluvial experiments.

2.1. Fluvial systems

The basic principles of a fluvial system are now well understood; water that reaches the ground through precipitation passes over or through the ground into streams that merge to form rivers that flow downstream and eventually end up in a final basin (e.g. often the oceans or seas) (e.g. Marshak, 2008). Along the way, fluvial systems erode, transport and deposit sediments along their course, adjusting the morphology along the way.

2.2. Morphological adjustment of fluvial systems

2.2.1. Dependent and Independent variables

There are a number of driving/independent variables for fluvial systems (Figure 2.1; Thorne (1997)). Some variables that are driving/independent variables (e.g. vegetation or hillslope) at long time scales/large space scales at shorter time and smaller space scales (Schumm & Lichty, 1965).

2.2.2. Equilibrium channel form, bankfull and dominant discharge

Fluvial systems adjust to these driving/independent variables at a range of time and space scales (e.g. Wohl et al., 2015), such that channel form is adapted to the imposed conditions. This leads to the concept of bankfull flow depth (the elevation of the flow that transports the most sediment over the long term dominant discharge concept) (Nanson et al., 2010) and hydraulic geometry (Eaton, 2006). Which type of geometric adjustment is dominant (widening or deepening) is controlled by the relative erodibility of the bed and banks (Simon & Darby, 1997). If the bed is more erodible than the banks, then the channel will incise preferentially. If the banks are more erodible, the banks will erode. Ultimately both processes lead to the same outcome; banks get steeper so less geotechnical stable.

2.2.3. Channel pattern classification

Although all fluvial systems are unique, in the past several methods and theories have been applied to classify or describe their behaviour in order to be able to predict and plan how certain rivers may behave (Leopold and Wolman, 1957; Kellerhals and Church, 1989; Alabyan and Chalov, 1998; Church, 2006). Kleinhans et al. (2010b) noted that most channel pattern classification methods are either based on flow strength or stream power (Leopold and Wolman, 1957) or based on sediment feed (Church, 2006; Ferguson, 1987; Kellerhals & Church, 1989). Leopold and Wolman (1957) initially differentiated between braided, meandering and straight channel patterns and linked this to mainly river discharge and, to a lesser extent, valley slope and sediment load. However, throughout their work, Leopold and Wolman (1957) emphasised

a continuum of form- channel patterns may not be distinct and instead a channel may have characteristics of stereotypically braided, meandering and straight channels. Furthermore, this continuum, and a natural system's ability to adjust in response to disturbance, is not well reflected by static classification systems (Simon et al., 2006).

Kellerhals et al. (1976) used four different multistage classification diagrams (channel pattern, vegetated channel islands, non-vegetated bars and lateral activity) that were primarily based on a wide range of planform characteristics. Schumm (1985) described a clear distinction between rivers with limited or no freedom, semi-bedrock rivers or bedrock rivers, and rivers with no limitations, alluvial rivers (Figure 2.1A). The present research will focus primarily on alluvial rivers in order to understand the natural processes and interactions and as such will ignore bedrock rivers. Alabyan and Chalov (1998) classified rivers using a combination of three main planform configurations (straight, meandering and branched) and three structural levels (valley bottom, flood channel and low water channel) (Figure 2.1B), relaxing the relation between discharge and channel pattern. Kellerhals and Church (1989) attempted to relate planform characteristics to sediment characteristics, hydrology and channel gradient in a single diagram from meandering towards braided based on predicted responses. Church (2006) reorganized these findings into a more coherent diagram (Figure 2.1C).

Church (2006) described channel pattern in terms of channel stability, the tendency a channel has to alter its course, either consistently or abruptly. The y-axis of his diagram (Figure 2.1C) shows the similar impact of an increased channel gradient and increased sediment size: both decrease channel stability as sediment can become more mobile due to potential of the flow. On the x-axis of Church's diagram is sediment supply: an increase in supply will decrease the stability of the channel as sheer volume of sediment will increase the pace at which change may occur and thus decrease the stability of the channel. Nonetheless, this is different from the effect of increased sediment size or valley gradient since increased sediment supply leads to increased channel belt width, which also promotes a higher likelihood for a multichannel pattern.

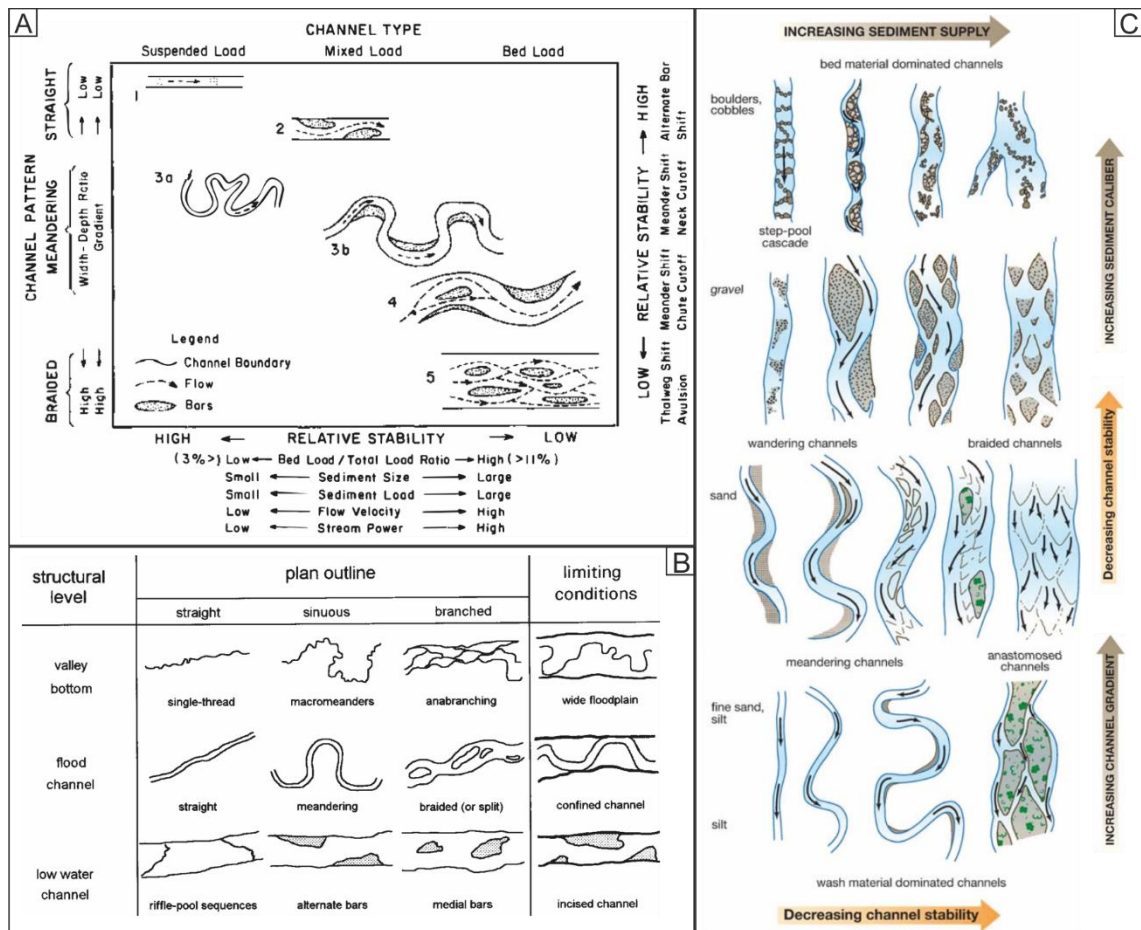


Figure 2.1: Classification diagrams for rivers of A) Schumm (1985), B) Alabyan and Chalov (1998) and C) Church (2006), modified from Church (2006).

The above classifications, although diverse all have their unique shortcomings, share a critical shortcoming; they all set aside bank strength as a primary determinant. However as already was highlighted by Ferguson (1987) and emphasised by Murray and Paola (1997) and Paola (2001) the balance between bank stability and floodplain sedimentation influences channel width and in extension channel pattern (Kleinhans, 2010). Indeed, Murray and Paola (1997) and Paola (2001) argued that ‘braiding is the fundamental instability of streams flowing on non-cohesive material’ (Paola, 2001, p. 22). In other words, braided systems are the norm if the width of rivers is not restricted by some form of bank strength, the only exception being straight rivers which are basically systems with a low width to depth ratio and a low sediment load (Bolla Pittaluga et al., 2003).

2.3. Bank stability

This obvious importance of bank stability being the key control of river channel pattern (Paola, 2001) stimulates an understanding of bank stability. Bank stability is primarily controlled by the driving forces of the shear stress applied by the flow and the weight of a potential failure block and the resistive forces of the weight of particles resting on the bank toe or face and the shear strength of the bank (e.g. Darby & Thorne, 1994; Osman & Thorne, 1988; Simon et al., 2000). The term bank stability thus comprises two distinct processes: fluvial erosion, driven by hydraulic shear forces, and mass failure events, driven by geotechnical forces. These processes are linked by the mechanism that was termed “basal endpoint control” by Carson and Kirkby (1972) and applied to riverbanks by Thorne (1982).

2.3.1. Fluvial erosion

Fluvial erosion is a process that generally takes place at the base of the bank, which is known as the bank toe (e.g. Simon et al., 2000). Here, water flows past and over the sediment, exerting an applied hydraulic shear stress to the bank toe materials. In sinuous channels, hydraulic shear stress is enhanced by a centrifugal force that naturally forces water towards the outer bank, thereby increasing water depth and flow velocity slightly (Simon et al., 2000). The local applied shear stress is resisted by two different components, ‘skin friction’ and ‘drag stress’ (Kean & Smith, 2006); skin friction is directly related to grain roughness while drag friction is related to larger scale morphological variations protruding into the flow. As a result, drag stress is the dominant force in natural banks which are often highly irregular (Kean & Smith, 2006). Erosion occurs if the combined hydraulic shear stress exceeds the critical shear stress of the bank materials (e.g. Partheniades, 1965).

For non-cohesive sediments, the critical shear stress of sediment depends on the grain size of the sediment (Shields, 1936, Figure 2.2). The Shields curve shows that the amount of shear stress needed to set a particle in motion reduces to a minimum Shields parameter of 0.03 at a non-dimensional grain size of approximately 2, coinciding with the fine sand range. However, critical

shear stress can be increased by variations in angularity, by mixed or non-evenly distributed sediments which influence interlocking and the angle of repose (which is equivalent to the friction angle in non-compacted sediments; Selby (1982)). For finer sediments, the shear stress needed to put a particle in motion increases sharply, reflecting the cohesive effect of finer particles (e.g. clay) which tend to form cohesive bonds or van der Waals forces (Peakall et al., 1996) and the pore-water pressure, which is controlled by the extent of saturation (Casagli et al., 1999). Saturated banks develop positive pore-water pressures that reduce critical shear stress (Fredlund & Rahardjo, 1993) while unsaturated banks develop negative pore-water pressure, or matric suction, that increases critical shear stress (Fredlund & Rahardjo, 1993). Thus, temporal or spatial variations in saturation can alter critical shear stress. In addition, critical shear stress can also be altered by the addition of vegetation, in particular the roots of vegetation which often act as a reinforced structure within the bank (e.g. Simon & Collison, 2002; Thorne, 1990). Therefore, the erosion rate, e , of cohesive materials is often expressed through an excess shear stress equation (e.g. Langendoen & Simon, 2008; Partheniades, 1965) with the erodibility coefficient k describing the rate of erosion for a given non-dimensional excess shear stress:

$$e = k \left(\frac{\tau_b - \tau_c}{\tau_c} \right)^\alpha \quad (2.1)$$

where τ_b = applied boundary shear stress, τ_c = critical shear stress and α = non-dimensional exponent that is commonly assumed to be equal to 1. The erodibility coefficient is controlled by the chemistry of the pore-water and river water, temperature, and other factors (e.g. Camporeale et al., 2005; Hanson & Simon, 2001; Kelly & Gularte, 1981; Mehta, 1991).

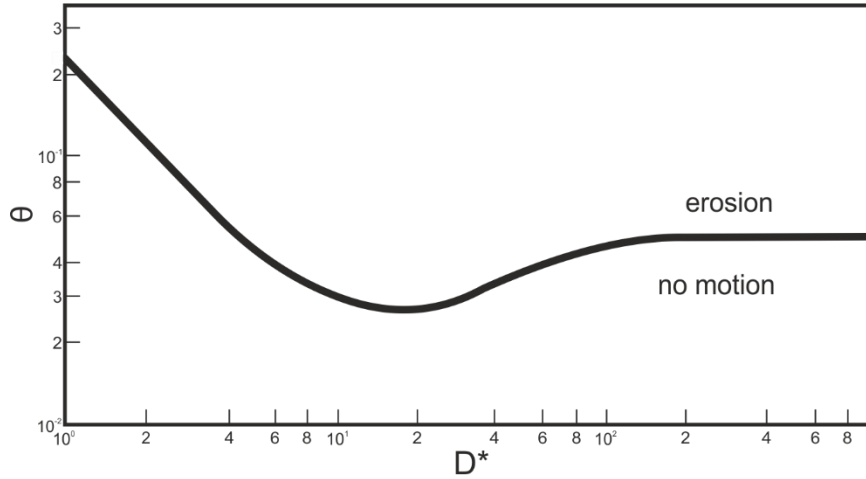


Figure 2.2: Shields diagram indicating the beginning of motion over different grainsizes. θ indicates non-dimensional Shields parameter, $\theta = \frac{\tau_b}{(\rho_s - \rho)gD_{50}}$, where τ_b = applied boundary shear stress, ρ_s = density of sediment, ρ = density of water, g = gravitational acceleration and D_{50} = median grain size, and D^* indicates non-dimensional grain size, $D^* = D_{50} \left(\frac{g(\rho_s - \rho)}{v^2 \rho} \right)^{1/3}$, where v = kinematic viscosity of water. Diagram based on van Rijn (1993).

2.3.2. Mass failure

The second process controlling bank stability, mass failure, is a discontinuous geotechnical process (Rinaldi & Darby, 2007). Mass failure is triggered when the driving geotechnical forces (component of the weight of the potential failure block parallel to the potential failure plane + positive pore-water pressure) exceed the resisting geotechnical forces (soil shear strength + hydrostatic confining force afforded by any water in the channel) (e.g. Langendoen & Simon, 2008)). Soil shear strength, τ_s , comprises a frictional component, a cohesive component, and a pore-water pressure component (Casagli et al., 1999; Simon et al., 2000):

$$\tau_s = c' + (\sigma - \mu_a)\tan\phi' + (\mu_a - \mu_w)\tan\phi^b \quad (2.2)$$

where c' = effective cohesion, σ = net normal stress on the failure plane which includes the component of the weight of the potential failure block perpendicular to the potential failure plane – hydrostatic uplift force, μ_a = pore air pressure, μ_w = pore water pressure, ϕ' = effective friction angle and ϕ^b = angle that reflects the proportionality between an increase of matric suction ($\mu_a - \mu_w$) and shear strength. Sandy and gravelly soils tend to have higher friction angles

but lack cohesion (e.g. Selby, 1982), while silty and clayey soils tend to have lower friction angles but have cohesion (e.g. Selby, 1982).

Mass failures occur along a weak 'failure plane' inside the bank. These failure planes are in general the weakest point of the bank and can include cracks, boundaries between different soil or sediment types or even larger root structures (Thorne & Tovey, 1981). Some failure planes are more susceptible to fail under specific environmental conditions, e.g. cracks can become more pronounced in dry or sub-zero conditions and layered banks can cause groundwater flow to prevail in wet conditions. There are three main types of failures (Hagerty et al., 1995):

1. Rotational failures often occur on higher banks with a relative gentle cross-sectional slope (FISRWG (1998) Figure 2.3A). Here, a failure plane is often shaped as rotational surface, partially moving the top of the bank downward and the toe into the flow. Rotational failures tend to be of larger scale and are often the 'least complex' type of mass failure as they are often the result of a change in mass balance between the toe of the bank and the mass higher up the bank (Langendoen & Simon, 2008). Whereas weaker failure planes (e.g. cracks or layers) can exist in rotational failures, they are often only limited to local failure planes (Langendoen & Simon, 2008);
2. Planar failures, in contrast to rotational failures, occur often on lower banks with a steeper cross-sectional slope (FISRWG (1998) ; Figure 2.3B). In these failures, sediment above a more or less straight failure plane slides down the bank and into the stream as a whole where it then can be removed by the flow (Osman & Thorne, 1988). Planar failures most often occur along a distinct layer boundary and can be weakened by changes in permeability or saturation. This weak layer then acts as a sliding surface along which the upper bank fails (Langendoen & Simon, 2008). Planar failures can extend all the way up to the surface but can be shortened by cracks or reinforcements (e.g. roots) across the sediment layers (Osman & Thorne, 1988); and

3. Cantilever failures are often seen in steep banks with several different sediment or soil layers (FISRWG (1998), Figure 2.3C). Cantilever failures are particularly abundant where a cohesive layer is positioned above a less cohesive layer (something common in temperate climates as vegetation forms a top soil layer that is in general more cohesive due the addition of organic materials). In these settings, toe erosion occurs dominantly in the 'weaker' bottom layer and thereby it will undercut more cohesive upper layers, causing an overhang of the surface layer(s). Over time, this cohesive overlaying layer becomes more susceptible to failure, which often occurs along a weak failure plane like a vertical crack (Thorne, 1992). Like the other types of mass failures, cantilever failure results in the deposition of a failure block at the bank toe, which temporarily buttresses the bank toe from erosion by the flow (Osman and Thorne, 1988).

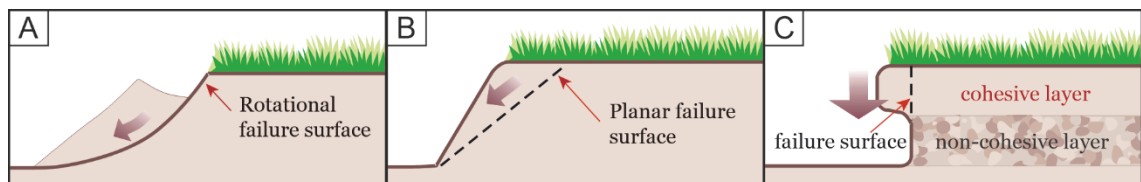


Figure 2.3. Schematic overview of three types of mass failure events along river banks; A: Rotational failure; B: Planar failure; C: Cantilever failure. Thick arrow indicates the direction of failure. Image based on FISRWG, Chapter 7 (1998).

As mentioned, fluvial erosion and mass failure are linked through a mechanism termed basal endpoint control (Carson & Kirkby, 1972). In this mechanism, an initial stable bank becomes subjected to the flow (e.g. during a flood event) and as a result erosion removes sediment from the toe. As a result, the bank steepens, causing the bank to be more susceptible to mass failure. Once mass failure occurs, the failed material of the bank is deposited at the bank toe. Here the mass of sediment forms a protective buffer in front of the part of the bank that is still intact. However, this material in front of the bank is often more susceptible to erosion than the previous stable bank due to looser materials and initially increases the drag fraction of the shear stress. Eventually the bank material is removed by the flow and a stable bank remains (Thorne, 1982).

2.4. Fluvial – vegetation interactions

Whereas fine cohesive sediments are often either restricted to specific geological settings or distal parts of fluvial systems (Marshak, 2008), vegetation impacts the fluvial system along its entire length (and to some extent promotes the availability of cohesive sediments). Vegetation plays a key role in both the driving and resisting forces: vegetation stems and leaves can deflect flow away from the banks and thus reduce boundary shear stress (Thorne, 1990) and it can increase the shear strength of the bank materials by increasing matric suction (Pollen, 2007) and by its roots acting as reinforcing elements. Soil is weak in tension but strong in compression, whereas roots are strong in tension but weak in compression (Thomas & Pollen-Bankhead, 2010), thus a root-permeated soil matrix is stronger under both tension and compression than soil alone.

Riparian vegetation thrives, changes or collapses with an altering climate or changing fluvial hydrographs. Conversely, plants are ecosystem engineers (e.g. Jones et al, 1994) and their activities tend to improve conditions for them to proliferate and thrive (e.g. Bertoldi et al., 2015; Corenblit et al., 2007; A. Gurnell, 2014). Thus, river channel flows impact plants but plants also impact river channel flows and morphology through a complex feedback loop (e.g. Braudrick et al., 2009; A. Gurnell, 2014).

The interaction of vegetation with the flow is often straightforward: vegetation increases the surface area of a cross-section of a river (e.g. Coulthard, 2005), increasing the total friction of a cross-section. However, as most vegetation is growing outside the channel on bars, floodplains or on the river bank, most interactions with the flow occur during floods or higher discharge scenarios. As water levels rise, vegetation becomes slowly submerged which, dependent on the type and shape of the vegetation, slowly increases the impact on the flow (e.g. A. Gurnell, 2014).

As vegetation obstructs the flow, water levels slightly increase and flow velocities decrease. In sub-critical flow, this effect is observed directly upstream of vegetation and fades out while it propagates further upstream due to a backwater effect (e.g. Kleinhans et al., 2013). The extent

of flow obstruction is dependent on the type, age and health of the vegetation, as these primarily determine how it interacts with the flow. Some vegetation is very sturdy (tree trunks) while other vegetation is very flexible and will bend with the flow (herbs). Moreover, some vegetation can be dense, permitting limited through flow, while other vegetation is very scattered, permitting more through flow (e.g. A. Gurnell, 2014). All these contribute to a complex determination of the drag enforced on the flow. At locations next to vegetation, water funnels past or in between vegetation, thereby increasing the flow velocity and water surface slope. As such, sediment in between vegetation is more likely to erode and as erosion takes place this area will slightly expand upstream. Meanwhile areas downstream of vegetation are more likely to experience deposition.

The impact of vegetation on streambank stability can be divided into hydrologic and mechanical effects (Simon & Collison, 2002). Mechanically, the strength of soil is high in regard to compressive forces but weak against tensile forces. In contrast, roots have a high tensile strength and low compressive strength. As such, a combination of both soil and roots will result in a composite conglomerate bank, which can withstand a wider range of forces compared to either parts on their own. Nevertheless, under increased stresses, the bank may fail and roots will either break or pull out of the soil intact. If root tensile strength and root length are functions of root diameter (e.g. Pollen, 2007; Pollen-Bankhead & Simon, 2008; Simon & Collison, 2002; Thomas & Pollen-Bankhead, 2010), which scenario takes place can be determined by a threshold root diameter based on the shear strength of the soil, which is dependent on soil type and moisture content (Pollen, 2007). Similar processes occur when vegetation is subjected to flowing water (Perona et al., 2014; Pollen-Bankhead et al., 2013). Shear stresses applied by flowing water can damage vegetation in several ways. Vegetation can lose branches or other parts of its biomass due to breaking of individual pieces. Further, vegetation can become separated from its roots by either root or stem breaking, and thus washed away by the flow with (part of) the roots still intact in the sediment (Pollen-Bankhead et al., 2013). Thirdly, vegetation may be uprooted by the shear stress of the flow overcoming the tensile strength or pull out

(frictional) resistance of the roots and thereby being washed away with the flow completely (e.g. Perona et al., 2014; Pollen-Bankhead et al., 2013). A particular case is when vegetation loses tensile strength in the roots due to sediment being eroded in between the roots, a process more common in the undercutting process of bank erosion (Pollen-Bankhead et al., 2013). Finally, vegetation can become buried by deposited sediment due to a change in morphology in the fluvial system.

Riparian vegetation alters the direct moisture content of the soil by canopy interception and evapotranspiration. As such, banks will have an increased stability due to reduced weight and lower pore-water pressures. On the other hand, riparian vegetation also decreases bank stability. Firstly, plants and trees add weight to the bank (Simon & Collison, 2002) and secondly plants will, when they interact with the flow directly, increase hydraulic roughness or will even divert the flow towards or away from the bank that may open a spatial window for bank instability (Rowntree & Dollar, 1999).

In riparian systems, longer periods of drought will shift the vegetation species to more drought-resistant species. In this process, species richness of the riparian zone is reduced and some hydrophilic species suffer mortality. Both a decline in biomass and a reduction in seedling survivability may be the result of these longer periods of drought. Seedling survival is in particular reduced, since due to a decline of the water table seedlings require longer roots for water uptake (Garssen et al., 2014).

In contrast, vegetation has the potential to be subject to higher magnitude, longer duration and more frequent high flow events as well. The response of vegetation to these changes is both uncertain and dependent on individual plant species. Experimental research on individual species has shown that survivability of seedlings and adult plants is reduced under longer flooding durations (Garssen et al., 2015). However, this is mainly valid for species that do not elongate their shoots while being submerged and obviously is linked to flood depth as well. As such, it is less contrary that a longer flood duration does not always lead to lower biomass, as

surviving species tend to increase in biomass as well. Furthermore, flood depth not only decreases plant survivability but also decreases plant biomass, as such this is in particular related to the submerged proportion of the plant (Garssen et al., 2015; Javernick, 2013).

Part of the effect of flooding on biomass is related to two variations in vegetation escape strategy (Puijalon et al., 2005). In the first, earlier mentioned as shoot elongation, plants tend to keep emerged from the water surface by making new and longer petioles and stems. As such biomass of these plants increase as long as they are able to keep up with the rise in water level. In the second escape strategy, plants tend to do the opposite, these quiescent plants wait out the flooding event by conservation of energy and reduction of growth as well as protection to counter cellular changes caused by flooding (Garssen et al., 2015; Munns et al., 2010). This variation of escape strategies describes not only the importance of understanding effects on different plant species but also the lack of knowledge in understanding the effect of flooding on the entire riparian zone.

Other factors like nutrient or seed supply are influenced by flood events as well, yet their effect is variable as they are dependent on spatial and temporal location as well as the subjected species.

2.4.1. Timescales of adjustment in braided rivers

River channels tend to widen until the shear stress applied by the flowing water at the bank toe, which is a function of the channel slope and channel depth, is less than the resistance of the bank materials to erosion (Hicks et al., 2007). Thus, over long timescales, channel width is in equilibrium with the imposed (average) hydraulic conditions (e.g. Parker et al., 2007). Paola (2001) introduced two key timescales describing the adjustment of braided systems. First, he considered that the timescale for lateral channel shifting should be related to a combination of lateral migration and siltation of channels (which he hypothesised would scale as the ratio of the (mean) volumetric sediment transport rate per unit width, q_s to a representative flow depth,

h). He thus proposed a time scale, T_{occ} , that describes the time needed to ensure that channels with wetted widths, b , have occupied the full braid plain width:

$$T_{occ} = (B_{bp} - \Sigma b) / \beta(q_s/h) \quad (2.4)$$

where B_{bp} = braid plain width (m), Σb = total wetted channel width (m), β = intermittency factor that defines the fraction of time that the system is active (-), q_s = (mean) volumetric sediment transport rate per unit width (m^2s^{-1}) and h = representative flow depth (m).

In natural braided river systems where the seeds of plants are delivered to the streambed, vegetation requires time to develop and stabilise in order to resist erosion by the fluvial system, preferably when it is not subject to submerged or erosive conditions. Thus, Paola (2001) proposed an additional key timescale: the time needed for plants to become stable and resistant to erosion, T_{veg} . The ratio of these timescales, a dimensionless time scale, T^* , describes the ability of plants to establish and stabilise the streambed:

$$T^* = T_{veg} / (B_{bp} - \Sigma b) / \beta(q_s/h) \quad (2.5)$$

Paola (2001) alternatively proposed:

$$T^* = T_{veg} / (b / e) \quad (2.6)$$

where T_{veg} is the time needed for plants to become stable and resistant to erosion (s), b is the (average) channel width (m), and e is the (average) bank erosion rate ($m s^{-1}$). The ratio b/e is effectively the time needed for a river to erode its full channel width (Hicks et al., 2007). Therefore, for $T^* \leq 1$, plants are able to become established quickly enough on the streambed that they can resist erosion (Hicks et al., 2007; Paola, 2001).

As such, the control of channel width by vegetation is restricted by the time afforded by the imposed hydraulic and sediment transport regime for vegetation to establish. Erosion rates are controlled by the extent of vegetation establishment and the discharge and sediment regime of the system. Therefore, negative feedback occurs in which vegetation constrains the width of the system and thus flow is more constrained, increasing erosive power, eventually reaching an

equilibrium channel width. Obviously, the driving factor is the potential 'space' vegetation has left to establish under the existing balance between fluvial discharge and sediment transport and the rate at which vegetation can establish, stabilise and proliferate. However, this driving factor is opposed by ongoing bank erosion that has the tendency to increase the potential existing space.

2.5. The application of physical modelling to fluvial science

To study the behaviour of rivers, three methods are commonly used: Fieldwork or field measurements, physical modelling and numerical modelling (e.g. Kleinhans et al., 2015). All these methods have their own advantages and disadvantages. For research at river reach scale, physical experiments are seen as a key approach. Compared to field measurements, physical modelling does not need the requirement of finding specific conditions in time or space, instead well-developed scaling techniques (discussed below) allow spatial and temporal scaling. Furthermore, unlike field conditions, physical modelling allows full control over both boundary and initial conditions. Additionally, there is also far more control on where to put measurement and monitoring equipment, something which in general results in more consistent and robust data. Finally, since physical models are scaled down, processes both occur faster and follow each other in shorter sequences, thus limiting the required time to capture morphodynamic processes. The majority of these benefits also hold for numerical modelling, and, since numerical models offer often more control, they can even enhance reproducibility and repeatability. However, in contrast to numerical modelling, physical models are able to overcome the issues that arise with predicting non-linear processes like sediment transport and biological interaction, two of the key uncertainties in natural fluvial systems, by using real physical material instead of numerical parameters. Nevertheless, the use of real natural materials stresses one of the biggest obstacles in physical modelling: scaling and how these models are validated over a range of time and space.

2.5.1. Scaling in physical models

Physical models span a wide range of different scales and therefore one of the prime decisions within physical modelling is to decide what scale of model suits the research best. Peakall et al. (1996) give an overview of different physical models and the relation between increasing time or spatial scale and a decrease in replicability of the original prototype (specificity) (Figure 2.4 A). The most straightforward model is a 1:1 model, in which the object of research is not scaled down and is just a copy of the prototype. Only boundary and input conditions may differ from the prototype. One step further are Froude scale models, in which the Froude number is correctly scaled. Froude number (Fr) is an indication of whether flow is subcritical ($Fr < 1$), critical ($Fr = 1$) or supercritical ($Fr > 1$) and effects whether downstream disturbances can propagate upstream. Froude number is related to both water depth and flow velocity:

$$Fr = \frac{u}{\sqrt{gh}} \quad (2.7)$$

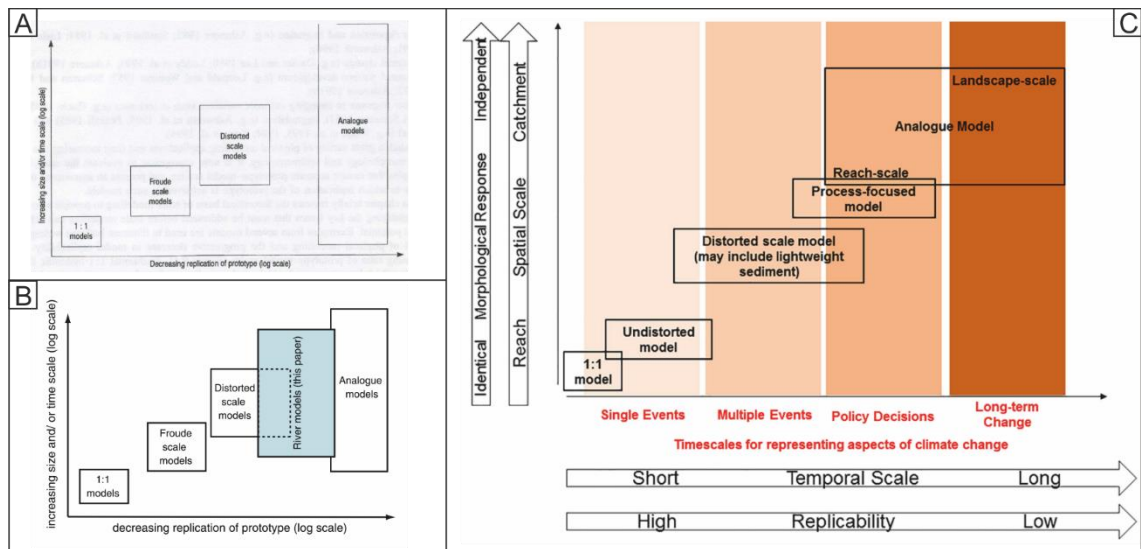


Figure 2.4: Overview of temporal-spatial diagrams that distinguish between different physical model types. A) Peakall et al.'s (1996) physical modelling overview; B) Schematic overview of implications on replication of prototype by increased time or space (Kleinhans et al., 2014) modified after Peakall et al. (1996); and C) Relative application of different approaches for physical modelling over different spatial and temporal scales, modified after Peakall et al. (1996).

The aim in Froude scale modelling is to maintain a Froude number in the model that approximates that in the prototype, or Froude similarity, $Fr_{model} = Fr_{prototype}$. If the model scale is denoted $1:\lambda$, this means that the velocity in the model must be scaled with a factor of $\lambda^{-1/2}$ relative to the prototype and process rates will speed up by a factor of $\lambda^{1/2}$ relative to the prototype (Johnson et al., 2013 in Frostick et al., 2013). In contrast to 1:1 models, the value of the Reynolds number (Re_f) in Froude scale models must therefore be relaxed unless it is possible to also modify the kinematic viscosity of the fluid, which has only been attempted by two studies (Young and Davies, 1991; Warburton and Davies, 1994). In the majority of hydrodynamic models this is generally not important as long as the flow remains fully turbulent. The level of turbulence is quantified using the Reynolds number of the flow (Re_f), which is dependent on flow velocity, water depth and kinematic viscosity:

$$Re_f = \frac{uh}{\nu} \quad (2.8)$$

where ν is the kinematic viscosity (m^2s^{-1}). Flow is normally fully turbulent with $Re_f > 500$ (Kleinhans, 2005).

For landscape or reach scale geomorphology, scales are increased further and distorted scale models are required. In these distorted scale models, horizontal scales are often decoupled from vertical scales to allow large scale features to be studied at a controlled small scale. In order to overcome scaling issues, these models often use increased longitudinal slopes or smaller sediment grain sizes, to ensure that Froude similarity is still achieved in these models. Analogue models are the final type of models. These models lack a specific prototype, have the largest temporal and spatial scale and are used to investigate general behaviour of even larger scale processes or landscape evolution. Despite their usually large temporal and spatial scale, there is the possibility to monitor smaller scale processes within the analogue models, something more common recently due a higher resolution in the collected data. Both Kleinhans et al. (2014) and Baynes et al. (2018) introduce an additional type of models; Kleinhans et al. (2014) introduce river models that in contrast to analogue models aim to better represent bank erosion and other

dependent factors within fluvial systems. Baynes et al. (2018) introduce process-based models that aim to understand smaller scale processes in or settings for the larger analogue models.

2.5.2. The “unreasonable effectiveness” of scaled models

Paola et al. (2009) introduce another vision on scaling experimental modelling, a vision in particular focused towards landscape modelling. In contrast to the classical scaling methods above where scaling is primarily for fluid flow, this approach focuses on spatial and temporal similarity. As such, it focuses on whether the resulting outcomes are similar in contrast to whether the processes that generate these outcomes are similar, like hydrodynamic scaling. Part of this is based on the assumption that the interaction between sediment and fluid flow is far more important than the characteristics of the fluid flow itself. Paola et al. (2009) claim that system scale dimensional numbers are far more effective when quantifying sediment transport and morphological interactions. The open question within this approach, according to Paola et al. (2009), is how the large-scale and fine-scale dynamics are coupled and how sensitive the former are to the latter.

2.5.3. Braided river experiments

Research on rivers with physical models tend to be done somewhere in the area in-between distorted scale models and analogue models (Kleinhans et al., 2015). Despite no specific prototype, research is often focused on a particular river type or discharge in order to understand whether behaviours seen in experiments are related to behaviours seen in real natural rivers. The ground-breaking research of Friedkin (1945) highlighted the key benefits of using physical models to understand alluvial rivers: physical models allow us to scale down time by using real rivers at a smaller scale and as such allow us to explore more settings and processes. His work focused on single channels yet were often dominated by braided results. Since, until recently, most research on experimental rivers focused on laboratory-scale braided rivers (Paola et al., 2009), despite braided rivers only making up a minority of present-day rivers (Leopold et al., 1964). Part of this is linked to sediment size of the channel belt; single thread

rivers are in general dominated by cohesive sediments while gravel is more common around braided systems. In experimental models, scaling cohesive sediments is far less convenient to scale down compared to gravel. Gravel size sediment naturally scales down towards sand, which thus can negate cohesion that is introduced when sandy sediment is scaled down towards silt or clay (e.g. Peakall et al., 2007). Nonetheless, over 80-years of research in physical modelling, techniques have improved and new concepts have been introduced. As such, for a clear understanding of the present-day state of research it is important to understand the evolution of fluvial physical modelling as listed below and summarized in Table 2.1.

2.5.3.1. Earliest experiments: explore variation in different fluvial systems

The earliest well-recorded fluvial studies with physical modelling in flumes were done by (Friedkin, 1945), whose experiments covered a wide range of fluvial settings. Whereas most of these experiments were favoured for meandering conditions, in a few of these experiments braided conditions were observed and investigated. The scope of this study was to investigate the lower Mississippi river, but the study also showed basic characteristics and processes that act and interact in a fluvial system. Friedkin's (1945) experiments consisted of several settings with both a straight and an imposed inflow angle as well as different variations in sediment bed texture and sediment input. The observed examples of braided patterns (Friedkin, 1945) occurred inadvertently in some of the meandering experiments. In these experiments, sediment erosion and reworking occurred at a high rate upstream, creating a steeper slope over the entire flume. The combination of this steeper slope and a higher sediment reworking was seen as an indication for favourable conditions for braided systems.

Table 2.1: Overview of previous physical modelling studies of fluvial systems, indicating institution and author as well as geometrical dimensions of the physical model (Length, width, slope). Overview includes sediment size, discharge and sediment rate as well as duration of the experiment (when available).

Authors, Year(s)	Instit. (Country)	Length (m)	Width (m)	Slope (m/m)	Discharge (L/s)	Sediment size (mm)	Sediment rate (g/s)	Duration (hr)
(Friedkin, 1945)*	USACE (US)	15 – 45	6	0.003 – 0.009	0.85 – 8.5	sand – silt	-	-
(Leopold & Wolman, 1957)	CALTECH (US)	18	0.9	0.0114	0.28 – 2.8	0.65 – 1.00	2	22
(Schumm & Khan, 1972)*	Colorado State (US)	30	7.3	0.0015 – 0.0040	-	-	-	-
(Hong & Davies, 1979)	Canterbury (NZ)	5	2	0.004 – 0.010	0.18 – 1.08	0.17	0.025 – 0.833	-
(Ashmore, 1982)	Edmonton (CA)	9	1 – 3	0.013	1	1.2	100	-
(Ashmore, 1991a, 1991b)	Western Ontario (CA)	10	2	0.010 – 0.015	1.5 – 4.5	-	-	-
(Ashworth et al., 1991)	Minnesota (US)	11	1	0.016	1.84 – 4.52	2.23	20 – 40	2
(Hoey & Sutherland, 1991)	Canterbury (NZ)	14.2	3	0.01	1.9	0.57	-	50
(Young & Davies, 1991)	Lincoln (NZ)	20	3	0.015 and 0.074	0.74 – 4.0	0.5	-	20
(Germanoski & Schumm, 1993)	Colorado State (US)	18.3	1.8	0.015 – 0.0375	2.4	0.87 or 2.19	-	-
(Leddy et al., 1993)	Leeds (UK)	5.5	3.5	0.02	-	0.28	-	6 – 9
(Warburton & Davies, 1994)	Lincoln (NZ)	20	3	0.0114	1.43	0.5	1.53	> 90
(Ashworth, 1996)	Minnesota (US)	11	0.9	0.016	1.84 – 4.52	2.2	1 – 8	-

(Sapozhnikov & Foufoula-Georgiou, 1997, 1999)	Minnesota (US)	5	0.75	0.15	0.2	0.12	0.6	> 6 days
(Gran & Paola, 2001)	Minnesota (US)	9	2	0.014	0.35	0.5	1.2	-
(Rosatti, 2002)	Trento (IT)	14.5	3.7	0.02	4.5	1.9	4.5	236.5
(Moreton et al., 2002)	Leeds (UK)	5.5	3.65	0.01	base: 1.8 events: 0.3 – 3.23	0.78	base: 4 events: 2 – 25	-
(Cazanacli et al., 2002; Sheets et al., 2002)	Minnesota (US)	6	3	0.017 – 0.079	0.14 – 0.51	0.12 – 0.46	8.4 – 31.43	30 – 99
(Metivier & Meunier, 2003)	St Maur de Fosses (FR)	1	0.5	0.033 – 0.0925	0.0155 – 0.0416	0.5	0.03 – 0.8	2 – 5
(Eaton & Church, 2004)	Lincoln (NZ)	20	3	≈ 0.1 (variable)	3.4	1.0	2.83	16
(Ashworth et al., 2004, 2007)	Leeds (UK)	5.5	3.6	0.008 – 0.014	1.8	0.39	2 – 16	28 – 208
(Bertoldi & Tubino, 2005)	Trento (IT)	12	0.6	0.01 – 0.02	167 – 500	0.5 – 1.3	0.267 – 3.00	-
(Egozi & Ashmore, 2008, 2009)	Western Ontario (CA)	20	3	0.015	1.4 – 2.8	1.17	-	-
(Hundey & Ashmore, 2009; Leduc et al., 2015)	Western Ontario (CA)	18	3	0.015	2.1	1.13	-	180
(Gardner & Ashmore, 2011)	Western Ontario (CA)	20	3	0.015	2.1	1.2	-	179
(An et al., 2013)	Taiwan	3	1.3	0.05	0.107 – 0.231	0.28	-	1.5, 3, 10
(van de Lageweg et al., 2013b)	Utrecht (NL)	10	3	0.01	base: 0.3 event: 0.25 – 0.5	0.51	-	120
(Reitz et al., 2014)	Paris (FR)	1.5	0.75	0.021 and 0.025	0.05 and 0.033	0.261	0.12 – 0.14	6 – 22.7

(Kasprak et al., 2015)	Western Ontario (CA)	20	3	0.015	2	1.2	-	-
(Garcia Lugo et al., 2015)	Trento (IT)	25	0.15 – 1.5	0.01	1.5 – 2.5	1	1.02 – 7.52	-
(Peirce et al., 2018)	Western Ontario (CA)	18.3	3	0.015 – 0.02	0.7 – 2.5	1.18	-	12 – 42
(Redolfi et al., 2018)	Trento (IT)	14	0.8 or 2.9	0.01	0.5 – 2.5	1	-	23 – 141

** Indicates non-braided physical modelling research*

Moreover, with this set of experiments, in conjunction with field observations, they validated that meandering, braided and straight channels are all characteristics for natural rivers, each working in interrelationship with the others. The resulting pattern is as such based on a selection of variables (e.g. discharge, sediment load, sediment calibre, channel width, channel depth, flow velocity, valley slope, roughness). Further physical modelling research has seen all these variables used individually or in pairs in order to understand what effect each has on channel pattern.

The next step in physical modelling was made by Schumm and Khan (1972). This research, primarily focused on meandering experiments, showed skills and outcomes that were used in or in the set up of numerous future physical experiments. Their experiments, executed in a 30 metre-long flume, were among the earliest experiments to control the behaviour of meandering. In their experiments, Schumm and Khan (1972) kept most variables constant while simultaneously increasing the valley/experimental slope. In order to keep the slope constant, the input of bed load also had to be increased. As their experiments focused on meandering, Schumm and Khan (1972) found a clear behaviour of sinuosity, the ratio of the channel distance to the valley distance (Hong & Davies, 1979), as a function of slope. In addition, they estimated both a straight-meandering as well as a meandering-braided transition zone. This meandering-braided transition was observed at slopes between 0.013 and 0.016. Although past research used different fractions of silt and sand (Friedkin, 1945) or only sand (Leopold & Wolman, 1957; Wolman & Brush, 1961), one of the key technical advances of Schumm and Khan (1972) was the addition of kaolinite as suspended load. Schumm and Khan (1972) specifically determined the fraction of suspended load (kaolinite) fed into the experiments. The addition of suspended load changed the behaviour of the channel; channels became narrower and deeper and channel sinuosity increased. The kaolinite appeared so effective that behaviour of channel dynamics were enhanced, in other words the meandering-braided transition was increased to higher slopes. As such a sediment load – slope diagram was introduced to discriminate between the different river patterns.

Hong and Davies (1979) were amongst the earliest to identify differences in number of braided channels in physical modelling. In a relatively small flume (5 m long), they investigated a small braided system and compared this with two of New-Zealand's braided rivers. This relatively steep flume (4 to 10 percent) behaved differently than previous studies; braided bars were formed due to chute cut-offs of meandering rivers and not by the interaction with the higher grainsize bed load particles seen by Leopold and Wolman (1957). On top of that, earlier suggested requirements for braided river systems, i.e. excessive bed load, range of flow rates and a decrease of bed shear stress, were found redundant in their small-scale steep sloped study. As such, they narrowed down the occurrence of braiding to three elements: valley slope, channel width/depth ratio and Froude number. Next to that, Hong and Davies (1979) used a unique approach for water inflow. In contrast to other research, they used a more laminar inflow. Moreover, whereas normally a braided river stream would impose turbulent water on itself due to the steep slope and rough bed, the use of a relatively small and steep flume would have brought the boundary conditions relatively far into the field of interest.

2.5.3.2. Next step: detailed research of individual features and sediment transport

Ashmore (1982) took a different approach to physical modelling experiments on braided rivers. In contrast to previous research, which predominantly focused on reach scale evolution or on what parameters have an impact on channel pattern evolution, this research took an approach to describe individual processes and features in experimental braided rivers under non-variable conditions. With this link, Ashmore (1982) successfully tried to describe the formation, development and evolution of natural gravel braided river bars by using smaller scale experiments (9 m long flume) with scaled down; i.e., sandy, sediment. Observations captured during these experiments have proven invaluable for further physical studies, like the initiation of braiding from a single straight channel via a series of active lobate bars, an observation that links to processes in natural gravel bed rivers. In addition, Ashmore (1982) detailed small-scale processes like downstream and upward fining of bars originating from gravity-induced processes

at the bar margins, but also included processes active over larger scales such as channel avulsions or braid plain morphology.

Further research in New Zealand followed a similar path. Hoey and Sutherland (1991) used a 14 metre-long stream table to observe braided river morphology and sediment transport rates. This research was able to distinguish three different phases (stable, aggradation and degradation) of fluvial behaviour over different cross-sections and time steps. These experiments also produced a large variation of sediment fluxes, variation that Hoey and Sutherland (1991) were able to link to higher peaks of sediment transport towards periods of degradation in one of the channels while linking the troughs in sediment output towards periods of shallow aggradation or channel bifurcation. As such, results of this study emphasise the connectivity between channel pattern and sediment transport, and show that sedimentation rates, because of dynamic equilibrium, can be averaged regardless of the high variability around this average. Research by Young and Davies (1991) focused on variations in slope as well as different hydrographs, to describe sediment transport in a 20 m long flume. Novel in contrast to previous research was the use of 30 °C water to reduce fluid viscosity and increase grain Reynolds number, an approach that, apart from consecutive research by Warburton and Davies (1994), has not been widely adopted since. Similar to Hoey and Sutherland (1991), they observed a pulsating bed load transport rate, independent of discharge or slope. However, under unsteady flow conditions with stepwise hydrographs, transport rates for bed load were lower compared to their equivalent transport rates with steady flow. Young and Davies (1991) concluded that this emphasised that bed load transport is more efficient under steady flow conditions than under unsteady flow conditions. Further research on bed load transport (Warburton & Davies, 1994) attempted to link bed load transport to channel pattern. In a similar experimental set-up to Young & Davies (1991), they aimed to look at the repeatability of experimental runs as well. Whereas only a weak relation between bed load transport and braiding index, the number of channels in a cross-section, or sinuosity could be made, the experimental runs themselves were relatively stable apart from the internal variability within the runs themselves. Ashworth et al. (1991) reported downstream

fining patterns in mid channel bars in their physical experiments in an 11 m long flume. However, as no such relation was found in natural braid bars, research would benefit on the effect both different and variable discharges as well as on sediment supply have on sediment fining of braid bars.

Ashmore (1991a, 1991b) focused on a sequence of Ashmore's (1982) set of experiments on the aspect of braiding index. These experiments showed that dynamic variability of braiding index (or braiding pattern) of an experimental model can be explained by a function of flume (or valley) gradient and river discharge, i.e. stream power. The latter would allow other research to extend this stream power relationship towards natural rivers that were not in a similar state of evolution (Ashmore, 1991a). Similarly, a distinction was observed between different types of morphologic processes, including central bar braiding (similar to Leopold and Wolman (1957)), transverse bar conversion, multiple bar braiding and chute cut-offs (Ashmore, 1991b). Further, with the principle of both water and sediment circulation he was able to circulate natural sediment pulses, which are common in braided river research due to the natural reworking of bars and bar systems. This technique would, if successful, counter or at least decrease the impact of the upstream boundary conditions. Further, this research observed the direct influence of these sediment pulses by altering braiding intensity of the upstream part of the experiments as well as identifying the positive relation with chute cut-offs (Ashmore, 1991b). Leddy et al. (1993) further described active processes in braided rivers, in particular processes related to anabranching in braided gravel-bed rivers. In a 5.5 m long, relatively wide, stream table, they were able to make a distinction of three different types of avulsions (choking, constriction and apex) that all have different causes related to them. However, Leddy et al. (1993) linked all of these avulsions together in a way that all are dominantly triggered, directly or indirectly, by pulses of sediment. As such, they underline again the effect observed in earlier experiments (Ashmore, 1991b).

Ashworth (1996) further explored the formation of mid-channel bars by looking in detail at the formation of such bars in a self-made confluence unit. Results show that initial mid-channel bar formation was symmetrical under identical discharge and sediment inflow conditions, furthermore bars remained symmetrical until the moment flow depth became too shallow. Additionally, Ashworth (1996) observed increased rates of bank erosion due to the formation of mid-channel bars, even though channel width did not significantly increase. This research roughly marks the end of a period of interest in detailed processes around braided river morphology (Ashmore, 1982, 1991b, 1991a; Ashworth et al., 1991; Leddy et al., 1993).

2.5.3.3. Upscaling: focus on planform morphology and braided patterns

Further research mainly evolved around larger scale patterns and using the processes observed in these smaller scale individual or combined units as a guideline to the processes observed at larger scales. A good example is a set of physical models that looked at overall braided morphological pattern (Germanoski & Schumm, 1993). Similar to Hoey and Sutherland (1991), Germanoski and Schumm (1993) explored morphological pattern under the three conditions of sediment supply; equilibrium, shortage (or degradation) and abundance (or aggradation). In this extended set of experiments, they used different valley slopes as well as two different well-sorted sediment mixtures. Although the behaviour of the braided pattern and the braided morphology did not differ widely over different slopes or sediment sizes, the effect of either aggradation or degradation dominated a change of pattern. Whereas sediment abundance provided favourable conditions for the existence of more braided bars and a coherent increase of braiding index, sediment shortage resulted in a decrease in braiding index as well as a reduction in number of bars. Furthermore, a sediment shortage would promote an incising single channel in the upstream area, thereby flattening out the experimental long profile.

Later research (Sapozhnikov & Foufoula-Georgiou, 1997), in a relatively small 5 m long flume started to look at the dynamic behaviour of individual features in a braided river system. This work indicated that any planform change in morphology is steered by the dimensions of that

feature or change. Therefore, the behaviour of larger features (scours, bars channels) steered the behaviour of smaller features while smaller features were not able to induce changes to larger features. This behaviour, well summarized as self-organisation, was further explored and tested in subsequent research (Sapozhnikov & Fofoula-Georgiou, 1999). Hence, with use of a sequence of experiments, sporadically clearing morphology between runs, they were able to show that their braided river systems would re-evolve to their old pattern over the span of an hour or two. However, slight changes, in particular vertical disturbances, never recovered and the system quite often shifted from a somewhat stable equilibrium state to a next quasi-equilibrium state. These observations suggest that there is no stable final equilibrium state but rather, a collection of quasi-final equilibrium states to which a fluvial system would organize. Although this observation can be seen as controversial, nonetheless Sapozhnikov and Fofoula-Georgiou (1999) relate these quasi-equilibrium states to combinations of discharge and slope and the fact that a change in slope was observed in the self-organisation process. Further, where ideally morphologic features should be looked at in three dimensions, at that period of experimental modelling the quality of imagery and tools was not sufficient to capture 3D morphology effectively (Sapozhnikov & Fofoula-Georgiou, 1997). Gladly, for the quality of experimental modelling, technology over the next decades caught up rapidly, allowing these technological barriers to be overcome rapidly in the future.

Self-organization (Sapozhnikov & Fofoula-Georgiou, 1999) was also observed in research by Rossati (2002). In a 14 m-long flume, Rossati (2002) showed that islands or representative mid-channel bars in the experimental flumes are not only similarly shaped, they also follow the same perimeter-area relation.

In a metre-long tabletop experiment, Metivier and Meunier (2003) analysed the effect of grain size distribution on bed load transport. In contrast to past research (Ashmore, 1991a; Ashworth et al., 1991; Hoey & Sutherland, 1991; Young & Davies, 1991) that used non-uniform sediment, this research chose a more uniform sediment. Nevertheless, or despite the more

uniform sediment distribution, braided patterns and characteristic bed load pulses were still observed in the output of the experiments.

This period introduced a wider range of dimensions in flumes as well; several experiments were done in wider flumes (Cazanacli et al., 2002; Moreton et al., 2002; Sheets et al., 2002). Some of this research focused on the evolution of braided alluvial fans (Cazanacli et al., 2002), while other research focused more on the evolution of source to sink systems (Sheets et al., 2002). Both forms of research contributed to our understanding of aggrading processes in braided rivers when flume width is not limiting. As they were predominantly aggrading experiments, the main purpose of these experiments was to explore and observe stratigraphy. Moreton et al. (2002) employed a different approach, in which the inlet channel was slowly raised while others used a slowly subsiding basement floor (Cazanacli et al., 2002; Sheets et al., 2002). Nonetheless, both methods allowed for accommodation room without altering the slope of the braided river system. Furthermore, both experiments included an additional sediment grain size fraction (up to 20 percent), intended to represent finer material seen in natural systems, combined with a dominant grain size. With the use of silica flour (Moreton et al., 2002) or crushed coal (Cazanacli et al., 2002; Sheets et al., 2002), these experiments can be seen as the first attempts to introduce surrogates into fluvial modelling. Almost simultaneously, Gran & Paola (2001) employed alfalfa to represent natural riparian vegetation in a braided river flume for the first time. Although the initial channel was braided, the addition of grown alfalfa seeds shifted the channel pattern back to a single channel. Because of the observed added cohesion in the experiments with the additional use of physical, chemical or biological surrogates, these surrogates were used primarily in modelling meandering or single-channel systems in the next decade(s).

Ashworth et al. (2004, 2007) continued in the direction of the work of Ashmore (1982, 1991b, 1991a) and Leddy et al. (1993) by looking at the effect of sediment supply on avulsion frequency. However, in contrast to previous fluvial experiments but similar to Leddy et al. (1993), they used a vertical adjustable inlet, as such the system allowed for natural aggradation in the system

without an adjustment of the valley slope. These experiments showed that an increase in sediment input makes the system more dynamic as avulsions become more frequent and channels are more likely abandoned. Controversially, due the set-up of the model, most avulsions occurred in the lateral central part of the channel, although total sedimentation was near uniform across the entire flume.

Research by Eaton and Church (2004) focused again on the overall behaviour of fluvial systems. In a 20-metre long flume they aimed to reach an equilibrium channel morphology. In their experiments, they investigated the effect of individual independent variables like discharge, sediment supply and valley slope on reaching a certain equilibrium morphology. Of these variables, valley slope was found to be the most dominant in determining channel morphology. However, any combination of sediment supply to water discharge ratio (Q_b/Q) changed the valley slope to a particular preference and also adjusted channel morphology. Additionally, they introduced the concept of memory in physical models. Similar to natural rivers, this memory showed up in two independent relatable instances. First, Eaton and Church (2004) showed that channels under the same slope, with the same sediment supply and under the same constant water supply but with a different initial geometry eventually turned into slightly different fluvial systems. In addition, they observed that a different order of events of slight variations in input conditions, in particular in the earlier stages of the experiments, actually influenced the channel throughout the entire experiment. This effect, according to Eaton and Church (2004), is related to the armouring of sediment in the physical fluvial system. Finally, these experiments showed a clear relation between sediment supply and estimated sediment mobility. In experiments with sediment supply above and below the estimated sediment mobility thresholds, the fluvial systems behaved differently, not only temporally but also spatially. These observations, according to Eaton and Church (2004), relate to which portion of the sediment was mobile as full mobility does not allow a non-cohesive system to create banks.

In a relatively narrow but long (20 m) channel, Bertoldi and Tubino (2005) looked at the evolution of alternate and mid-channel bars in a single channel as well as how these impact bifurcation processes. They were able to relate the longitudinal spacing of bifurcations to the lengths of bars that formed in the initial channel, however, they were also able to determine the flow and geometric properties of the onset of channel bifurcations in more detail. Along the way, they gained knowledge that could improve parameter selection in numerical models, and thus facilitate the coupling of numerical and physical models.

2.5.3.4. Physical research evolves: Braided fluvial system research becomes more distinct

In the last two decades, more and more physical research started to focus on meandering river types (Peakall et al., 2007), and in particular on experiments with the addition of vegetation (Braudrick et al., 2009; Coulthard, 2005; Gran & Paola, 2001; Perona et al., 2012; Tal & Paola, 2007, 2010; van de Lageweg et al., 2010). However, Egozi and Ashmore (2008, 2009) investigated braiding indices and the overall braided channel patterns in flumes. Within these sets of experiments, in a 20-metre long flume, they executed one of the first experiments to use different discharges within the same experimental run. Their experiments not only introduced a subsequent increased discharge on an established system, they also introduced a sequence of a five staged pyramid discharge with an hourly increase (or decrease). Egozi and Ashmore (2009) found that braiding index was positively related to discharge. However, braiding index is inherently dependent upon discharge and depth: when water levels rise or fall, bars naturally emerge or submerge and channels may fall dry or become active. This consequently alters braiding index without a change of the morphology. To overcome this, the active braiding index was introduced, which indicates the number of channels that transport sediment in a cross-section (Bertoldi, Zanoni, et al., 2009) and is thus seen as less impacted by changes in water level. By relating the number of active channels to the total number of channels, Egozi and Ashmore (2009) found a relation independent of river discharge. Still, this relation took time to set up (over 40 hours, dependent on the overall change in discharge), as braiding index does not

instantaneously adapt to a change in discharge. Similar research on braided river channel networks found similar relations of braiding and active braiding index (Bertoldi, Zanoni, et al., 2009). Their results suggested that the dynamic braided system reaches an equilibrium in 10 to 20 hours. Next, by introducing the term statistical stability, they were able to more or less quantify the dynamic behaviour of a braided river system and observe (or calculate) when a braided river system reaches a (quasi-) steady state or equilibrium. Research by Hundey and Ashmore (2009), showed the density of braided patterns, i.e. the distance between a confluence and a bifurcation, is strongly related to the channel width of the individual channels and is equivalent to pool-riffle spacing in meandering single thread rivers

Gardner and Ashmore (2011) developed another method of quantifying braided channel mobility. By introducing a minimum surface prediction of digital elevation models (DEMs) at an hourly interval they were able to determine channel movement and link these areas spatially with grain size using a grain-size mapping technique (Gardner and Ashmore, 2011). Similar research (Leduc et al., 2015) showed that after 40 hours of experimental time an active layer in a braided physical model is still well mixed, with no specific sorting over elevation between different grainsizes.

Experiments by van de Lageweg et al. (2013b) were set up within a sequence of physical modelling of meandering rivers (van de Lageweg et al., 2013a; van Dijk et al., 2012). Their experiments took place in a 10-metre long parallel channel set-up with automatically moving inlets. These inlets, which moved left and right at a low rate (0.01 m hr^{-1}), were designed to represent the upstream dynamic mobility of an inflowing river reach. Furthermore, van de Lageweg et al. (2013b) were one of the first to compare the effect of hydrographs to experiments without specific hydrographs. Amongst the experimental runs, they used a flood cycle of three hours with 30 minutes of high flows and 2.5 hours of low flow conditions which was repeated 40 times. They were able to compare these runs to constant flow experiments with the same order of magnitude water volume. Both these experiments only showed a weak

braided pattern, with an effective active braided index (ABI) below 2, but still showed a morphological impact of the variable flood events. During high flow events, larger lateral migration rates were observed and larger areas were reworked compared to constant flow conditions. Further, bar architecture behaved differently under high flow conditions, as they became both longer and were more often incised by chute cut-offs.

2.5.3.5. Last decade: development of high-resolution monitoring approaches

Despite the quantity of research done over the last half-century, physical research on braided rivers continues today. Whereas some research focused more on developing vegetation or vegetation artefacts (e.g logs), in braided rivers (Bertoldi et al., 2014, 2015; Javernick, 2013; van Dijk, Teske, et al., 2013), other research focused on elaborating existing or filling knowledge gaps in physical modelling of braided rivers. This has been facilitated by the development of new techniques to collect higher quality and resolution morphological data. For example, terrestrial laser scanners, traditional digital photogrammetry, or Structure for Motion (SfM) techniques are able to capture both high precision and high-resolution elevation data (e.g. Leduc et al., 2019). Due to the high quality of the generated DEMs, it became easier to look in more detail at changes of morphology as well as to look over a larger scale. Kasprak et al. (2015) successfully used these techniques to understand sediment transport and deposition on and around braided morphologic features like lateral and central bars, banks and chutes. The use of coloured tracer particles of diameter $2D_{50}$ allowed them to determine depositional areas. With their high resolution DEMs, they observed that these particles predominantly deposited on bar heads or margins and in particular on areas of minor deposition. Although their results are possibly biased by the inability to detect buried particles or by the interaction of the particles with the overall sediment mixture, this research was amongst the first to effectively apply the SfM technique to laboratory experiments.

Garcia Lugo et al. (2015) were able to use high resolution elevation data to systematically explore and quantify the effect of the confined channel/bed width on planform morphology and

sediment transport, something which often had been either a process of trial (and error) or decided by the available flume or stream table. Garcia Lugo et al. (2015) observed a wide range of bed/channel widths without altering discharge values; their experiments showed a wide range of river patterns ranging from alternating bars in single channels to full braid plain morphology. Their results showed that braided rivers had a larger variability in morphology, something they related to a decrease in stream power caused by a larger active width.

Active width, often recognized as the lateral area of the channel with bed load transport, has recently been further explored by Peirce et al. (2018). For this research, in an 18.9-metre long flume with a fixed bed width, discharge was varied between runs in order to capture different stream power conditions. Peirce et al. (2018) found active width to be positively related to stream power, supporting the results of Garcia Lugo et al. (2015). Concurrently, these experiments showed that active depth is positively related to stream power, though its effect is limited for higher values of stream power. Additionally, Peirce et al. (2018) looked at the effect of a sequence of different discharges in a pyramid shape, similar to past research by Egozi and Ashmore (2008) and with similar results. However, in the experiments of Peirce et al. (2018) more attention was put on the delay towards equilibrium. Active width was always higher at the start of the experiments before it gradually lowered until it reached a dynamic stable value. This effect was also shown in the pyramid hydrograph experiments where active width was relatively high when adapting towards a higher discharge/stream power setting (i.e. the rising limb).

This relation between different hydrographs and bed load transport in braided rivers was further explored by Redolfi et al. (2018) in a 24-metre long flume in a research programme that was relatively similar to past research (e.g., Young & Davies, 1991) but with more advanced data collection instruments. This research not only used a steady discharge but also used stepped discharge, placing blocks of time of high discharge in between periods of constant discharge, as well as a pyramid discharge that consisted of a discharge that continuously went up or down at a constant rate between a minimum and a maximum value. The steady discharge experiments

showed again that bed load sediment transport is widely variable in braided river systems (Ashmore, 1991b; Eaton and Church, 2004; Garcia Lugo et al., 2015; Peirce et al., 2018). However, within the variable discharge experiments, Redolfi et al. (2018) found adaptability or hysteresis. For the blocked higher discharge, a positive overshoot of sediment transport was observed at each increase of discharge, similarly a negative overshoot of sediment transport was observed at each decrease of discharge. For the pyramidal hydrographs this highlighted a form of hysteresis; sediment transport at the rising limb was constantly higher compared to expected values whereas on the falling limb it was equal or less than expected. This is opposite to previous research (Warburton & Davies, 1994). This hysteresis was more pronounced on steeper/shorter triangular discharges and more pronounced in narrow flumes (0.8 m wide) than in wide flumes (2.9 m wide). Although such results would initially favour larger flumes over smaller flumes for experimental modelling as well as longer time periods, it is debatable whether the need for larger space scales or longer time scales would answer questions in regard to system response to changes in input conditions like discharge or sediment transport.

Recently, an overarching study employing threshold theory (Kleinhans & van den Berg, 2011), based on width-depth ratio and discharge (Métivier et al., 2017), was able to look at differences between braided and single channel physical experiments. By including real world and experimental rivers, Métivier et al. (2017) were able to show that all experimental rivers have an above average dimensionless width but are not offset from their natural counterparts. However, comparison between single and braided channels indicates braided channels have a relatively larger dimensionless width, and as such are further from the natural threshold theory.

2.5.3.6. What is next: possibilities, trends and challenges

In relation to the outcomes of the most recent experiments (Egozi & Ashmore, 2009; Peirce et al., 2018; Redolfi et al., 2018), it would be good to continue to focus physical modelling capacity towards the impact of different discharges on existing morphology. The use of these different hydrographs is not novel, but stepwise increases in discharge were mainly used for correlation

to field events (Young & Davies, 1991). The above attempts were all made to explore the effect of a variable discharge as well as a changing discharge during a particular run. Most attention was given to the repetition of events, in order to create a sufficiently large dataset from which to extract conclusions. Therefore, so far, no research has successfully attempted to explore the effect of different sequences of different events, which could provide a distinction between the effect of a change itself or of the magnitude or direction of the change.

2.5.4. Vegetation in large scale physical experiments

The above paragraphs gave an extended overview of the evolution of physical modelling of braided systems. Despite having briefly touched upon the use of surrogate vegetation as a cohesive agent (Gran & Paola, 2001) the use and representation of vegetation has been predominantly ignored. As such, this section will describe and critically assess research with surrogate vegetation or research on natural vegetation in physical river models.

As discussed above, field studies or observations have shown the importance of vegetation in river systems (e.g. A. Gurnell, 2014), however field studies lack the ability to isolate and quantify these effects in detail. Numerical modelling studies have made progress to incorporate the effects of vegetation in their models but so far numerical models have used simplified versions of the interaction between sediment, water, vegetation and resulting morphology (Gurnell et al., 2016). Only recently, van Oorschot et al. (2016) successfully implemented vegetation in a more dynamic way for meandering river bends.

The first physical experiments with surrogate vegetation were executed two decades ago (Gran & Paola, 2001). With their experiments, they showed that the addition of alfalfa (*Medicago sativa*) to experimental rivers was able to turn a braided river system into a (wandering) single channel system. This research linked the added surrogate vegetation to increased bank stability and thus a decrease in channel migration that eventually evolved towards narrower and deeper channels. The success of this research initiated the use of vegetation in future research, both for braiding and meandering river research. Tal and Paola (2007) showed that a braided river system

with alternating periods of small discharges and short periods of high discharges will evolve into a single-thread channel solely due the addition of vegetation (Tal & Paola, 2010). Tal and Paola (2007) used a channel reworking high discharge of $2.0 \times 10^{-3} \text{ m}^3\text{s}^{-1}$ with no bed load transport and a small discharge of $4.0 \times 10^{-4} \text{ m}^3\text{s}^{-1}$ for the majority of time. These experiments were run in two sessions, each with a different flood interval (6 or 3 days), that spanned over 100 days. Other experiments (Braudrick et al., 2009; van Dijk, Teske, et al., 2013) used alfalfa seeds in experiments with lower magnitude valley slopes to investigate processes related to meandering rivers. Like Gran and Paola (2001), these experiments observed narrower and deeper channel(s) as well as lower bank erosion rates with added vegetation. In addition, van Dijk et al. (2013) observed sediment deposition upstream of vegetation patches. More recently, a sequence of experiments have used semi-natural obstructions in the flow, in particular large woody debris (Bertoldi et al., 2014, 2015). Although a combination of woody debris with surrogate vegetation has proven to be effective, the addition of woody debris alone has proven to be of limited effect (Bertoldi et al., 2015).

2.5.5. Use of surrogate vegetation

Although live plants have been used in experimental modelling, often this vegetation had to be scaled down in order to represent vegetation-fluvial interactions in natural rivers. As such, a couple of studies have looked at what type of small-scale vegetation is suitable to use as a surrogate. As mentioned, alfalfa was used in a large number of physical experiments as the main type of surrogate vegetation (Bertoldi et al., 2015; Braudrick et al., 2009; Gran & Paola, 2001; Tal & Paola, 2007; van Dijk, Teske, et al., 2013). However alternative approaches exist, such as Perona et al. (2014) who preferred the use of catgrass (*Avena sativa*) over alfalfa due the larger and more countable seeds. In other studies, larger, over 50 mm diameter, non-germinating, plant species like Gomprena and Petunias were used to focus primarily on trees (Coulthard, 2005).

Next to the research on the effects of surrogate vegetation in physical models, some studies focused on surrogate vegetation itself. Van de Lageweg et al. (2010) used different types of surrogate vegetation (garden cress pepperweed, garden rocket, thale cress and alfalfa) as well as different environmental variables (moisture saturation, light, temperature and pH) to understand the behaviour of vegetation under various environmental conditions. Van de Lageweg et al. (2010) showed that, if anything, a lack of soil saturation by water increases the germination and growing time. Further, it introduced the use of grow lamps (that resemble natural sunlight and thus emit plant-enhancing near-infrared light) that resulted in the most dense vegetation (van de Lageweg et al., 2010). Clarke (2014) determined the effect of different growing and seeding conditions for alfalfa and catgrass and highlighted the necessity of a fully saturated soil. Furthermore, the level of light was shown of less importance, as long as it reached above a certain threshold. Clarke (2014) also showed that seeds that are buried by a 5-10 mm thick layer of sediment are more consistent and successful in germination than seeds placed at the surface. Of the range of used species, van de Lageweg (2010) favoured garden rocket due to its faster growth than alfalfa and more representative root system with small side branches compared to garden cress pepperweed which has a single deep root). Clarke (2014) favoured alfalfa over catgrass as it was both less dependent on environmental conditions and had a higher sprouting rate.

Sequential research by van de Lageweg (2013) used surrogate vegetation (alfalfa and garden rocket) in small scale bank erosion experiments to understand its cohesive effect. In these experiments, based on past bank erosion experiments (Friedkin, 1945), different seeding densities as well as different growing strategies were used. They showed that for 2-day old garden rocket, both vegetation and vegetation density barely influence erosion rate in contrast to bare control experiments. In contrast, for 6-day old garden rocket, higher vegetation density results in a more resistant substrate. Van de Lageweg (2013) showed that the cohesive effect of alfalfa is larger for lower densities. At higher densities, there is still some added cohesion, but its net effect is smaller. Garden rocket behaves similarly, but because of smaller variations

between the different growing or density stages, van de Lageweg (2013) suggest that alfalfa is more controllable in large scale physical experiments.

2.5.6. Other surrogates

The use of surrogate vegetation to represent natural vegetation around rivers in physical modelling allows not only a representation of the effect vegetation has on bank strength and cohesion but also allows vegetation-flow interactions by stems standing out from the sediment. Although surrogate vegetation is in general the most realistic approach to represent vegetation and the use of living surrogates allows natural aspects like root distribution or stem flexibility to be incorporated naturally, its use is also limited by one big drawback; i.e. time. The growing time for surrogate vegetation is anywhere between several days up to several weeks. Whereas in a few experimental settings, vegetation may be prepared and grown outside the flume, in most scenarios that involve the interaction with morphology, seeds have to be applied on this morphology, which results inevitably in experimental downtime due to growing.

To overcome this growth-related experimental downtime, more and more interest is put into a solution to overcome this limitation (Baynes et al., 2018). Vegetation has been used previously as a method to introduce more cohesion and bank stability to physical fluvial models (Gran & Paola, 2001). More recently, the development of techniques to model cohesive sediment has further evolved, unlocking the potential for the use of these materials to simulate the effects of vegetation. As such, it is important to have an overview of the use of these finer and cohesive materials over the last decades of physical modelling.

First attempts, as well as the majority, to bring cohesion into physical modelling used clay, either in small fractions mixed through the sediment (Schumm & Khan, 1972) or as a top layer over a sandy layer (Schumm et al., 1987). Smith (1998) started using lightweight sediments like rock flour in combination with 10-30 % clay to create a consistent meandering pattern. Research on meandering rivers (Peakall et al., 2007) also used silica flour (1-20 μm) to represent cohesion, experiments that showed an active meandering channel can be created by fine-grained

sediment without the addition of surrogate vegetation. More recently, Braudrick et al. (2009) used non-cohesive fine lightweight plastic sediment in combination with coarser regular sand and alfalfa vegetation. In these experiments, the plastic sediment was intended to represent the finer sandy sediments found in natural gravel bed (meandering) rivers. Alternatively, Ganti et al. (2016) employed crushed lightweight walnut shells (D50 0.7 mm) to scale sandy sediment without increasing cohesion in their experimental models of lowland deltas.

2.5.7. Extracellular polymeric substances (EPS)

Over the last 20 years, another type of surrogate has been used more and more in order to increase the cohesion of sediments: extracellular polymeric substances (EPS). EPS are of organic origin and are originally secreted from benthic organisms (Tolhurst et al., 2002), thereby forming a biofilm (Decho, 2000). EPS concentrations can be as high as 5% in estuarine environments, whereas concentrations of natural EPS can range from 0.01 to 1% in other muddy or even sandy mud environments (Malarkey et al., 2015). All EPS are able to increase cohesion and shear strength of sediment. In order to understand the effect of natural EPS on submerged morphology, several types of non-natural EPS have been chosen in order to represent natural EPS in physical laboratories (Malarkey et al., 2015; Parsons et al., 2016). Malarkey *et al.* (2015) and Parsons *et al.* (2016) used Xanthan gum, a bacterial polymer used in the food industry, at a concentration of 0.01 – 1% by mass of sediment. These low concentrations of Xanthan gum have the benefit of not directly interacting with the flow, but small variations due to less homogeneous mixed substances may extend their impacts. Moreover, Xanthan gum, and EPS in general, are soluble and can ‘disappear’ from the sediment (Malarkey et al., 2015) by being dissolved in the fluid. This not only alters the sediment mixture, it is also able to trigger another property of EPS, reduced drag. In high pressure tubes, EPS are used to decrease drag forces and thus loss of energy (Wyatt et al., 2011; Wyatt & Liberatore, 2009). Wyatt et al. (2011) showed that Xanthan gum reduces drag by almost 20% at concentrations of 100 ppm. As Xanthan gum is applied to the sediment and not to the water directly in physical modelling, it is debatable what actual concentrations would be reached when dissolved into the fluid. Although polymers

in general are susceptible to degradation, Xanthan gum is less susceptible to shear degradation in contrast to other polymers (Wyatt et al., 2011).

This extended list of experimental research indicates the wide range of experimental research as well as the steps that have explored over the past decades. Research on braided rivers made large steps to understand morphologic features (e.g. Ashmore 1982) in these fluvial systems and evolved in understanding the behaviour of specific grainsizes (e.g. Bertoldi & Tubino, 2005) or even particles (e.g. Peirce et al., 2018a, 2018b). Further research showed reach scale behaviour of fluvial systems and the dominant influence on flood events on channel morphology (e.g. van Dijk, 2013a). Gran and Paola (2001) introduced vegetation into physical research and showed the key importance of it to reinforce banks to restrict a braided river from braiding in conjunction with their perspective that a lack of bank strength is the fundamental characteristic of braiding. However, in order to fully control these aspects of experimental fluvial research, further understanding is required on the use of vegetation. Van de Lageweg (2013) highlighted potential key differences between different used species, while Clarke (2014) investigated the impact of environmental variables on alfalfa growth in a controlled experiment. However, so far no research successfully used vegetation growth on full scale fluvial experiments, often hampered by the time constraint that comes with vegetation. In the past a range of experiments (e.g. Braudrick et al., 2009; van Dijk, van de Lageweg, et al., 2013) were set to develop meandering systems by using cohesive materials, however despite effective increased cohesion and successful dynamic single channel system, control was limited and often enforced due initial conditions or lightweight particles. As such two significant gaps exist:

1. a way to understand the behaviour of evolving vegetation on braided systems.
2. a way to implement similar surrogates that would reduce experimental time while mimicking the effect of vegetation.

3. Small scale experimental research on bank erosion

3.1. Introduction to bank erosion and cohesion in natural systems

Chapter 2 gave an overview of fluvial systems existing around the world. It also described the different parts of a fluvial system which contribute to channel stability, e.g. Church (2006) and showed one of the key aspects that contributes to channel mobility is bank stability; a river with more stable banks will be less dynamic compared to a river with less stable banks. This is also shown by Murray and Paola (1997) who show that rivers without cohesive banks or other restrictions naturally widen and braid.

Bank stability is not a single process but is instead a combination of several interlinked processes. Osman and Thorne (1988) give an extended overview of the processes and variables in bank erosion. Although their focus is bank toe erosion, the most basic form of bank erosion, these processes can be extended to all relevant forms of bank erosion (e.g. Figure 3.1) including mass-failure mechanisms like cantilever or planar failures whose material will eventually end up at the bank toe (Darby & Thorne, 1994; Thorne & Tovey, 1981) where the sediment is further eroded. Hence, Osman's and Thorne's (1988) overview on bank stability (Osman & Thorne, 1988) can be summarized by the interaction of two processes; shear strength of the bank and shear stress of the fluid. When shear stress of the fluid (τ) overcomes the critical shear stress of the bank toe (τ_c), sediment can become entrained and the bank toe begins to erode (Osman & Thorne, 1988).

Shear stress of the fluid is controlled by flow velocity (chapter 2, equation 9) as well as water depth and channel slope and can be enhanced by transported sediment (or other natural and anthropogenic materials) or secondary flows. The critical shear stress in steeper banks is dependent predominantly on the soil characteristics and to a lesser extent on the water content in the soil pores and the total mass of the bank. First, critical shear stress describes the shape of the bank face. Banks in non-cohesive material have a shape dominated by the angle of repose. In contrast, for banks in cohesive material the shape is mainly determined by the apparent

cohesion. Apparent cohesion is composed of effective cohesion that is driven by the bonds between cohesive particles (van de Waals forces) and matric suction that is driven by the pore-water pressure in the voids between particles (Casagli et al., 1999; Rahardjo & Fredlund, 1995; Simon et al., 2000). Second, individual soil particles determine the critical shear stress of the bank material, which is higher for smaller soil particles due to apparent cohesion (see Shields diagram; chapter 2).

The second process is mass failure, which is a more intermittent process where (part of) a bank collapses before it is (slowly) entrained by the flow. Mass failure is also controlled by grain size through the effective angle of internal friction (= angle of repose in non-cohesive sediment) and effective cohesion, but also by the total mass of the bank, which is a function of bank height, failure width, bank material density and moisture content. Mass-failure events coincide with bank toe erosion in particular in more cohesive settings where the apparent cohesion makes the upper bank lag behind the more exposed lower banks. In this process, 'basal end-point control', where sediment of mass failures ends up as excess sediment at the toe of the bank reduces bank toe erosion rate based on fluid characteristics and thus controls the vertical bank profile (Carson & Kirkby, 1972; Thorne & Tovey, 1981).

The bank failure mechanisms described above suggest there are two approaches to reduce natural bank erosion rates. The first option is to increase bank strength by altering the chemical and/or physical composition of the soil, together with reducing the moisture content of the soil. The second option is to reduce the applied fluid shear stress, for example by lowering flow velocities or diverting flow. In natural systems, both link to one key aspect; vegetation. Roots of riparian vegetation are able to generate internal co- or adhesion to the soil, keeping the soil together; vegetation also deflects or slows flow down.

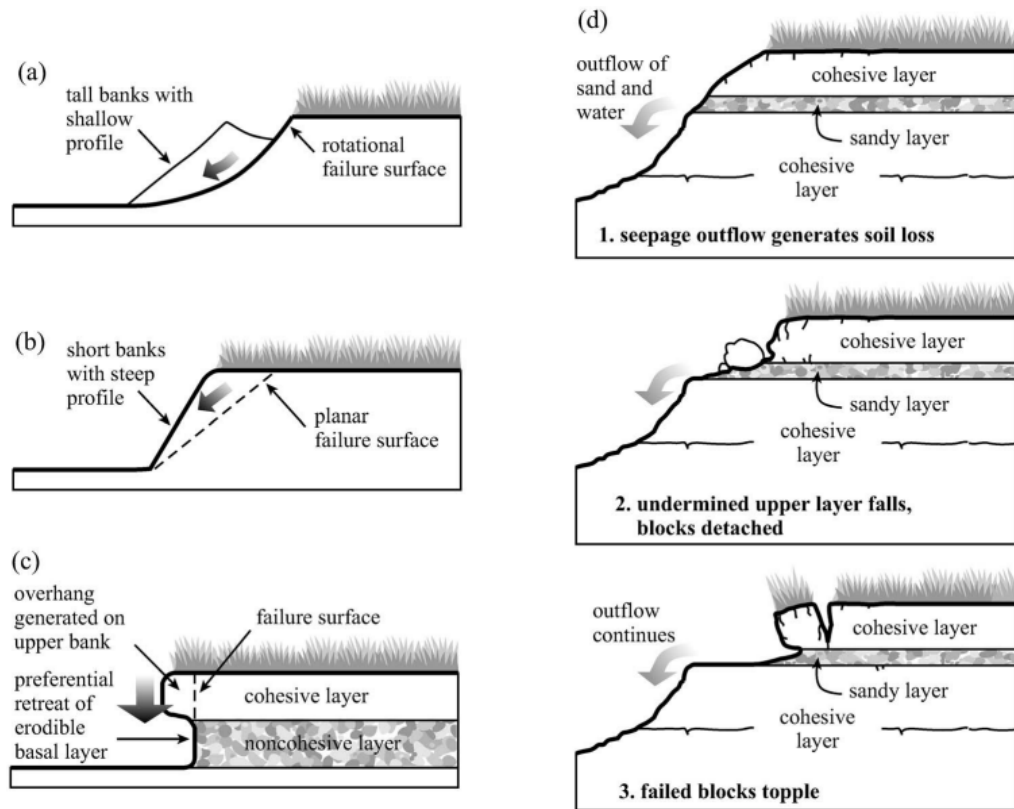


Figure 3.1: Bank failure mechanisms: (a) rotational; (b) planar; (c) cantilever; and (d) piping or sapping. From (Langendoen & Simon, 2008).

A wide range of field studies exist that show flow-vegetation interactions for above surface biomass, e.g. Boothroyd (2017), as well as several lab-based studies, e.g. Frostick et al. (2014). Research on below surface biomass, in contrast to above surface biomass, requires either more complex measurement devices or uprooting of the sample that both may damage the sample and/or the environment and thus reducing the potential for repeatability or comparisons in different environmental conditions (Dick et al., 2014). So far, below surface biomass has had only limited attention within physical modelling (Frostick et al., 2014) despite it accounts most of the added shear strength of biomass.

Below surface biomass could include roots and other organic components of plants, however in the remainder of this thesis, roots or root systems refer to all below surface biomass. Furthermore, like above ground biomass, root systems of different plants behave differently dependent on species, location or conditions (e.g. Stromberg (2013), Tron et al. (2015), Gurnell

et al. (2019)). The impact of this variation predominantly relates to three aspects. First, there is root size, a combination of root diameter, root taper angle and root length. Overall, larger diameter roots can withstand a larger tensile stress and require more force to break (e.g., Thomas and Pollen-Bankhead (2010)). Second, there is root flexibility or tortuosity that describes how likely and how far a root can bend before it will break (Schwarz et al., 2010). Both flexibility and root size determine whether roots break or bend which changes the stability of a bank differently. Third, root architecture, the spatial distribution and number of roots (Figure 3.2). The impact of geotechnical shear stress varies based on whether the root architecture is a plateroot, heartroot or taproot system. Additionally, root architecture for a single species also changes from a seedling towards a full mature plant or tree.

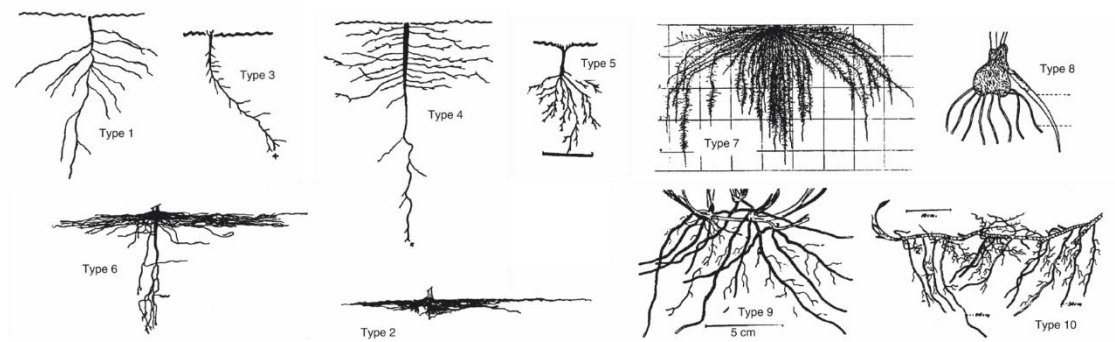


Figure 3.2: Overview of a range of root architecture types reworked from Pagès (2011) based classification of Cannon (1949).

Bank erosion processes under the influence of vegetation are temporally and spatially complex and quantification is generally destructive (e.g. Simon and Collison (2002); Pollen (2007)). Modelling, both physically and numerically, is a commonly used approach to understand larger spatial and longer temporal processes like system evolution in fluvial systems. Hence physical modelling, by decreasing the spatial scale, allows a faster evolution of these processes without simplifying the natural processes like numerical modelling. Over the last decades, as experimental modelling has become more sophisticated and data collection technologies have improved, it has become more common to add more complexity to physical models. One of these key techniques was the addition of surrogate vegetation into physical models.

3.1.1. Vegetation in physical experimental models

Introduction of vegetation in physical models has a wide range of implementations, as discussed in chapter 2. This section as such will focus on the use of small, cress like, sprouting vegetation as a model of prototype vegetation. Since the introduction of alfalfa (*Medicago sativa*) by Gran and Paola (2001) to stabilize their laboratory river model, small living vegetation has commonly been used with success in analogue river scale models, both in large scale geomorphic fluvial research (Bertoldi et al., 2015; Braudrick et al., 2009; Tal & Paola, 2010; van Dijk, Teske, et al., 2013) and in smaller scale experimental research on processes (Clarke, 2014; van de Lageweg et al., 2010). The larger scale experimental research has all used the behaviour of alfalfa to understand a system with more stability.



Figure 3.3: Plan-view overview of fluvial geomorphic research with alfalfa from A) Tal and Paola (2010), B) Braudrick et al. (2009) and C) Bertoldi et al. (2015).

These examples of experimental research show that alfalfa reduces channel width, increases bank and bar stability, reduces sediment reworking and/or induces fluvial system shift. The initial choice of alfalfa (Gran & Paola, 2001) is not recorded and most latter experimental research (Bertoldi et al., 2015; Braudrick et al., 2009; Tal & Paola, 2007, 2010; van Dijk, Teske, et al., 2013) do not elaborate on the choice of alfalfa further than the success of previous experimental research. Other similar cress-like vegetation has been attempted in large scale models, e.g. Catgrass (Perona et al., 2012) which has a slightly shorter duration of growth, but

has a root structure that consists of a bunch of parallel roots (Jiang et al., 2009), in contrast to single rooted alfalfa.

As discussed in chapter 2, the success of the use of biological surrogate vegetation like alfalfa in physical models is accompanied with one main downside; time to grow and develop vegetation and thus experimental downtime. As such, methods to reduce this downtime would benefit research outcomes and efficiency.

3.1.2. Introduction to polysaccharides

One approach to overcome this experimental downtime is to use a quasi-instantaneous method to represent the effects of natural vegetation. For this, two different aspects of vegetation need to be considered. First, the interaction of the stem and leaves with the flow to reduce flow velocities and enhance sediment trapping can be represented by using, for example, sticks and other shapes from different materials (e.g. McBride et al., 2007). Second, the root system interacts with the sediment to generate a higher bank and system stability. This interaction, and its simulation using chemical surrogates, is the focus of the present research.

Increased bank strength was the initial underlying reason why surrogate vegetation was introduced in physical models (Gran & Paola, 2001). Previous studies attempted to increase bank strength through the addition of kaolinite (Schumm & Khan, 1972; Smith, 1998), silica flour (Moreton et al., 2002), crushed coal (Cazanacli et al., 2002; Sheets et al., 2002) or silt (van Dijk, van de Lageweg, et al., 2013). Recently, within geomorphic physical modelling there has been a shift back towards the use of natural cohesive agents, such as extracellular polymeric substances (EPS), which are natural substances secreted by microorganisms that exist in all kinds of environments. When these secretions become common or dominant they can transform into biofilms (Tolhurst et al., 2002), mats of sediment particles and microorganisms cemented in a matrix of the secreted EPS (Decho, 2000). Next to any chemical or biological impact, these mats also alter the physical interaction of hydrodynamics and in particular sediment transport. Due the matrix, sediment is harder to erode and as such, soils or beds become protected by these

biofilms in certain flow conditions. Research by Malarkey et al. (2015) introduced EPS into a physical lab to show their impact on the mobility and formation of small bed forms. In order to represent the natural biotic EPS, abiotic EPS or polysaccharides were introduced. These abiotic polysaccharides have similar behaviours as natural biotic EPS, and by using them in a submerged environment these polysaccharides enhanced the co/adhesive effect of the bed and altered the behaviour of small ripples (Malarkey et al., 2015; van de Lageweg et al., 2018; Wu, 2017).

On a similar note, reintroduction of these chemical agents as a representation for the root system of surrogate vegetation is now feasible as recent research showed that chemical agents can also have a stabilizing behaviour in soil samples (Chang et al., 2015). Furthermore, the application of chemical agents is quasi-instantaneous since it does not require time to grow or develop. To date, these chemical agents have not been introduced to fluvial geomorphic research where both dry, wet and submerged areas all co-exist. As such, there is a potential to develop protocols for using chemical agents in new ways and for quantifying their behaviour when used in these novel approaches.

3.1.3. Use of small-scale experiments to understand large-scale processes

Small-scale experimental models are a great way to explore these new approaches and protocols as they allow us to focus on specific processes. This approach, where individual processes like bank erosion, sedimentation rates, and flow structures are observed as small 1:1 scale models from physical models has been successfully applied in the past (Kleinhans et al., 2014) and is an effective method to model the effect of specific variables and to explore conditions that can be applied in larger experiments. Moreover, small experiments, due to their limited spatial dimensions and their relatively short running time, both increase the potential number of replications and reduce the costs of running experiments. This, as such, provides the opportunity to understand the behaviour of chemical agents and quantify these behaviours by comparison with biological surrogates.

3.1.4. Outline of this chapter

The previous sections show the benefits to reduce experimental downtime caused by the growth and germination of living surrogate vegetation. Whereas this experimental downtime can be reduced through optimization of lighting and watering strategies (e.g. Clarke, 2014), the physical modelling community would benefit from a near-instantaneous method of representing and applying vegetation. Hence, this chapter will assess the potential of different surrogates that reproduce the cohesive effects of vegetation that can be applied rapidly to an experimental set-up, enabling reduced experimental downtime. Four alternative surrogates are assessed: two previously documented surrogates, alfalfa and xanthan gum, and two novel surrogates, carrageenan and sodium alginate. The effectiveness of the different surrogates will be assessed by comparison of the mean erosion rates, variability of erosion rates and morphological characteristics of bank erosion using a series of small-scale bank erosion experiments, similar to those of van de Lageweg (2010).

The chapter is organised as follows. First, the concepts of erosion rate and its variability are introduced within the experimental set-up, employing a selection of different grainsizes (sections 3.3.1 and 3.3.4). Second, the impact of growth period duration and seed density of alfalfa (*Medicago sativa*), a commonly-used cress-like surrogate (e.g. Gran & Paola, 2001; Tal & Paola, 2010), on erosion are explored to give baseline measurements for comparison (sections 3.3.2 and 3.3.5). Increased duration of growth and increased seed density are both expected to reduce erosion rates. Third, the impact of varying the concentration of two chemical surrogates, carrageenan and xanthan gum, on erosion are explored (sections 3.3.3 and 3.3.6). Past experiments (Malarkey et al., 2015; Parsons et al., 2016) showed that these chemical surrogates enhanced cohesion and higher concentrations were therefore expected to result in reduced erosion rates and a change in morphological behaviour from steady, continuous erosion to episodic erosion associated with mass failure events. Fourth, the impact of varying the concentration of a novel chemical surrogate, sodium alginate, on erosion rates is explored (sections 3.3.7 and 3.3.8). Finally, in a development novel to this thesis, sodium bicarbonate of

varying concentrations is added to the eroding water to explore whether it is possible to control deterministically the erodibility of sodium alginate-dosed bank materials (sections 3.3.7 and 3.3.8). Hence, this chapter aims to understand how different surrogates impact erosion rates and erosion behaviour. Furthermore, it aims to find whether chemical surrogates are able to represent erosion rates of surrogate vegetation.

3.2. Experimental methodology

Friedkin (1945) and van de Lageweg (2013; 2010) previously used small scale experiments to investigate bank erosion (Figure 3.4). Herein, a set-up similar to van de Lageweg (2010) was used, which enabled the methodology to be easily developed and compared with existing data.

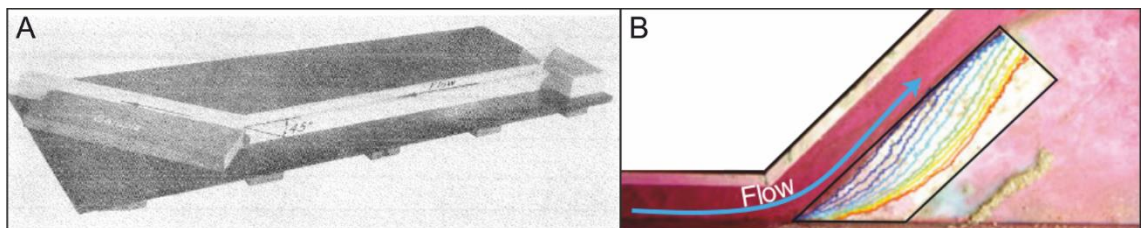


Figure 3.4: Small scale experimental set-ups of A) Friedkin (1945) and B) van Dijk et al. (2013).

The present study consists of two different sets of experiments. The first set of experiments comprises three different sections; erosion with bare sediment (experiments 1-3), erosion with added surrogate vegetation (experiments 4-9) and erosion with added chemical agents (experiments 10-18). The second set of experiments arose as a result of limitations identified during the first set of experiments and comprises two sections; erosion with an additional, novel, chemical agent (experiments 19-21), and erosion using that agent under bicarbonated water conditions (experiments 22-27). Within each set of experiments, different preparation methods were employed and different variables were controlled (e.g. grainsize, seed density or concentration (see Table 3.1 and section 3.2.2)). Within the first set of experiments (experiments 1-18), different hydrodynamic conditions and data collection methods were employed than in the second set of experiments (experiments 19-27). In the text that follows, where there were

differences parameter values between the first and second sets of experiments, those for the second sets of experiments (exp. 19-27) are shown in brackets.

3.2.1. Experimental set-up

The experimental research was conducted within a 2.2 m × 1.2 m × 0.25 m polyethylene stream table at the University of Hull (Figure 3.5 A). Inside the stream table, a 1.5 m × 0.4 m × 0.05 m foam insert was installed at the upstream end to allow free drainage of water and sediment. The interior of the stream table had a slope of 0 m m⁻¹ and an outlet with a diameter of 53.7 mm in the floor at the centre of one of the short sides. This set-up (Figure 3.5 B), had an 8.1 mm thick barrier to create a 50 mm wide, 1.10 m long inlet channel parallel to the stream table wall. The 40 mm high barrier was bent to form a 45° angle between the last 325 mm of barrier and the stream table wall. Foam-metal-basin contacts were sealed to prevent water egress. All surfaces within the inlet channel and experimental area were coated with medium sand (434 µm, see section 3.2.3.1) to generate a uniform rough surface.

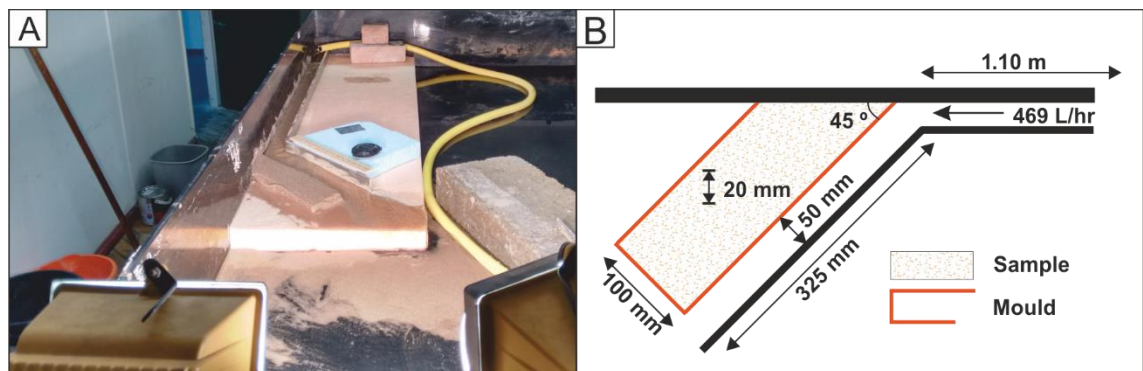


Figure 3.5: A) Overview of the experimental set-up during an active run (image taken from downstream position). B) Schematic planform overview of the experimental set-up, including removable mould for placement of each sample.

*Experiments 19-27 have an input discharge of 479 L/hr.

Samples of sediment to be eroded (further referred to as the erosion block), were placed at the same location each time using a mould (Figure 3.5 B). This 100 mm wide, asymmetric U-shaped metal mould, with legs of 220 and 320 mm, was 20 mm high. Fixed blocks were used to keep the distance between the mould and the barrier at 50 mm.

A simple submergible pump in an 80-90 litre (40 litre for experiments 19-27) tap water filled end-tank provided flow in an enclosed water circulation system. After each experiment, the end tank was emptied and refilled, thus limiting, in experiments with chemical agents, the potential for drag reduction often linked with use of these agents (Wyatt et al., 2011). The pump provided water by a hose at a constant discharge at the upstream end of the inlet channel. The 1.1 m-long inlet channel dampened flow field perturbations induced by the pump system. The outflow of the pump, calibrated by measuring the time taken to fill 10 litre buckets, was 469 L hr^{-1} ($\pm 5 \text{ L hr}^{-1}$), a value similar to 400 L hr^{-1} used in previous experimental research by van de Lageweg (2013). For the second sets of experiments, flow was calibrated at 479 L hr^{-1} . Simple flow velocity measurements, using floating particles and a stopwatch, indicate a constant inlet flow reading of 0.26 m s^{-1} ($\pm 1 \text{ m s}^{-1}$). Water depth in the channel was 11 mm ($\pm 1 \text{ mm}$), with subcritical flow ($Fr = 0.79$). Over time, as the erosion block eroded, channel width increased near the erosion block thereby reducing water depth and potentially reducing flow velocity and/or increasing Froude number. Furthermore, due to the set-up, water depth along the block of sediment was not constant over the length of the erosion block as it slowly decreased towards the end of the block.

A 5 megapixel (2560×1920 pixels) GoPro Hero 3 was mounted 0.96 m vertically above the block of sediment and recorded time-lapse imagery every 30 seconds. Object-space pixel size was 0.6015 mm (0.5114 mm in experiments 19-27). An excavation lamp, downstream of the experimental set-up, cast a shadow from the erosion block into the water, enabling the use of shadowgraphy to track the retreat of the erosion block (see 3.2.4).

3.2.2. Experimental Runs

Out of a total of 314 runs, 261 runs spread over 27 different experiments were selected for analysis. For the first set of experiments, this includes three experiments with bare sediment blocks (experiments 1-3, see section 3.2.3.1), six experiments with sediment blocks with surrogate vegetation (experiments 4-9, see section 3.2.3.2), nine experiments with chemical

agents (experiments 10-18, see section 3.2.3.3) and six experiments with both the novel chemical agent and an altered fluid type (experiments 19-21, see section 3.2.3.4) and six experiments with both the novel chemical agent and an altered fluid type (experiments 22-27, see section 3.2.3.4). Table 3.1 gives an overview of runs and settings for the first set of experiments. Table 3.2 (see section 3.2.3.4) gives an overview of runs and settings for the second set of experiments. Each experiment included 10 runs, replicates of each other, which allows the description of the variability between runs. Several experiments with sediment blocks with surrogate vegetation have fewer replicate runs as the longer growth duration was not compatible with available experimental time.

Table 3.1: Overview of first set of experiments, experiments 1-18, with conditions, repetitions and characteristics.

Set nr	Sediment	Added Agent	Concentration	Seed Density	Growth Length	Repetitions	*
1	458 μm	-	-	-	-	10	
2	190 μm	-	-	-	-	10	
3	458 μm / 190 μm	-	-	-	-	10	^
4	458 μm	xanthan gum	0.125 g kg ⁻¹	-	-	10	
5	458 μm	xanthan gum	0.250 g kg ⁻¹	-	-	10	
6	458 μm	xanthan gum	0.500 g kg ⁻¹	-	-	10	
7	458 μm	xanthan gum	1.000 g kg ⁻¹	-	-	10	
8	458 μm	carrageenan	0.125 g kg ⁻¹	-	-	10	
9	458 μm	carrageenan	0.250 g kg ⁻¹	-	-	10	
10	458 μm	carrageenan	0.500 g kg ⁻¹	-	-	10	
11	458 μm	carrageenan	1.000 g kg ⁻¹	-	-	10	
12	458 μm	carrageenan	0.750 g kg ⁻¹	-	-	10	
13	458 μm	alfalfa	-	1.1 seed/cm ²	7 days	10	
14	458 μm	alfalfa	-	1.1 seed/cm ²	10 days	10	
15	458 μm	alfalfa	-	1.1 seed/cm ²	13 days	6	
16	458 μm	alfalfa	-	2.2 seed/cm ²	7 days	10	
17	458 μm	alfalfa	-	2.2 seed/cm ²	10 days	10	
18	458 μm	alfalfa	-	2.2 seed/cm ²	13 days	5	

^ sediment is dry mixed with 500 g 458 μm and 500 g 190 μm per sample.

For each run in each experiment, the experimental procedure was identical. After a previous run was finished, data collection was stopped and the remainder of the sediment still left in the experimental area was removed. Next, flow was stopped and any remaining sediment was

removed from the basin. Once the experimental area was clean and wet (if no runs were run on the same day, the experimental area was first wetted by turning on the pump/flow for several minutes), erosion block preparation (see section 3.2.3) was started. After erosion block preparation and placement was finished, the mould was carefully removed immediately before the start of measurements. This included triggering the time lapse camera, starting a stopwatch when the second image was taken and starting the pump at 19 seconds, to allow water to reach the erosion block 1-2 seconds before the next image. Measurements finished when either the sediment block was completely eroded, the sediment block was fractured in two parts, or 2 hours had elapsed. Over the course of the experiments the maximum duration was reduced to 1.5 hours to increase the number of potential runs.

3.2.3. Preparation of sediment blocks

The erosion blocks used in the different experiments (i.e., bare blocks, blocks with surrogate vegetation and blocks with chemical agents; sections 3.2.3.1 to 3.2.3.4) all had a similar geometry but required a different preparation method.

3.2.3.1. Bare sediment blocks

Three different sediment mixtures are used for these experiments of these mixtures several were used throughout the entire thesis (Figure 3.6). This included a very fine sand ($D_{50} = 190 \mu\text{m}$, Redhill 110) and two medium sand mixtures (Chelford CH30, $D_{50} = 434 \mu\text{m}$ and Chelford CHSP30, $D_{50} = 458 \mu\text{m}$). This slight difference between both Chelford mixtures will be ignored further in this thesis as variance within the mixture may contribute to similar offsets in distribution. As such the Chelford medium sand fractions are considered to have a D_{50} of $458 \mu\text{m}$.

For the bare sediment blocks three sediment mixtures were used based on lab availability. Two unimodal mixtures and one bimodal mixture composed of a 50:50 mix of the two unimodal mixtures: the medium sand ($D_{50} = 458 \mu\text{m}$) and the fine sand ($D_{50} = 190 \mu\text{m}$). The medium sand fraction is similar to the poorly sorted sand fraction ($D_{50} = 470 \mu\text{m}$) used in the experimental

research of (van de Lageweg, 2013). The very fine sand fraction exhibited behaviour resembling cohesion in previous experimental research due to its angularity (Houseago, 2018, pers. comm.), which caused significant interlocking of grains (e.g. Taylor (1948)).

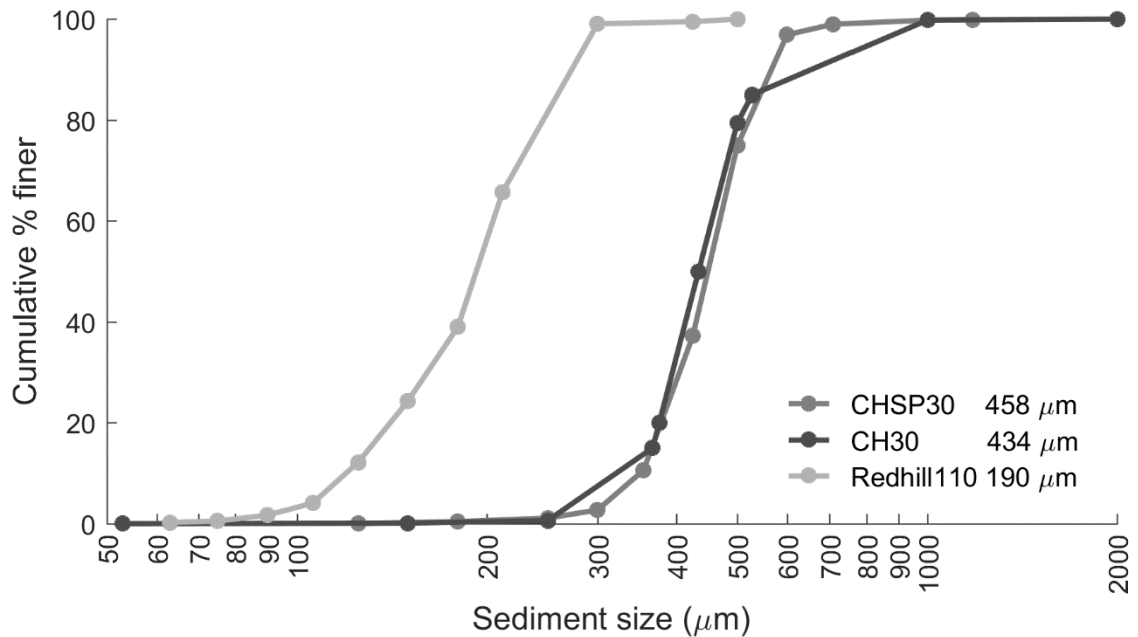


Figure 3.6: Cumulative grainsize distribution for CHSP30, CH30 and Redhill110 sediments.

To generate similar conditions for all runs, the sediment in the blocks was saturated at the start of the run. For the single grainsize runs, sediment was submerged before being placed in situ in the mould. Upon placement, sediment was pressed further into the mould with a trowel and extraneous sediment was removed from the erosion block and experimental area. For the 50:50 runs, 0.5 kg of each sediment was weighed, before dry mixing using the lowest speed of a standard 3-speed hand mixer (Kenwood M225, 150 Watt). After 30 seconds, 230-250 mL water was poured into the mixture, that then was hand mixed for 30-60 seconds until the sediment was saturated and all standing water was dispersed. Each erosion block was prepared within 15 minutes of the start of the run.

Results (see section 3.3.1) of these bare experiments indicated high erosion rates for blocks composed of medium sand ($D_{50} = 458 \mu\text{m}$), as blocks were eroded within 15 minutes. Therefore,

this sediment was selected for all runs with surrogate vegetation and all runs with chemical agents.

3.2.3.2. *Sediment blocks with surrogate vegetation*

For the experiments with surrogate vegetation (experiments 4-9), this research employed *Medicago sativa*, commonly known as alfalfa, a small cress-like, fast growing plant that has been widely used in physical models (as discussed in section 3.1.1). Past research has shown that alfalfa, compared to other species, is more robust and less sensitive to environmental conditions common in flumes (Clarke, 2014) while it still has a prominent root structure (van de Lageweg et al., 2010). Two contrasting seed densities, 1.1 seeds cm⁻² and 2.2 seeds cm⁻², were used. This is similar to other analogue experimental research (2.2 seeds cm⁻² and 4.4 seeds cm⁻² in van de Lageweg et al. (2010), 1 seed cm⁻² in Tal and Paola (2007), 1.5 seeds cm⁻² in van Dijk et al. (2013) and 1.2, 4.2 and 9.2 seeds cm⁻² in Gran and Paola (2001)). For experimental research with vegetation, a clear distinction is required between seed and stem density. Seed density is the number of seeds seeded on a specific area while stem density only includes sprouted seeds. Stem density is far more common in field related studies, since seeding densities are often not measured in the field (Bankhead et al., 2016), nor in physical experimental research where seeds are distributed by the flow (van Dijk, Teske, et al., 2013). Research by Clarke (2014) indicated that sprouting rates are dominated by different environmental conditions (e.g. light, moisture, seed preparation and growing time) and that sprouting rates plateaued around 80-90%.

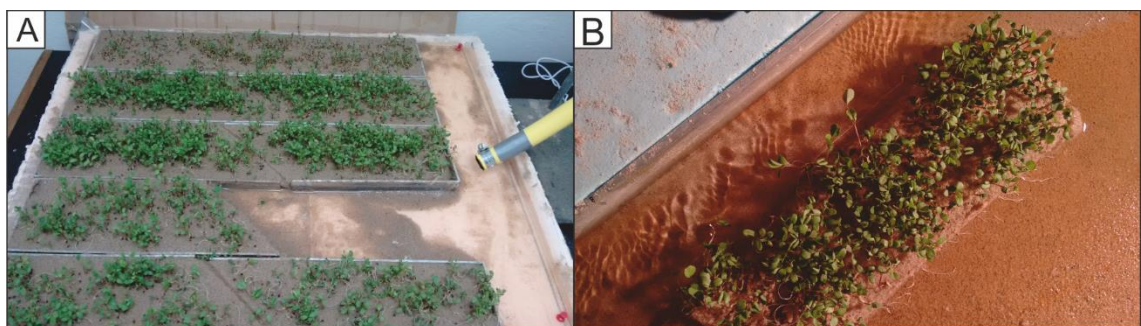


Figure 3.7: A) Overview of set-up during the growth phase of alfalfa samples. B) Example GoPro time-lapse image during one run with high-density vegetation. Image highlights the difficulties with capturing the bank line due to the overlapping vegetation.

Blocks with surrogate vegetation require a different sample preparation approach from the bare blocks, since growing vegetation in situ would not produce the required number of replicates within the experimental time frame. To overcome this time constraint, a simple foam basin (0.54 × 0.67 m) was used with upstanding foam barriers (see Figure 3.7 A). An added watertight layer of plastic was placed in this basin to maintain a water table 10-15 mm deep.

Ten metal moulds, identical to the mould used for the bare blocks, were placed upon this layer (Figure 3.7 A). By interlocking the moulds only a small body of standing water remained at one side, about 65,000 mm², which allowed water to drip in from a watering system. This basic watering system, comprising a funnel, a short length of hose and cork stopper, allowed slowly dripping water (1 Litre) into the side of the basin over the course of several hours. At the start and end of every working day, water in the basin and in the funnel was replenished. Although the water table dropped up to 15 mm overnight and at the weekend, sediment remained saturated and plants showed no clear signs (e.g. bending over or yellowing) of drought.

The moulds were filled with sediment prepared in the same way as the bare blocks (see section 3.2.3.1), mixing 2 kg of sediment with 460 mL of water for each interlocked pair of moulds. On these smooth, stroked surfaces, 58 g (low density) or 116 g (high density) (+/- 1 g) of alfalfa seeds were seeded manually. This represented ~300 or ~600 seeds and a seed density of 1.1 or 2.2 seed cm⁻². In contrast to previous studies (Clarke, 2014; Gran & Paola, 2001), seeds were seeded dry and unprepared. Alternative methods (e.g. pre-soaking or placing them in wet paper towel inside a fridge), that decrease germination time prevent uniform spreading of seeds by hand.

This basin was placed in a laboratory at the University of Hull, where temperature and light could be controlled. In this laboratory, temperature varied between 16 and 20°C, which according to Clarke (2014) would not alter the stem length or germination rate. A special bulb (33200 lm), 1.05 m above the growing basin, was active for 24 hours every day. Illuminance above the growing bed ranged between 520 and 720 lx.

Alfalfa was grown on the erosion blocks for either 7, 10 or 13 days before the erosion blocks were used in experiments. To transport the erosion blocks and mould into the experimental area, a thin slice of metal the same planform shape and size as the mould was pushed under the block to support the sediment. Interlocked samples were cut vertically through the boundary of both samples to allow individual transportation. Blocks that were disturbed during transport were filled up with excess sediment on the critical upstream corner, to prevent flow separation. Once a block was transported into the experimental area, the experimental procedure followed that of the bare sediment blocks.

In several runs with surrogate vegetation, uprooted vegetation surrogates were collected, spread out and photographed for further analysis. These photographs were used to determine several key root-system morphology characteristics (Pérez-Harguindeguy et al., 2013). This included taproot length (the length of the longest root of the sprout), total root length (the total length of all roots), the number of nodes (location where a root splits) and specific root length (SRL), which is the ratio of the tap root length to the total root length (Pérez-Harguindeguy et al., 2013). This data was extracted from the photographs using ImageJ© (version 1.52d, Rasband (2019)).

3.2.3.3. Blocks with chemical agents

For the experimental runs with chemical agents applied to sediment blocks, two different agents were used: Xanthan gum (experiments 10-13) and Carrageenan (experiments 14-18) which have both been shown to increase cohesion in previous experimental research (van de Lageweg et al., 2018). In these tests, nine experiments were conducted with different concentrations of each agent.

Xanthan gum ($C_{35}H_{49}O_{29}$), a common thickening agent and food additive (Baynes et al., 2015; van de Lageweg et al., 2018), is a polysaccharide, and has been used previously to represent biofilms or microbial-induced cohesion in physical modelling experiments (Malarkey et al., 2015; Parsons et al., 2016; Tolhurst et al., 2002; van de Lageweg et al., 2018).

Carrageenan is a polysaccharide made from red seaweed that is also a commonly used food additive which, in contrast to xanthan gum, has additional sulphate groups ($C_{24}H_{35}O_{25}S_2$) (van de Lageweg et al., 2018; Williams, Houseago, et al., 2018). Carrageenan has been used less frequently than xanthan gum to represent biofilms and cohesion in physical modelling experiments and the experiments described here use an iota-type powder identical to that used by Van de Lageweg *et al.* (2018) produced by Alfa Aesar.

Previous research has demonstrated that increased concentration of these chemical agents increases their cohesive effect (Malarkey et al., 2015; van de Lageweg et al., 2018). (Malarkey et al., 2015) used xanthan gum concentrations as high as 2.5 g kg^{-1} , but initial tests found that erosion blocks with this concentration of xanthan gum were not erodible. Hence, the concentrations used for this research are significantly lower for both xanthan gum and carrageenan with a concentration of 0.125, 0.250, 0.500 and 1.000 g kg^{-1} . For carrageenan, an additional experiment with a concentration of 0.750 g kg^{-1} was also conducted. Recent experimental research highlighted two different approaches for mixing chemical agents with sediment: wet-mixing and dry-mixing (Fernandez et al., 2019; Williams, Houseago, et al., 2018). Wet-mixing requires mixing (or dissolving) the agent in water before adding it to sediment (Fernandez et al., 2019). In dry-mixing, the sediment and the agent are mixed together before adding water (Williams, Houseago, et al., 2018). For these experiments, a dry-mixing method was used following a strict procedure for the quantities and timing of preparation (see Figure 3.8).

First, 1.0 kg of sediment was weighed, next the required amount of the chemical agent ($\pm 1 \times 10^{-5} \text{ kg}$) (see Table 3.1) was weighed separately. Both were poured together into a small clean and dry plastic bucket and stirred with a metal rod to spread the sediment over the entire bowl. Next, 230 mL tap water was poured into the mixture, where it was mixed with a hand mixer (see section 3.2.3.1) at the lowest speed. The mixer was used for up to 60 seconds before the mixture was placed into the mould using an identical method as the bare erosion blocks (see section

3.2.3.1). The total length of preparation procedure for polysaccharide mixtures, from dry-mixing to starting the flow in a run took about 10 minutes. Preliminary experiments showed that preparation in advance (over 60 minutes) significantly reduced erosion rates.

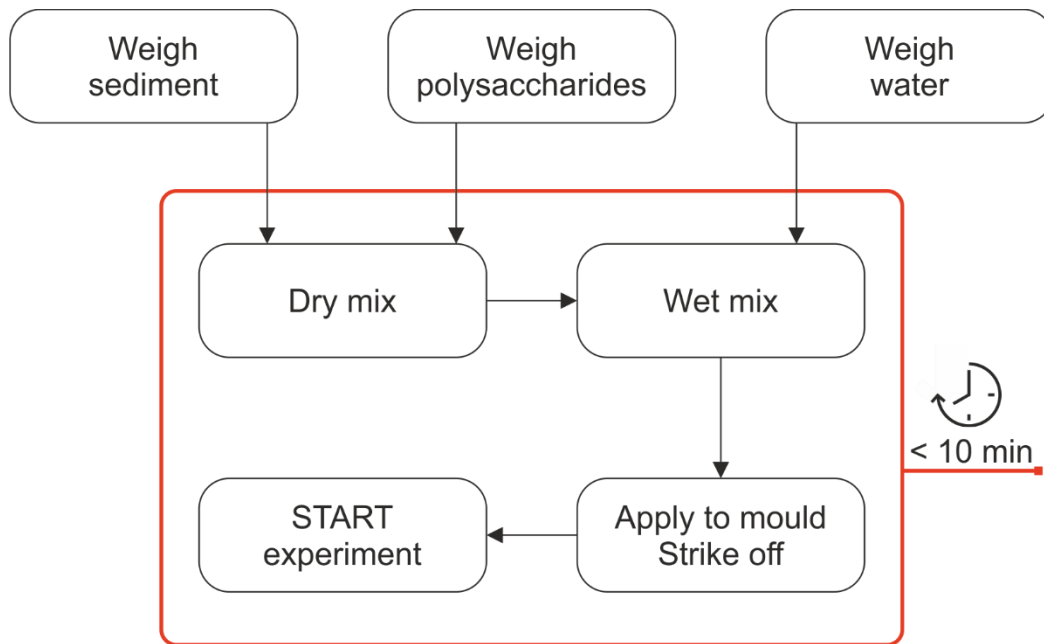


Figure 3.8: Schematic overview of the experimental procedure for polysaccharide sample preparation

3.2.3.4. An additional approach

The results from the first set of experiments (see sections 3.2.3.3 and 3.3.3) with xanthan gum and carrageenan show a positive relation between increased chemical agent concentration and a reduction in the rate of erosion. However, those experiments also highlighted several major limitations on use and application, especially if chemical surrogates are intended to represent surrogate vegetation (discussed further in section 3.4.3). As such a third chemical was introduced in an attempt to overcome shortcomings of xanthan gum and carrageenan. This chemical agent that is more controllable and easier to apply was introduced to the same experimental set-up: sodium alginate. Sodium alginate was suggested (M. Lorch, 2018, pers. comm.) as it forms a gel in the presence of divalent cations (e.g. Ca^{2+}) but dissociates its polymers with monovalents (e.g. Na^+) (Lee & Mooney, 2012).

Table 3.2: Overview of second set of experiments, experiments 19-27, with conditions, repetitions and characteristics.

Set nr	Sediment	Added Agent	Concentration	NaHCO ₃ concentration	Repetitions	*
19	458 µm	-	-	-	10	
20	458 µm	sodium alginate	0.250 g kg ⁻¹	-	10	
21	458 µm	sodium alginate	0.500 g kg ⁻¹	-	10	
22	458 µm	-	-	10 g L ⁻¹	10	
23	458 µm	sodium alginate	0.250 g kg ⁻¹	10 g L ⁻¹	10	
24	458 µm	sodium alginate	0.500 g kg ⁻¹	10 g L ⁻¹	10	
25	458 µm	-	-	20 g L ⁻¹	10	
26	458 µm	sodium alginate	0.250 g kg ⁻¹	20 g L ⁻¹	10	
27	458 µm	sodium alginate	0.500 g kg ⁻¹	20 g L ⁻¹	10	

In order to put this theoretical approach in practice, sodium bicarbonate was used as a dissolved medium in the eroding fluid. Once dissolved, sodium bicarbonate has a monovalent sodium cation (Na⁺) and a monovalent bicarbonate anion (HCO₃⁻). To determine the appropriate concentrations of sodium bicarbonate and sodium alginate, a small test set-up was staged. In this set-up (Figure 3.9A), three small petri dishes were filled with a sediment-sodium alginate mixture, mixed according to the mixing method described in section 3.2.3.3. Each filled small petri dish was placed upside down in a larger petri dish. The larger petri dishes were filled with a solution to about half full. One dish was filled with only tap water, the other two were filled with two different concentrations of sodium bicarbonate. A fourth small petri dish, acted as a reference and was only filled with sediment and placed in tap water. Observations to determine what concentration would be most suitable for future experiments were made at structurally increasing time intervals until the end of the test after 20 hours. After 20 hours (Figure 3.9 B), the sodium alginate sample in the highest concentration of sodium bicarbonate was fully disintegrated at the edges of the sample (a). The sodium alginate sample in low concentration sodium bicarbonate showed some localized disintegration but was mainly intact (b). The sodium alginate sample in tap water had no visual change (c). Finally, the sample without sodium

alginate collapsed fully into an almost complete pile of sand (d). Observations over the course of the test indicated a release of air bubbles from the samples in sodium bicarbonate during the disintegration of the sample. As this process was not observed during the disintegration of the reference sample and as no measurements were done on these air bubbles, it is suggested that these air bubbles are carbon dioxide and that they give an indication of a chemical reaction between the sodium alginate and the sodium bicarbonate.

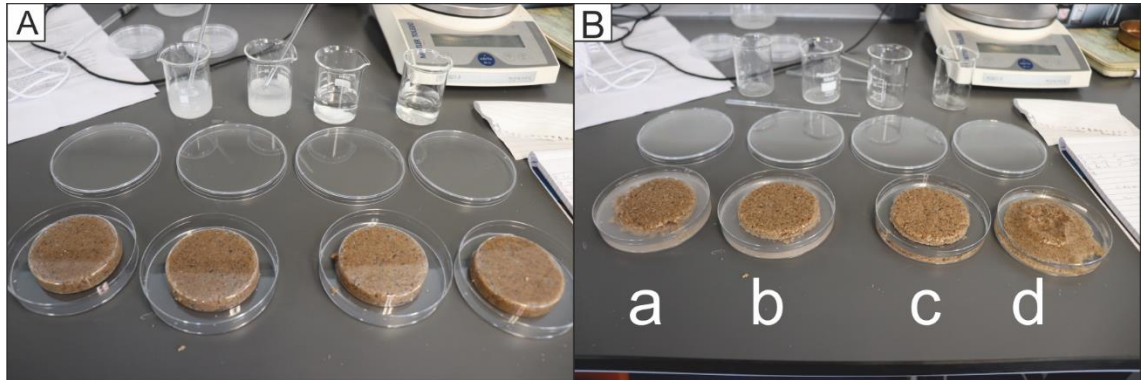


Figure 3.9: Overview of smallest scale preliminary tests with sodium alginate (SA) and sodium bicarbonate (SB), A) start of experiment, B) after 20 hours. Petri dishes from left to right show a) $1 \text{ g kg}^{-1} \text{ SA} + 20 \text{ g L}^{-1} \text{ SB}$, b) $1 \text{ g kg}^{-1} \text{ SA} + 10 \text{ g L}^{-1} \text{ SB}$, c) $1 \text{ g kg}^{-1} \text{ SA} + \text{tap water}$, d) sand + tap water.

These tests were repeated at a larger scale (Figure 3.10 A) to rule out the impact of a shortage of sodium bicarbonate. Here, an irregular u-shape mould, as described in section xxx, was filled with 1 g kg^{-1} of sodium alginate-sand mixture and placed in a square $0.42 \times 0.42 \text{ m}$ overflowing basin. A recirculating water system with an overflow and a peristaltic pump slowly fed the solution from a 3 L overflow basin towards the experimental basin. Each hour, starting from a concentration of 0 g L^{-1} , the concentration of sodium bicarbonate was increased by 5 g L^{-1} up to a final concentration of 30 g L^{-1} by adding and mixing sodium bicarbonate in the overflow basin. The block of the sodium alginate-sediment mixture showed no change under tap water conditions, bar some initial collapses of air spaces inside the sediment caused by inconsistent application. An increase in sodium bicarbonate concentration resulted in a slow disintegration of the block along the edges, accompanied with the release of air bubbles (Figure 3.10 B). At times, in contrast to the smaller test, larger blocks separated from the main block of sediment

and disintegrated more rapidly once isolated. The increase of the concentration of sodium bicarbonate resulted in increased disintegration rates that eventually transformed the block of sediment into a bar of sediment, thereby halting further disintegration (Figure 3.10 C and D). As such, these tests showed two things: 1. the used range of concentrations is sufficient to include conditions in the experiments; and 2. the extent of these tests is limited by contact area due to the lack of sediment transport by flow.

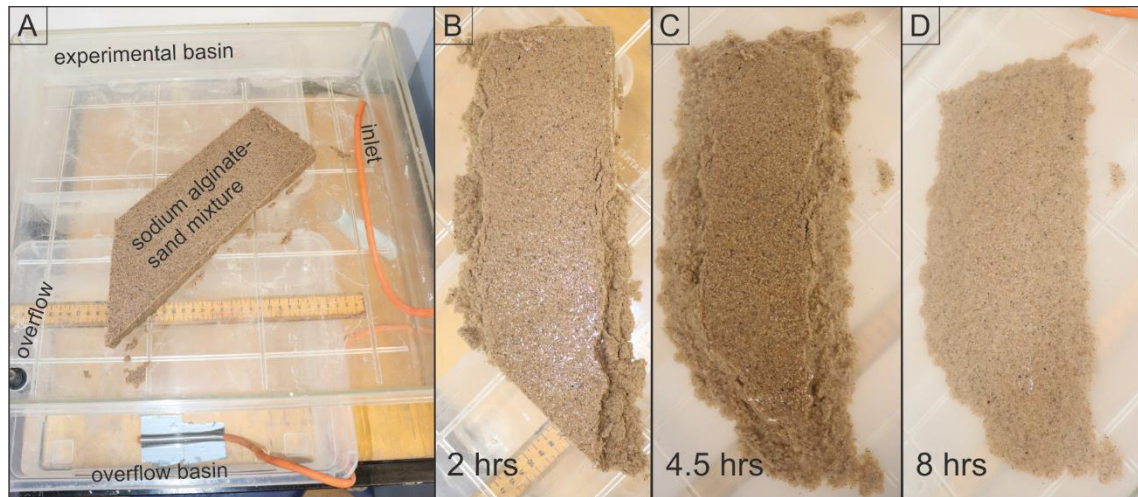


Figure 3.10: A) Experimental set-up of up-scaled preliminary test. B-D) Top-view experimental sample after B) 2 hours (10 g L^{-1}), C) 4.5 hours (20 g L^{-1}) and D) 8 hours (30 g L^{-1}) in the experiment.

The preliminary tests identified nine main settings for further bank erosion experiments: three different sodium alginate concentrations (0 g kg^{-1} (bare), 0.25 g kg^{-1} (low) and 0.5 g kg^{-1} (high)), and three different concentrations of sodium bicarbonate (0 g L^{-1} (tap water, exp. 19-21), 10 g L^{-1} (low, exp. 22-24) and 20 g L^{-1} (high, exp. 25-27)). Each sodium alginate concentration was run at each sodium bicarbonate concentration (see Table 3.2). For preparation, sodium bicarbonate was dissolved in buckets of 10 L of tap water and stirred for up to 1 minute until the sodium bicarbonate was visually dissolved before pouring these buckets in the 40 L end tank of the experimental set-up. All used concentrations were far below the solubility threshold of sodium bicarbonate in water (80.7 g L^{-1} at $20 \text{ }^\circ\text{C}$, (Thieme, 2000)).

3.2.4. Data processing

The extent of the blocks was captured over time using time-lapse imagery that was post-processed and subject to image analysis (see Figure 3.11 for a flow diagram describing the image processing steps).

GoPro imagery is renowned for its fisheye effect, which distorts images towards their edges (e.g. Martinez et al., 2017). Although distortion was limited for the experimental area, camera calibration was executed using black and white checkerboards to obtain camera parameters. This allowed the rectification of each image using MATLAB© 2016a and allowed the determination of the mean scale of the area of interest in the images ($0.6015 \text{ mm pixel}^{-1}$ for experiments 1-18 and $0.5114 \text{ mm pixel}^{-1}$ for experiments 19-27).

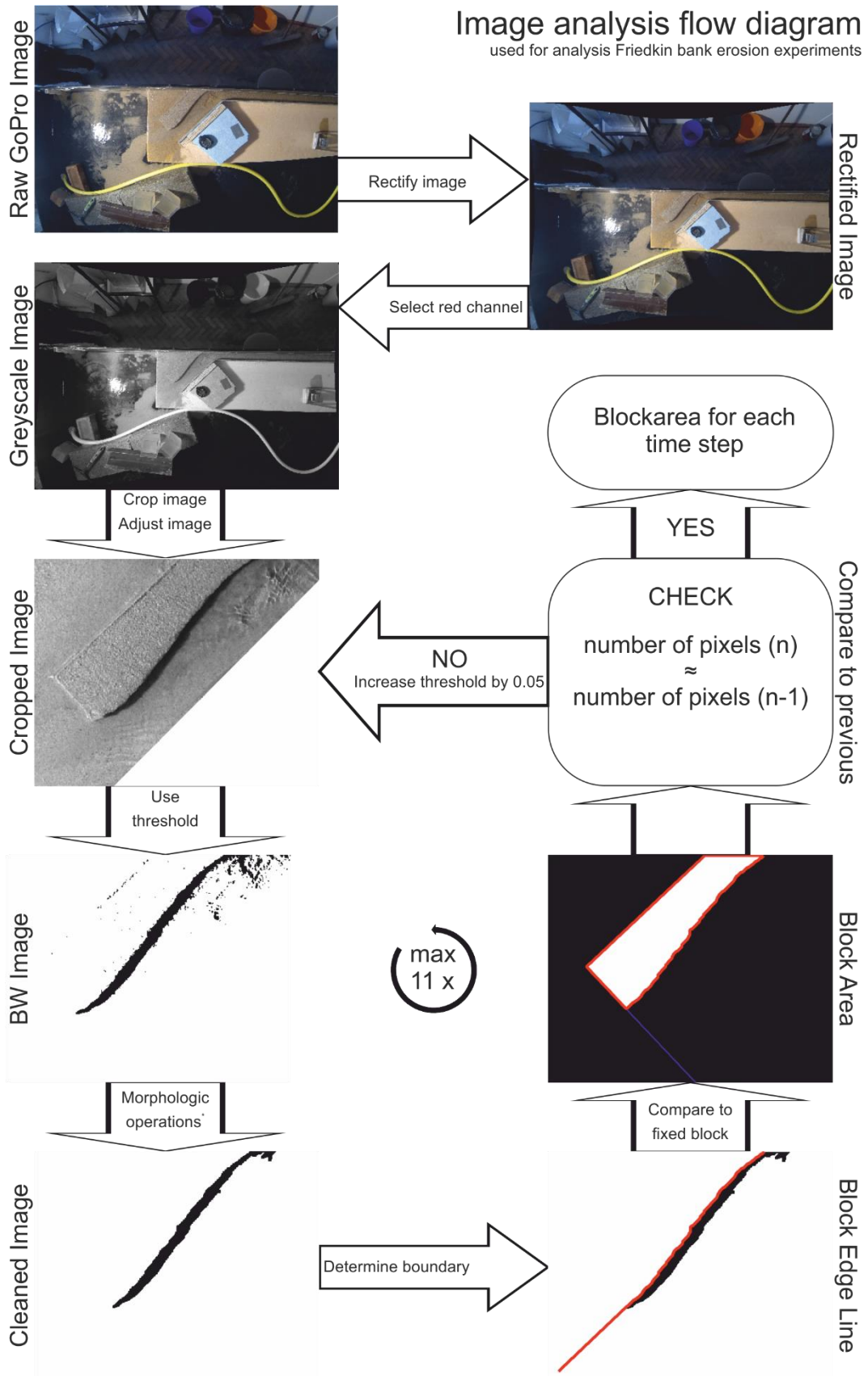
Further post processing was also done with MATLAB© 2016a. This analysis was adapted from an image analysis script for bank erosion experiments by van Dijk et al. (2013) and tracks the boundary of the block (block edge) in each overhead image. The block edge is tracked by locating the high contrast between the surface of the erosion block and the surface of the water next to the erosion block. In the present experiments, this contrast was enhanced by the addition of a lighting source oriented in the upstream direction casting a shadow from the erosion block on the water. This image processing pipeline was automated and thoroughly tested via trial and error in order to maintain consistent results that described the block edge most accurately. The fundamental steps of this process are explained below and shown in Figure 3.11.

The initial step in the image processing pipeline was to simplify the coloured rectified image into a grayscale image. For this, the red colour band was used to discriminate effectively between sediment and shaded water (red is common in brown coloured quartzite sediments and more likely to be refracted in the more shaded and darker areas of water (van der Meer & de Jong, 2006). The resulting single band grayscale image was cropped towards an area of interest and a saturation adjustment filter (`imadjust`) was used to increase the contrast in the masked image.

The next step (`im2bw`) thresholded the cropped greyscale image (range [0,1]) into a black and white (BW) image. The threshold value was initially set at 0.10 for exp. 1-18 and 0.15 for exp. 19-27 for each image but was increased by a value of 0.05 for exp. 1-18 and 0.025 for exp. 19-27 for each outcome that did not match the outcome criteria (explained below), up to a maximum of 11 times (0.65) for exp. 1-18 and up to a maximum of 8 times (0.325) for exp. 19-27.

The resulting BW image was subject to a sequence of morphological operations that created continuous areas of black pixels (see Figure 3.12 A-E). This included standard operations like `imcomplement` (which inverts the black and white in the image), `erode` (which turns the pixels at a boundary between white and black into black), `dilate` (which turns the pixels at the boundary between white and black into white) and `imfill` (which fills areas of white pixels surrounded by black pixels with black). Additionally, to overcome more irregular bank lines, `erode` and `dilate` were used in a single diagonal direction (parallel to the bank) only. This combination of operations removed shadow mid-block (due to dense vegetation or a disturbed erosion block surface) and connected disconnected shadows (due to vegetation stems or due to the erosion block edge being parallel with the light source).

From this selection of continuous areas of black pixels, the largest area by circumference was selected and the array of boundary pixels (which form the circumference) was used to determine the edge of the erosion block. By selecting the pixels on the left side (based on maximum and minimum y coordinates) of the circumference, an estimate was made on the location of the erosion block edge (see line C0, Figure 3.13).



* Morphologic operations consist of a sequence of erode, dilate, fill and complement.
 Image analysis process adapted from van Dijk (2013a)

Figure 3.11 Schematic flow diagram of the image analysis processing using MATLAB®.

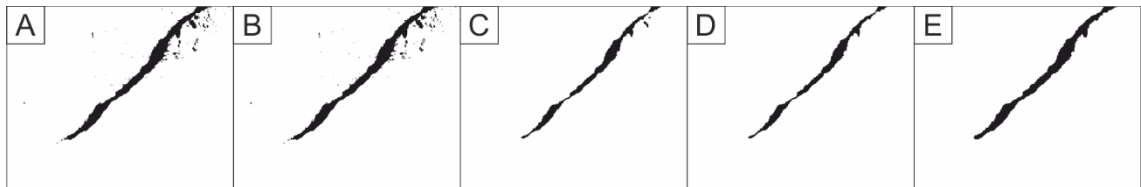


Figure 3.12: Sequence (A – E) of morphological operations used in the image analysis process. A) initial thresholded black and white image following `im2bw`. B) image following application of `imcomplement` and `bwareaopen`. C) image following application of `imdilate` and `imerode`. D) image following application of `imcomplement`, `imfill`, `imcomplement`, `imfill` and `imcomplement`. E) final image following application of `dilate`, `imfill` and `erode`.

In order to enhance the robustness of erosion rate estimates that employed the erosion block edge line, several additional simplifications and clean-up actions were required (Figure 3.13). First, a back line (C1) of the erosion block was determined about 10 mm before the actual back of the erosion block but parallel with the back edge of the block. This allowed automatic exclusion of the thinner remnants of the erosion block that either: 1) did not cast enough shadow; 2) were pushed backward by the force of the flow; or 3) were breached. Second, an end line (C2) on the downstream side of the block was determined about 20 mm before the actual downstream end of the block, perpendicular to the block and the dominant flow direction. This allowed the hydrodynamic influence of a sudden widening of the flow to be ignored and avoided issues with the smaller shadow cast at the downstream edge. When C0 did not intersect C2, C0 was arbitrarily extended up to C2. This added extension usually resembled the true behaviour of the erosion block edge better in comparison to the use of the non-extended C0. Outcomes were discarded if the extended line became longer than 82 mm (100 pixels along x-axis). Third, an upstream line (C4) parallel to the wall of the experimental box was set about 3 mm from the wall. This allowed irregularities at the wall-block boundary, reflections and shade cast from the outer wall of the stream table to be ignored.

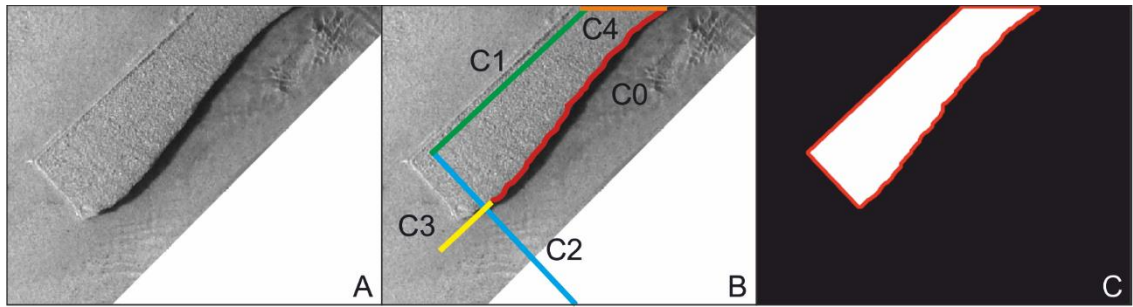


Figure 3.13: Block area selection. A) Original grayscale image, B) Schematization of lines that identify the final block area (C).

Next, the number of pixels that were enclosed by the lines (C0, C1, C2, C3 and C4) were summed to give the total area of the erosion block remaining at each time step in pixels. This value was then used in a check loop to determine whether an increase in the black and white threshold value was required. For this check, the estimated block area (in number of pixels) was compared to the block area of previous time step(s) to assess the rate of change (effectively acting as a range filter on the erosion rates).

The first two images of each run have no water nor erosion and thus indicate the full extent of the erosion block. As such, for these images, the estimated block area was compared to a predetermined block area of 54,000 pixels. This value, further referred to as reference block area, was determined by trial and error and represents approximately 70 per cent of the average initial block area of experiment 1. Any estimated block area greater than this reference block area was accepted, but any estimated block area smaller than the reference block area indicated an inaccurate estimate. Therefore, the black and white threshold value was increased (Figure 3.11), the morphological operations repeated (Figure 3.12), the block outline recomputed (Figure 3.13) and the estimated block area recomputed until the estimated block area was greater than the reference block area.

From the third image of each run onwards, the estimated block area, A_n , was compared with the block area of the previous image, A_{n-1} . As such estimated block areas that satisfied the condition

$A_{n-1} + 2000 > A_n > A_{n-1} - 4000$ (pixel counts that were 3.5 and 7 per cent of reference block area, respectively) were retained. If A_n was outside the range, the image was rejected, the black and white threshold was increased (see above) and the previous steps repeated (Figure 3.11 -Figure 3.13). If the estimated block area for all threshold values was rejected and the maximum threshold value was reached, the block area was not assigned a value.

If a previous image had no value stored, the estimated block area, A_n , was compared to the last accepted block area, A_{n-k} . In this case, to consider ongoing erosion of the block over time (and thus over missing images), the lower limit was adjusted by 1000 pixels for every invalid image, $A_{n-k} + 2000 > A_n > A_{n-k} - (4000 + 1000k)$.

The eroded area of the block in pixels was transformed to object space by multiplying by the pixel area ($0.36 \text{ mm}^2 \text{ pxl}^{-1}$). To facilitate comparison and avoid uncertainties associated with differences in the initial projected block location, block areas were normalized by the area of the initial block of that run. This remaining normalized block area described the behaviour of each of the experimental runs over time. For each run, the last image before the block fractured or the last image before a continuous shadow line was broken was determined manually to exclude further images from analysis. An average over all 10 runs of each experiment was computed for each time step up to the elapsed time of the earliest final image of that experiment to get the evolution of the remaining normalized block area for that experiment (e.g. lines in Figure 3.14 for exp. 1-3). All rejected images were excluded (not replaced) in the computation of the average.

3.3. Results

In the following sections, results are described structurally in a thematic approach. First, the erosion behaviour is described for all experiments in the three different sections (exp. 1-18: bare erosion blocks, erosion blocks with surrogate vegetation and erosion blocks with chemical agents). This representation consists of data points that represent the outcome of individual runs as well as lines that represent the average of an experiment. Second, the variation of erosion block volume over time and experiment is described using an identical visualization.

3.3.1. Normalized eroded area of bare blocks

The bare sediment experiments give an overview of the impact of the different grainsizes on the erosion times of the blocks. Figure 3.14 shows that the blocks composed of the coarser sediment (458 μm) eroded at an almost constant rate and took on average just over 600 seconds to erode. A slight variation exists between the individual runs, but all completed within a few minutes of each other. Initially, there was rapid erosion of 10-15 percent of the surface area of the block over the first time step (30 seconds) but after this initial erosion, rates slowed and stabilized. This initial drop is a result of an interaction of three components. First, how the data is computed (based on the planform area of a block). Second, the initial shape of the block (a 20 mm vertical bank between the two horizontal surfaces of the channel floor and the top surface of the block). Third, the physical erosion processes. The flow deforms the block edge to a different, experiment-specific, quasi-equilibrium bank profile shape. The resulting bank profiles are generally steeper for more cohesive materials than less cohesive materials but vary amongst the different agents.

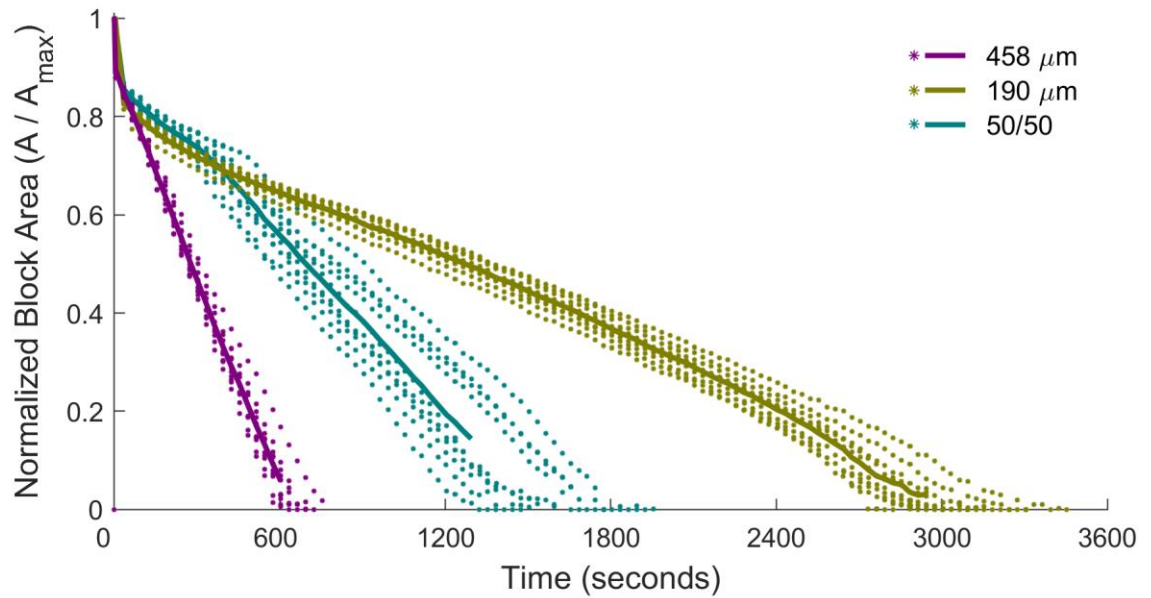


Figure 3.14: Normalized block area (block area at each time step divided by the maximum area of each sample) against time for bare block experiments with coarse sand, fine sand and a bimodal mixture composed of 50:50 fine and coarse sand. Dots indicate measurements for each individual run at each time step. Lines represent average for each experiment.

For blocks composed of finer sediment (190 μm), a similar trend, with initial rapid erosion, is observed (Figure 3.14). However, further erosion of the block is much slower than for the coarser sediment blocks. This finer grained experiment has erosion times around 3000 seconds, about 5 times slower than the coarse sediment experiment. In contrast to the coarse sediment experiment and all other experiments in this thesis, blocks in the fine sediment experiment show increasing erosion rates towards the end of the runs. This behaviour is unexpected since applied hydraulic shear stresses should reduce as channel widening occurs and thus sediment transport capacity should also reduce. Therefore, it is speculated that this increase in erosion rates is caused by geotechnical processes such as a loss of apparent cohesion (i.e., loss of matric suction over time (Simon et al., 2000), although this research has not measured this.

Experimental runs with mixed sediment (50 % 190 μm and 50 % 458 μm sand) show erosion rates in between the erosion rates of the finer and coarser experiments. Following initially rapid erosion, erosion rates are similar to those observed in the fine sediment experiment for the first

300-600 seconds, before erosion rates increase to relatively stable values in between the coarser and the finer experiments. Although the instant in time that erosion rates accelerate varies between runs, it occurs in all samples and is similar to the late-stage convex behaviour shown in all runs in fine blocks. This may suggest that it originates from the finer 190 μm sediment and relates to a loss of matric suction, which occurs earlier for the 50:50 mix because void spaces between the larger particles are larger. Further, compared to the unimodal grainsize samples, the variation between the individual runs is larger towards the end, where an almost bimodal split in the erosion curves occurs from 900 seconds onward. This bimodal split could be explained and linked to the bimodal nature of the sediment in this mixture. These behaviours result in block erosion times of between 1380-1980 seconds, roughly double that of the coarse blocks and roughly half that of the fine blocks.

3.3.2. Normalized area of erosion blocks with surrogate vegetation

Overall, blocks with surrogate vegetation behaved similarly to the bare erosion blocks. However, the presence of surrogate vegetation was found to influence the image analysis process. Stems and leaves of vegetation cast shadows on top of blocks, thereby resulting in underestimates of the block area. This effect was most noticeable in runs with a higher biomass (e.g. long growing duration and/or high seeding density) but was present to an extent in runs in all experiments with surrogate vegetation.

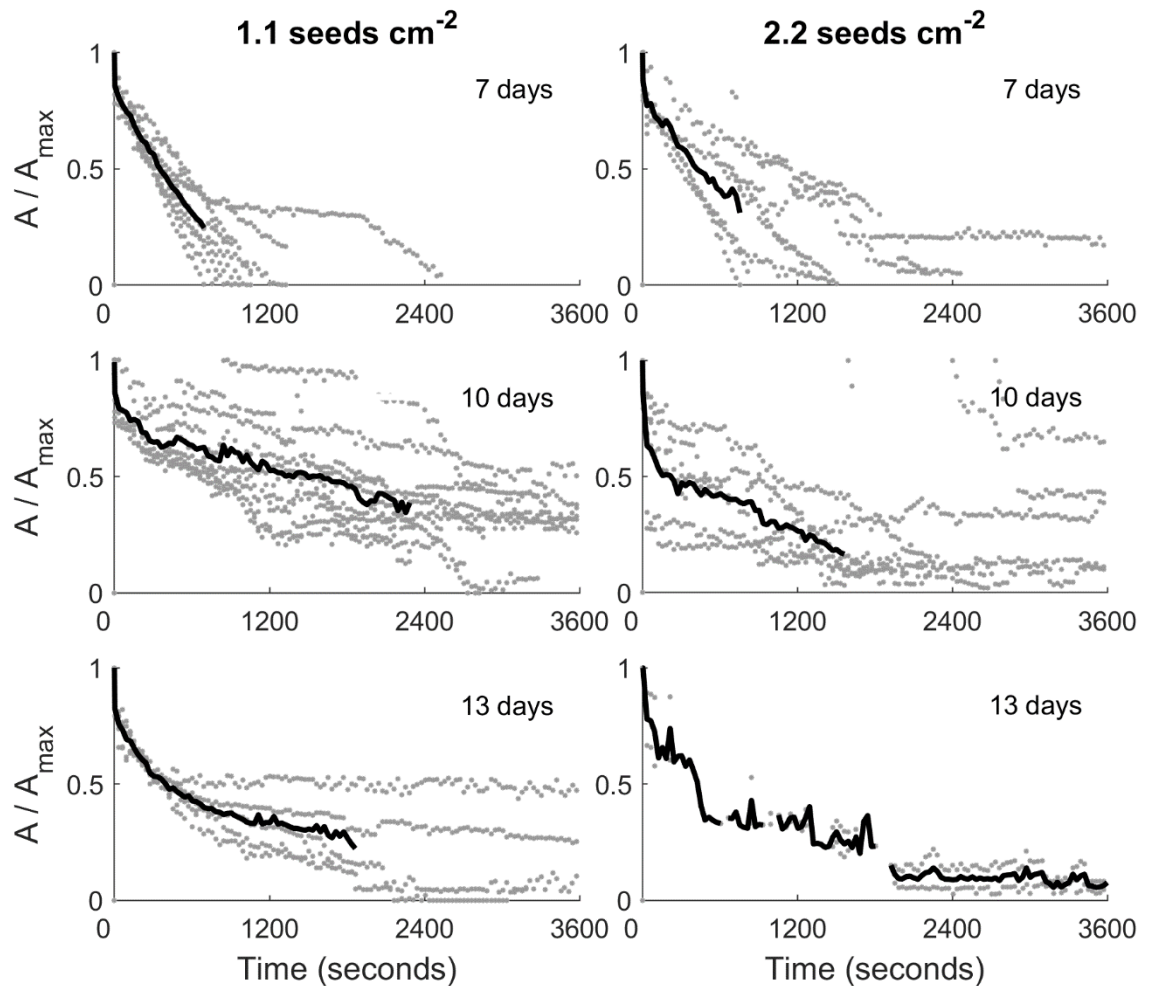


Figure 3.15: Overview of normalized block area over time for all experiments with vegetation. Seed density increases towards the right subplots, age of vegetation increases further down in the subplots.

The experiment with the youngest surrogate vegetation (7 days) and low seeding density (1.1 seeds cm^{-2}) (Figure 3.15, top left) showed a similar pattern to the bare block experiments with coarse sediment. Block area initially dropped rapidly before erosion rates reduce to a slower, but relatively constant rate for the latter part of each run. Most runs of this experiment completed between 900 and 1200 seconds after commencement with a few runs taking longer and completing at around 2400 seconds, but erosion rate reduction mainly occurred in the latter stage of the runs (after 900 seconds). The variability between runs was larger than the variability in the different bare block experiments.

Blocks with more mature low-density surrogate vegetation (10 days old) behaved differently. Again, there was a rapid reduction of block area over the initial time step followed by a slow

constant decline in block area, which resulted in the first blocks in this experiment eroding within 3000 seconds while others took longer and had erosion times exceeding 3600 seconds (Figure 3.15, central left). Erosion times were more than double those of the low-density experiment with the younger surrogate vegetation. Furthermore, the variability between runs was even larger, with block areas of individual experiments varying by up to 50% at a similar time step.

Blocks with the most mature low-density surrogate vegetation (13 days old) exhibited similar erosion rates as those with 10-day-old surrogate vegetation (Figure 3.15, bottom left). However, a clear difference existed between the two experiments. In the experiment with 13-day-old vegetation, after the initial reduction of block area, erosion rates were relatively fast but decreased gradually over time and in some cases became asymptotically zero, indicating a lack of erosion. The variability between individual runs was again large, particularly towards the end of the runs, but was less than that for the blocks with 10-day-old surrogate vegetation.

Blocks seeded with higher density (2.2 seeds cm^{-2}) surrogate vegetation (Figure 3.15, right column) showed similar trends as their lower density counterparts but results are less clear due to biomass impacting the image analysis process. Higher density (2.2 seeds cm^{-2}) blocks with the youngest surrogate vegetation (7 days old), exhibited erosion times that were on average longer than their lower density counterparts. Although some runs in this experiment completed at 900-1200 seconds, a higher number of runs exceeded 1200 seconds and some even exceeded 2400 seconds, suggesting greater variability amongst runs.

For the older surrogate vegetation experiments, variability was very large, masking any real trends. In particular, estimated block areas for a few runs with 10-day-old surrogate vegetation drop down under 50 percent at the first time step, which does not match visual observations. It is suspected that these issues are a result of the shade cast on top of the block by the vegetation which interferes with the shadow cast by the block edge used in the image analysis (section 3.2.4) and should be treated with caution. The only clear conclusion that can be drawn is that

erosion times for 10- and 13-day-old high-density surrogate vegetation blocks are longer than those for 7-day-old high-density surrogate vegetation (Figure 3.15).

3.3.2.1. Root structure

37 uprooted plants were captured from runs from the experiments and had their key geometric characteristics analysed (Figure 3.16). Average values for each growing duration (7, 10 or 13 days) are listed in Table 3.3. These outcomes indicate an increase in tap root length, total root length, Specific Root Length (SRL) and number of nodes over time. This is matched by observations, as the older surrogate vegetation showed root morphology that was not observed in younger root structures. For 7-day-old vegetation, although the root length differed, the vast majority of the samples had side roots. Most vegetation had developed side roots after 10 days, which were often limited in length up to 10 mm. Most vegetation had developed fully-grown side roots more than 10 mm long after 13 days. Across the board, variation existed, as growing speeds are naturally subject to variability.

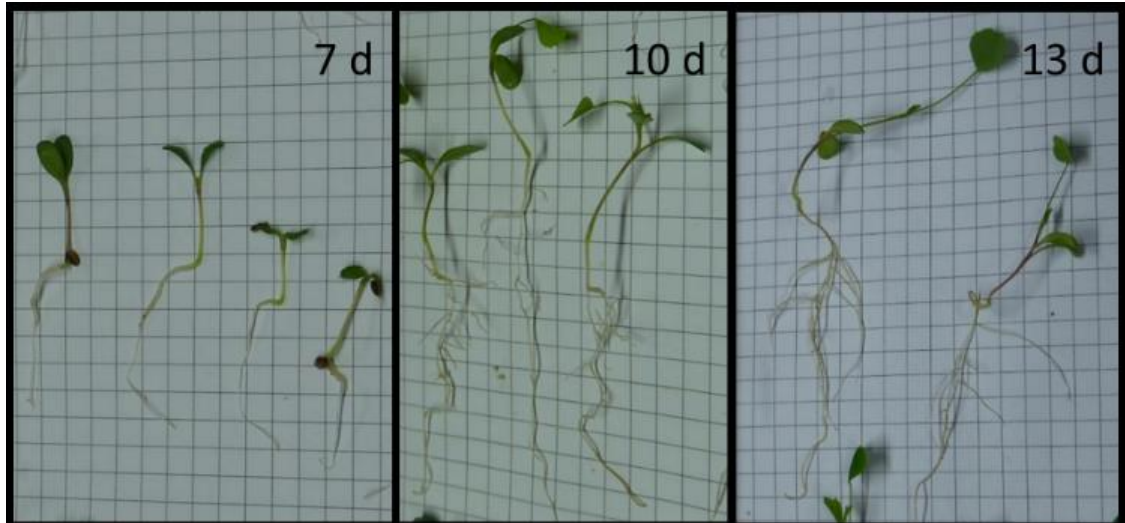


Figure 3.16: Selection of captured uprooted surrogate vegetation from the experimental runs, subdivided between samples that have grown for 7, 10 or 13 days.

Table 3.3: Vegetation root characteristics measured from photographs taken from uprooted surrogate vegetation (see examples in Figure 3.16).

	7 day	10 day	13 day
Tap root length (mean \pm standard deviation (mm))	54.0 \pm 17	68.0 \pm 23	76.0 \pm 27
Total root length (mean \pm standard deviation (mm))	54.0 \pm 17	93.0 \pm 28	151.0 \pm 73
Specific root length (SRL) (mean \pm standard deviation (-))	0.99 \pm 0.02	0.75 \pm 0.17	0.57 \pm 0.22
Number of nodes	1	6	8

The differences in erosion rate and erosion pattern for different vegetation experiments indicate a difference caused by the different experimental variables. Whereas seed density is transferable into a quantitative factor, vegetation age is more abstract. In this experimental set-up, vegetation was growing from the top of the block, thereby creating a root system inside the block and a stem-leaf structure above the block. The water level during the experimental runs was always below the block, and therefore water flows past the erosion block and interacts with the root system only (and not with the stem system). However, when surrogate vegetation fell into the flow, it could protect the block and divert flow around itself. This effect lasted until the surrogate vegetation was completely uprooted and it was transported and deposited downstream by the flow.

3.3.3. Normalized area of blocks with chemical agents

For blocks with chemical agents, a clear trend is seen related to the concentration of the agents. Erosion of blocks with chemical agents is always slower than erosion rates of bare blocks and the higher the concentration of the chemical agent, the longer it takes to erode the blocks. However, slight variations exist between the different chemical agents.

Blocks with xanthan gum (Figure 3.17, left column), show a similar behaviour to the bare blocks. All blocks exhibit an initial drop in area, but the magnitude of this drop decreases from 12-15 percent in the lowest concentration experiment to less than 5 percent in the highest concentration experiment. Furthermore, there is a clear negative relation between concentration of xanthan and time of erosion. Blocks with the lowest concentration of xanthan gum, 0.125 g kg^{-1} , behave in a similar manner as bare blocks composed of coarse sediment. Blocks with a concentration of 0.125 g kg^{-1} xanthan gum erode in about 900 to 1200 seconds, only 300 seconds longer than bare blocks composed of coarse sediment. With higher concentrations of xanthan gum, erosion times increase to up to 1800 to 2400 seconds for the 0.250 g kg^{-1} experiment, 2700 to 3600 seconds for the 0.500 g kg^{-1} experiment and, in many cases, greater than 7200 seconds for the 1.000 g kg^{-1} experiment. However, in contrast to the lowest concentration and the bare sediment examples, there is greater inter-run variability.

Blocks with carrageenan (Figure 3.17, right column) behaved differently than those with xanthan gum. Blocks with lower concentrations of carrageenan (0.125 g kg^{-1} , 0.250 g kg^{-1} and 0.500 g kg^{-1}) all behave similarly to each other, with block erosion times of 600 to 900 seconds. This is shorter than the lowest concentration of xanthan gum (900 to 1200 seconds) and the same rate as bare blocks composed of coarse sediment. The shape of the mean curve for each of the three experiments is similar to the bare experiments, with a steep initial drop in block area followed by a gentler, constant-rate, decrease in block area. A small exception exists for the 0.250 g kg^{-1} concentration experiment, in which a few runs had elapsed times just over 900 seconds and thus more variability than both the higher (0.500 g kg^{-1}) and lower (0.125 g kg^{-1}) concentration experiments. This pattern does not extend into experiments with the higher concentrations of carrageenan (0.750 g kg^{-1} and 1.000 g kg^{-1}). The second highest concentration (0.750 g kg^{-1}) experiment consisted of runs where block erosion times spanned between 900 seconds for the quickest run up to over 3600 seconds for the slowest run. This experiment shows inter-run variability that exceeded that for all other carrageenan, xanthan gum and bare erosion block experiments. Erosion time increased from an average of 780 seconds in the three experiments

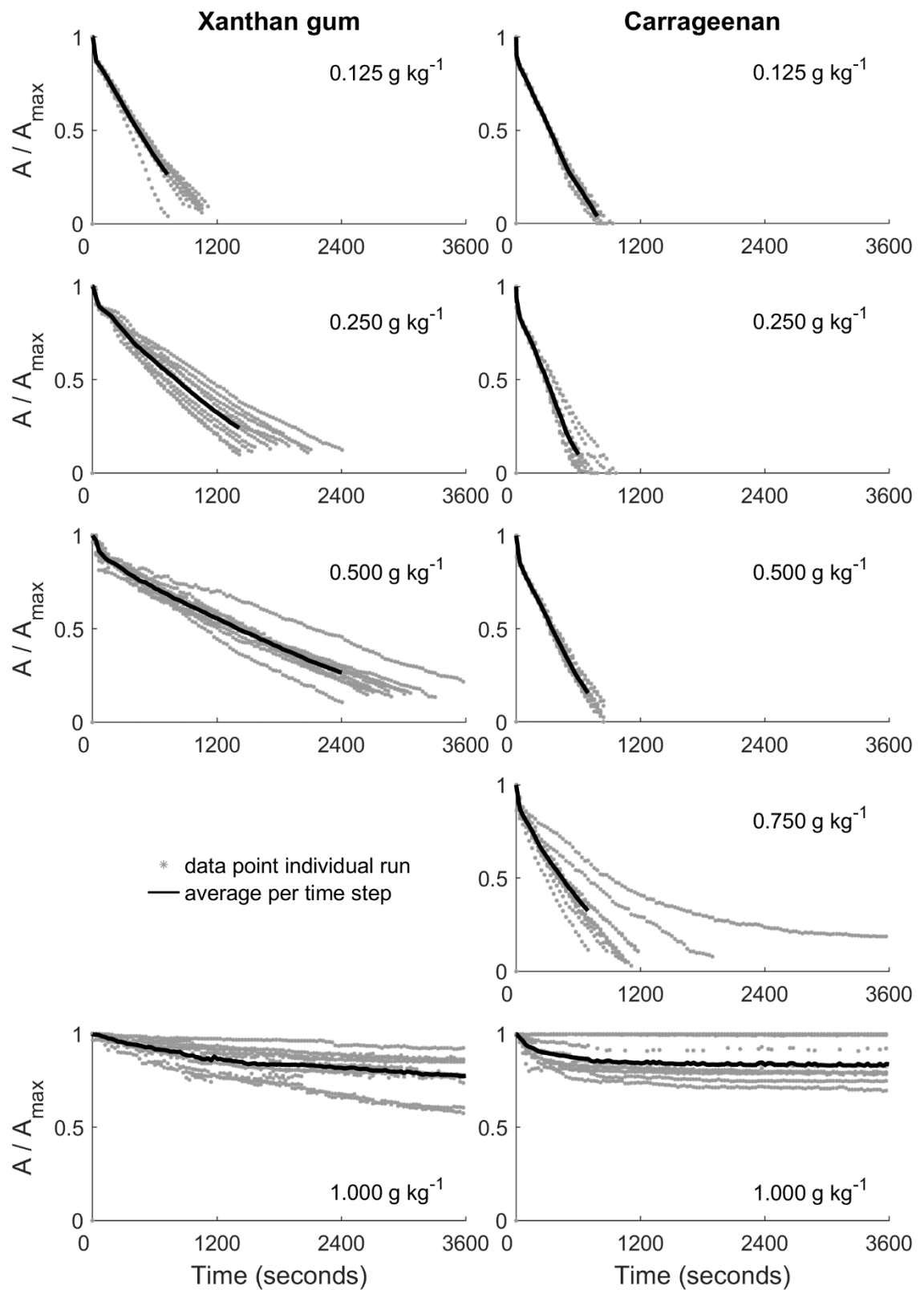


Figure 3.17: Overview of normalized sediment block area against time for all experiments with chemical agents. Xanthan gum in the left column, carrageenan in the right column. Concentration of chemical agent increases downward. Carrageenan samples show five sequential increments of concentration, the column of xanthan gum only four. Rows show the same concentration for different chemical agents.

with the lowest concentration of carrageenan to almost 1200 seconds for the 0.750 g kg^{-1} experiment and to even longer times in the experiment with the highest concentration of carrageenan (1.000 g kg^{-1}). This experiment includes both runs in which blocks did not erode at all and blocks that ceased eroding after an elapsed time of 1800 seconds. This behaviour is similar to that of the highest concentration of Xanthan gum (1.000 g kg^{-1}), but the carrageenan experiment has a steeper initial drop and erosion rate becomes more asymptotic in the latter stages of the runs.

3.3.4. Variation and erosion rate for bare blocks

Quantification of erosion rates per time step, averaged over all runs of an experiment, allows for comparison of erosion rates independent of the size of the erosion block.

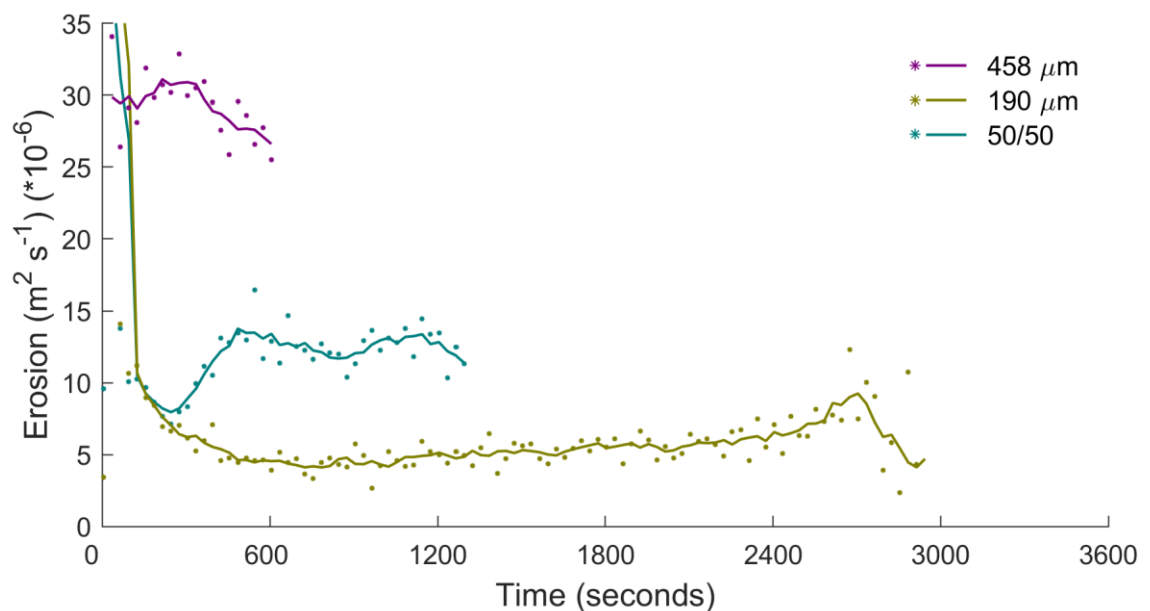


Figure 3.18: Average erosion rates ($\text{cm}^2 \text{ min}^{-1}$) against time for bare sediment block experiments with coarse sand, fine sand and a 50:50 mixture. Individual dots indicate averages over all runs per experiments for each time step; lines indicate 2.5-minute moving average. Rapid erosion in the initial time step exceeds the range of this plot.

Figure 3.18 shows that erosion rates were fastest for the bare experiment with a coarser grainsize compared to the finer grainsize experiments, similar to Figure 3.14. Nevertheless, differences exist between the experiments. The coarser experiment had a high erosion rate ($15\text{-}20 \text{ cm}^2 \text{ min}^{-1}$) that, after an initial high (first minute), dropped down to $26 \times 10^{-6} \text{ m}^2 \text{ s}^{-1}$ before it

increased over time for the first 5 minutes to $33 \cdot 10^{-6} \text{ m}^2 \text{ s}^{-1}$. Hereafter it decreased over time for the next 5 minutes (from $33 \cdot 10^{-6} \text{ m}^2 \text{ s}^{-1}$ to $25 \cdot 10^{-6} \text{ m}^2 \text{ s}^{-1}$). This effect is different to the erosion rate for the other two experiments in which erosion rates reduced from $14 \cdot 10^{-6} \text{ m}^2 \text{ s}^{-1}$ to $7 \cdot 10^{-6} \text{ m}^2 \text{ s}^{-1}$ in the first 5 minutes. Erosion rates for the finest sediment blocks dropped further before they stabilized at a rate of $4 \cdot 10^{-6} \text{ m}^2 \text{ s}^{-1}$ after 8 minutes. From 15 minutes onwards, this rate gradually increased to $7 \cdot 10^{-6} \text{ m}^2 \text{ s}^{-1}$ after 45 minutes. For bimodal sediment blocks, erosion rates increased to $13 \cdot 10^{-6} \text{ m}^2 \text{ s}^{-1}$ after 8 minutes, after which they stabilized until the end of the runs.

Figure 3.18 indicates that differences between individual runs is not always the same for each experiment. Using the 10 runs of each experiment, inter-run variation has been quantified for each experiment. This variation is estimated as a modified standard error that was calculated by dividing the standard deviation (σ) by the difference between the maximum area of the block (A_{max}) and the mean area of the block (A_{mean}) and allows normalization over each time step. In Figure 3.19, modified standard error (mse) is plotted against mean normalized block area, a time independent variable. Modified standard error for the bare sediment blocks, is stable with increasing block area after the first 15 percent of the block is eroded. The blocks with a bimodal mixture have the highest modified standard error (0.1 – 0.15), while both blocks composed of unimodal sediment exhibit less difference in modified standard error (0.05). Similar to erosion rate, blocks composed of bimodal sediment show a steep increase in modified standard error between mean normalized block areas of 70 and 80 percent, but remain constant between 0.1 and 0.15 afterwards.

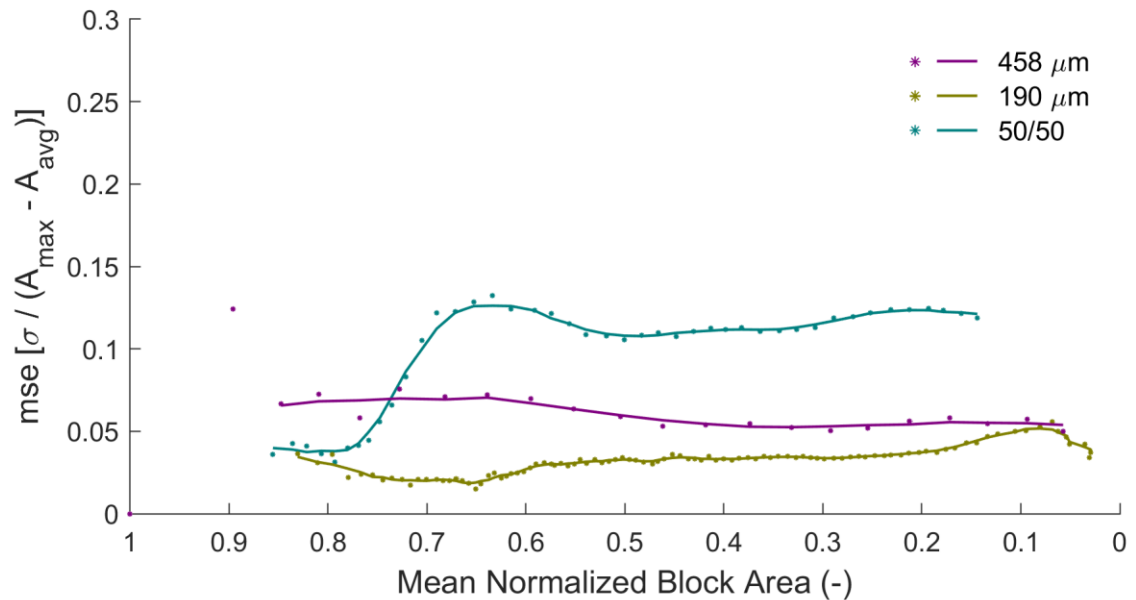


Figure 3.19: Variance against mean normalized block area for bare experiments. Mean normalized block area is determined by the average block area at each time-step divided by the maximum average block area for each experiment. Modified standard error (mse) is shown as standard deviation divided by the difference of maximum and average area. Individual points indicate modified standard error per time step, per experiment; lines indicate a 5-sample (150 second) moving average of modified standard error.

3.3.5. Variation and erosion rate for blocks with surrogate vegetation

Erosion rates for the blocks with surrogate vegetation are consistently lower than the erosion rates of blocks composed of bare coarse sediment (Figure 3.20). This reduction in erosion rates is limited for blocks with young (7 day old) vegetation with erosion rates just around $20 \text{ m}^2 \text{ s}^{-1}$ but is particularly reduced for blocks with more mature vegetation, with erosion rates below $5 \text{ m}^2 \text{ s}^{-1}$ with rates being tenfold smaller. In the blocks with high density surrogate vegetation, the effect is larger for the younger (7 day old) vegetation with erosion rates just around $15 \cdot 10^{-6} \text{ m}^2 \text{ s}^{-1}$, but the effect is less clear for older vegetation, with erosion rates between 0 and $10 \cdot 10^{-6} \text{ m}^2 \text{ s}^{-1}$. Part of this difference can relate to the larger variability of erosion rate; compared to blocks composed of bare sediment the extent of the point clouds (difference between lowest and highest erosion rates) is larger for blocks with vegetation, and largest for blocks with high density mature vegetation.

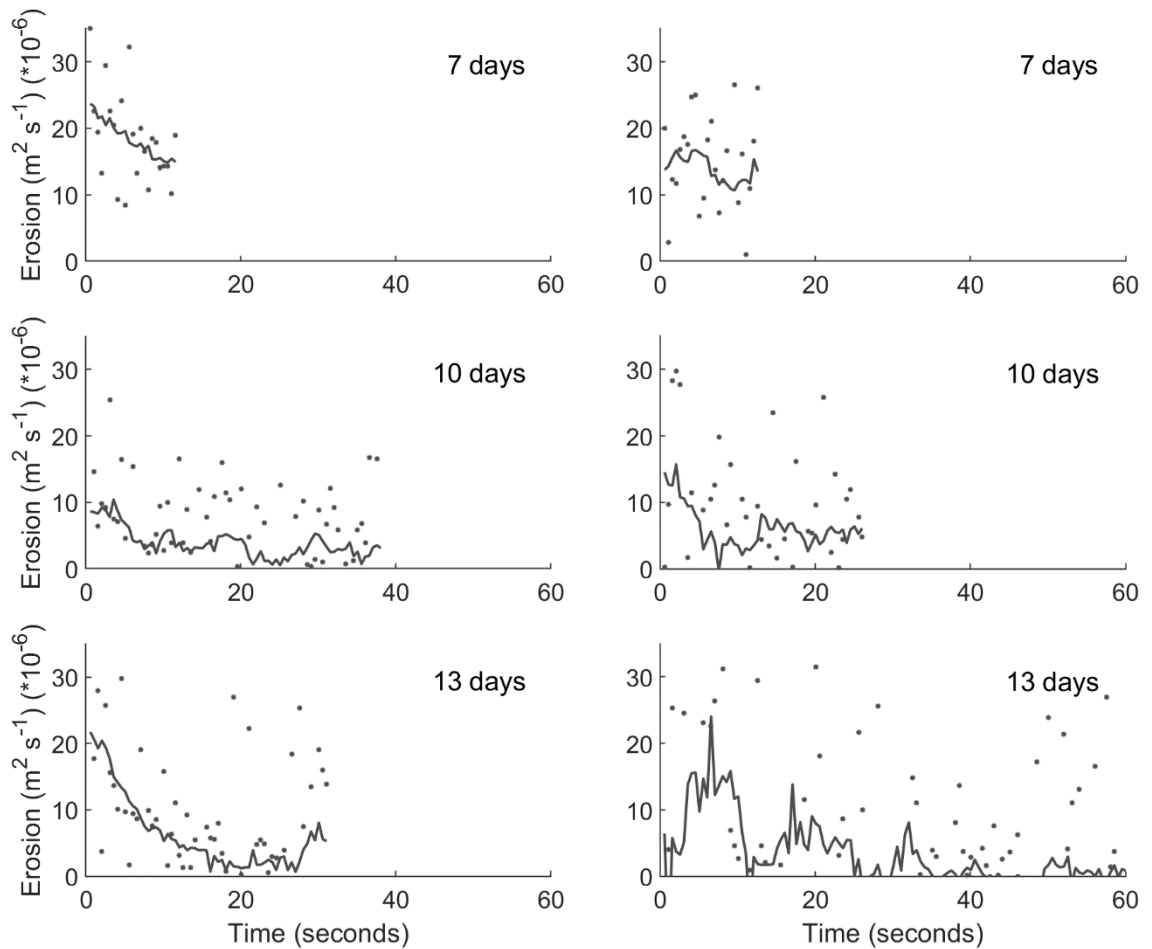


Figure 3.20: Overview of erosion rates for all sediment blocks with surrogate vegetation; seed density increases towards the right, growth duration increases further down the subplots. Points indicate average erosion rate per time step, lines indicate moving average over 5.5 minutes.

A similar effect is seen in the modified standard error of individual blocks within each experiment. Compared to bare sediment blocks, with a modified standard error of 0.05, blocks with surrogate vegetation show higher modified standard errors, up to 0.3 for blocks with low density surrogate vegetation and even higher for blocks with high density surrogate vegetation (Figure 3.21). However, compared to the bare sediment experiments, the modified standard error is diverse and best described as a point cloud. Figure 3.21 shows that point clouds of modified standard error of erosion rate of blocks of low vegetation converge to about 0.2 when two thirds of the block is eroded. In the blocks with high density vegetation, this convergence of

modified standard errors is less clear, as traces only exist for the blocks with the youngest surrogate vegetation.

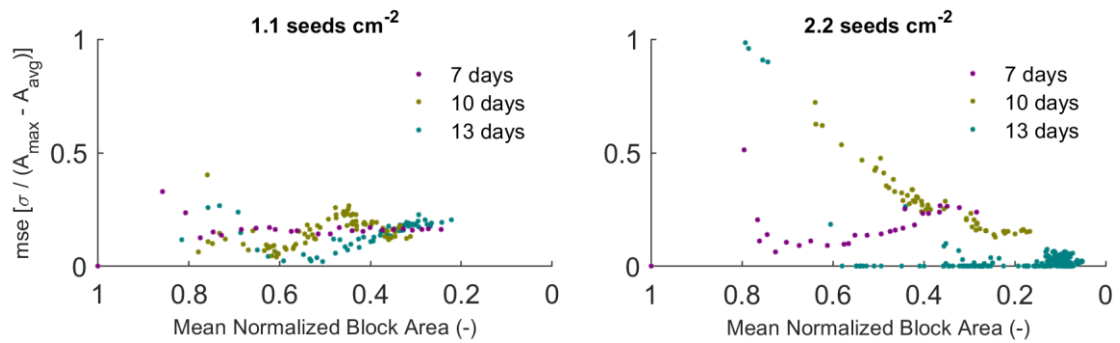


Figure 3.21: Modified standard error in erosion rates for erosion blocks with low density surrogate vegetation (left) and for erosion blocks with high density vegetation (right).

3.3.6. Variation and erosion rate for blocks with chemical surrogates

The experiments with chemical agents indicate the effect that chemical agents have on erosion rates. Overall, the experiments show reductions in erosion rates for experiments with a higher concentration of chemical surrogates, however both surrogates behave dissimilarly from each other and non-linearly to the concentration of the chemical surrogate (Figure 3.22).

A closer look at the erosion rates of experiments with added xanthan gum shows that erosion rates gradually decrease with an increased concentration of xanthan gum; after an initial peak in erosion rates at the start of the experiment, erosion rates plateau towards a slightly decreasing trend afterward. These plateaus occur at different rates (roughly at $20 \cdot 10^{-6}$, $10 \cdot 10^{-6}$, $7 \cdot 10^{-6}$ and $2 \cdot 10^{-6} \text{ m}^2 \text{ s}^{-1}$) that, together with the bare sediment erosion rate (roughly $30 \text{ m}^2 \text{ s}^{-1}$, Figure 3.18), form an ever decreasing sequence.

The experiments with carrageenan show a different behaviour, the erosion blocks with lower concentrations of carrageenan all have erosion rates of the same order of magnitude as the bare blocks ($25 \cdot 10^{-6}$ - $35 \cdot 10^{-6} \text{ m}^2 \text{ s}^{-1}$). Of these, the blocks with 0.250 g kg^{-1} carrageenan exhibit erosion

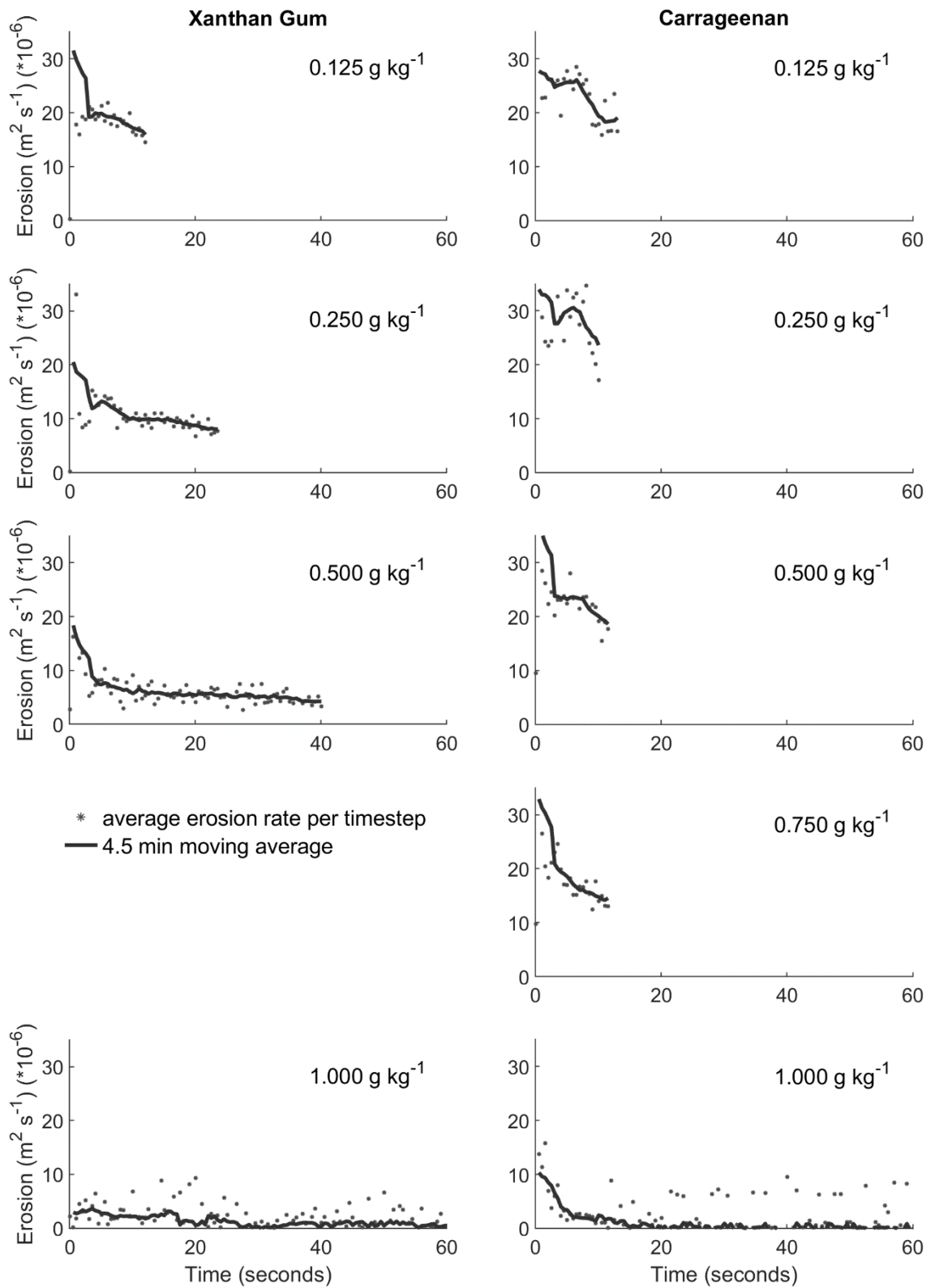


Figure 3.22: Overview of average erosion rates against time for all experiments with chemical surrogates. Left column shows all experiments with xanthan gum, right column shows all experiments with carrageenan. Concentration of chemical agents increases downward and matches horizontally. Lines indicate a 9-sample (270 second) moving average for each experiment.

rates that are slightly higher ($30 \cdot 10^{-6} \text{ m}^2 \text{ s}^{-1}$) than those of the bare blocks. These findings stand in sharp contrast to results from the erosion rates of blocks with high concentration of carrageenan. Here, erosion rates are lower, about $16 \cdot 10^{-6} \text{ m}^2 \text{ s}^{-1}$ at 0.750 g kg^{-1} and less than $1 \cdot 10^{-6} \text{ m}^2 \text{ s}^{-1}$ at 1.000 g kg^{-1} , the latter even lower than all blocks with xanthan gum.

Modified standard error of erosion rates for blocks with vegetation is a lot higher than for bare blocks. Blocks with chemical surrogates show a mixed behaviour (Figure 3.23). For blocks with the lowest concentration of xanthan, variance is of a similar magnitude as the variance in erosion rates for bare blocks. The modified standard errors of erosion rates in the next two concentrations are initially high but converge over time to the modified standard errors of the blocks with the lowest concentration. After the first 20% of the block is eroded, both these concentrations behave near identical, however in the first 20% the modified standard errors of the higher concentration (0.500 g kg^{-1}) is up to four times higher. The highest concentration of xanthan gum (1.000 g kg^{-1}) behaves differently, with a less stable trend and has a modified standard error between 0.5 and 0.6, much higher than other experiments with xanthan gum.

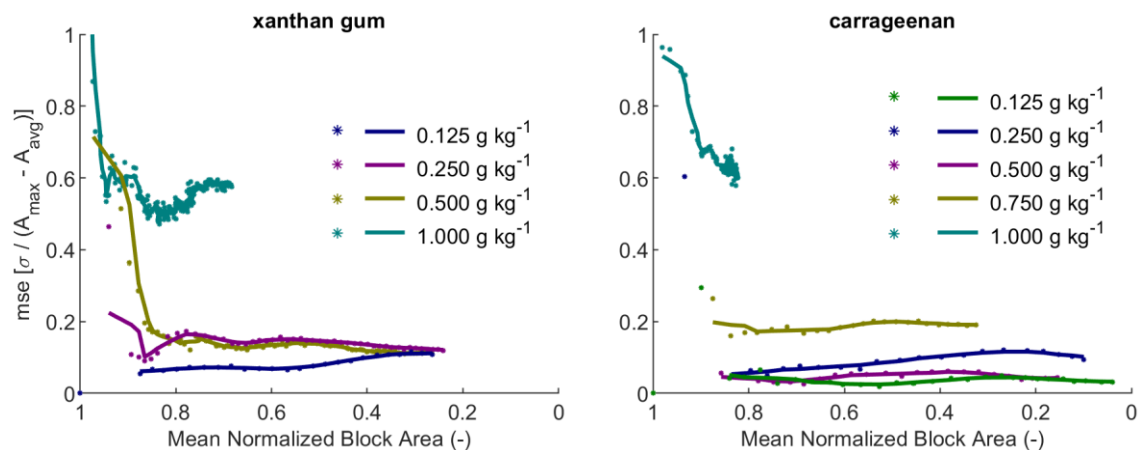


Figure 3.23: Modified standard error in erosion rates against mean normalized block area for blocks with chemical surrogates; 4 concentrations of xanthan gum on the left, 5 concentrations of carrageenan on the right. Dots indicate modified standard error per time-step, lines indicate 9-sample (270 second) moving average.

Carrageenan shows a similar behaviour, here the three lowest concentrations (up to 0.500 g kg^{-1}) have a stable trend that is even slightly lower than the modified standard error of erosion

rates for bare blocks or blocks with xanthan gum. However, as the concentration of carrageenan increases further, the modified standard error of erosion rates also increases. Erosion blocks with the second highest concentration of carrageenan have a modified standard error twice as high, erosion blocks with the highest concentration of carrageenan have a modified standard error more than five times higher, a modified standard error slightly higher than was seen in the blocks with xanthan gum. This change of the modified standard error for carrageenan resembles the moment where the concentration of carrageenan starts to decrease erosion rates.

3.3.7. Normalized area of blocks with sodium alginate

The bare erosion blocks (exp. 19) (Figure 3.24), that act as a reference that can be linked with the bare experiment (exp. 1) in the initial set-up, show a similar behaviour as these earlier bare erosion blocks (Figure 3.14). After an initial drop in block area (about 20 percent) at the first time step, the reduction in block area remains fairly constant and results in fully eroded blocks in 8 to 10 minutes, slightly faster than the bare sediment blocks in section 3.3.1. This difference, its consequences and reasons are discussed in section 3.4.1.

The addition of sodium alginate to the sediment blocks increases erosion times. For the lowest added concentration of sodium alginate (250 g kg^{-1}), a similar initial drop (about 20 percent) in block area over the first time step was observed (Figure 3.24). However, thereafter block reduction is slower which result in complete erosion times predominantly between 15 and 20 minutes. On top of this trend, a larger variance is seen, some experiments take over 3 times more time to erode a full block. This is in contrast to the experiments with the highest added concentration of sodium alginate (0.500 g kg^{-1}). In these experiments (Figure 3.24) only a relatively small (< 5 percent) initial drop in block area occurs, likely related to collapses of the block in the first seconds, after which blocks remain stable in area. Amongst the runs for this experiment no erosion records over ten percent, thus suggests fully stable conditions matching visual observations.

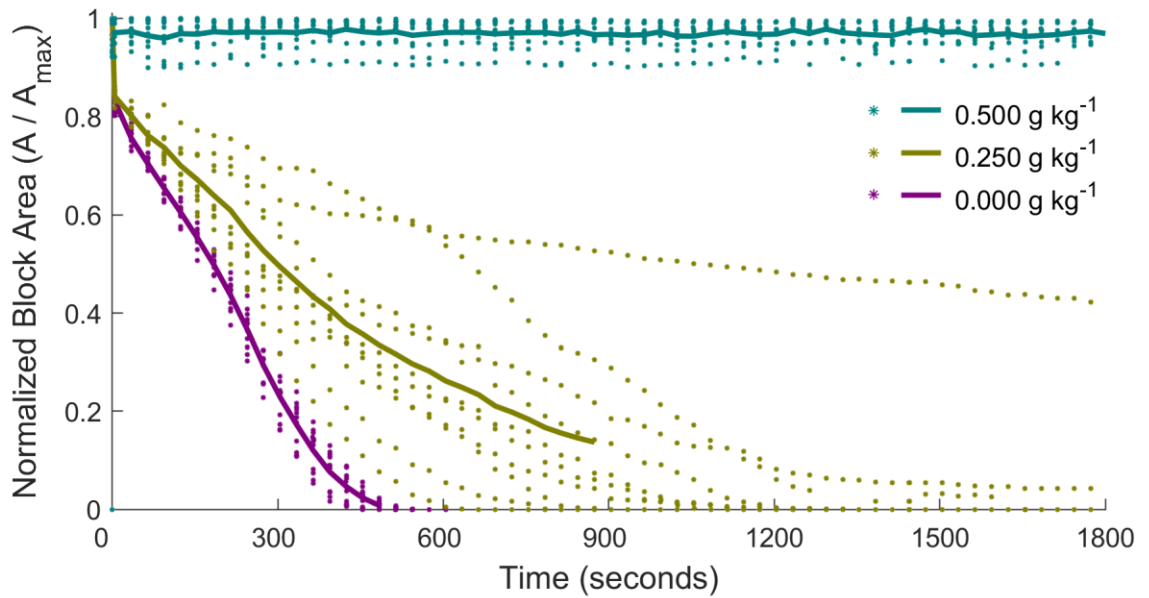


Figure 3.24: Normalized block area against time for experiments with an increasing concentration of sodium alginate under tap water flow conditions. Dots indicate individual data points. Solid lines show averages over time per experiment.

The second set of sodium alginate experiments (exp. 22-24) uses a low concentration of sodium bicarbonate in the tap water (10 g L^{-1}) instead of plain tap water. Here, the bare sediment block shows an identical drop of about 20 percent in block area over the first time step (Figure 3.25). Thereafter, block erosion slows down to a relatively constant rate over time which results in a complete erosion of blocks in 10 to 12 minutes. The experiment with a low concentration of sodium alginate (exp. 23) has a similar initial reduction in block area at the first time step, similar to both the bare experiments (exp. 19 and 22) and the experiment with a low concentration of sodium alginate in tap water (exp. 20). However, after the initial time step the block area over time follows a near-identical pattern as the bare erosion block under similar fluid conditions (exp. 22). As such at least ten minutes faster as the identical concentration of sodium alginate in tap water. For blocks with a high concentration of sodium alginate, a similar behaviour is seen. Here, in contrast to the high concentration sodium alginate blocks in tap water, the erosion blocks actually erode. It takes still more time than blocks with a lower concentration of sodium

alginate but an average reduction in area of 60 percent in the first half an hour is significantly larger than the less than 10 percent reduction observed in tap water.

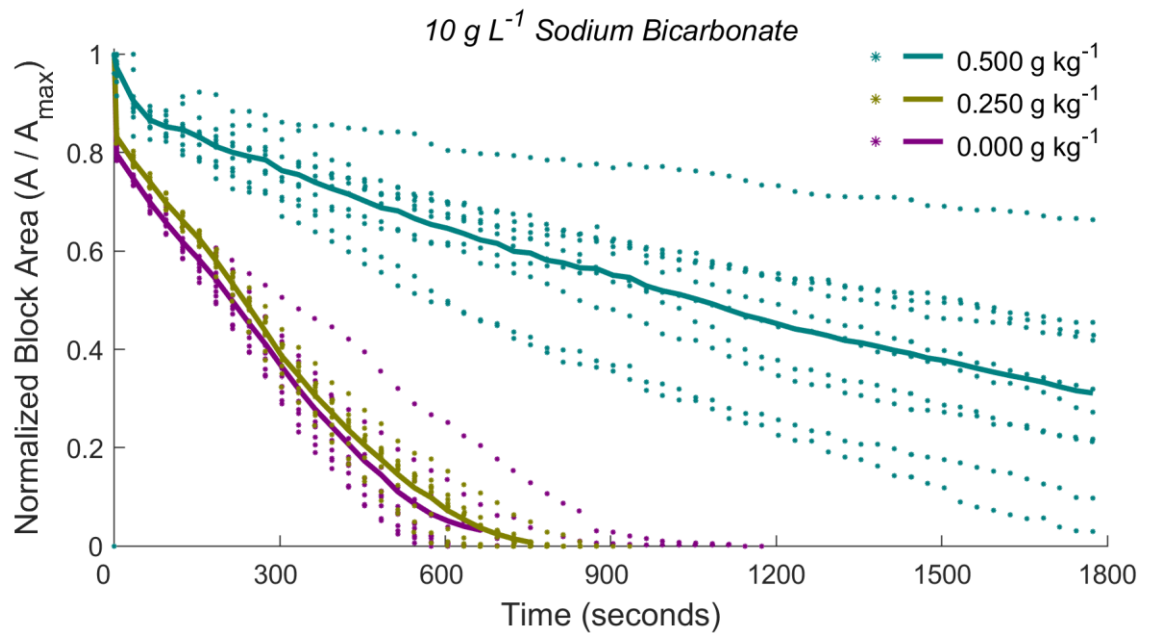


Figure 3.25: Normalized block area over time for experiments with an increasing concentration of sodium alginate under flow conditions with a low concentration of sodium bicarbonate. Dots indicate individual data points. Solid lines show averages over time per experiment.

In the experiments with the highest concentration of sodium bicarbonate (exp. 25-27, Figure 3.26), these trends develop further, but with subtle differences. First, the bare erosion blocks (exp. 25) behave very similar to the bare erosion blocks under other fluid conditions (exp. 19 and 22). However, after about 5 minutes the rate of erosion becomes suddenly faster and results in an erosion times of 7 to 8 minutes for the entire block, faster than any other experiment. The erosion blocks with a low concentration of sodium alginate (exp. 26) have an opposite behaviour; here, the reduction of block area is identical over the first 5 minutes but is reduced in the period thereafter which results in total erosion times between 13 and 15 minutes. The erosion blocks with the highest concentration of sodium alginate (exp. 27) follow a trend set by the high concentration sodium alginate experiments in settings with less dissolved sodium bicarbonate; here erosion proceeds faster, indicated by half the block area being eroded in 13 to 14 minutes compared to 18 minutes in the less concentrated fluid setting.

The internal variation per experiment (described by a mean standard error) is relatively low, and as such comparable to experiments with other chemical agents (section 3.3.6). Only three experiments have an increased mean standard error, all experiments that have mid-range erosion times (15 minutes to 45 minutes); experiments 20, 24 and 27.

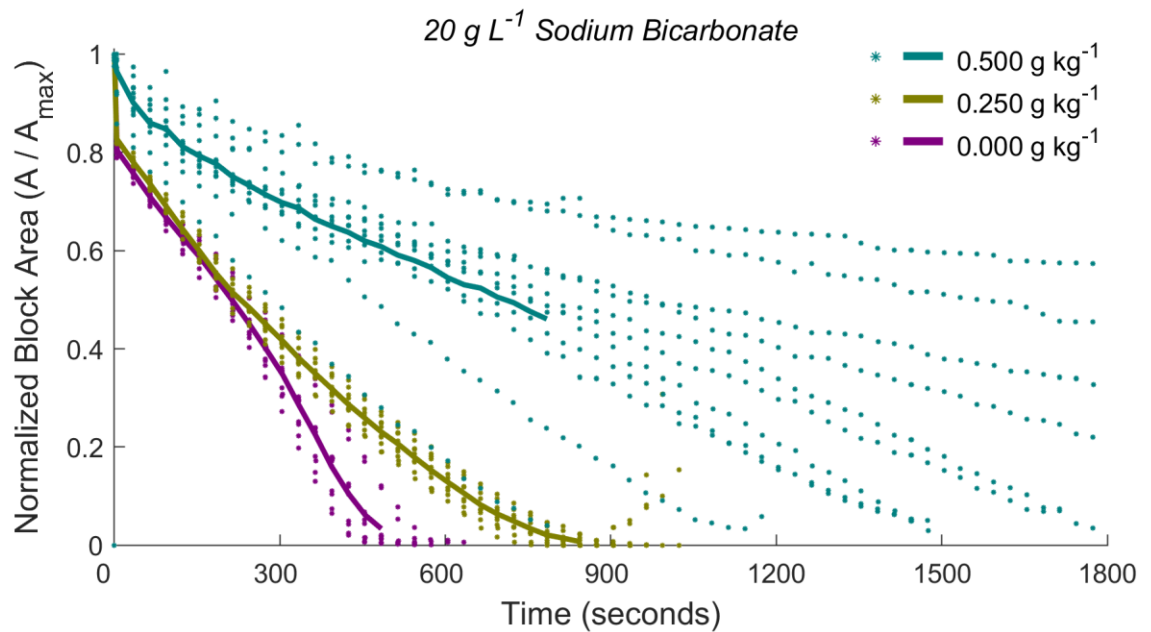


Figure 3.26: Normalized block area against time for experiments with an increasing concentration of sodium alginate under flow conditions with a high concentration of sodium bicarbonate. Dots indicate individual data points. Solid lines show averages over time per experiment.

3.3.8. Erosion rates for blocks with sodium alginate

Figure 3.27 indicates higher erosion rates for the bare erosion blocks (exp. 19), around $40 \cdot 10^{-6} \text{ m}^2 \text{ s}^{-1}$, than for the erosion blocks with a low concentration sodium alginate (exp. 20), $20 \cdot 10^{-6}$ - $25 \cdot 10^{-6} \text{ m}^2 \text{ s}^{-1}$, over the first 5 minutes. However, after the first 5 minutes erosion rates drop in both experiments; steeply to $15 \cdot 10^{-6} \text{ m}^2 \text{ s}^{-1}$ in the bare experiment (exp. 19) and more gradually to $7 \cdot 10^{-6} \text{ m}^2 \text{ s}^{-1}$ in the low concentration sodium alginate experiment (exp.20). The high concentration sodium alginate experiment (exp. 21) does not show a trend over time and has a running average around $0 \text{ m}^2 \text{ s}^{-1}$ continuously.

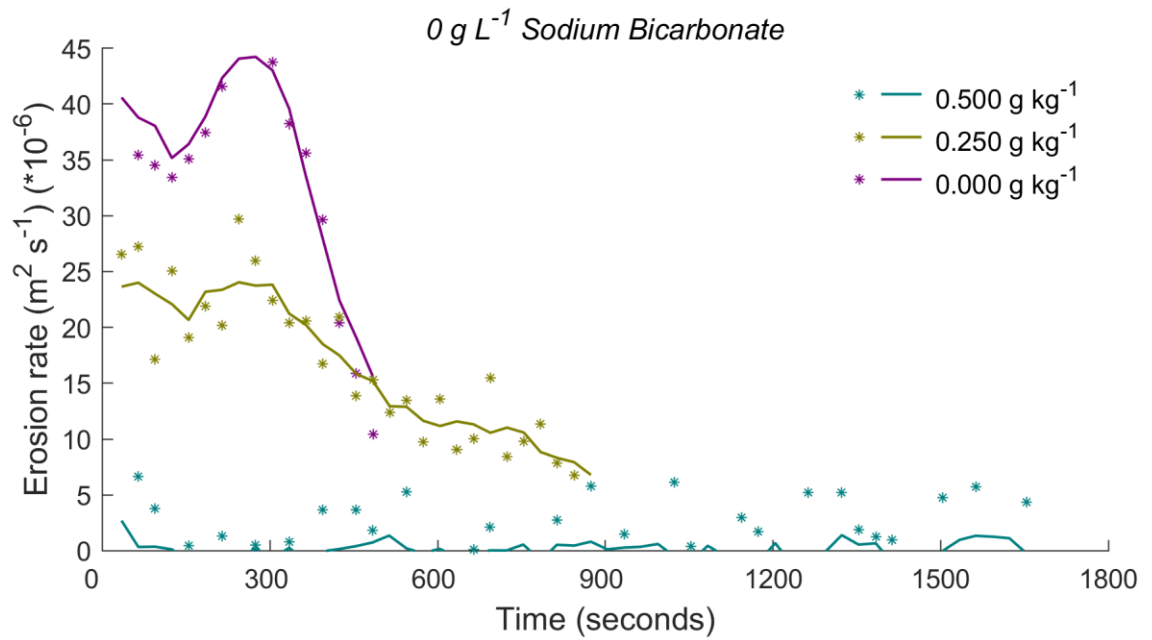


Figure 3.27: Erosion rates averaged per time step for experiments with an increasing concentration of sodium alginate under tap water flow conditions. Dots indicate average erosion rate per time step. Solid lines show a 2.5 minutes moving average.

The experiments (exp. 22-24) that used a low concentration of sodium bicarbonate in the water have a similar trend (Figure 3.28). Here, both the bare experiment (exp. 22) and the low concentration sodium alginate experiment (exp. 23) indicate an identical evolution of erosion rates. Both start with erosion rates around $30 \cdot 10^{-6} \text{ m}^2 \text{ s}^{-1}$ over the first 5 minutes before erosion rates gradually drop to reach rates of $7 \cdot 10^{-6} \text{ m}^2 \text{ s}^{-1}$ just after 10 minutes of experimental time. The high concentration sodium alginate experiment (exp. 24) in these low bicarbonate fluid conditions does not match this behaviour. After an initial high erosion rate at the initial time step, the erosion rate stabilizes at about $8 \cdot 10^{-6} \text{ m}^2 \text{ s}^{-1}$ only to reduced gradually to $5 \cdot 10^{-6} \text{ m}^2 \text{ s}^{-1}$ after 30 minutes.

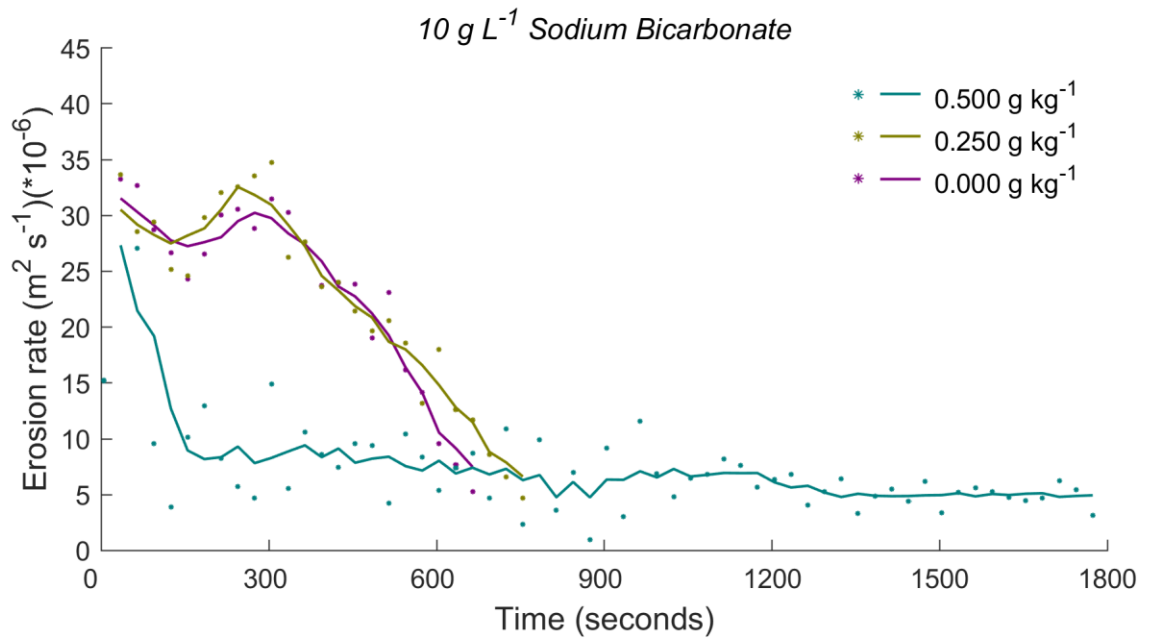


Figure 3.28: Erosion rates averaged per time step for experiments with an increasing concentration of sodium alginate under flow conditions with a low concentration sodium bicarbonate. Dots indicate average erosion rate per time step. Solid lines show a 5-point (2.5 minute) moving average.

Experiments (exp. 25-27) with the highest concentration of dissolved sodium bicarbonate show erosion rates that are similar with the other fluid settings (Figure 3.29). The bare experiment (exp. 25) in these fluid conditions places itself in between the bare experiments (exp. 19 and 22) of both other fluid settings, with erosion rates slightly lower than the tap water equivalent but with a smaller decrease in erosion rates towards the end of the experiment. The experiment with a low concentration of sodium alginate (exp. 26), in contrast to the equivalent low concentration experiments (exp. 20 and 23), does not stabilize and gradually decreases from erosion rates of $30 \cdot 10^{-6} \text{ m}^2 \text{ s}^{-1}$ towards rates around $6 \cdot 10^{-6} \text{ m}^2 \text{ s}^{-1}$ towards the later stages of the experiment. The experiment with a high concentration of sodium alginate (exp. 27) does stabilize after a few minutes to rates around $10 \cdot 10^{-6} \text{ m}^2 \text{ s}^{-1}$.

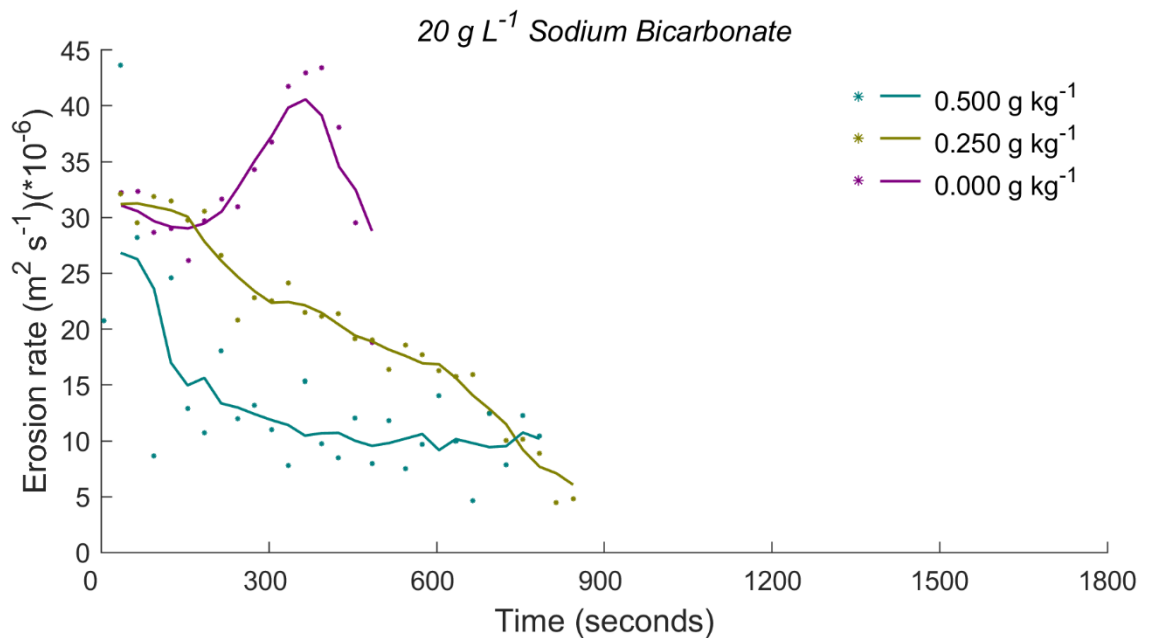


Figure 3.29: Erosion rates averaged per time step for experiments with an increasing concentration of sodium alginate under flow conditions with a high concentration of sodium bicarbonate. Dots indicate average erosion rate per time step. Solid lines show a 5-point (2.5 minute) moving average.

3.4. Discussion

3.4.1. Bare blocks

The experiments with bare sediment blocks underline the general concepts of sediment transport and bank erosion and as such solidify the results of this experimental research. Hence, these bare sediment experiments showed slower erosion rates for runs with finer sediment (190 μm) compared to runs with coarser sediment (458 μm). The location on the critical Shields curve or threshold for the beginning of motion for both sediments (Figure 3.30) does not suggest significant increases in internal cohesion between the finer sediment in comparison to the coarser sediment. As such this difference is likely associated with the angularity of the individual grains that cause internal cohesion due interlocking grains as suggested in section 3.2.3.1.

The bimodal mixture showed erosion rates between the rates of both its components as well as a larger variation between the individual runs. Both can be explained by the bimodal sediment distribution, a less uniform grainsize due to manual mixing and thus less impact of the interlocking of angular grains. Nonetheless the reasoning behind the unique behaviour of this

mixture with sudden shift in erosion rates (identical to the fine experiment for first 5-10 minutes before erosion increases after) remains unanswered. Even when considering flow conditions, which remained continuous over that time period.

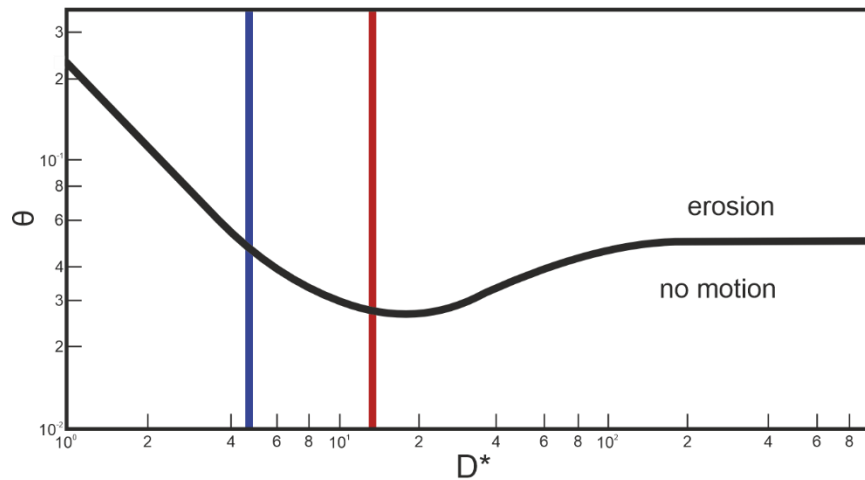


Figure 3.30: Diagram for the threshold for motion of different grainsizes based on van Rijn (1993). Red line indicates the 458- μm sediment, blue line indicates the 190 μm sediment.

3.4.2. Blocks with surrogate vegetation

The variation of outcomes for blocks with surrogate vegetation allows the estimation of the controlling factors for erosion rates, like qualifying the relative impact of seed density and growth duration. By comparing these experiments to the bare blocks composed of coarse sediment, a quantification is made on the impact of the added vegetation on the erosion rate. Hence, an average erosion rate over each experiment is introduced as the average of a sequence of time step averaged over all runs of the experiment. In this computation, the first five minutes are excluded, as the rapid initial erosion is not representative for the overall behaviour. Moreover, this computation averages over either the next 40 minutes or less when runs in an experiment completed earlier. This 40 minute period is arbitrary chosen to be long enough to dampen outliers and short enough to exclude static behaviour in latter stages of some of the experiments. All values are normalized by dividing by the erosion rate of the blocks composed of bare coarse sediment.

Table 3.4 shows that adding alfalfa surrogate vegetation to blocks reduces erosion rates. 7-day-old alfalfa reduces erosion rates by more than 40%, older alfalfa reduces erosion rates by almost 90%. Nevertheless, only a minor difference between 10-day-old and 13-day-old alfalfa exists (90% vs 85%). There is only a slight difference between low and high seed densities for 7-day-old alfalfa (13%), but this difference decreases for older alfalfa. Furthermore, differences induced by vegetation density are small compared to the age-induced difference.

Table 3.4: Normalized average erosion (-) (normalized by erosion of bare blocks composed of coarse sediment (exp. 1)) for all experiments of blocks with vegetation organized by seed density and vegetation growth duration.

	7 days	10 days	13 days
1.1 seeds cm⁻²	0.57	0.10	0.15
2.2 seeds cm⁻²	0.44	0.14	-

These effects agree with other research that looked at alfalfa up to 6 days old. Van de Lageweg (2010) showed by using growth durations of 2- and 6-day-old alfalfa and three seeding densities (0.5 seeds cm⁻², 2.2 seeds cm⁻² and 4.4 seeds cm⁻²) that vegetation growth duration was dominant over seed density, like the outcomes of this research. This outcome is also supported by Clarke (2014), who indicates that alfalfa sprouting normally occurs between 50 and 100 hours, about 2-4 days, comparable to the findings of van de Lageweg (2010). Van Dijk et al. (2013) extended this research by studying the effect of 4-day-old vegetation and found that 4-day-old vegetation behaved similar as 2-day-old vegetation, in contrast to 6-day-old vegetation caused different, more cohesive behaviour. Isolated research does not exist on growth durations over 6 days old. However, a range of larger physical experiments (Bertoldi et al., 2015; Gran & Paola, 2001; Tal & Paola, 2010; van de Lageweg et al., 2010) suggests the combination of longer growth and/or increased seed density increase bank/system stability without quantification. As such, this research expand the general known database on alfalfa from 6 days up to 14 days.

3.4.3. Blocks with chemical agents

The experiments with blocks with chemical agents demonstrate that chemical agents are effective at reducing erosion rate. However, they also show different chemical agents behave differently. Quantification of these effects (Table 3.5), by using average erosion as introduced in section 3.4.1, underlines the difference between xanthan gum and carrageenan. Erosion rates in runs with xanthan gum gradually reduce with increased concentrations, the lowest concentration (0.125 g kg⁻¹) shows a 30% reduction while erosion rates in runs with the highest concentration (1.000 g kg⁻¹) of xanthan gum are reduced by 95%. For carrageenan, the reduction for the lower concentrations is less pronounced, but at higher concentrations carrageenan becomes substantially more effective, almost nullifying erosion rates at the highest concentration (1.000 g kg⁻¹). For sodium alginate, the reduction is even more pronounced. For the lowest concentration of sodium alginate (0.250 g kg⁻¹) a reduction over 50 percent is already observed, for the highest concentration of sodium alginate (0.500 g kg⁻¹) the reduction is extreme and nullifies erosion rates.

Table 3.5: Normalized average erosion (-) (normalized by erosion of bare blocks composed of coarse sediment (exp. 1)) for all experiments of blocks with chemical agents organized by concentration and chemical agent (Xanthan gum, Carrageenan and sodium alginate).

Concentration (g kg⁻¹)	bare	0.125	0.250	0.500	0.750	1.000
Bare sand (exp. 1)	1	-	-	-	-	-
Xanthan gum	-	0.64	0.35	0.19	-	0.05
Carrageenan	-	0.77	0.98	0.76	0.55	0.02
Sodium Alginate	-	-	0.47	0.00	-	-

For comparison with rates of both previous experimental research as well as natural systems, this research normalizes bank erosion rates by the length of the sediment block. This length of the block reduces over time, from 0.3 m to about 0.205 m over the course of the run. Hence, in

this experimental research, erosion blocks that erode the fastest have erosion rates between $0.96 \cdot 10^{-4}$ and $1.42 \cdot 10^{-4} \text{ m s}^{-1}$. Friedkin (1945), used sediment composed of different mixtures of plaster and coarse sand, slightly higher energetic conditions with increased water depth, increased block height and over three times more discharge, and found erosion rates up to $2.5 \cdot 10^{-4} \text{ m s}^{-1}$. Friedkin (1945) showed that an increase from 6 to 12 per cent in plaster concentration reduced erosion rates to values of $0.33 \cdot 10^{-4} \text{ m s}^{-1}$. This rate of reduction is of a similar order of magnitude as what is found with different concentrations of chemical agents in the present experimental research. However, the baseline comparison cannot be completed as the experimental research of Friedkin (1945) did not include a base sample with only coarse sand.

Van de Lageweg (2013) introduced a concept of block half-life time. Half-life time is the time it takes before an erosion block is reduced to 50 % of the initial block area. Computation of half-life time (Figure 3.31) emphasises the different behaviour of xanthan gum runs; half-life times increase with increased concentration, and carrageenan, half-life times cluster around 0.09 hours and only are increased from 0.750 g kg^{-1} and higher. Furthermore, over both experiments with xanthan gum and experiments with carrageenan the spread of the individual runs increases with longer half-life times. The low concentration of sodium alginate has a similar mean half-life time as carrageenan but with a wider spread. Van de Lageweg (2013) added bentonite in similar experiments and found half-life times over 1800 seconds (0.5 hour) for most concentrations. Values that are larger than the half-life times in this research that only accidentally had half-life times over half an hour. Nevertheless, the behaviour of xanthan gum is similar to the behaviour of bentonite that saw a gradual increase in half-life times.

As highlighted earlier (see section 3.1.2), within physical modelling the addition of cohesive material to increase sediment shear strength has been attempted several times but no consistent material has been selected to represent cohesion in experimental models. The present research, with chemical agents xanthan gum, carrageenan and sodium alginate, indicate

that attempts to increase co- or adhesion are controlled by the concentration of the added agent, higher concentrations being more effective to reduce erosion rates. However, the present research also highlights that reduced erosion does not follow the same linear or exponential trend for different chemical agents. Therefore, the use of these agents needs to be selected based on the required type of co- or adhesion in physical experimental research.

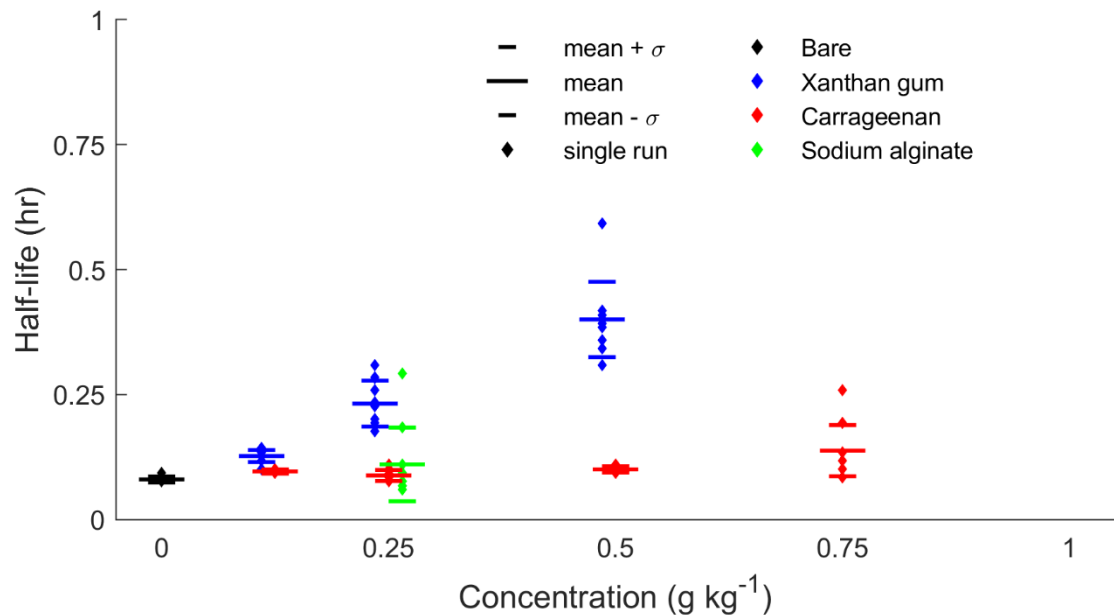


Figure 3.31: Half-life time (hr) for all runs with chemical agents (xanthan gum (blue), carrageenan (red) and sodium alginate (green)) against concentration (g kg⁻¹) of the chemical agent and half-life time (hr) for coarse sand runs with 0 g kg⁻¹ of added chemical agent. Experiments that did not finish are excluded. Experiment 7 (Xanthan gum 1.000 g kg⁻¹) is off the chart, with half-life times over 1 hour.

3.4.4. Can chemical agents replace surrogate vegetation?

Results above indicate that chemical agents are able to reduce erosion rates, similar to how surrogate vegetation can reduce erosion rates. However, to successfully introduce chemical agents as a replacement of surrogate vegetation, the chemical agents need both to be representative and practical in use.

3.4.4.1. Are chemical agents representative of surrogate vegetation?

Similarities between the used chemical agents and surrogate vegetation exist across the entire range of experiments. However, for this comparison, focus is on the surrogates with the clearest

results; Xanthan gum as a chemical agent and low-density alfalfa as a surrogate vegetation. The average erosion curves (Figure 3.33) show that all low-density surrogate vegetation experiments fall in between the xanthan gum experiments. Rapid erosion over the first timestep is in the range of 15-20% for surrogate vegetation experiments, which is larger than the 10% in the xanthan gum experiments and results in erosion curves for surrogate vegetation with initial low block areas. Ignoring this initial drop, young vegetation (7-day-old) is best represented by the lowest concentration of xanthan gum, although the latter erodes slightly faster. Older vegetation (10- and 13-day-old) is best represented by higher concentrations of xanthan gum, although the highest concentration in this research is too resistant to represent any surrogate vegetation experiment. This same effect is highlighted in a comparison of average erosion (as introduced in section 3.4.2) for xanthan gum and low-density surrogate vegetation (Table 3.6). Here, relative erosion rates for 0.125 g kg^{-1} xanthan gum (0.57) are similar to relative erosion rates of 7-day-old vegetation (0.64) and relative erosion rates of the higher density xanthan gum (0.500 g kg^{-1} and 1.000 g kg^{-1}) encapsulate relative erosion rates of 10- and 13-day-old vegetation.

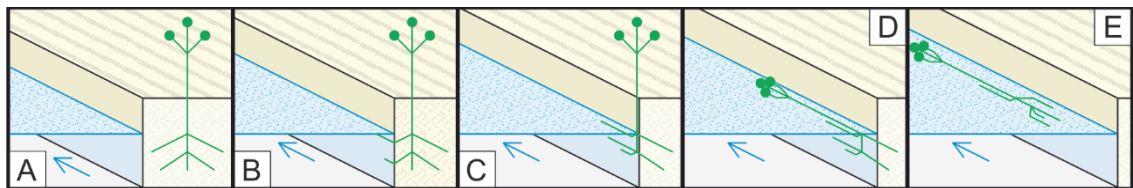


Figure 3.32: Schematic erosion steps of an alfalfa sprout (green) in the experimental set-up under simplified erosion. A) Unaffected sprout; B) Soil matrix is eroded from around some lateral roots which deflect with flow; C) Soil matrix is eroded from around the main tap root, which deflects with flow; D) Stem bends and fall into flow; E) Last roots lose matrix (break or pull out). Average flow direction indicated by blue arrow.

Table 3.6: Normalized average erosion (-) (normalized by erosion from bare blocks with coarse sediment) for three experiments of blocks with xanthan gum and for three experiments with low-density alfalfa surrogate vegetation.

Xanthan Gum	0.125 g kg ⁻¹	0.500 g kg ⁻¹	1.000 g kg ⁻¹
	0.64	0.19	0.05
Alfalfa	7 days	10 days	13 days
(1.1 seeds cm ⁻²)	0.57	0.10	0.15

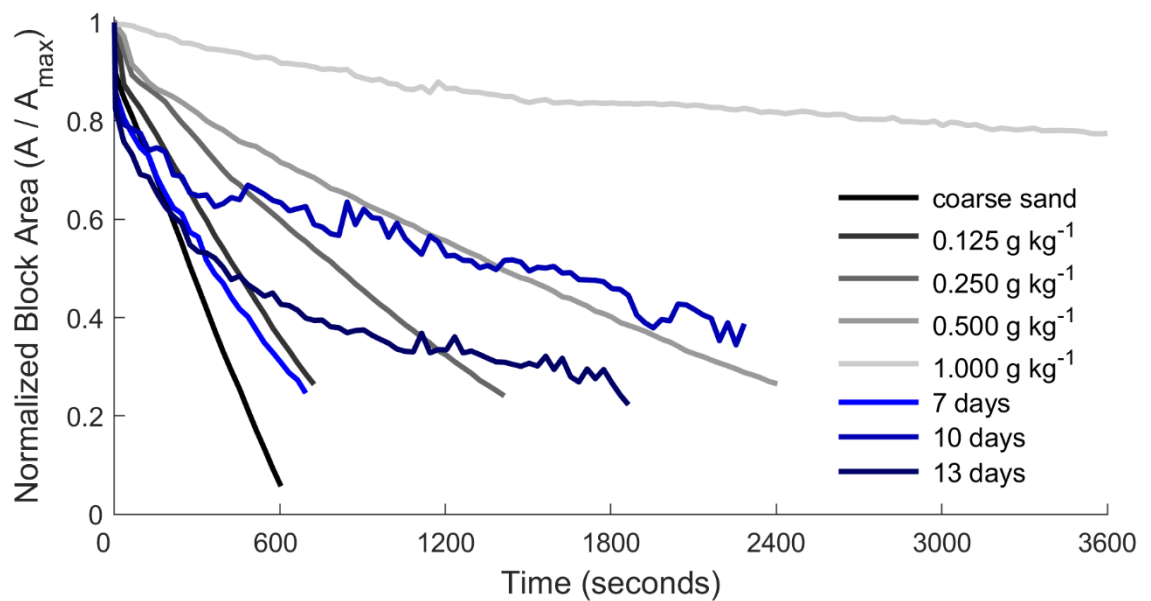


Figure 3.33: Average erosion rates against time for sediment blocks composed of bare coarse sand, blocks with xanthan gum and blocks with low-density surrogate vegetation.

As explained above, erosion of alfalfa vegetation is not linear and a few distinct stages are identified (Figure 3.32). At the fourth stage (D), the alfalfa vegetation shelters the block in its wake and upstream as backwater effects slow the flow. A similar effect occurs if at the last stage (E) vegetation is captured by downstream vegetation (Figure 3.34 A). Although this research has not qualified the importance of these individual stages, observations suggest that it reduces the linearity of erosion rate. The numerous individual alfalfa sprouts interacting with each other at different stages enhances this over time and space. The above effect requires time to develop.

As such, a more rapid erosion for blocks with alfalfa vegetation, compared to bare blocks and blocks with chemical agents, can be ascribed to a lack of latter stage (Figure 3.32 C-E) sprouts at the start of experimental runs.

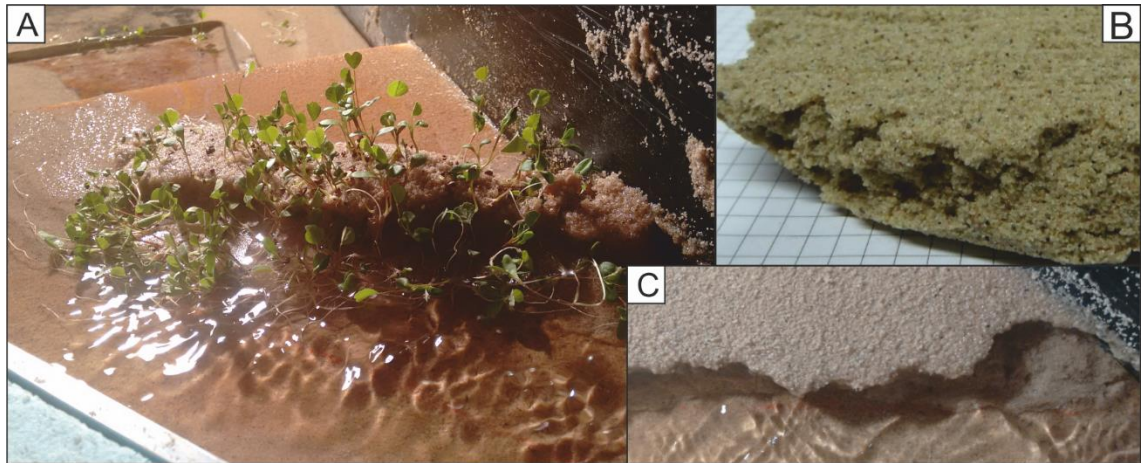


Figure 3.34: A) Experimental run with surrogate vegetation. Some individual alfalfa sprouts are floating on the water while others are captured downstream by neighbouring alfalfa sprouts. B) Erosion block with chemical agent (Xanthan gum), being dried in situ for several days. C) Experimental run with chemical agent indicating spatial irregularity in erosion.

Another observation indicated a high spatial irregularity in blocks with high concentration of chemical agents (Figure 3.34.C). This effect, physically only explained by poor mixing, could relate to how these chemical agents react with each other and the sediment matrix. Whereas the present experimental research had no acknowledged control over this effect, the pattern of this effect can be linked with patches of dense vegetation or remnants of larger vegetation (or rock formation) embedded in the soil (e.g. large fallen trees). Therefore, further understanding of these types of processes may enhance the use of these chemical agents to mimic natural systems.

3.4.4.2. *Practicality of the application of chemical agents*

To be useful in larger physical experimental research, chemical agents, like surrogate vegetation, must be practical in use and relatively easy to apply. Chemical agents have been introduced in larger scale physical experimental research using different methods. Van de Lageweg (2018)

used chemical agents as a proxy for biofilms where the chemical agent was spread in dry powder form over a moist sediment surface before draining the surface slowly. In his research, a gel-like film formed that partly encapsulated the upper layer of sediment, a result less effective for fluvial-based physical experimental research. Research by Fernandez et al. (2019), as discussed in section 3.2.3.3, introduced chemical agents by mixing them first with water before mixing the entire solution to sediment. Observations from preliminary attempts to wet mix chemical agents (using a similar method as dez et al. (2019)) and observations of experimental research of van de Lageweg (2018) showed that both methods were not practical to use in the present experimental research nor in larger physical models for fluvial systems. Moreover, these methods generated gel-like structures and less uniform concentration of the added chemical agent as would be reached with the present approach (see section 3.2.3.3). Furthermore, the outcomes of the present research provide a promising guideline on what concentration of chemical agent to use for substitution of certain surrogate vegetation conditions. Nevertheless, one large practical disadvantage is associated with the method of this research. Sediment is mixed with chemical agents in a dry state before it is placed in situ, as such it is near impossible to utilise the dry mixing approach in situ on existing morphology without disturbing the morphology.

Another effect observed during this experimental research is related to the sensitivity of the chemical agents (xanthan gum and carrageenan) in combination with both air and water. These agents can and are stored dry and do not require to be stored air locked. However, these agents activate on contact with water and form either a gel or another interlocking structure. Past research has not reported significant behaviour change when these agents are kept under water after activation (Parsons et al., 2016; van de Lageweg et al., 2018). However, by using these chemical agents in a non-submerged state, this research witnessed an increase in ad- or cohesion when these activated chemicals are emerged from water over a longer period. Although quantification of this period is beyond the scope of this research, allowing the complete mixture (sediment, chemical agent and water) to be exposed for 70 minutes before

the start of a run would double to triple an erosion time of 50 minutes. Furthermore, blocks that were left to dry in situ transformed into a brick-like feature in a time span of 10-20 hours (Figure 3.34 B). This effect has been observed by Chen et al. (2019) in small scale experimental research on physical shear strain with xanthan gum mixed through slightly finer sediment ($\sim 200 \mu\text{m}$) under controlled drying conditions and is probably reflected in the use of Xanthan gum as a binding agent in gluten-free baking (Xavier et al., 2019). In the present study, blocks with a chemical agent showed a reduction in erosion over time, an observation that could link with the above process. However, widening and shallowing of the channel/flow (see section 3.2.3.1 and discussed in section 3.4.5) and thus a reduced applied fluid shear stress, produce a similar effect behaviour that it is not possible to differentiate.

The above shortcomings highlight that further development of application methods for chemical agents in larger physical models is required. However, overcoming these shortcomings would grant physical modelling the use of a benefit of these chemical agents. Application of chemical agents takes between tens of minutes to hours dependent on the size of an experiment. This period is near instant in contrast with surrogate vegetation that takes several days to sprout and even more days to develop.

3.4.5. Temporal and spatial variations in erosion rates

The inlet channel width remains constant, however the channel between the erosion block and the metal barrier (in this section further referred to as channel) increases in width over time. As such, water depth and thus shear stress is reduced, which under similar flow conditions can result in lower rates of block erosion. The qualification of these rates depends on whether a bar is formed (Figure 3.35 B) next to the metal barrier or no bar is formed (Figure 3.35 A). This bar, with similarities to inner-bend bars in coarse meandering rivers, follows the curve of the flow and expands slowly outward. As such, the bar reduces effective channel widening, prevents standing wave trains that relate to supercritical flow conditions and maintain water depths at the block edge. This bar, uniquely formed at experiments with high erosion rates, is associated

with reduced sediment transport capacity. As such, the lack of a bar in high cohesive experiments indicates transport capacity of the flow is sufficient and the cohesion of the block is the limiting factor.

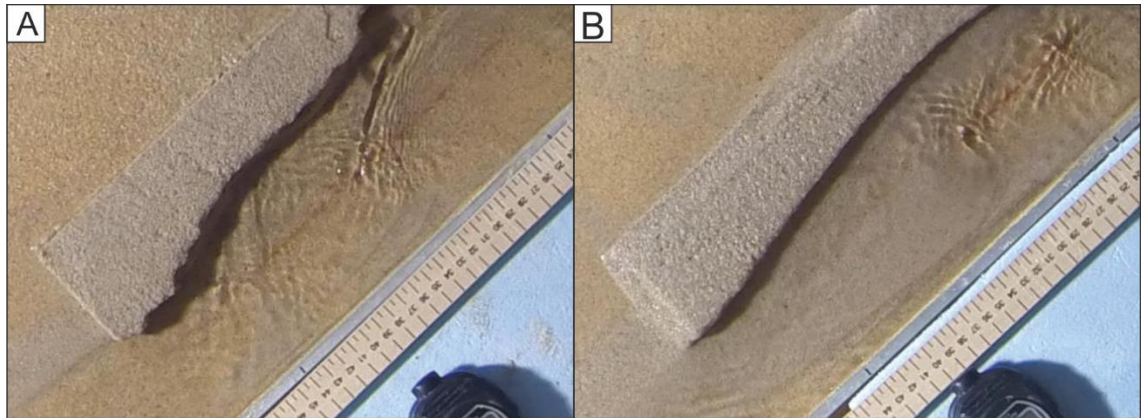


Figure 3.35: Example of two time-lapse images without (A) and with (B) a bar forming on the inside of the experimental set-up. Progress in block area is similar on both images.

Furthermore, water level is spatially not constant along the block edge, an effect that originates from the widening of the channel at the downstream end of the block and is enhanced by the lack of bed slope in the experimental set-up. Because of the widening, water depth is reduced at the downstream end of the block and causes an along-channel water surface slope. Rough estimation indicates a slope of one percent. For banks with lower shear strength, where transport capacity is limiting, the impact is small. However, for conditions where critical shear strength has been enhanced by additional cohesion, a 20-30% decrease in water depth will decrease effective erosion rates. This causes a gradient over the length of the block, a gradient that over time is balanced out by the discrepancy in channel widening as discussed above.

In the experimental runs, the often blocks erode in a specific arc-shape pattern. The highest retreat rates occur in the second quadrant of the block length. This peak retreat migrates slowly downstream as more of the block is eroded away, an effect observed in previous experimental research (Friedkin, 1945; van de Lageweg, 2013; van Dijk, Teske, et al., 2013). The shape of this arc was dependent on block erodibility, with a more straightened arc in rapid erosive experiments and a curved arc in more cohesive experiments. This arc-like shape is augmented

by a conjunction of variable erosion rates due to longitudinal variation of depth and temporal variation of channel width. Furthermore, most cohesive blocks show an irregular bank line. Here, the block edge line followed an arc shape but diverted locally up to 10 mm to either side. This irregular bank shape dominantly occurred as parts of the block collapsed, thereby depositing large chunks of material in the flow. This then induced local variation of the flow, both upstream due to a sudden rise in water level and downstream due to sheltering from the flow. However, to understand the impact on erosion rates of this process, which is also seen in natural, steep-banked, river systems(e.g. Micheli & Kirchner, 2002), further research is required with small scale physical models.

3.4.6. Husbandry of surrogate vegetation

For this research, alfalfa was chosen as a surrogate vegetation, a choice based on its root structure and robustness under variable growing conditions (3.2.3.2). Observations and outcomes from the present research, and observations from other experimental research (Williams et al. (2018) and chapter 5), highlight the robustness of alfalfa under different conditions. However, these observations showed that the root structure was sensitive to ambient conditions like light and moisture. As such, chapter 6 will look more into the impact of these ambient conditions.



Figure 3.36: Examples of bank erosion; A) Potential for undercutting of a grassy bank at Waiau river (NZ). B) Failure blocks resulting from cantilever failure of an undercut bank in a small braided river (Dingle Burn (NZ)). Pictures by Bas Bodewes (2020).

In the experiments reported in this chapter, the alfalfa root structure extended to lengths beyond expectation, most likely enhanced by the combination of growing conditions. Alfalfa roots reached lengths over 80 mm, resulting in significant lateral root growth in the 20 mm thick block. Not only will this impact scour patterns around an individual sprout, it will also strengthen the entire block further as individual root structures integrate with each other.

3.4.7. Effectiveness of image analysis

As highlighted in sections 3.2.1 and 3.2.3, this research consists of two similar sets of experiments with slightly different hydrodynamic parameters. However, as shown in this section, the data processing is slightly different between two different datasets as well. Part of this is explained by a different camera resolution ($0.6015 \text{ mm pixel}^{-1}$ versus $0.5114 \text{ mm pixel}^{-1}$), however some variation is an artefact of differences in how trial and error has been applied during post-processing of both experimental sets. In the first set of experiments the threshold and range were tuned to include both vegetated and bare sediment blocks. In the second set of experiments, the threshold and ranges were tuned to include only bare sediment blocks. Moreover, the second set included a different coloured (bright blue) surface area that altered threshold and contrast values. On top of that both settings were subject to changing ambient light conditions (both natural and artificial). For both sets, the post-processing algorithms were a process of trial and error and best fit for a selection of the experimental runs with a global check to check for outliers.

This latter part also touches on a key aspect of image analysis, and more specifically in pattern recognition; the balance between automation of the process and precision of the outcome. For this research, automation is often favoured in order to acquire a larger dataset at the cost of more precise outcome. Part of this can be seen in the allowed range that was used in first sets of experiments. The allowed variation between two subsequent images had a lower limit of acceptance around 8 pixels (or 4-5 mm) on average across an entire cross-section per 30

seconds. Standalone, this value accounts for erosion rates up to nearly $50 \times 10^{-6} \text{ m}^2 \text{ s}^{-1}$, just over 1.5 times the erosion rate of a bare sediment block.

The error this generates will be small and consistent and as such have a limited impact on qualitative outcomes. Additionally, the method to systematically filter out outliers results in some of the runs missing continuous data.

3.5. Conclusions

This chapter has utilised small-scale bank erosion experiments to explore the impact of different surrogates on erosion rates and erosion behaviour and on whether chemical surrogates are able to simulate vegetation. This chapter has found that:

- Added chemical agents and surrogate vegetation both reduce erosion rates of blocks of sediments.
- An increase in concentration of xanthan gum decreases erosion rates of this block of sediment.
- An increase in concentration of carrageenan does not decrease erosion rate until a certain threshold, after which erosion rates asymptotically decline to zero.
- A higher vegetation density slightly increases erosion rates of this block of sediment.
- Older vegetation increases erosion rates, a change effective in particular between 7 and 10 days.
- An increase in concentration of sodium alginate decreases erosion rates of this block of sediment.
- An increase in sodium bicarbonate reduces the effectiveness of decrease of erosion rates for block of sediment with sodium alginate, nearly negating its potential effect to bare sediment.
- Chemical agents, and in particular xanthan gum and sodium alginate, are a representative of surrogate vegetation in specific physical modelling settings.

4. Controlling chemical cohesive agents in small scale fluvial experiments

4.1. Introduction

The previous chapter, chapter 3, compared bank erosion rates with different chemical surrogates being used to represent vegetation in physical models of fluvial systems. The outcomes demonstrated that chemical surrogates produced similar reductions in erosion rates as surrogate vegetation. However, the results also highlighted that the methodology for applying chemical surrogates to sediment with a physical model needs to be considered, particularly for its application to larger scale physical experiments. Results from chapter 3 also highlight the opportunity for controlled behavioural change of chemical surrogates by the use of an additional dissolved agent. For example, it shows that sodium bicarbonate, once dissolved in the water, reduces the cohesive properties of sediments containing sodium alginate resulting in increased erosion rates. This presents the opportunity for controlled behavioural change of chemical surrogates (like vegetation growth or decay) during an experimental run by either the (re-)application or modification of a chemical surrogate within the experimental system.

This chapter will evaluate the experimental potential and opportunities for the combined application of sodium alginate and sodium bicarbonate in larger physical models. Experiments will be performed to test the hypothesis that temporal behavioural change in erosion patterns can be achieved by altering the sodium bicarbonate concentration of the flow in sediments mixed with sodium alginate.

4.1.1. Description of the problem

Chapter 3 introduces sodium alginate and sodium bicarbonate in a controlled erosional experiment, demonstrating that increasing concentrations of sodium alginate mixed through sediment reduces sediment erosion rates and the addition of sodium bicarbonate to the water increases erosion rates of sediments negating the cohesive effects of sodium alginate. However,

to use this approach with chemical surrogates in a dynamic fluvial physical model, three questions require to be explored. First, is the outcome of increased and decreased erosion rates repeatable when there is an alternate increase and decrease in the concentration of sodium bicarbonate; i.e. can we represent 'seasonal' changes in vegetation effects? Second, is the effect of sodium alginate on sediment cohesion persistent during a model run when erosion and deposition takes place; i.e. does the cohesive effect of sodium alginate persist after sediment has been eroded and then deposited elsewhere? And finally, is the method representative; i.e. is the dynamic behaviour of the sodium bicarbonate – sodium alginate interaction comparable to the use of surrogate vegetation?

4.2. Methodology

To address these questions a set of planform river experiments are conducted in a small fluvial system. Here, a selection of concentrations from Chapter 3 is used to mimic the behaviour of surrogate vegetation in a larger, fluvial set-up. These experiments are set-up in the stream table (see chapter 3.2.1). A 1.50 m long, 0.50 m wide experimental area constrained by two, 50 mm high, parallel foam boards on either side and a 5 mm deep, 23 mm high, plastic boundary at the downstream end forms the spatial set-up of the experiment (Figure 4.1 A-B). Here, the upstream 0.20 m is reserved for the water inflow system, hence the effective experimental length is 1.30 m. On the sides, inside the experimental area, two guide rails are fixed symmetrically with a slope of 0.015 m m^{-1} . These guide rails are used to create a similar initial bed for each experiment by using a 0.50 m wide scraper board that can be moved manually over the guides to flatten the bed. Bed thickness is 33 mm at the downstream end, 10 mm above the downstream boundary, and increases to over 50 mm at the upstream end. At the upstream part of the experimental area, where the top of the bed elevates above the foam boards, small (< 5 mm high) ridges of sediment are manually placed to prevent water leaving the experimental area by overland flow. An 80 mm wide, 10 mm deep straight channel is carved in the experimental bed at the start of each experiment.

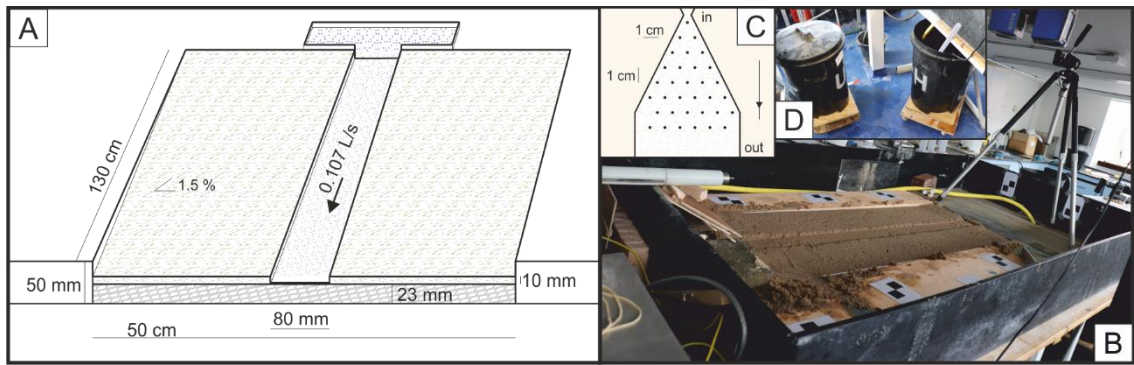


Figure 4.1: A) Schematic overview and dimensions of the experimental basin. B) Overview of initial set-up of a planform river experiment looking sideward in downstream direction. C) Schematic view of spacing of nails in the spreading device based on a quincunx pattern. D) Close up on movable end tanks at the downstream end of the stream table.

The flow system is set-up in a similar way as the bank erosion experiments (see section 3.2.1). Water from the end tank, at the downstream end, is pumped up towards the inflow area of the experiment. Here, the water flow dampens by a sequence of rocks and small basins in such way that the outflow is neither too turbulent nor predominantly flowing in one lateral direction. The outlet of the last upstream basin has an identical width (80 mm) as the carved channel but with sides 6 mm higher than the main experimental basin, to allow space for dynamic vertical variations in bed level. The inflow system is not watertight in the downstream direction, as such up to a few percent of the inflow may enter the system as subsurface flow. After 23 mm of drop at the downstream end of the experiment, water and sediment enters a basin where all bed load sediment could settle. At the end of this basin, water flows back into the end tank. At the start of each experiment, the end tank is (Figure 4.1 D) filled with 60 L of fluid, to allow the submerged pump to provide a stable flow of 0.107 L s^{-1} at the upstream inlet over the duration of the experiment.

For these experiments, a sediment feeder is installed at the upstream end to enable an equilibrium longitudinal slope to be maintained. The sediment, the $458 \mu\text{m}$ sandy sediment previously used (see section 3.2.3, is fed at a constant rate of 0.15 g s^{-1} . From the feeder, the sediment enters a handmade Galton board (Figure 4.1 C) to ensure an even distribution over the width of the channel. This device is constructed out of two wooden boards connected by

nails positioned in a pyramid shape, roughly resembling a quincunx pattern. The quincunx pattern has a 10 mm separation in both horizontal and vertical directions and a 5 mm offset between subsequent rows. The final width of the quincunx is 75 mm, 5 mm smaller than the channel width. This device is placed at a 50-degree angle, its outlet placed 10-20 mm above and about 5-10 mm downstream of the water inlet.

Morphological data are collected using a FARO X330 TLS terrestrial laser scanner (see chapter 5.2.3 for full details). This terrestrial laser scanner is located 0.77 m above the experimental set-up, a location georeferenced with 12 targets across the floor and sides of the stream table. The scanner is used with both high- and low- quality settings during this set of experiments. The low-quality setting, with a resolution of 1/8, a quality of 2, no colour capturing and about 1-1.5 minutes scan time, is used for scans every 10 minutes when an experiment was running. The high-quality setting, with a resolution of 1/5, a quality of 4, no colour capturing and about 6-7 minutes scan time, is used for scans without flow, between the individual periods of the experiments (see section 4.2.1). A GoPro Hero 3, mounted about 1 m above the stream table, captures time-lapse imagery every 60 seconds and a Cannon EOS 600, mounted facing upstream about 0.50 m above the downstream basin, captures time-lapse imagery every 60 seconds.

4.2.1. Settings and experimental runs

A total of 9 different experiments are undertaken (Table 4.1). Each experiment is unique but all experiments are set-up following a similar experimental procedure. At the start of each experiment, after the initial bed and channel are created, a single high-quality scan captures the initial bed topography. This is followed by a 50-minute long experimental period. During this period, continuous GoPro and Canon time-lapse imagery are collected alongside rapid, lower-resolution laser scans at ~10 minute intervals (10, 20, 30, 40 and 49 minutes). Fourteen minutes after the end, a high-resolution scan is collected. Finally, excess sediment is collected and removed from the downstream basin for post-experimental analysis. Approximately 25 minutes after the flow is stopped, a new period is started. Each experiment has several (3 or 4)

subsequent periods of 50 minutes and with a unique combination of settings for each experiment as shown in Table 4.1.

Table 4.1: Overview of planform river experiments. First column indicates initial bed content; sand refers to 458 μm sediment, sodium alginate refers to 0.5 g kg^{-1} premixed sodium alginate. The subsequent four periods show whether the experimental period runs with tap water or with bicarbonate solution. In experiments 6-8, conditions change mid-experiment, noted by the addition of sodium alginate spray or 10-day old vegetation. * This period is only 40 minutes long. ** This initial bed has sodium alginate mixed in in only the upstream 0.15 m and the outermost 0.10 m on each side.

	Initial bed	period 1 (50 min)	period 2 (50 min)	period 3 (50 min)	period 4 (50 min)	
Experiments	1	sand	tap water	tap water	tap water	tap water
	2	sand + sodium alginate	tap water	tap water	tap water	tap water
	3	sand + sodium alginate	bicarb sol.	bicarb sol.	bicarb sol.	
	4	sand + sodium alginate	tap water	bicarb sol.	tap water	bicarb sol.
	5	sand + sodium alginate	bicarb sol.	tap water	bicarb sol.	tap water
	6	sand	tap water	tap water	tap water	bicarb sol.
					SA spray	SA spray
	7	sand	tap water	tap water	tap water	bicarb sol.
					SA spray	SA spray
8	sand	tap water	tap water *	tap water	tap water	
				10 day veg.	10 day veg.	
9	sand + sodium alginate **	tap water	tap water	tap water	tap water	

Amongst the experiments, there are control experiments (experiments 1, 2, 3 and 9), where all periods use fluid from a single end tank and a single type of surrogate, there are alternating experiments (experiments 4 and 5) where fluid supply is alternated between tap water and water with added sodium bicarbonate every other period and there are perturbed experiments (experiments 6, 7 and 8) which commence with an untreated sand bed but have surrogates (i.e., sodium alginate spray or alfalfa vegetation) added in between periods. In experiments 6 and 7 fluid properties are changed only in experimental period 4.

4.2.2. Sediment and bed preparation

The initial experimental basin was filled with sand with a D_{50} of 458 μm . After some preliminary test runs to fine-tune conditions, the top layer of about 20 mm thickness was removed and replaced with a new sediment layer. This was repeated for each experiment, preventing excessive use of unnecessary sediment. For the untreated experiments (experiments 1, 6, 7, 8 and 9), this sediment layer was saturated with water in a similar way as in the bank erosion experiments (see section 3.2.3.1); sediment was mixed with 230 mL of water for each kg of sediment and placed in the experimental basin. Sediment was slightly compacted before it was scraped into a smooth initial bed.

4.2.2.1. *Sodium Alginate*

For the experiments with sodium alginate mixed into the sediment, a similar procedure was followed. Considering the sensitivity to air, 2 batches of 10 kg sediment were thoroughly dry mixed with 5 g of sodium alginate each (representing a 0.5 g kg^{-1} concentration) before being mixed with 2300 mL of tap water for 2 minutes. This mixture was then placed in the experimental basin where, after scraping the initial bed, any excess sediment was removed.

4.2.2.2. *Sodium Alginate Spray*

Sediment beds in the experiments that used an experimental spray were prepared in the same manner as the untreated experiments. For the spray itself, 5 g of sodium alginate was dissolved in 1 L of 60°C tap water with glass-stirring rods. Tests determined that 60°C tap water create the most uniform and viscous mixture which would not precipitate as quickly over time. The resulting solution was spread over the bars, banks and unaltered areas outside the initial channel using simple plant sprinklers, before the start of the third period of the experimental run. The total amount of solution applied was about 0.5 L. Visual observations of the solution remaining in the plant sprayer suggest that it was slightly more viscous than that applied to the sediment surface. Hence, the amount of sodium alginate applied to the experimental setup is

probably less than 50% of the sodium alginate that was dissolved, representing an application rate of less than 5 g L⁻¹.

4.2.2.3. *Alfalfa vegetation*

Sediment beds in the experiments with surrogate vegetation were prepared in the same manner as the untreated experiment, but for this experiment specifically, the entire basin was emptied initially to prevent any interaction between traces of sodium alginate and surrogate vegetation. After two experimental periods, the experiment was paused and surrogate vegetation (alfalfa seeds, similar to chapter 3 but from a new batch) was seeded on bars, banks and unaltered areas outside the initial channel, a spatial distribution identical to the sodium alginate spray. The seeds were manually distributed at a density of 1 seed cm⁻² and allowed to grow for 10 days before starting the last periods of the experiment. This 10-day duration matches the bank erosion experiments (chapter 3.2.3.2). In this growing period, a small flow was maintained to keep the bed moist. Vegetation was allowed to sprout and grow in situ, with natural day/night cycles enhanced with normal fluorescent light at office hours on weekdays; room temperatures ranged from 17 to 25 °C.

4.2.3. Sodium bicarbonate preparation

Several experiments (experiments 3, 4, 5, 6 and 7) required changes between normal tap water and sodium bicarbonate solution which was achieved using two mobile water storage tanks (Figure 4.1 D) that could be swapped between experimental phases. One storage tank was filled with tap water, the other with 10 g L⁻¹ sodium bicarbonate solution. Water temperature (°C), pH (-) and conductivity (mS) were measured in the end tanks between experimental periods.

4.2.4. Sediment collection

Sediment was collected from the end basin after each experimental period and oven-dried overnight at 105 °C. The oven-dried sediment was weighed; net sediment output rates were computed by subtraction of dry sediment input from the dry sediment output.

4.2.5. TLS processing

The terrestrial laser scans, collected with the FARO X330 TLS, were processed using a similar method as the terrestrial laser scans in the large-scale braided river experiments that will be explained in detail in chapter 5.3. As such, three programs were used (Faro Scene v6.2.5.7, CloudCompare v2.9.1. and Matlab© 2017a) with minor differences in methods that will be described below (see Figure 4.2).

Due to the limited scan area (seven to eight times smaller than the scans in chapter 5), scans were processed as a single cluster per experiment. In the cluster, each individual scan was then subject to target-based registration using checkerboards only (12 checkerboards total, in and along the stream table). After manual removal of each 'false' checkerboard for each scan, a cluster registration (see section 5.2.3) was performed for each cluster (i.e. experiment) before scans were exported as individual 'e57' point clouds.

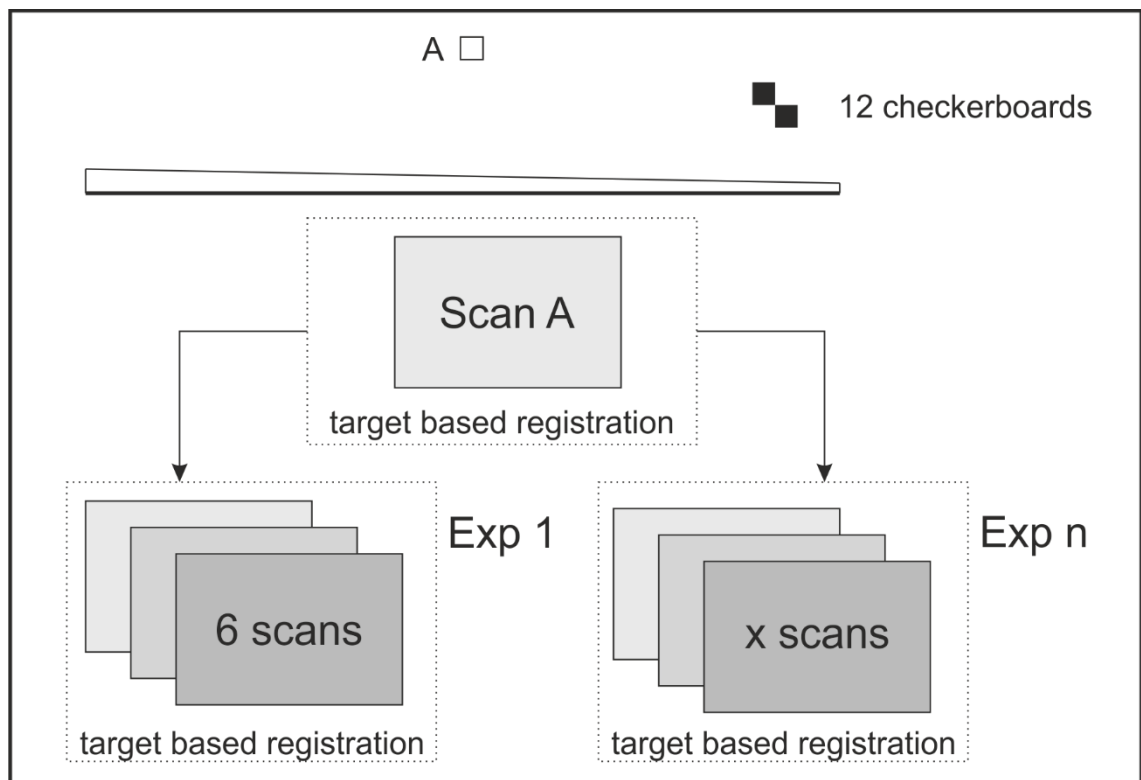


Figure 4.2: Initial post processing steps Faro X330 terrestrial laser scans for each scan, using Scene 6.2.5.7. Target-based registration uses a selection of 12 checkerboards located in and around the stream table. Target-based registration is done separately for each experiment ($n = 1$ to 9).

These 'e57' point clouds were imported and processed individually in CloudCompare using a four-step process (Figure 4.3). First, point clouds were transformed to align with a Cartesian grid with the origin on the true left upstream corner on the floor of the stream table. Second, point clouds were cropped to exclude points outside a predefined box. Third, points affected by either standing water or reflections were removed using a colour intensity threshold (points with red intensities smaller than 100 were rejected, a best practice method based on trial and error with the most disturbed datasets of these experiments). Fourth, the point cloud was rasterized into a DEM with a grid size of 0.001 m, no interpolation and retaining the maximum elevation in case of multiple co-located points.

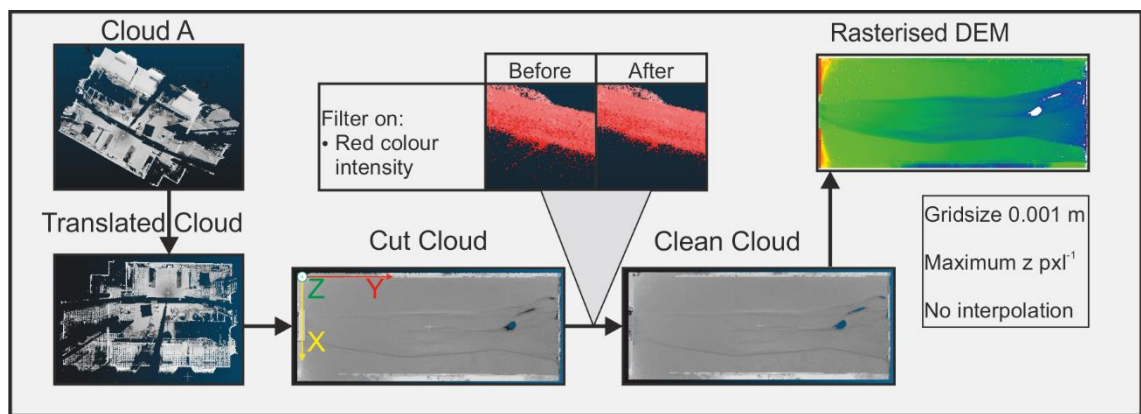


Figure 4.3: Second set of post processing steps in Cloud Compare v.2.9.1 used to transform point clouds into a rasterized digital elevation model (DEM). This includes translation and removal of standing water and reflections.

The next set of post-processing steps were undertaken in Matlab© 2017a to generate continuous digital elevation models (DEM) (Figure 4.4). First, imported matrices were trimmed to remove a final row of y-values, guaranteeing matrices of identical size. Next, cells with missing data (NaN) were filled by a sequence of four steps. Each cell with missing data was assigned the 8-neighbourhood mean of the surrounding cells, excluding NaN values. This step was repeated three times. Lastly, all remaining empty cells were clustered by connectivity, each cluster given the 0.35 quantile of the original circumference cells of this cluster (Figure 4.4).

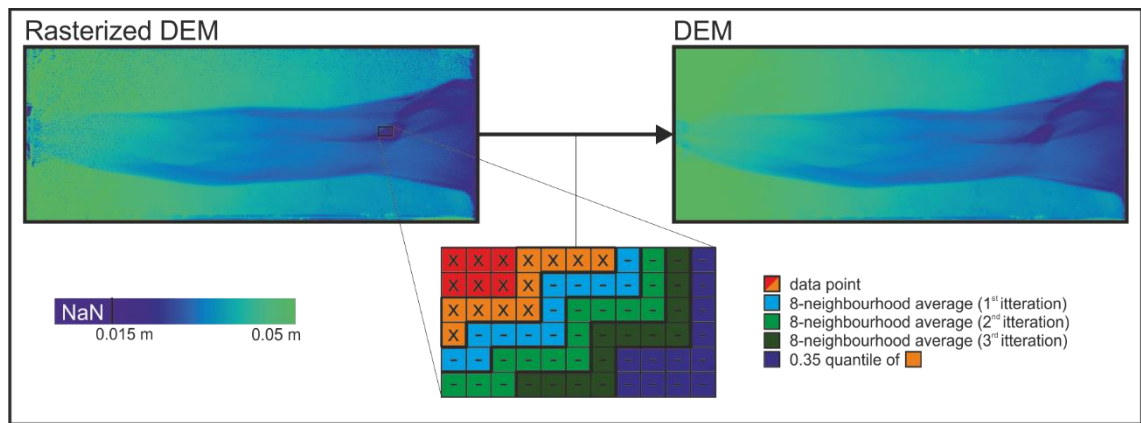


Figure 4.4: Interpolation of missing values (NaNs) in rasterized digital elevation model (left) to a digital elevation model (DEM) without missing values (right). Missing values (-) were interpolated using neighbouring values (x) using a 4-step algorithm (colour coded) as indicated by the close up (bottom).

The DEM generated by the above method was used to set-up three different raster-based maps that were used in conjunction with each other for the analysis; a detrended DEM, a DEM of difference and a channel map, all with a resolution of 0.001 m (Figure 4.5). For the detrended map, the DEM was normalized over the slope, using the predetermined slope of 0.015 m m^{-1} with the downstream barrier as origin (0.025 m above base). For the difference map, two successive DEMs were differenced.

A logical channel map to distinguish between channel (true) and non-channel (false), was generated from the channel map of the previous time step and the difference map. For the initial time step ($t=0$), the channel map was true for cells with a detrended elevation less than 2 mm and false for other cells. A set of morphological operations (further elaborated in chapter 5.2.5 (Figure 5.10)) were used to remove isolated cells. Finally, the channel area was expanded by two cells in any direction. At successive steps ($t>0$), non-channel areas were checked for elevation differences. Following sensitivity testing to identify the most appropriate threshold elevation difference, differences over 3 mm were set to change a cell from non-channel area to channel area to avoid spurious channel detection in depressions outside the real channel belt.

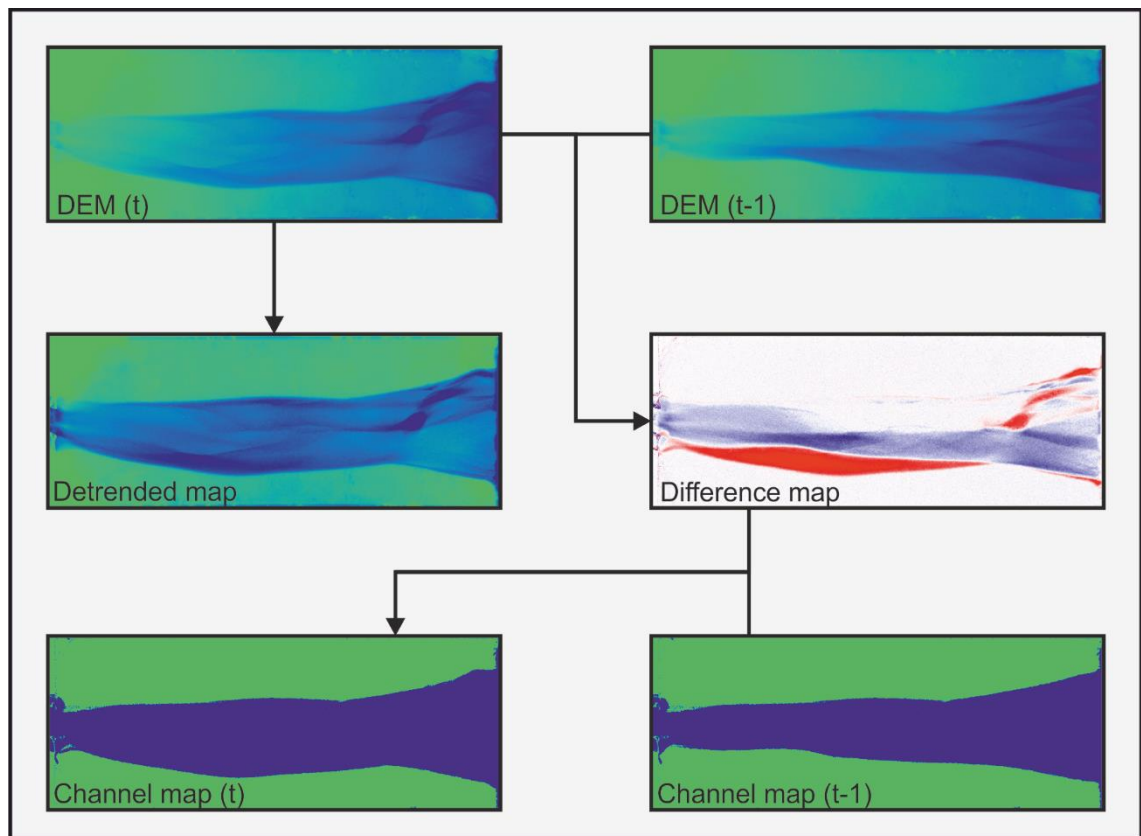


Figure 4.5: Flowchart of creating detrended, difference and channel maps for the analysis of digital elevation models (DEM). All maps show experiment 1 after 3 periods of flow (t) and after 2 periods of flow (t-1).

4.3. Results

Note that in the following, the term channel could be used for two distinct features. To avoid confusion, herein the term channel will be used solely for elongated depressions within the system, whereas the total extent of the system will be referred to as the channel belt or river. Therefore, in general the channel and channel belt only have the same extent at the start of each experiment.

4.3.1. Constant conditions

4.3.1.1. Planform behaviour

In the reference experiment (Experiment 1) with untreated sand (Figure 4.6, first column), the channel evolves from a single thread to a more braided system. Over time, the single channel transforms into a system with weak alternating bars that become more pronounced over time. The system evolve further into a braided system with features resembling mid-channel bars with

channel-like features on either side. In this untreated experiment, initial widening occurs at the downstream end, nonetheless further widening of the system was initiated by slight continuous alterations at the upstream end. Synchronous with channel belt widening, a more distinct relief occurs within the channel belt, with higher elevated bars and narrower, deeper channels.

In Experiment 2 with sodium alginate added to the substrate, the behaviour is completely different (Figure 4.6, middle column). Here, the initial single channel remains a single channel and is static over time, indicating the co- or adhesive strength of the sodium alginate-sediment mixture.

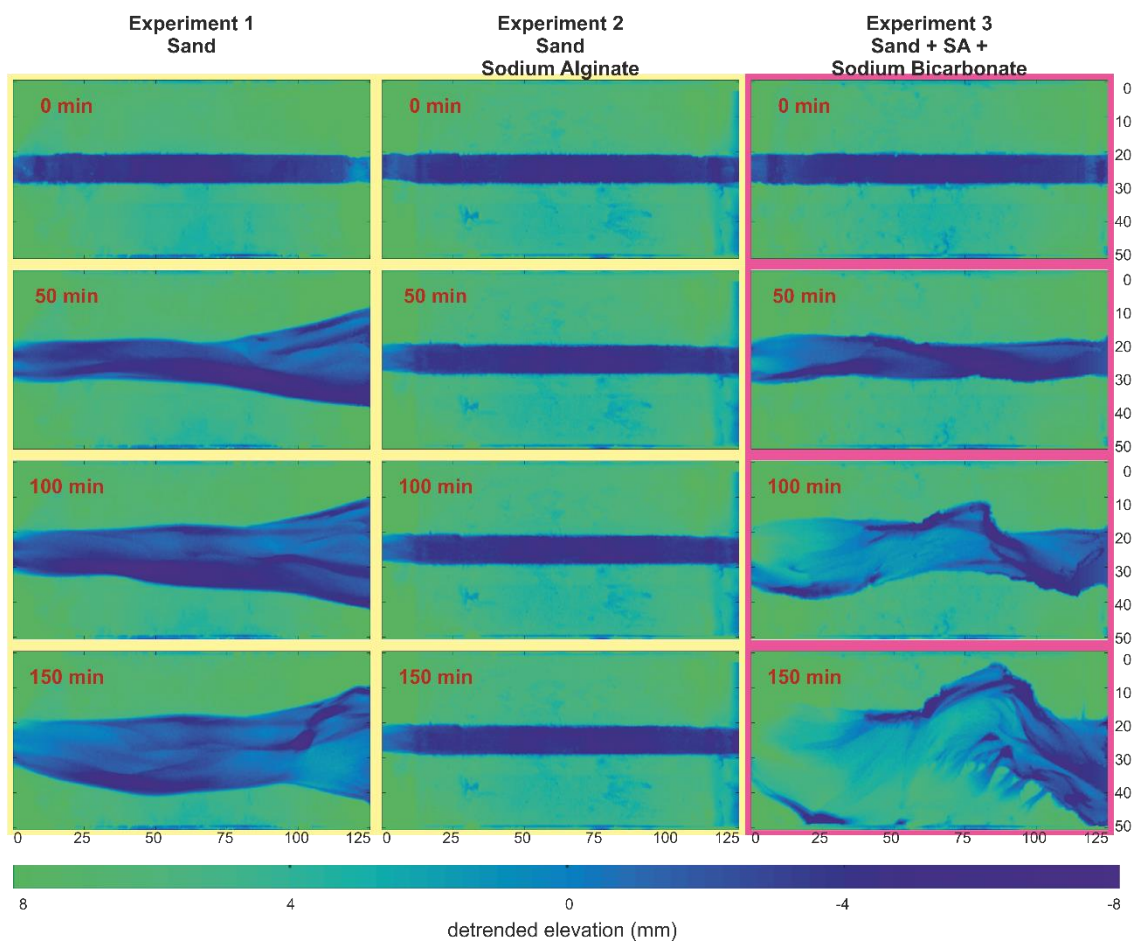


Figure 4.6: Planform evolution against time (top to bottom) of experiments 1, 2 and 3 described by detrended digital elevation models. Coloured boxes indicate tap water flow (yellow) or 10 g L⁻¹ sodium bicarbonate per litre tap water (magenta). Spatial units in centimetres, elevation in millimetres.

Experiment 3 (Figure 4.6, last column), with sodium bicarbonate added to the fluid flow and sodium alginate added to the sediment, shows significantly different behaviour compared to

Experiment 2. This demonstrates the impact of the altered fluid on the sodium alginate-sediment mixture. The single thread channel in Experiment 3 transforms into a system with three sequential alternate bars. As these bars build up over time, the channel erodes the banks to develop matching river bends. In contrast to the untreated experiment (first column) the bends are more angular, more pronounced relatively static (almost fixed) and only move downstream due to expansion of their radii. Visual observations during the experiments indicated that banks remain steep compared to the untreated experiment where banks are more likely to reshape towards the natural angle of repose. Finally, the fluvial system in this experiment need time to develop; change in the first period is limited, but thereafter the river expands relatively quickly in the lateral direction which eventually causes boundary issues as the channel belt expands to the side of the experimental basin about 20 minutes before the end of the experiment.

4.3.1.2. Sediment transport and channel characteristics

Observations indicate internal variations in sediment output over time in the periods of the experiments, in particular when bars migrate into the far downstream section or when channels avulse. However, these fluctuations will be smoothed over the 50 minute experimental period over which sediment transport rates are calculated.

Sediment output highlights the differences between the three experiments and matches the visual differences in channel behaviour (Figure 4.7 A). The untreated experiment starts with a very high sediment output rate which drops over time towards equilibrium (sediment in = sediment out) (Figure 4.7 A). This near equilibrium state is also observed throughout Experiment 2 (Figure 4.7 A). Experiment 3 does not reach equilibrium; here the first time period has slightly lower (3 vs 4) net output rates than the untreated experiment, but the sediment output rates remains about double the sediment input rate in later periods (Figure 4.7 A).

These variations in sediment output rates are projected into changes in channel belt area (Figure 4.7 B) and channel belt volume (Figure 4.7 C) over time as well. Again, experiment 2 indicates

little change in channel belt area (Figure 4.7 B) or volume (Figure 4.7 C) over all time steps. For the other experiments, channel belt area (Figure 4.7 B) behaves similarly to sediment output. For the bare experiments, channel belt area almost doubles over the first period of 50 minutes, before dropping down to values of 30 to 40% change in the latter periods (Figure 4.7 B). Conversely, the third experiment exhibits the opposite behaviour; a change of 30% in the first period is followed by a change of 70% in the next two periods (Figure 4.7 B).

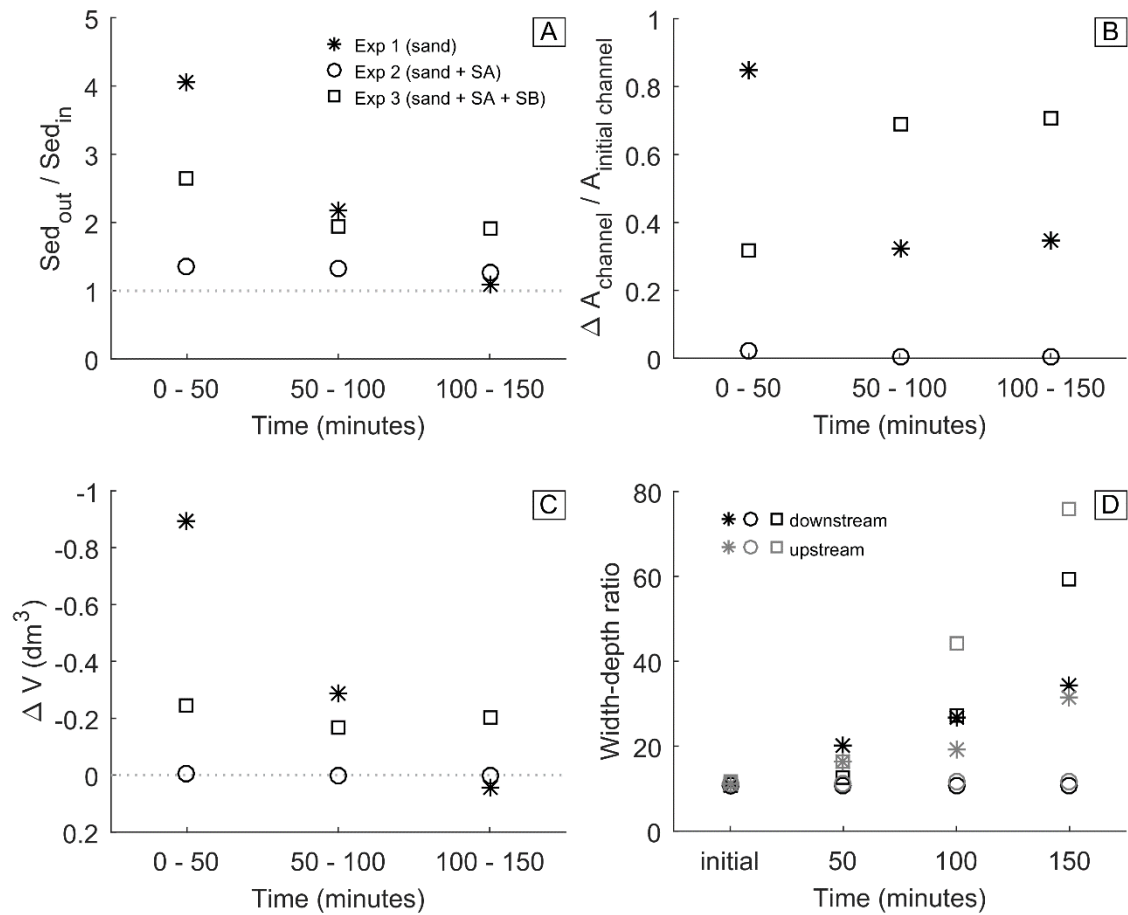


Figure 4.7: Subplot of different variables against time describing experiments 1, 2 and 3. Symbols and legends match all individual figures. A) Relative sediment output (Sed_{out}/Sed_{in}) over three consecutive periods. Dotted line ($y=1$) indicates equilibrium, observations above indicate deposition of sediment. B) Relative expansion of the planform channel belt area per period. C) Volumetric change per period; Negative values indicate net erosion, positive values indicate net deposition. D) Width to depth ratio at the end of each period, distinction between an upstream area (0.25 m – 0.65 m) and downstream area (0.65 m – 1.05 m).

Figure 4.7 C indicates that changes in sediment volume drop gradually towards no net change in subsequent time periods for the bare experiment. As channel belt area still increases (Figure 4.7 B), this suggests synchronous shallowing of the channel belt in the last period. A similar effect is observed in experiment 3, where changes in volume remain fairly constant over time (150 to 250 cm³ per period) (Figure 4.7 C). As such, the increase in channel belt area over the last two periods (Figure 4.7 B) coincides with a shallowing of the effective channel belt area.

The combined effect of volumetric changes in sediment storage, changes in channel belt area and changes in sediment output can be summarised by variations in the width to depth ratio (Kleinhans & van den Berg, 2011). For these experiments, the width to depth ratio (Figure 4.7 D) is determined for an upstream part (0.25 m – 0.65 m) and a downstream part (0.65 m – 1.05 m) using the average depth of the channel belt area using an arbitrary water level of 0.005 m. All experiments start out with an initial width to depth ratio of 10 to 11, reflecting the narrow, carved, channel in the initial bed but further changes in the width to depth ratio during the different experiments highlight the channel evolution during each experiment. Figure 4.7 D shows a fixed width to depth ratio for experiment 2 over time, which demonstrates that the channel does not change, in contrast to the other two experiments that have an increasing width to depth ratio over time. For experiment 1, this increase is linear over time and shows a width to depth ratio of 35 at the downstream part as well as an upstream width to depth ratio that is only slightly lower. This reflects the widening of the channel belt is initiated by downstream change due to lateral channel migration. For experiment 3, the increase is exponential, with width to depth ratios double those of experiment 1 by the end of the experiment. Further, in contrast to experiment 1, width to depth ratios in experiment 3 are consistently larger in the upstream area, reflecting the aggressive infilling in the upstream section of the experiment (Figure 4.7 D).

4.3.2. Planform river, alternating conditions

The previous section highlights the differences in planform evolution of the river systems under constant but different substrate and water chemistry (untreated, sodium alginate and sodium alginate in a fluid of dissolved sodium bicarbonate). This section explores changes to planform evolution when substrate and water chemistry is altered during individual experiments.

4.3.2.1. *Planform behaviour*

Figure 4.8 gives an overview of the planform behaviour of experiments 4 and 5. Both experiments are subject to two periods of 50 minutes of tap water flow and two periods of 50 minutes of sodium bicarbonate solution flow, however the order is reversed between experiment 4 and experiment 5 (Table 4.1). The channel adjustment behaviour in the first 50 minutes of experiment 4 (Figure 4.8, left column) is identical to experiment 2. However, in the next 50-minute period, when sodium bicarbonate solution is added, the single thread channel starts to widen. This widening is not as large as in experiments 1 and 3 but is a significant change compared to the first period or experiment 2. The change in planform behaviour occurs mostly in the upstream section, with the development of a single alternate bar on the true right and erosion of the bank on the true left. Downstream, the impact of adding the sodium bicarbonate is less noticeable. In the third period, the channel is immobile and no widening or changes in morphological features occur. In the last 50-minute period, the channel widens by the further expansion of the alternating bar and bend. In contrast to the previous periods, change also occurs further downstream where a secondary bar and bend start to form.

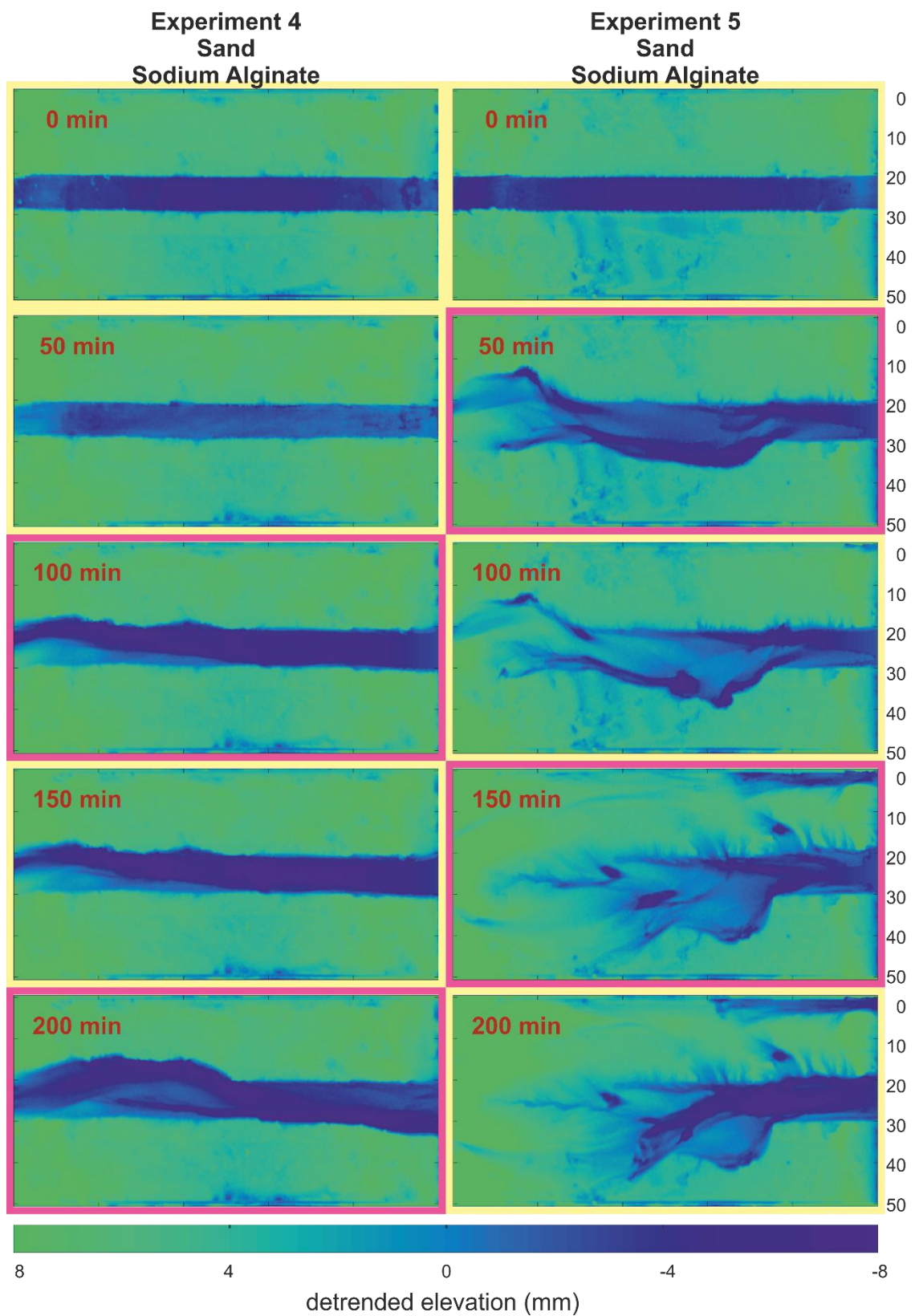


Figure 4.8: Planform evolution over time (top to bottom) of experiments 4 and 5 described by detrended digital elevation models. Both experiments have an alternating fluid content of tap water (yellow box) and 10 g L^{-1} sodium bicarbonate per litre tap water (magenta box). Spatial units in centimetres, elevation in millimetres.

The second experiment (Figure 4.8, right column) behaves differently. In this experiment, after 50 minutes of flow of a sodium bicarbonate solution, the single thread channel is transformed into a braided-like system, with multiple channels and mid-channel bars. The rate at which this change occurs is twice as fast as in experiment 3 (Figure 4.6) for the same conditions. Changes over the following period with tap water flow are small with bars increasing in elevation and bank edges retreating locally. In the last 50-minute period, with regular tap water, changes occur only within the channel belt as the channel deepens/forms in the central part of the experiment.

4.3.2.2. *Quantitative analysis*

Sediment output rates for the alternating experiments show three different behaviours (Figure 4.9 A). First, there is a greater total output of sediment from experiment 4. Second, when dissolved sodium bicarbonate is used, there is normally a higher sediment output than when tap water is used (except for the last period in experiment 5). Third, sediment output rates for periods with sodium bicarbonate solution are in the same range (2 to 3 times sediment input rates) as the identical conditions in experiment 2 (Figure 4.7 A).

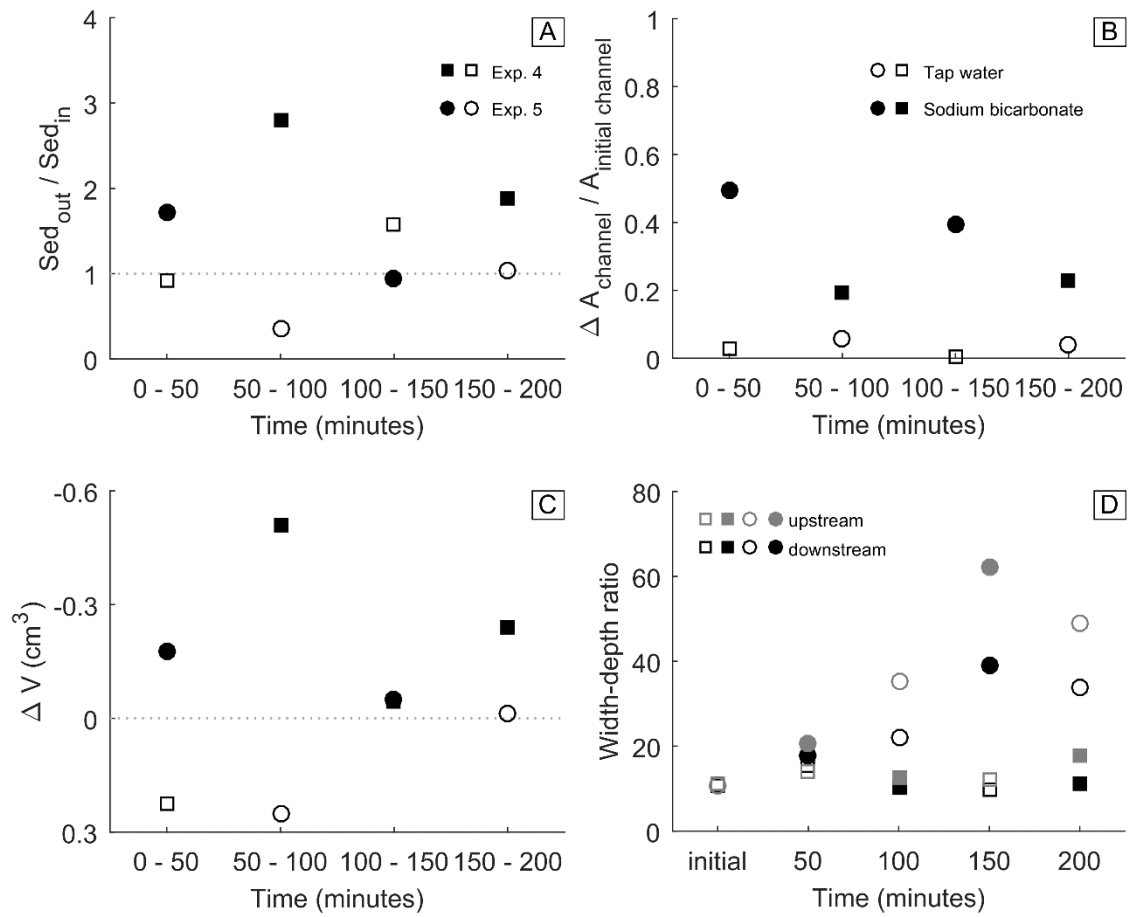


Figure 4.9: Subplot of different variables against time describing experiments 4 and 5. Symbols and legends match all individual figures. A) Relative sediment output (Sed_{out}/Sed_{in}) over three consecutive periods. Dotted line ($y=1$) indicates equilibrium, observations above indicate deposition of sediment. B) Relative expansion of the planform channel belt area per period. C) Volumetric change per period; Negative values indicate net erosion, positive values indicate net deposition. D) Width to depth ratio at the end of each period, distinction between an upstream area (25 cm - 65 cm) and downstream area (65 cm - 105 cm).

Looking at the channel belt area (Figure 4.9 B), differences between periods of sodium bicarbonate solution and periods of tap water are distinct from each other. When the inflow is tap water, the channel belt area shows little change (< 6%) whilst, in contrast, there is substantial change in channel belt area during periods of dissolved sodium bicarbonate inflow (20 – 50%). Furthermore, changes in channel belt area are higher in experiment 5, an experiment that starts with a period of dissolved sodium bicarbonate.

As such, the changes in channel belt area do not explain the reduced sediment output during the later periods of experiments 4 and 5. Instead, these effects relate to volumetric changes in both experiments (Figure 4.9 C). These volumetric changes show three behaviours: 1. periods with dissolved sodium bicarbonate always decrease the volume of sediment (net erosion) whilst periods with tap water either increase the volume of sediment (deposition) or decrease the volume of sediment by only a fraction; 2. in the second part of both experiments 4 and 5 volumetric changes are always smaller, both for the periods with dissolved sodium bicarbonate and for periods with tap water; and 3. volumetric changes suggest that experiment 4 is predominantly a degrading system while experiment 5 is predominantly an aggrading system.

The above characteristics match with the width: depth ratio of the channel belt for both experiments (Figure 4.9 D). In experiment 4 the width to depth ratio remains near-constant with values between 10 and 20 and an upstream area slightly higher than the downstream area. In contrast, experiment 5 behaves more like the constant experiment 3 (Figure 4.7 D) with width to depth ratios that increase continuously over the first three periods and that are higher in the upstream area. However, in contrast to experiment 3, the width to depth ratios drop slightly during the last period (Figure 4.7 D).

4.3.3. Planform river, surface adjustments

The examples above demonstrate the effectiveness of using a sodium alginate sediment mixture in combination with sodium bicarbonate solution. However, to investigate whether sodium alginate can be used to simulate vegetation growth during an experiment, experimental runs are conducted using a sodium alginate spray which can be applied on the surface of the sediment during an experiment as a surrogate for vegetation growth. For these tests, experiments 6 and 7 use sodium alginate spray to simulate the growth of surrogate vegetation whilst experiment 8 uses grown alfalfa as a direct comparison.

4.3.3.1. *Planform behaviour*

The first two periods of experiments 6, 7 and 8 are all similar untreated conditions, identical to the untreated conditions in experiment 1. As such, planform evolution over these first two periods is expected to be similar. Figure 4.10 (row 1, 3 and 5) highlights these similarities. In all three experiments, the single thread channel evolves via several alternating bars into a small braided system. Like experiment 1, the content of the channel area is marked by smooth curved banks. However, in contrast to experiment 1, where lateral expansion occurs dominantly at the downstream part for the first two periods, experiments 6, 7 and 8 all develop a bend just before the halfway length of the experiment. Nonetheless, these three experiments have bar features of similar length, shape and spatial distribution, enabling a comparison between the next period(s) of each experiment.

The first 50-minute period after the application of the sodium alginate spray, under tap water conditions, shows limited change. In both experiment 6 (Figure 4.10, second row) and experiment 7 (Figure 4.10, fourth row) change occurs mainly within the channel belt, either by deepening of channels (experiment 7) or by deposition on bars (experiment 6). Over this period both channel belts expand slightly outward, but at a rate far lower than previous periods (and experiments), thereby steadily transforming banks into a more angular planform shape.

Over the last 50-minute period of experiments 6 and 7, under a sodium bicarbonate solution, the channel belt expands again. However, because in both experiments the channel belt reaches the lateral boundary of the experiment, the full extent of this evolution is not captured. Nonetheless, the channelization that occurred in the previous 50-minute period is partly reversed by formation of new bars and smaller channels.

The stabilization in the third period (100-150 minutes) of experiments 6 and 7 with sodium alginate spray is very similar to the stabilization by alfalfa vegetation (experiment 8, Figure 4.10, bottom row). In this experiment, initial changes occur in the channel belt as well. In the downstream part of the experiment a more pronounced channelization occurs. In contrast, in

the upstream part, previous channel forms (Figure 4.10, fifth row) infill. This infilling eventually leads to bank overtopping and limited sheet flow over the areas outside the channel belt. However, after two periods of flow, the majority of the channel belt vegetation survives because only a small fraction of the banks erode as channels cut laterally into bars.

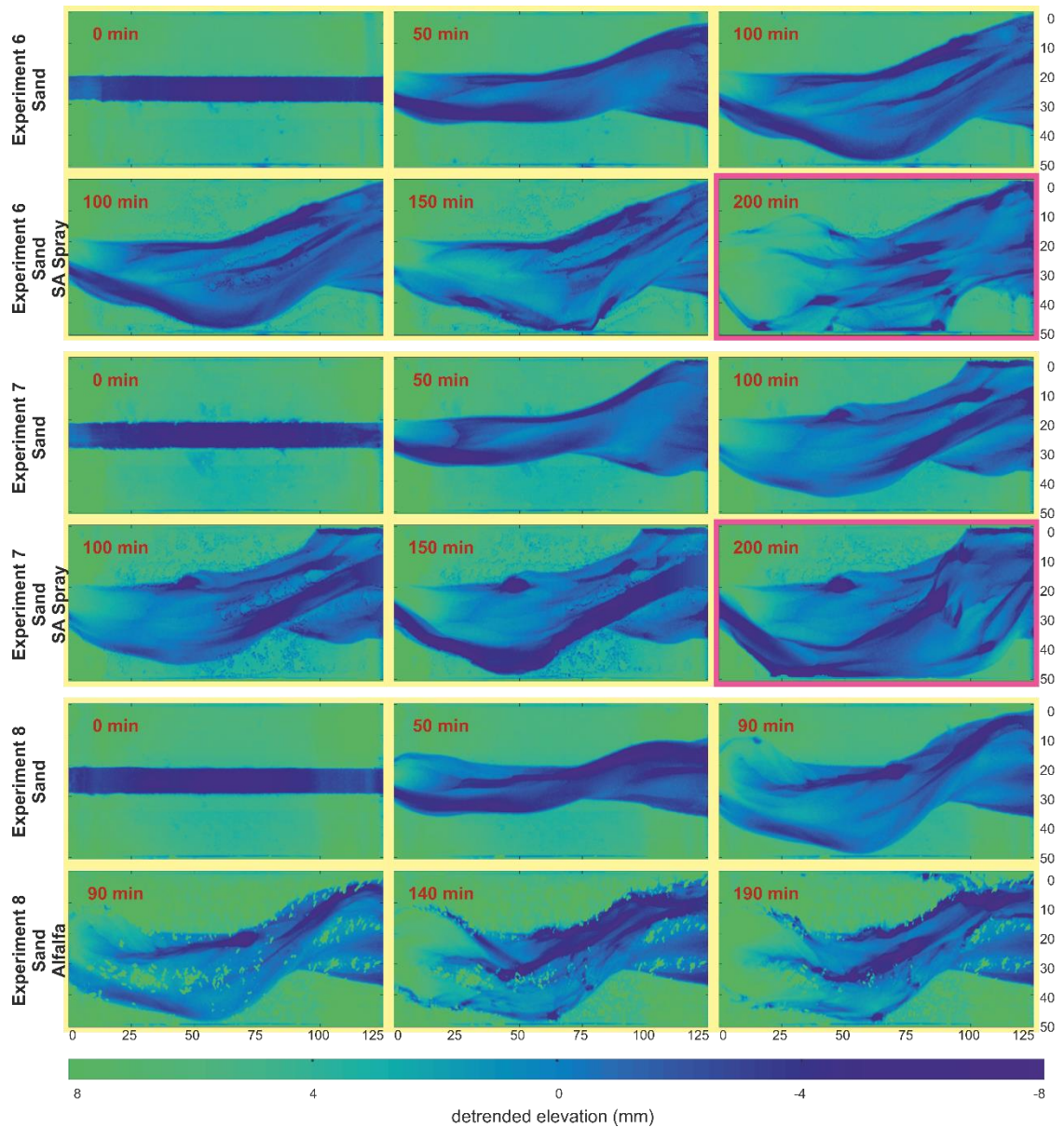


Figure 4.10: Planform evolution over time (left to right) of experiments 6, 7 and 8 described by detrended digital elevation models. Each experiment is captured in two rows, the top row shows the evolution under bare conditions, and the bottom row of each experiment show the evolution when a cohesive agent is added (sodium alginate spray for experiments 6 and 7 or 10-day old alfalfa vegetation for experiment 8). Coloured boxes indicate tap water flow (yellow) or 10 g L^{-1} sodium bicarbonate per litre tap water (magenta). Spatial units in centimetres, elevation in millimetres.

4.3.3.2. Quantitative analysis

Sediment output rates for the first two periods in experiments 6, 7 and 8 all match the behaviour of experiment 1 (Figure 4.11 A) with a steady decrease in sediment output over time. However, over the last two 50-minute periods, the experiments behave differently.

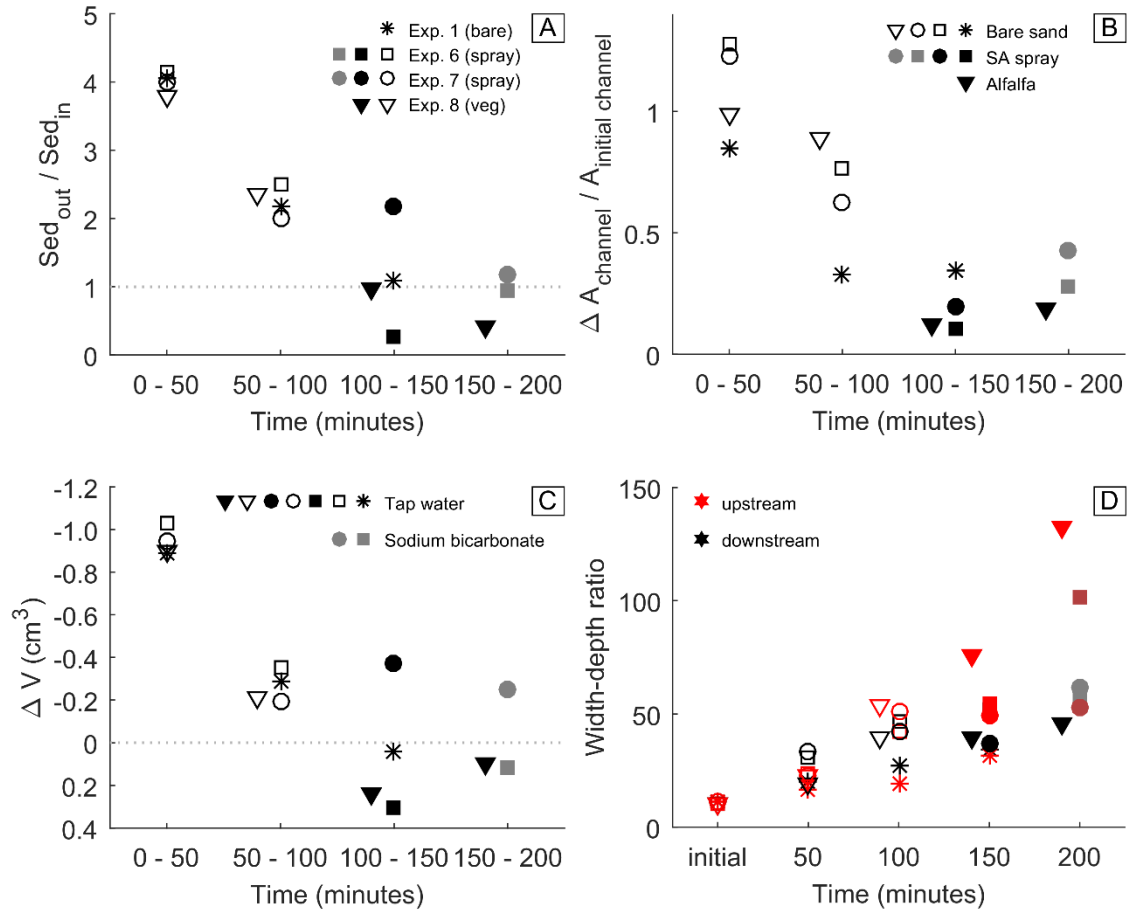


Figure 4.11: Subplot of different variables describing experiments 1, 6, 7 and 8 over time. Symbols and legends match all individual figures. A) Relative sediment output (Sed_{out}/Sed_{in}) over three consecutive periods. Dotted line ($y=1$) indicates equilibrium, observations above indicate deposition of sediment. B) Relative expansion of the planform channel belt area per period. C) Volumetric change per period; Negative values indicate net erosion, positive values indicate net deposition. D) Width to depth ratio at the end of each period, distinction between an upstream area (25 cm - 65 cm) and downstream area (65 cm - 105 cm).

In the third 50-minute period, sediment output in the experiment with vegetation (experiment 8) reduces to reach quasi-equilibrium, where sediment output approximates sediment input, similar to experiment 1 (Figure 4.11 A). In contrast, sediment output in the experiment 6, with

sodium alginate spray, reduces to a fraction of the input rate, indicating an aggrading system. Conversely, sediment output in experiment 7, with sodium alginate spray does not decline and is more than double the input rate, indicating a degrading system.

In the last 50-minute period of the experiment, sediment output for experiment 8, with alfalfa vegetation, declines further, switching from quasi-equilibrium to aggrading conditions. Experiments 6 and 7, with added dissolved sodium bicarbonate in the flow over this last period, show sediment output rates match sediment input rates.

In contrast to sediment output rates, which match experiment 1 for the first two periods, the change in channel belt area for experiments 6, 7 and 8 is higher (Figure 4.11 B). In the third period, with more cohesive conditions, changes in channel belt area are at least 5 times smaller than previous periods and at least 2 times smaller than the reference experiment, experiment 1. In the final period, after the addition of dissolved sodium bicarbonate, the change in channel area is again larger for the experiments with sodium alginate, thereby on a similar level as the bare experiment (experiment 1).

Like the sediment output rates, volumetric changes exhibit variations between the experiments (Figure 4.11 C). In the first two periods, volumetric changes of experiments 6, 7 and 8 align with the volumetric changes in experiment 1. However, in the third period, a similar split, as observed in sediment output rates, is observed in the volumetric change of experiment 6 (net deposition) and experiment 7 (net erosion). This variability is larger in the third period, with tap water, but, in contrast to the relative sediment output (Figure 4.11 A), this is still true for the final period with dissolved sodium bicarbonate. As such, of the sprayed experiments, only experiment 6 matches the volumetric changes of the experiment with alfalfa, where net deposition is observed over the last two periods of the experiment.

The origin of these variations is likely related to the width to depth ratio of these experiments (Figure 4.11 D). Over the first two periods, a gradual increase in width to depth ratio is observed

in all experiments. The cohesive settings in the second part of the experiments show two distinct observations.

First, experiment 8 (with vegetation) has a distinct behaviour between up and downstream width-depth ratios. Downstream width to depth ratios remain constant over both periods. In contrast, upstream width to depth ratios increase to 3 times the downstream width to depth ratio. This effect can be associated with upstream infilling and overbank flow.

Second, the introduction of sodium alginate spray freezes width-depth ratios for the period with tap water flow, effectively stabilizing the system. Over the last period, with added dissolved sodium bicarbonate, width to depth ratios increase slightly until the channel area is constrained due the lateral capture of the experimental edge.

4.3.4. Conductivity and other environmental parameters

The complete set of experiments show a relation between erosion rate and/or morphological change and the use of sodium alginate and dissolved sodium bicarbonate. The bank erosion experiments (see chapter 3.3) highlight different outcomes by using different concentrations of both sodium alginate and dissolved sodium bicarbonate. Small preliminary experiments (see section 3.2.3.4) indicated that reduced local concentrations of sodium bicarbonate could limit its influence in reducing cohesion. As such, it is important to monitor the effective activity of this chemical agent.

Conductivity is found to be related to the activity of the sodium bicarbonate, with a decrease in conductivity over time in periods with a sodium bicarbonate solution and an increase in conductivity over time in a period with just tap water (Figure 4.12), which could underline the importance of an excess buffer of sodium bicarbonate. Over the experiments, conductivity of the sodium bicarbonate solution decreased over time, from 16 mS at the beginning of experiment 3 to 15 mS after 100 minutes (Figure 4.12 A). Simultaneously, in experiment 2 with tap water and sodium alginate, conductivity increased from 0.72 mS to 1.06 mS over 150 minutes (Figure 4.12 A). Although these variations are small, in the alternating experiments

(experiments 4 and 5) the changes in conductivity are more extreme (Figure 4.12 B). Over the first period, conductivity changes are in line with the constant experiments. However, thereafter the increase in conductivity of about 1 mS per 50 minutes in tap water and the decrease in conductivity of about 1 mS per 50 minutes in sodium bicarbonate solution is significant. Not only do these changes indicate a gradual mixing between the end tanks, it also could relate to a longer storage time for sodium bicarbonate in the system.

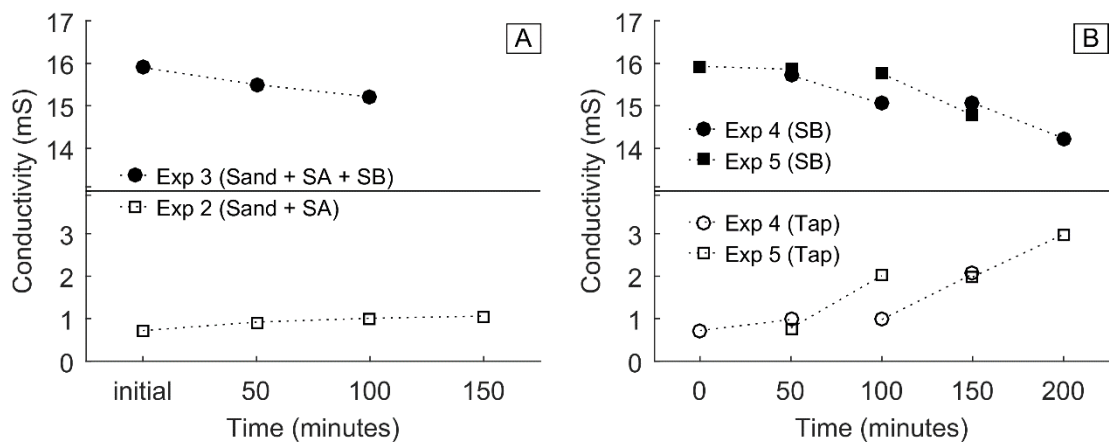


Figure 4.12: Conductivity (mS) over time for A) experiments 2 and 3 and B) experiments 4 and 5. Open markers indicate tap water measurements, closed marker indicate sodium bicarbonate solution measurements.

4.4. Discussion

4.4.1. Sodium bicarbonate

The experiments show that all periods with sodium alginate completely stabilize the system under tap water conditions and maintain a single channel with solely sediment throughput, replicating the behaviour of the sediment blocks with 0.500 g kg⁻¹ sodium alginate in bank erosion experiments (see section 3.3.6). Similarly, in the alternating planform experiments 4 and 5 morphological change in periods with tap water is limited to reworking (or deposition) of loose sediment within the channel belt area. In contrast the addition of sodium bicarbonate to the tap water causes an abrupt shift. Once sodium alginate enhanced sediment comes in contact with the dissolved sodium bicarbonate the flow starts to erode the sediment once again, like the sodium alginate wasn't mixed in with the sediment. Furthermore, the experiments, like the

experiments in chapter 3, show no signs of memory; channel expansion follow similar patterns as shown by the outcomes of the sodium alginate bank erosion experiments of chapter 3.

4.4.1.1. *Chemistry*

Apart from the physical results of the combination of these two chemical agents, it is important to understand what chemical reactions or basic processes play a part in the change of cohesion. First, the sodium alginate, $C_6H_9NaO_7$, chemical agent forms cohesive (or adhesive) bonds around and between the individual grains of the sediment thereby increasing the cohesion of the sediment. Due to the limited use of sodium alginate, there is no exploration of these specific processes, however it is assumed the processes are similar to co- and adhesive processes between xanthan gum and grains of sediment as explained in Parsons et al. (2016).

The other chemical agent, sodium bicarbonate ($NaHCO_3$), is dissolved in tap water thereby breaking up the molecules into Na^+ and HCO_3^- ions. Of these two, Na^+ is a salt and as such directly linked to the conductivity measured in the experiments. As conductivity values goes down in fluids with sodium bicarbonate over the course of each experiment (Figure 4.12), it is expected that part of the Na^+ is either fixated or removed from the system. In the alternating experiments, as conductivity values in tap water increase by the same order of magnitude as the conductivity values decrease in the dissolved sodium bicarbonate water it is assumed that the Na^+ remains in the system. The fact that conductivity does not decrease or increase as much in non-alternating experiments suggests there is an enhancing effect by the alternation. However, due to limited repetitions, research and skill on this topic, it can only be assumed that Na^+ ions that precipitated in the fluid under high conductivity conditions dissolve again in fluids with low conductivity (tap water), which suggests the sodium alginate – sodium bicarbonate-induced reaction does not dissolve the alginate. Nonetheless, in order to fully understand the dynamics, it is strongly advised that the behaviour of these chemical components should be explored in further research.

4.4.2. Application of sodium alginate

As discussed in chapter 3, the application of sodium alginate and the practicality of the method for doing so is very specific and therefore this research aims for a robust and repeatable method for doing these types of experiments. The first step is made in the preparation of the experiments, here exists a distinction between dry mixing (similar to chapter 3) and wet mixing (Fernandez et al., 2019). This research has explored both methods, both with their own pros and cons.

4.4.2.1. *Dry mixing*

The dry method is the most straightforward way of mixing sodium alginate into the sediment. Chapter 3 (see section 3.2) uses this method for three chemical agents (e.g. xanthan gum, carrageenan and sodium alginate) in static bank erosion experiments. This research uses this method on a larger scale. In comparison, the application is easier at a smaller scale (1 kg of sediment) owing to shorter mixing times. For the experiments at larger scale (using 20 kg of sediment) the method is still applicable. Nonetheless, for larger quantities (e.g. bed sizes used in experiments in chapter 5) it is strongly advised to speed up the mixing process (e.g. by acquiring heavier mixing equipment or additional manpower) to promote identical conditions across an entire bed. This enhancement of application speed is important as sediment-chemical agent mixtures can dry out over time and thereby have the potential to change their cohesive characteristics (as emphasised in chapter 3).

The exact behaviour of this characteristics is not determined within this research, however the experiment is set up in such way potential shortcomings can develop. Between the two alternating experiments (experiments 4 and 5), experiment 4 (start with tap water) expands laterally at a slower rate in the second period than experiment 5 (start with sodium bicarbonated flow) in the first period. One explanation for this can be related to the time the sodium alginate has been exposed to dry air, which is longer in experiment 4 which has an additional 20-25 minutes of drained conditions between the first two periods in addition to an initial 20 minutes

before the experiment. This research is not set-up to further investigate this behaviour, nor is a similar behaviour recorded by other research. As such the importance of this temporal delay is advised to be investigated in further research to distinct this temporal cohesive effect from natural geomorphic adjustment processes.

4.4.2.2. *Wet mixing*

The wet mixing method is used in previous research (Fernandez et al., 2019; van de Lageweg et al., 2018) and has potential to be applied more locally over space and time, thus resulting in different upscaling issues differentiated over mixing and application.

Mixing sodium alginate in water is tricky, as it starts to form a cohesive gel on reaction with water that results in gel flocs floating on the water surface because the flocs are less dense than water. To prevent settling, continuous stirring is recommended, preferably with stirring devices with smooth surfaces to prevent sticking. This research used manual rods, but mechanical stirring equipment is feasible if care is taken to prevent blades/equipment from clogging up. This also reduces control over the final mixture strength.

The second issue with these experiments is application. Polysaccharides like sodium alginate are relatively easy to apply in a gel structure, but under these conditions the generated cohesion is too strong and as such only representative of biofilms or vegetation that exhibits dominant horizontal root growth. In order to dilute these gels, the sodium alginate mixture must be applied with use of a spray can. A regular plant sprayer, used in these experiments, can clog up during application, leaving part of the mixture unused.

The use of this spray comes with benefits as well. For example, the spray can be applied to specific locations (e.g. bars which are prone to settlement of vegetation). Additionally, application of the spray can be done at any moment, granting the potential to mimic the effect of growing or pioneering vegetation. Furthermore, spraying allows the sodium alginate to remain wet over a longer period and as such potentially requires a longer time to enhance additionally (unwanted) cohesive strength. This moisturizing behaviour comes with a price

though because moisturized surfaces have naturally a high reflectiveness which interfere with data collection equipment like terrestrial laser scanners and thus require care when collecting data at those areas.

4.4.2.3. *Conductivity relationship with sodium bicarbonate*

Conductivity is a measure to describe to what extent a medium is able to conduct electricity. In fluids, this often relates to the number of dissolved ions in solution which is dependent on whether the dissolvent is strong or weak (i.e. how likely disassociation for a dissolvent is). This relation itself is a root square relation; initially, as concentration increases, conductivity also increases because distances between single ions are reduced but, as concentration increases further, individual ions may interact and disturb conduction thereby reducing the rate of increase of conductivity with concentration. Within this research, the experiments are all located at the low end of conductivity and solubility of sodium bicarbonate (Thieme, 2000). As such, conductivity is expected to be controlled by the concentration of dissolved sodium bicarbonate. Hence, a reduction in conductivity indicates a reduction in conductive ions thus indicating reaction(s) with the sodium alginate in the experimental samples. Thus, over all experiments, conductivity values decrease or increase over time. However, the rate of decrease/increase was stronger in the alternating experiments (experiment 4 and 5) and in periods following a single swap in fluid (e.g. end of experiment 6 and 7) which suggests that sodium bicarbonate (either dissolved or in other form) is at times delayed within the system and thus carries over to the next period of the experiment.

4.4.3. *Experimental considerations*

One aim of this experiment is to create a basic and quick but robust and repeatable experiment to qualify the impact of a narrow range of cohesive surrogates and altering agents and show that results obtained in the small-scale bank erosion experiments (section 3.3) are applicable to larger spatial scales. As such, the dimensions of the experiment is chosen to effectively fit within an existing experimental set-up. As a result, and due the natural behaviours of rivers to expand

laterally, some of the experiments (experiments 3, 5, 6, 7 and 8) have their lateral expansion limited by the boundary walls of the experimental bed. Once flow touches a wall, lateral migration of the channel is halted at that location and flow then favours downstream erosion above lateral erosion. Furthermore, due a variation in roughness between the wall and the sediment, flow behaviour potentially alters. As such, experiments that reached this wall were stopped at the end of the ongoing 50-minute period.

4.4.3.1. Inlet conditions

In experimental systems, fluvial patterns are often influenced by inflow conditions (e.g. method of mixing of flow and sediment, sediment input rate), channel width to depth ratios as well as water turbulence effects. Naturally, for each combination of these individual conditions a specific fluvial system is favoured and as such, experimental systems tend to adapt and rework towards a system favoured by those inflow conditions, similar to how natural rivers adapt to upstream changes.

One of the issues in the braided experiments (chapter 5), is the single source sediment input which eventually leads to a split channel. To prevent or delay this impact, sediment was added through simplified quincunx to provide a curtain of sediment. However, as the quincunx mechanism is not idealized for specific flow conditions, its impact only delays and alters the characteristics. The curtain of sediment provides an initial symmetric distribution, which prevents the formation of a central bar, however as channels naturally start to migrate laterally, flow and thus sediment transport capacities shift within the channel, which eventually (in half the experiments) leads to excess deposition at either the true left or true right of the channel, a self-enhancing effect that closely relates to avulsing in natural systems (Kleinhans et al., 2013). Whereas the effect occurs on either side of the channel, the stronger scenarios all have a channel shift towards the true right. Although this could relate to asymmetry in the quincunx, it is more likely related to the inflow of the water, which originates from the true left.

In future, to further diminish the effect of this asymmetry, a combination of two solutions is strongly suggested: 1. mixing of the sediment and water more thoroughly, either by a pumping mechanism that mixes the sediment and fluid or by having longer inlet; and 2. introducing a mechanism that allows the channel to migrate dynamically by simulating the downstream effects of migrating bends upstream. Both these methods have been applied successfully (van Dijk, van de Lageweg, et al., 2013) but are too complex for the scope of these experiments.

4.4.3.2. Channel patterns

In the experiments, some dominant channel patterns occur. For example, bends form and expand naturally over the course of each experiment except the most cohesive one (i.e. experiment 2). In experiments without added agents, three alternating, roughly evenly spaced, bends occur. Over time, these bends expand, both spanwise and streamwise, and eventually push the third bend downstream out of the experimental bed. For experiments with sodium alginate (and sodium bicarbonate), three bends initially occur as well. However, these bends are more stable and expand in the streamwise direction at a lower rate. As such, they remain within the experimental bed for most of the experimental periods.

4.4.3.3. Future possibilities

These experiments showed a selection of limitations and possibilities for future experimental work. For example, the effective use of sodium alginate as a cohesive agent was shown. Additionally, experiment 9 (Figure 4.13) shows that erosive features only occur downstream of the initial sodium alginate dosed section. However, because the initial sections dampen the lateral mobility of the system, the effectiveness of the lateral cohesive boundaries is not be confirmed. This additional experiment therefore shows that the use of sodium alginate, when applied selectively, grants several opportunities for future experimental work. First, by using a more cohesive fraction at the entrance of our experimental inlet it can fix the inlet to allow it to have a more uniform sediment distribution without an alteration in bed roughness. Second, when cohesive fraction is applied strategically at the sides of an experimental bed, it can provide

a more resistant (but similar roughness) boundary layer, preventing, or at least delaying, boundary effects at the side of an experimental bed. Third, the incorporation of strategic localized layers or bodies of sodium alginate mixture could mimic specific more resistant layers. Not only can this promote research on alluvial rivers, it also has the potential to benefit research on bedrock rivers or even geologic settings by using organized patches of sodium alginate as non-erosive layers.

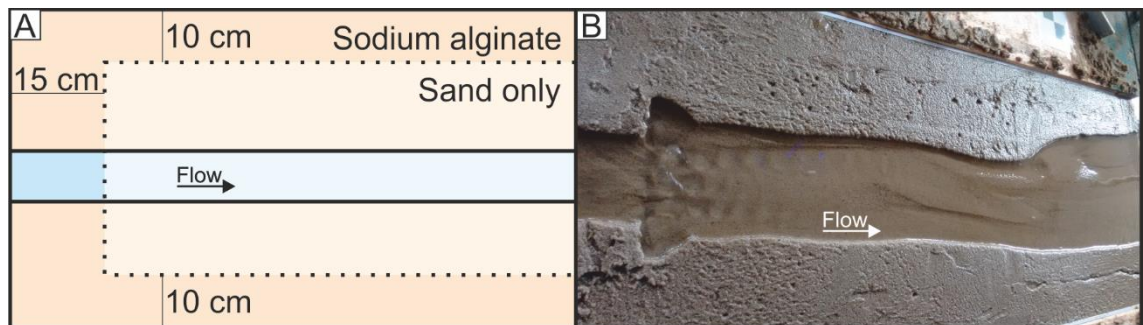


Figure 4.13: Experiment 9; A) Overview spatial distribution sodium alginate at start of the experiment. Blue indicates initial channel, darker shades indicate 0.5 g kg^{-1} sodium alginate – sediment mixture. B) Experiment during the third period (100 – 150 minutes).

Simultaneously, the use of sodium alginate can represent bank strength (or bed strength) with only a very limited direct effect on the sediment transport in the system since, in contrast to clay, it only affects sediment entrainment. Finally, there are no observations of reactivation of cohesion in deposited areas which suggesting sodium alginate is washed out upon entrainment of the sediment. As such sodium alginate is more effective in representing vegetation effects, which nominally are only in effect in situ in contrast to cohesive material like clay which is cohesive regardless of the location in the system.

4.5. Conclusion

This chapter gave an overview of the impact sodium alginate has on system mobility in conjunction with (or without) sodium bicarbonate. Therefore it shows that:

- The sodium alginate agent can be used effectively to enhance cohesion in small landscape fluvial models.

- Sodium bicarbonate can be used effectively to decrease the added cohesion of sodium alginate enriched sediments in small landscape fluvial models.
- The cohesive effect of sodium alginate on the sediment can sequentially be switched on and off by altering the concentration of sodium bicarbonate in the fluid.
- Spatial variation of sodium alginate can potentially open up new venues for physical modelling of fluvial systems.

5. Erosion rates in experiments with braided rivers to understand the impact of Alfalfa vegetation

5.1. Introduction

The previous chapters investigated a small increase in the size of the experiments; showing the impact of surrogate vegetation in physical modelling to enhance erosion resistance on individual banks (chapter 3) and small-scale rivers (chapter 4). Moreover, the bank erosion experiments showed the impact of vegetation age (and associated growth) on the resistance to erosion. In this chapter the focus of the research shifts towards an even larger temporal and spatial scale to understand the impact of vegetation growth on the dynamics of a developed fluvial system. Hence, it attempts to understand how to incorporate vegetation in physical modelling to mimic the impact of vegetation in natural systems subject to a change of external forcings. These changes in forcing mimic the changes in climatic conditions (see chapter 2) that are predicted to alter the forcing on fluvial systems, for example by changing frequency and magnitude of rainfall events (IPCC, 2014), which is the primary forcing in rainfall-dominated rivers and a key forcing in most snowmelt rivers.

For braided systems this change of forcing can have an even larger impact on the system dynamics. Their less cohesive banks and the instability of braided systems increases the potential for climatic forcing to alter the stability of these systems. To enhance complexity, some braided systems have vegetated banks with either trees, shrubs or grassy vegetation combined with dynamic braids that are covered with all growth stages of vegetation from pioneer to mature. This vegetation, as well as being the subject of the same climatic forcing, is also subject to irregular hydrographs or flood events associated with altered rainfall events that physically destroy or alter the growth of vegetation (Garssen et al., 2014, 2015; Gurnell, 2014).

In the channel belts of braided systems, vegetation predominantly grows on bars, that can be deformed or destroyed during a flood event, thereby damaging or removing local vegetation.

Naturally, in-between flood events, vegetation has time to recover and can proliferate. However, when the time between two flood events is reduced, vegetation may not potentially have sufficient time to recover from the previous event and may therefore be more susceptible to the next event (Garssen et al., 2015). Simultaneously, as most braided systems are subject to seasonality, flood events are often more abundant or intense in specific periods of a year (e.g. spring), and some vegetation adapt their life cycle (sprouting, growing and seeding) to the occurrence of these flood events. As such, a mismatch of life cycles and flood events can have an even greater impact on the vegetation than would be expected (Garssen et al., 2014, 2015). Nonetheless, this timing of vegetation growth is only part of the story. Next to vegetation being affected by flood events, the existence of vegetation itself in the channel belt also alters the flood events as well as the resulting morphology (Corenblit et al., 2007). The impact of vegetation is twofold: (i) it changes the flow resistance and surface roughness which alters the behaviour of the flow by increasing the flow resistance; and (ii) it increases sediment cohesion as roots tend to reinforce surrounding soil, increasing its resistance to erosion. Consequently, a change of frequency or duration of flood events may weaken this interaction and thus increase the susceptibility of sediments to erosion.

As this dynamic interaction between vegetation, morphology and climatic forcing is changing rapidly, field research can struggle to keep pace. In particular, when changes in climatic forcing outpace cycles of vegetation growth. One alternative to improve understanding of these processes, is the use of physical modelling (see chapter 2), which due to the use of scaling has more opportunities in both space and time. However, although physical research has used surrogates for vegetation in the past (Gran and Paola, 2001; Tal and Paola, 2010; Welber et al., 2013), the actual understanding of this surrogate vegetation is fairly limited and mainly curtailed as an approach to increase the resistance to erosion.

Chapter 3 explored the behaviour of one of these surrogates, alfalfa, in small-scale physical experiments with isolated bank erosion. The outcomes highlighted the phased impact

vegetation age (or maturity) had on the erosion rates of sediment blocks. Furthermore, it emphasised the importance of vegetation age in comparison to vegetation density but suggested that the interplay between the two should not be neglected.

This chapter aims to expand the findings of chapter 3 to understand the behaviour of this surrogate vegetation in physical modelling. Using both a larger experiment and a longer sequence of flood events, this chapter will investigate both the best practice for using surrogate vegetation in experiments and how vegetation can change the behaviour of a dynamic braided system. The focus of the experiments is to understand the cohesive effect of the vegetation, an effect that is predominantly associated with the root structure of surrogates (alfalfa sprouts). As such this research ignores (or neglects) the impact of flow resistance of above surface biomass of which the large majority exist above the flood level water surface (see Figure 5.1).



Figure 5.1: Alfalfa vegetation under high flow conditions in run 2, images highlight that most above surface biomass of alfalfa is located above the flood level.

5.2. Experimental methodology

5.2.1. Experimental set-up

The set of experiments is conducted at the Total Environment Simulator (TES), an experimental flume of the University of Hull. Due to the multifunctional behaviour of the TES, the experiments are set-up within the limits of the 12 m long × 6 m wide TES.

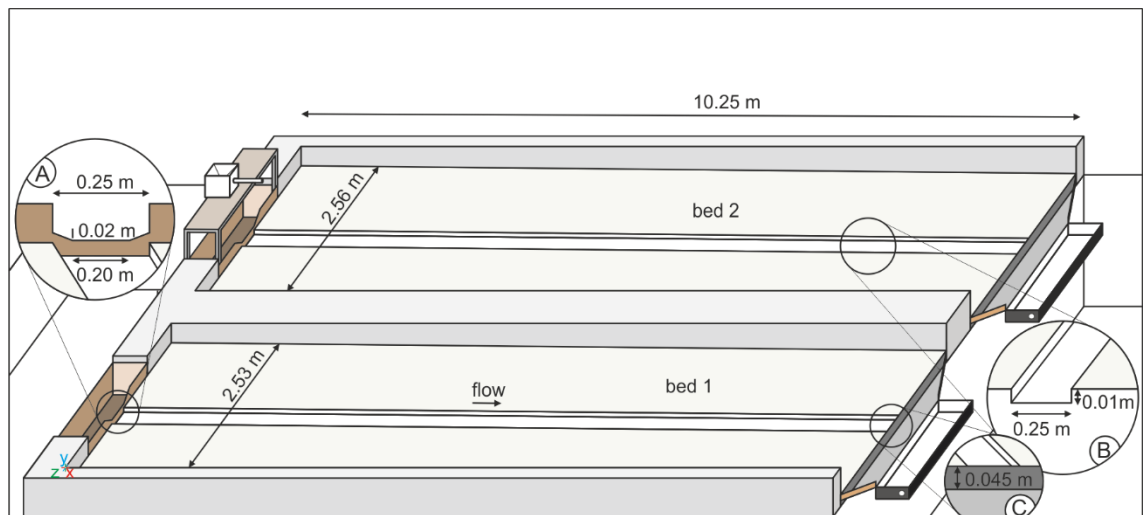


Figure 5.2: Overview of the experimental flume with two parallel beds, initial channels and the sediment and water in- and output locations with dimensions. Insets for inlet (A), initial channel (B) and outlet (C). Flow direction from left to right.

For the experiments, two parallel beds are used. Each channel is 10.25 metres long and of similar width (2.53 and 2.56 metres) (Figure 5.2). A wall of breeze-blocks, made watertight with a plastic membrane, separates two beds filled with sandy sediment ($D_{50} = 458 \mu\text{m}$). Both beds are levelled manually with a channel-wide scraper, producing a near identical experimental bed at the start of each experimental run. The scraper moves over guiderails attached on the breeze-blocks on either side of the bed under an angle that provides an initial bed slope of 0.015 m m^{-1} . This bed slope is chosen to be similar to other physical experiments on braided rivers (e.g. 0.016 m m^{-1} (Ashworth, 1992), 0.015 m m^{-1} (Tal & Paola, 2010), 0.013 m m^{-1} (Ashmore, 1982; Bertoldi et al., 2014), Table 5.1) as well as being similar to some natural braided rivers (e.g. South Ashburton (NZ), 0.013 m m^{-1} (J. H. van den Berg, 1995)). The scraper itself has an extension that creates an initial, straight channel (0.25 m wide, 0.01 m deep) along the centreline of each channel (Figure 5.2 inset B). The resulting sediment bed has a thickness of at 0.20m at the upstream end, decreasing to about 0.05 m at the downstream end.

Table 5.1: Key dimensional variables (length, width, sediment size, discharge and slope) for various experiments on braided rivers.

Authors	length	width	d ₅₀	Q	Slope
Bertoldi (2009)	25 m	2,90 m	0.63 mm	0.3-1.5 l/s	0.7 / 1.3 / 1.7 %
Egozi (2009)	18 (12 m)	3 m	1.2 mm	1.4 / 2.1 / 2.7 l/s	0.015
Gran (2001)	9 m	2 m	0.5 mm	3/5*10-4 m ³ /s	0.014
Tal (2010)	16 m	2 m	0.5 mm	low (0.4*10 ⁻³), high (2.0*10 ⁻³)	0.015
Bertoldi (2014)	10 m	1.7 m	0.73 mm	1.26 l/s	0.013
Leddy (1993)	5.5 m	3.5 m	0.28 mm		0.02
Perona (2014)	9 m	1.86 m	0.46 mm	3-5 l/s	0.01
Kasprak (2015)	20 m	3 m	1.2 mm	2 l/s	
Ashmore (1991)	10 m	2 m	1.16 mm	0.00120/0.00150/ 0.00300/0.00450 m ³ /s	0.010, 0.013, 0.015
Ashworth (1992)	11 m	1 m	2.23 mm	1.84-4.52 l/s	0.016
Ashworth (2007)	5.5 m	3.6 m		1.8 l/s	
Ashmore (1982)	9 m	1.3 m	1.2 mm	1 l/s	0.013
This research	10 m	2.5 m	0.46 mm	1.5 – 3 l/s	0.015

Tap water was used in the experiment, recirculated from the downstream water basin to the upstream water basin via a sump below the flume. From the upstream basin, two pumps provides water equally into two identical wooden flow control boxes (1.4 m long, 0.4 m wide and 0.28 m deep), their long side perpendicularly to the bed at the upstream end of each bed. The inlet into each box is underneath several layers of pebbles that, in combination with the volume of the box, dampens the turbulent flow of the pump and prevent dominant directional flow to occur. The boxes themselves have a trapezoidal outlet in the long side that is aligned with the centre of the channel (Figure 5.2 inset A, Figure 5.3 A). This outlet of the box is located less than 0.01 m above the channel bed. Each channel has a sediment feeder that provides an input of dry 458 µm sediment that drops into the flow about 0.01 to 0.05 metres downstream of the outflow of the box, roughly at the centre of the initial channel.



Figure 5.3: Selections of images of the experiments taken during events 11-14 of run 2. A) Close up of inlet and sediment feeder. B) Longitudinal view of bed 2, looking downstream from inlet. C) Downstream weir and water and sediment collection basin(s). D) Upstream view of both beds including cameras positioned 2.5 m above the bed on the ceiling, Faro scanning locations A and B are located directly above the central wall, 2.5 m above the bed and 4 m apart.

At the downstream end of the bed, a 0.045 m high barrier holds sediment in place and forces, in conjunction with the inflow weir, a constant average longitudinal channel bed slope of 0.015 m m^{-1} (Figure 5.2, inset C). Beyond the barrier, water and sediment drop onto a graded ramp and into a small downstream basin acting as sediment trap capturing transported bed load (Figure 5.3 C).

Small plastic deflector groynes, up to 0.1 m long, prevent flow from sticking to the outer channel walls. In run 2, the principle of, high density seeding of alfalfa at the outer edges of the experimental bed enhances this effect.

5.2.2. Experimental settings

This set of experiments consists of two experimental runs in both parallel beds. The first run (run 1) is a bare sediment run, the second run (run 2) includes alfalfa (*Medicago sativa*) as surrogate

vegetation. Both runs start with a spin-up period to develop an initial, dynamic braided system. In this spin-up period, both channels are subject to a selected flow of 1.5 L s^{-1} to resemble a scaled down river on the 2-metre-wide bed and an associated 5.8 g s^{-1} equilibrium sediment input using computations of Bertoldi et al. (2015) in previous experiments. This spin-up period is 45.5 hours in run 1 and 21 hours in run 2 as systems were found in equilibrium based on bed slope and sediment throughput.

After this spin-up period, the experiment starts as a sequence of alternating small and large flood events of 60 (+0-2) minutes (Figure 5.4). The large flood events are characterized by a flow of 3.0 L s^{-1} and a 15.5 g s^{-1} sediment input. Small flood events have a flow of 2.0 L s^{-1} and a sediment input of 8.0 g s^{-1} . At times, e.g. event 13 in run 2 at bed 1, regular small flood events are replaced by small flood events with a sediment deficit of over 80 percent to 1.5 g s^{-1} (Figure 5.4) in an attempt to mimic sediment starved conditions sometimes associated with longer periods of drought

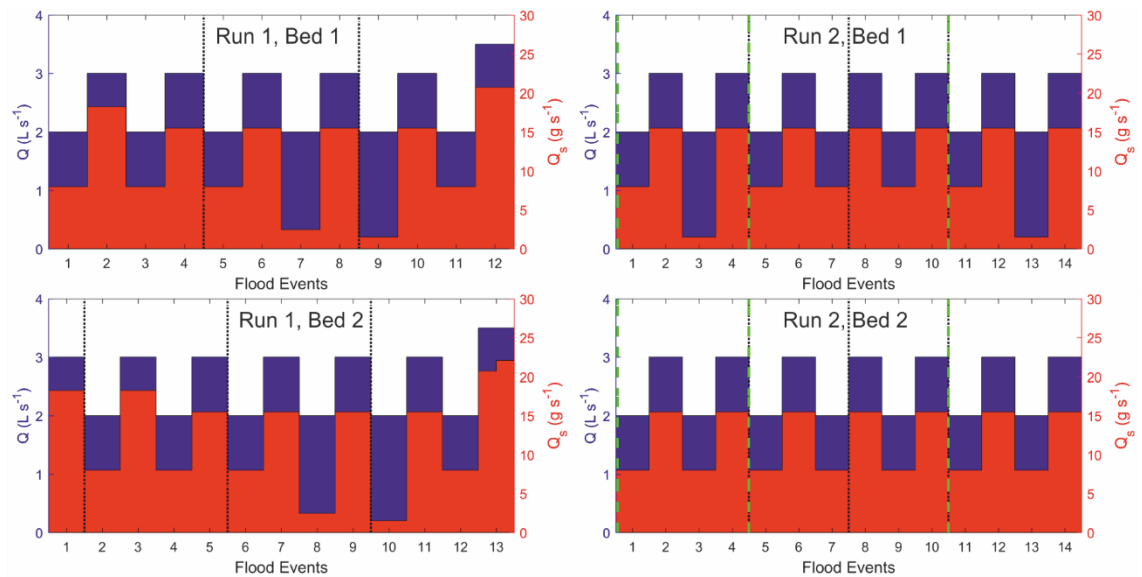


Figure 5.4: Schematic overview of experimental runs with alternation of 1-hour long flood events. Blue bars indicate discharge (L s^{-1}), red bars indicate sediment input (g s^{-1}). Each event is separated by a 40-60 minute data collection interval which is extended to at least 14 hours (14 hours for runs on subsequent days, or more for weekends or vegetation growing periods) at vertical dotted lines that mark a day break. Vegetation is seeded between events separated by dashed green lines.

A sequence of up to four flood events is executed on a single day, each separated by a 40-60 minute period without flow to allow data collection. Beyond these sequences, experimental runs are broken up by periods of 1 night up to several days without flow, neither of them with an impact on the progress of the experimental run. For run 2, with alfalfa vegetation, this approach changes. Here, to stimulate alfalfa growth and maintain a constant moisture gradient over the course of these breaks, a small porous hose, connected to a water tap, extends over the width of each bed at the upstream side of the experiment. This hose is removed during the flood events.

In run 2, alfalfa of the same supplier as chapter 3 is used as surrogate vegetation. The preparation method is similar to in the preparation method in chapter 3 (see section 3.2.3.2). Based on the outcomes of chapter 3, that show a more distinct evolution due vegetation age for the lower seeding density (see section 3.3.2), an initial seeding density is used of 1 seed cm^{-2} . After the initial spin-up period, seeds are evenly spread out manually, over 0.25 m^2 patches of the existing morphology, covering the entire bed of both experimental channels. After seeding, the bed is subjected to a small flow of 0.8 L s^{-1} with a sediment feed of 2.76 g s^{-1} for 4 minutes to wash out any seeds from the centre of the channels. Both parallel beds are reseeded once more, as the first sequence of flood events removed a large part of the existing vegetation. In contrast to run 1, the duration of the breaks in run 2 are experimentally scheduled to mimic an evolution of the vegetation. Hence, outcomes of previous experiments with alfalfa (section 3.3.2) are a guideline to determine the duration of each of those breaks in the experiment (Figure 5.5).

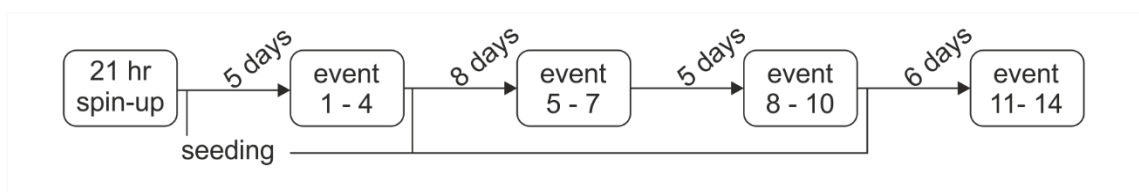


Figure 5.5: Schematic overview of the vegetation experiment (run 2), including the spin-up interval, growing breaks, flood events and seeding of alfalfa seeds.

5.2.3. Data collection

The downstream basins that trap sediment are located on mechanical mass-balances that provide a record every 5 seconds. Additionally these collection basins are emptied of sediment between each event as well as up to once during the event when a risk of overtopping sediment could occur. After collection, the sediment is drained and weighed using a hand balance. As the mass-balances were broken down during run 2, the weight data used in further analysis is uniquely from the hand balances. A comparison between mass-balance data in run 1 and hand balance data in run 1 show that both follow similar trends. Therefore, bucket weight is found representative for the qualitative response of the experiment. Before their malfunction, the scales were used to monitor and estimate sediment throughput and system equilibrium of the fluvial system in the experiments to determine the end of the spin-up interval.

In between each event the morphology of the parallel beds is scanned using a Faro X330 terrestrial laser scanner. This scanning takes place 30 minutes after the pump (and inflow) of the experimental beds is stopped, to allow drainage of standing water in scour holes. Scans are taken from two fixed locations (Figure 5.3 D), about 2.5 m above the bed and about 4 m from each other. Scanning is in sequence, scanning the upstream location (A) first before scanning the downstream location (B). Over the course of the experiments, scan settings remain identical (quality setting 1, resolution setting 0.5). These settings are selected as the shortest duration without a loss of quality in the point cloud and resulting digital elevation model (DEM) (see section 4.2.5.).

Over the course of each event, ten cameras capture imagery at various fixed locations along the flume and channel beds. Four GoPro Hero 4 cameras are mounted to cover the entire bed in longitudinal direction; two for each bed, one facing upstream, one facing downstream. These cameras capture timelapse photography with a 30-second interval over the duration of an entire flood event. Six remote-controlled cameras are mounted to the roof and capture synchronous

time lapse photographs every 1 minute (Figure 5.3 D). The field of view of the six cameras captures the central part of the bed ($x = 2.5$ to $x = 8.5$ m).

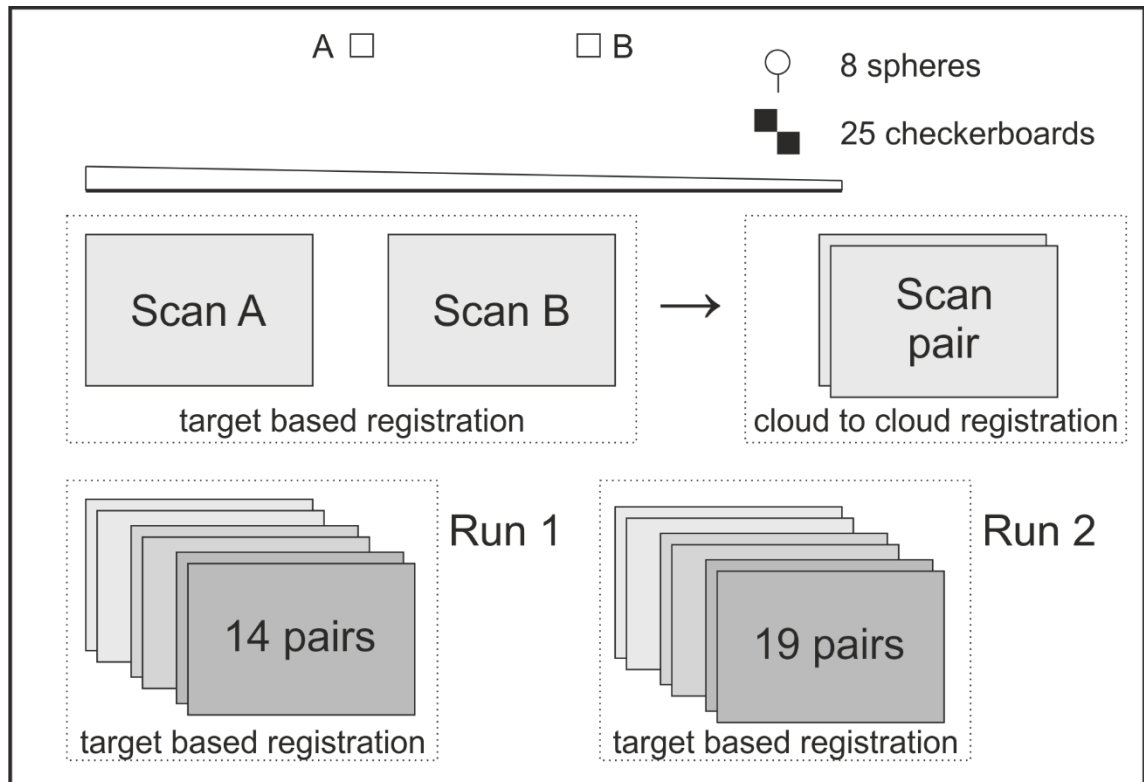


Figure 5.6: Initial post processing steps for the Faro X330 terrestrial laser scans for each scan pair A-B, using Scene 6.2.5.7. Target based registration uses a selection of 8 spheres and 25 checkerboards located in and around the flume.

5.2.4. Post processing

Scans are post processed in several distinct sequential steps (Figure 5.6 - Figure 5.10) that are explained in detail. Raw scans (Figure 5.6) are imported to FARO Scene version 6.2.5.7 and are arranged in pairs (A-B / up- and downstream). Each pair is pre-processed to detect 25 checkerboards and 8 spheres scattered in and around the flume. False targets are removed before applying a target-based registration where targets with errors above 10 mm are ignored. This target-based registration is followed by a cloud-to-cloud registration. Afterwards each scan pair of a single run (run 1 or run 2) is combined in a final target-based registration before both scans are exported to CloudCompare v2.9.1.

Individual scans are imported in pairs as a point cloud in CloudCompare to merge into a single scan. In this process points from outside the flume are removed (Figure 5.7). The merged scan is then translated (rotated and shifted) to fit into a three-dimensional predetermined grid, with the origin on top of a breeze-block in the true right upstream corner of bed 1 (xyz-location in Figure 5.2 or Figure 5.7). Distorted points, caused by remnants of standing water and other reflections, are removed using a 0.66 threshold filter on a 0 to 255 red colour scale. Additional points outside a -0.36 to -0.10 elevation (z) range are removed. Finally, the point cloud is 2D-rasterized, with a grid size of 0.001 m and is exported as .txt matrix file for further analysis.

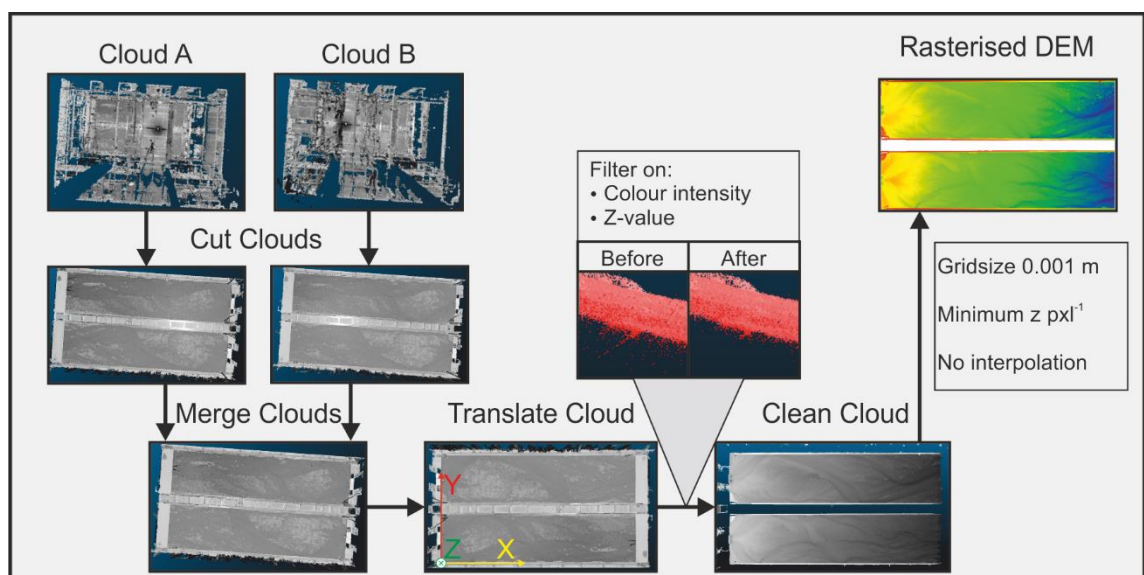


Figure 5.7: Second set of post processing steps in CloudCompare v.2.9.1 that transforms pairs of point clouds into a rasterized digital elevation model (DEM). This include merging, translation and a removal of standing water and reflections.

Resulting .txt files are imported in Matlab© 2017a, which is used for the remainder of processing and analysis. In Matlab©, beds are separated and trimmed to remove areas outside the bed, which results in a 10000 x 2415 (bed 1) and a 10000 x 2440 (bed 2) digital elevation model. Missing values (NaNs) in the matrix are interpolated by a double sequence of an 8-neighbourhood average (Figure 5.8). Any remaining missing values are interpolated with a 0.35 quantile value of the original boundary cells of a connected group of missing values. The resulting elevation matrix is the base for the analysis and further referred to as the DEM.

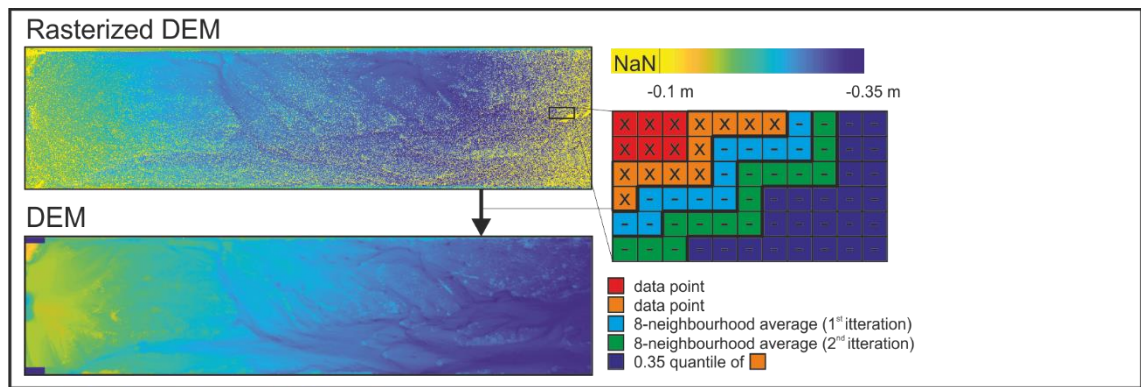


Figure 5.8: Interpolation of missing values (NaNs) in rasterized digital elevation model (top) towards a digital elevation model (DEM) without missing values (bottom). Missing values (-) are interpolated using neighbouring values (x) using a 3-step algorithm (colour coded) as indicated by close up (right).

The scanner will detect stems/leaves of vegetation above the sediment surface, yielding elevation values that do not represent the surface elevation. In order to smoothen out this effect, a new matrix (D1) is created, each cell in this new matrix being the minimum of the cell in the old matrix and its 8-neighbourhood cells (3x3 moving window) (Figure 5.9). Additionally, another matrix (D2) is created in a similar way using a 25x25 moving window, to be used further in the analysis.

5.2.5. Analysis

The key aspect of this chapter is to understand erosion (and deposition) rates of the braided system over time. Hence this research stores erosion (and deposition) data in a dataset that is extracted from the collection of 55 DEMs by several analysis steps and algorithms that are highlighted in Figure 5.9 and are explained below. For consistency in the analysis, the object-based structure of Topotoolbox 2 (Schwanghart & Scherler, 2014) was used in the majority of the analysis. Moreover, any plan view overviews are referred to as maps in the continuation of this chapter.

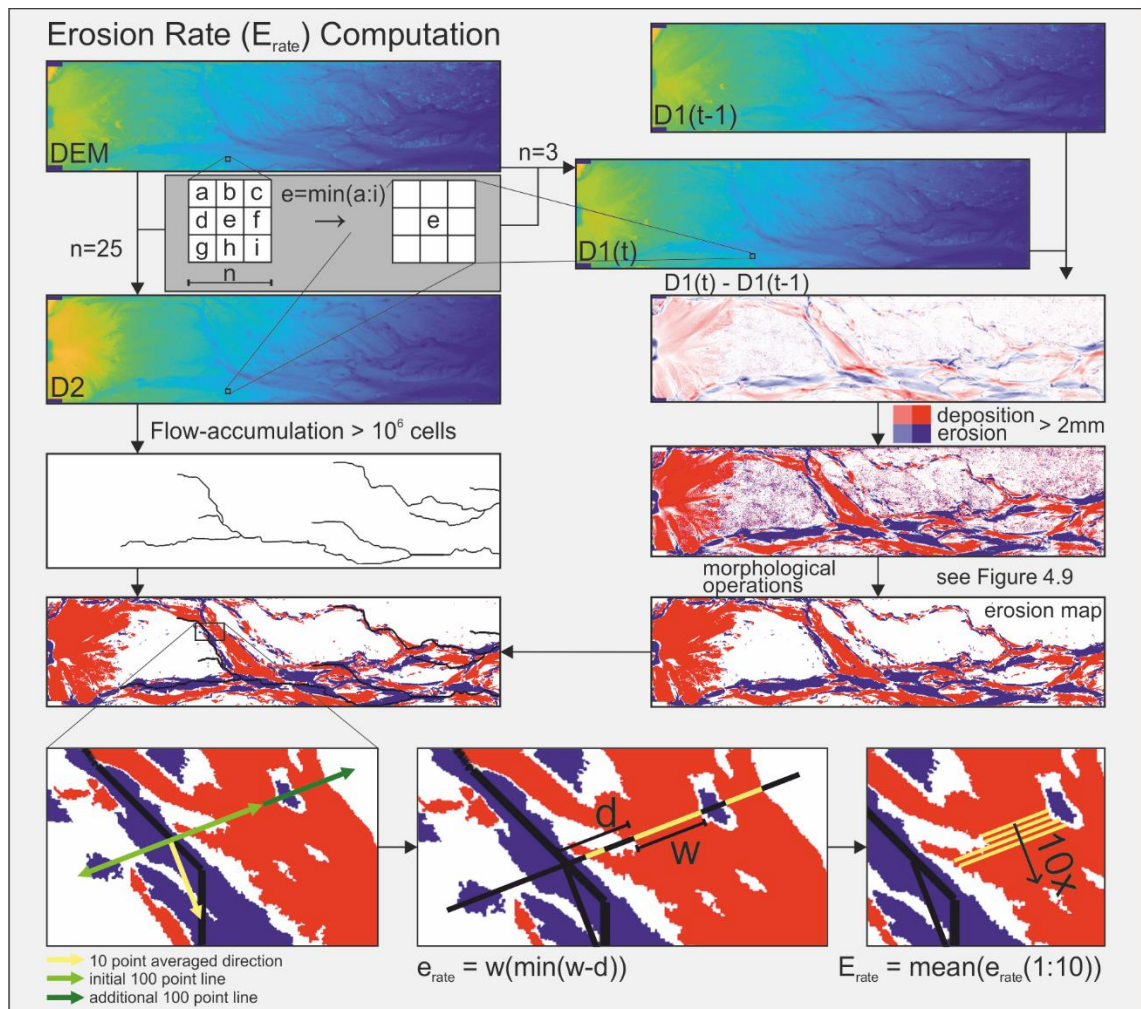


Figure 5.9: Post processing and pre-analysis steps to determine erosion rates using Matlab© 2017. Flowchart includes DEMs of difference and erosion maps (right) and flow accumulation maps using Topotoolbox 2 (Schwanghart & Scherler, 2014) (left).

First, the digital elevation models (D1) of two subsequent events are subtracted from each other and the outcomes are classified in erosion ($< -2\text{ mm}$), deposition ($> 2\text{ mm}$) and no change (thresholds based on best practice of several (1-5 mm) symmetrical thresholds). The outcome, a classified DEM of difference, is split into erosion and deposition maps for each event. These binary erosion and deposition maps (1 = erosion/deposition, 0 = no change) are then subject to a sequence of morphological operations (see Figure 5.10) to generate more continuous areas of erosion and deposition. Finally, areas of erosion/deposition smaller than 150 cells (1.5 cm^2) in areas of no change are reverted to no change and areas of no change smaller than 150 cells (1.5 cm^2) within areas of erosion/deposition are changed to erosion/deposition to create finalized

erosion/deposition maps. In the remainder of the analysis, erosion and deposition are analysed separately but in an identical way, therefore the remainder of this section will only explain the methodology adopted to compute erosion rates.

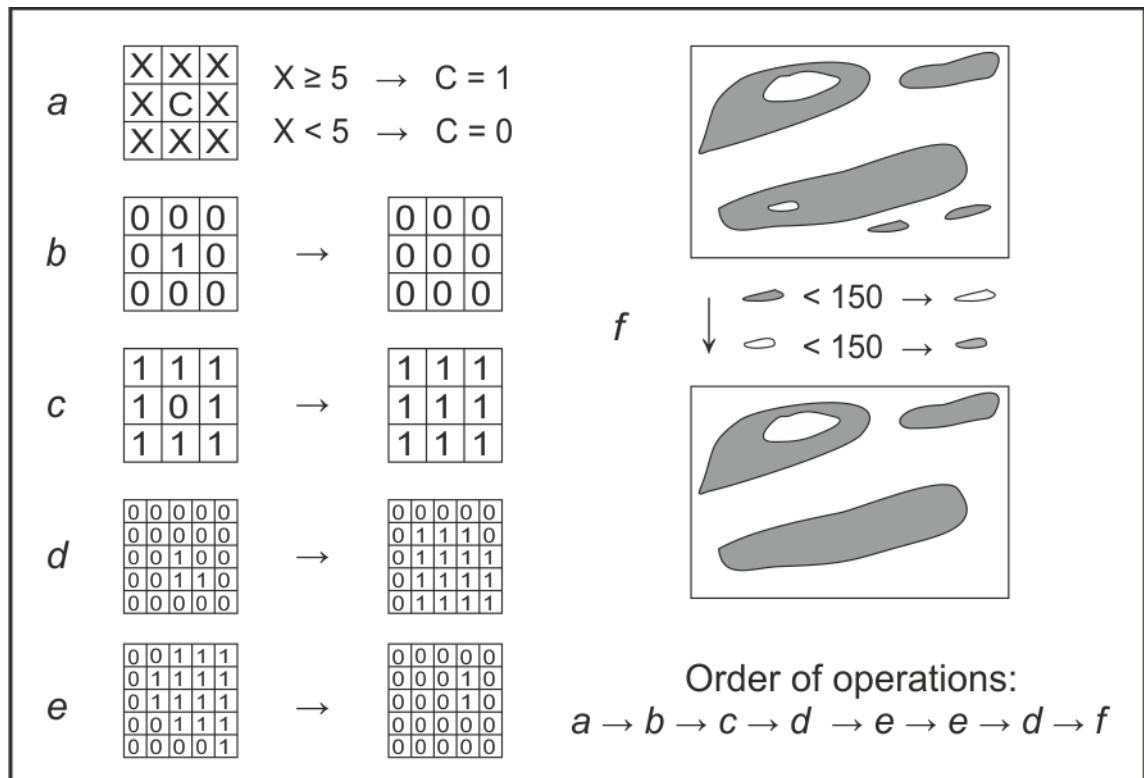


Figure 5.10: Overview and order of morphological operations used to clean classified erosion maps (Figure 5.9Figure 5.9).

Secondly a channel pattern was detected with the use of flow and stream objects in Topotoolbox 2 (Schwanghart & Scherler, 2014). On the smoothed digital elevation model (D2), flow accumulation was determined (Figure 5.9). Cells with a flow accumulation (upstream cells) over 1000000 (1 m²) were accepted and formed a channel network. To force the flow accumulation towards the downstream end of the map, the outermost cells to the true right and true left of the bed were given a value of 0 (high elevation). The strings of the channel network were then split to force each tributary in a separate string (further referred to as streamline).

As a third step, the channel network after an event was overlain on the erosion map of the same event to determine erosion rates (see Figure 5.9). Here, each individual streamline was cut into sections of 10 subsequent coordinate pairs. For each section, a direction was determined based

on the first and last coordinate pair. Perpendicular to this direction, a line was constructed with the first point as the origin that stretches 100 coordinate pairs in each direction. The line (a string of coordinate pairs) was checked pair by pair on whether the erosion map showed erosion (1) or no change (0). When the last coordinate pair showed erosion, the line was extended by another 100 coordinate pairs. In these resulting strings, successive values of erosion were grouped. Each group was then ranked on group size (number of successive 1s) subtracted by the distance to the origin. The largest outcome was accepted as the erosion length. This action was repeated for each 10 coordinate pairs of the section and the erosion length of the section was averaged over the 10 pairs. Finally, this average erosion length in cells was transformed to an average erosion rate per millimetre. This approach was repeated for each section of 10 coordinate pairs on each streamline to create a dataset of 2000-4000 records of erosion rates per map and over 70000 records in total.

5.3. Results

5.3.1. Sediment output

The outcomes of sediment output weight were not consistent, nonetheless sediment output is clearly influenced by different types of events. Figure 5.11 A shows a clear indication between large and small events. Whereas the minimum output of the large events is similar to the small events, the mean and variability is larger than those of the small events (e.g. a mean sediment output of 40 kg hr^{-1} vs 20 kg hr^{-1}). This difference is far more distinct than the difference between the two parallel beds. Both beds have a mean and range similar to each other over both magnitudes of events that allows to merge data of bed 1 with bed 2 in the remainder of this sediment weight comparison (Figure 5.11 B and C).

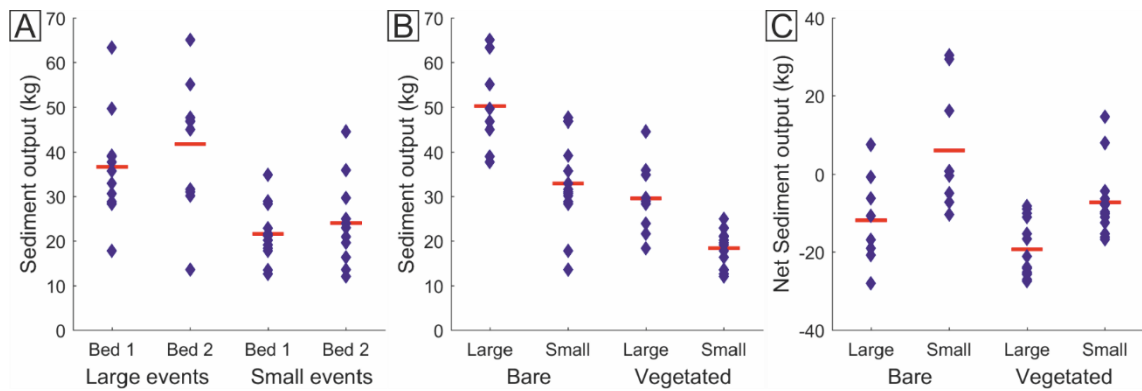


Figure 5.11: Overview of sediment output, blue diamonds indicate a single event, red line indicates mean of each dataset. A) Sediment output (kg) for all large and small flood events split between bed 1 and bed 2. B) Sediment output (kg) for all bare and vegetated events split between large and small flood events. C) Net sediment output (kg) for all bare and vegetated events split between large and small flood events.

Hence, the comparison in sediment output between the bare experiments and vegetated experiments show more difference. Like Figure 5.11 A, Figure 5.11 B shows higher sediment outputs for the large events (about 10 to 20 kg hr⁻¹ more) in comparison to the small events. However, Figure 5.11 B also indicates a clear difference between the bare events and the vegetated events. On average, sediment output is reduced by adding vegetation into the flume. For large events, a reduction of 20 kg hr⁻¹ or 40 percent is observed. For the small events there is a reduction of only 10 kg hr⁻¹, or 33 percent.

All events had a net negative sediment output (e.g. sediment is stored on the bed), except all the small events with a sediment deficit and one large event following a run with sediment deficit. Within the dataset, there is a slight variation between large events (less sediment output) and small events (more sediment output) as well as between vegetated events (less sediment output) and non-vegetated events (more sediment output) (Figure 5.11).

5.3.2. Area of change

This impact of the vegetation on the raw sediment output can also be observed in spatial changes along the surface of the channels. Figure 5.12 shows the spatial evolution over each of the events indicated as an area of change. This area of change, the percentage of pixels with an

absolute change in elevation over 2 mm (e.g. erosion map in Figure 5.9 explained in section 5.2.5) between two time steps, is projected over time steps and split between the non-vegetated (Figure 5.12 A) and vegetated events (Figure 5.12 B). First, large flood events cause a larger area of change, consequently larger (about 10-15 percent) than sequential small flood events. Second, there exists a trend over time. This trend, less distinct in the non-vegetated events, shows a reduction of the hourly area of change by 10 (small events) or 15 (large events) percent over the course of the 13-hour long experiment (Figure 5.12 A).

A similar effect can be observed in the experiments with vegetation. Here, the reduction in area of change is even more pronounced with a reduction of over 25% for both the large and small flood events. Nonetheless, most of the reduction occurs between the first pair of experimental days, while limited change occurs over the course of the other experimental days. Finally, overall the area of change in the vegetated events is generally lower than the area of change in the non-vegetated events, reflecting the results in the sediment output in Figure 5.11.

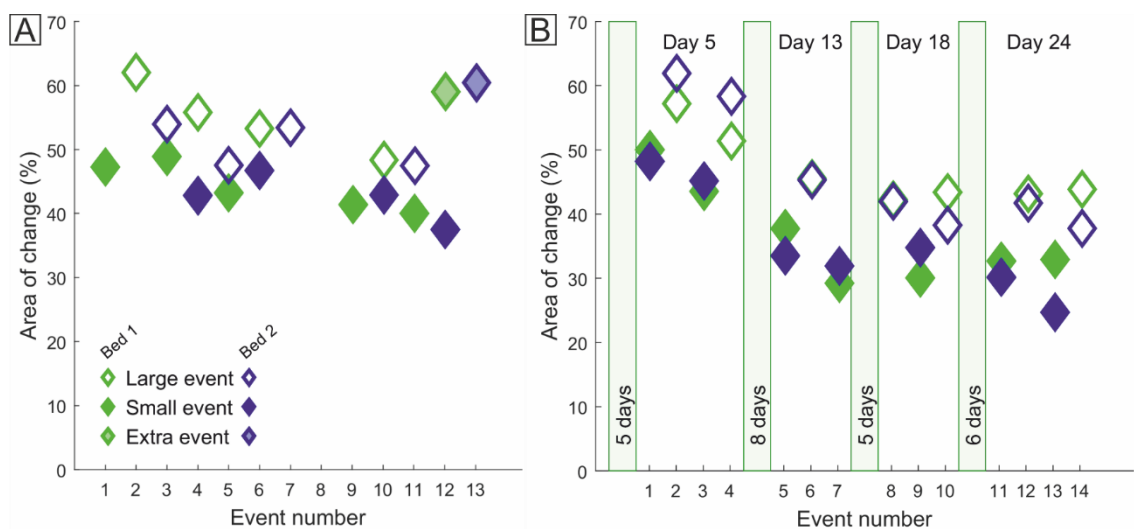


Figure 5.12: Area of change (areal percentage of the bed with a change of elevation over 2 mm) for large (open diamonds) and small (closed diamonds) flood events in bed 1 (green) and bed 2 (blue) for A) run 1 and B) run 2. Green bars indicate duration of growing breaks, time on the top shows total duration of vegetation cover.

5.3.3. Rates of erosion and deposition - probability density functions

Rates of lateral erosion and deposition have been determined for each major channel in each individual event (see section 5.2.5). The resulting dataset consists of over 70,000 erosion rates and over 60,000 deposition rates, which are now investigated considering different variables (e.g. different beds, different magnitude, vegetation or no vegetation). Below, this data is represented as logarithmic probability density functions in combination with a median (given in mm hr^{-1}) (e.g. Figure 5.13). For visualisation, erosion/deposition rates are clustered in 5 mm hr^{-1} wide bins.

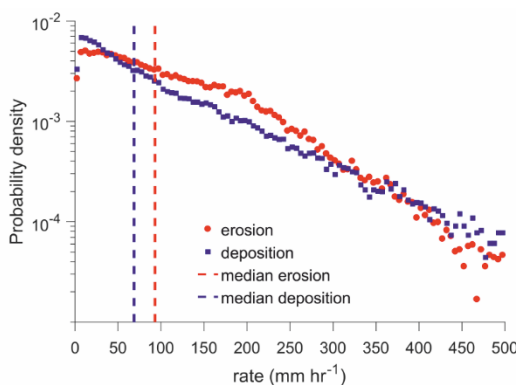


Figure 5.13: Probability density of erosion (red) and deposition (blue) rates collected from all experiments. Vertical lines indicate median of the dataset.

Figure 5.13 indicates a clear difference between the distribution of erosion rates and deposition rates. Deposition rates follow a near logarithmic trend, but erosion rates have an overrepresentation of medium to high erosion rates (50 to 300 mm hr^{-1}) and consequently an underrepresentation of low (and to a lesser extent very high) erosion rates. This trend is obviously captured in the median of both datasets, with a median erosion rate of 93 mm hr^{-1} and a median deposition rate of 69 mm hr^{-1} .

5.3.4. Comparison between channel beds

The above comparison assumes the parallel beds in the experiments can be used as replicates of each other. Figure 5.14 (right) indicates that the median deposition rate is similar (70 vs 67 mm hr^{-1}), but mid to high erosion rates were more common in bed 1 than bed 2 (Figure 5.14Figure

5.14 (left)), resulting in a higher median erosion rate for bed 1 than bed 2 (87 vs 97 mm hr⁻¹). In addition, there is a slight difference of about 5-10% between the number of output values (number of calculated erosion/deposition rates) for bed 1 and bed 2.

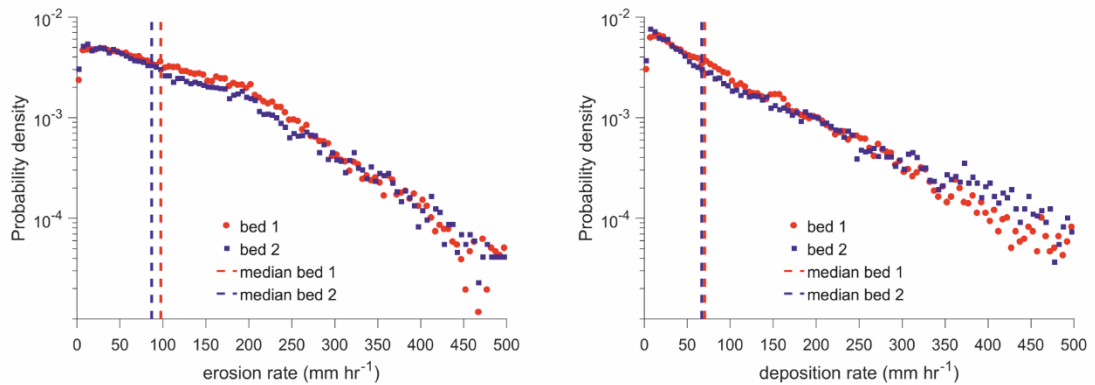


Figure 5.14: Probability density of erosion (left) and deposition (right) rates collected from all events in bed 1 (red) and bed 2 (blue). Vertical lines indicate median of each dataset.

5.3.5. Impact of vegetation on erosion/deposition rates

Referring back to Figure 5.12 B, which indicated a reduction in area of change for the vegetated experiment, a similar trend is visible when comparing non-vegetated and vegetated events (Figure 5.15). The probability density shows a tail with a greater number of high erosion rates, combined with fewer low erosion rates. This effect, resulting in a median erosion rate reduction of about 14 mm hr⁻¹, is slightly different from the effect the vegetated bed has on deposition rates. In terms of deposition rates, the difference in mean deposition rate of 8 mm hr⁻¹ is primarily related to their being fewer high deposition rates, and an over-representation of lower deposition rates. Furthermore, there is a 20% increase in records of deposition for vegetation events, in addition to the increase attributed to their being 20% more recorded vegetated events.

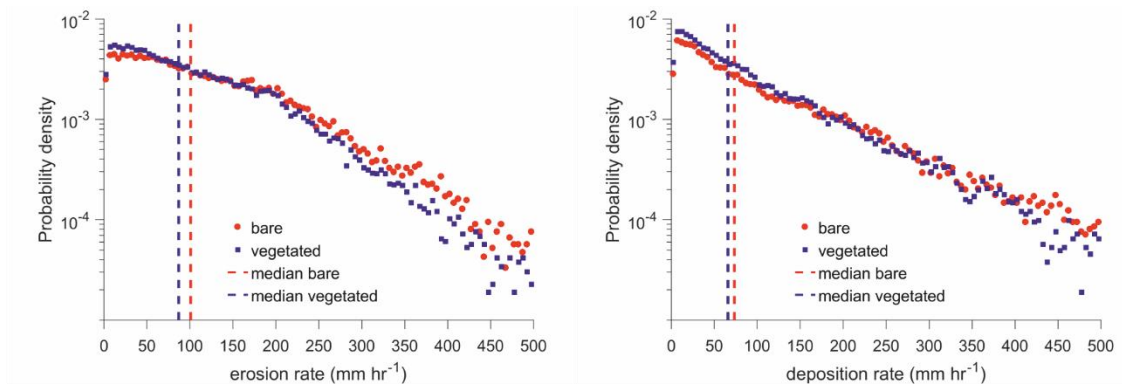


Figure 5.15: Probability density of erosion (left) and deposition (right) rates collected from all events in the non-vegetated experiment (red) and the vegetated experiment (blue). Vertical lines indicate median of each dataset.

5.3.6. Impact of flood event scale on erosion/deposition rates

The impact of alternating small and large flood events on erosion and deposition rates shows a contrasting result. Whereas the scale of flood events is influencing erosion rates, with median erosion rates reduced from 102 mm hr^{-1} for large flood events to 84 mm hr^{-1} for small flood events, there is little to no influence on deposition rates (68 to 70 mm hr^{-1} ; Figure 5.16). In addition, the records in the datasets for erosion and deposition are evenly distributed across the two types of flood events.

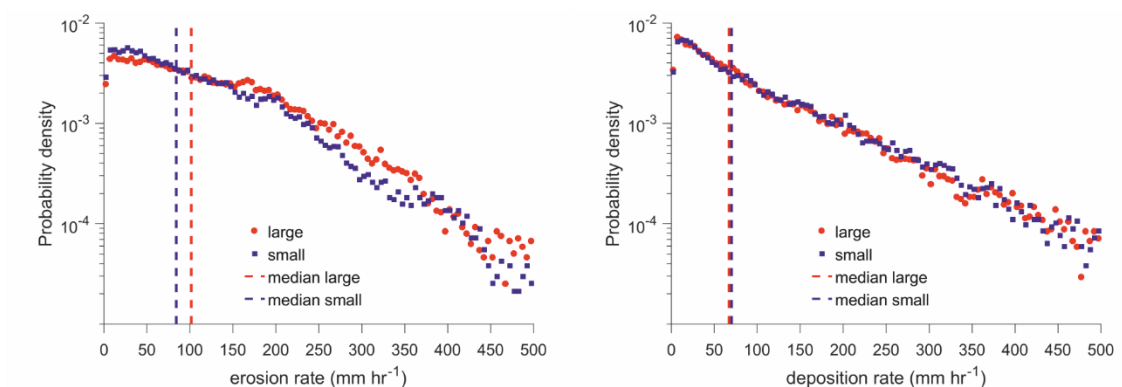


Figure 5.16: Probability density of erosion (left) and deposition (right) rates collected from all large flood events (red) and all small flood events (blue). Vertical lines indicate median of each dataset.

5.3.7. Combining flood events with vegetation

The above figures indicate different implications on erosion/deposition rates due to flood event magnitude or a vegetated surface. However, separating these variables out in each individual combination allows to pinpoint the origin of these differences. Figure 5.17 shows that differences mainly originate from two specific settings. While comparing the non-vegetated events with vegetated events, small flood events show a median reduction in erosion rates of about 22 mm hr^{-1} and large flood events show a median reduction in deposition rates of about 18 mm hr^{-1} . Conversely, the vegetated surface does not impact the erosion rates of large flood events, nor does it impact the deposition rates of small flood events.

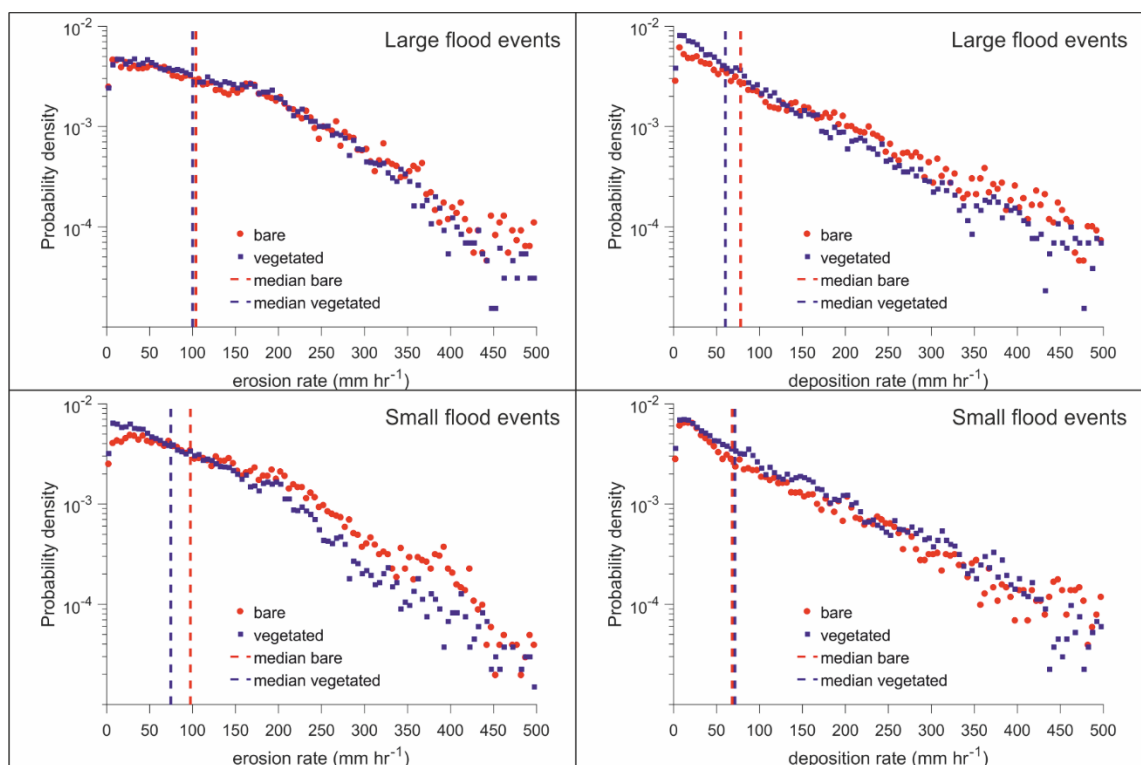


Figure 5.17: Probability density of erosion (left) and deposition (right) rates collected from all large flood events (top) and small flood events (bottom) for the non-vegetated (red) and vegetated experiments (blue). Vertical lines indicate median of each dataset.

5.3.8. Impact of the evolution of vegetation

In the above section, differentiation was made between non-vegetated and vegetated surfaces, despite vegetation being allowed to develop and grow over time. Due the succession of events and the difference in numbered events per day (see Figure 5.5), each comparable record only

consists of 1 or 2 similar events that are doubled due the use of two experimental beds. The median of each data set (either around 3000 or around 6000 records deep) is plotted over time (Figure 5.18).

For the large flood events (Figure 5.18 (left)), a clear evolution is seen in both erosion rates as well as deposition rates. Here, erosion and deposition rates are reduced when vegetation becomes more established/older. This reduction is enhanced for the erosion rates and is most pronounced in the initial time steps. On top of that, erosion rates are about 20-30 mm hr⁻¹ higher than deposition rates. Acknowledgement should be given to the difference between the median values of the non-vegetated events. The median of the non-vegetated deposition rates extends the trend seen in the vegetated events, being higher than the median at all different time stages. Conversely, erosion rates in the first stage of vegetation are 16 mm hr⁻¹ higher, before the rates drop to rates similar or just below the median erosion rate for non-vegetated events. This trend is not visible at all for the small flood events (Figure 5.18 (right)). Here, both erosion and deposition rates behave very similarly to each other and neither have a clear trend over time. In conjunction with Figure 5.16 (left), Figure 5.18 (right) indicates consistently lower erosion rates for small flood events and consistently slightly higher deposition rates compared to the median rates of erosion and deposition for the non-vegetated events.

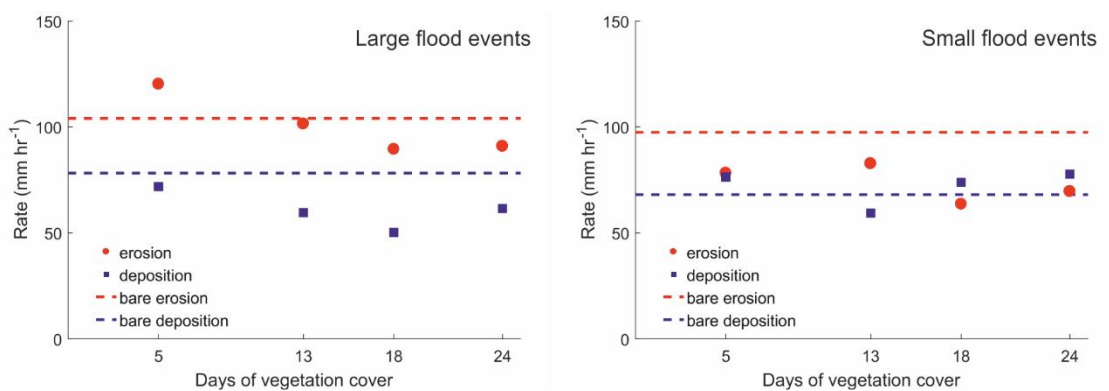


Figure 5.18: Median of erosion (red) and deposition (blue) rates for experiments with vegetation cover differentiated over days of vegetation cover before the event for large flood events (left) and small flood events (right). Lines indicate the mean of the bare experiments under further identical conditions.

5.4. Discussion

Braided river systems are composed of dynamic morphologic features that may or may not shift with every sequential flood event. As a result, systems like these are often described using reach scale or channel width averages (e.g. braiding index or width to depth ratio (see chapter 2)), a method often more time-effective than monitoring or measuring individual bars or channel features (e.g. Leopold and Wolman (1957)). Another approach to understanding these systems is the tracking of individual bars using a shape outline of these features. Whereas the above methods are all developed to gather specific data from these systems, they all lack the ability to monitor the direct impact of a vegetated (and as such more cohesive) surface within the channel belt. The method used here is developed for this specific case and introduces a different approach, primarily focused on understanding reach-scale trends of erosion (and deposition).

5.4.1. Erosion and deposition rates

The method used in the previous section uses temporal change of elevation to indicate channel mobility. Therefore, this method is effective in analysing changes at a high spatial resolution across the entire channel belt. However, the approach has several shortcomings, that will be elaborated on after some clarification of terminology is introduced. This section uses the terms erosion rate and deposition rate in a different way to previous sections.

Erosion rates in the previous section were describing bank retreat, and as such described an area of retreat per bank length per time unit (Figure 5.19 B). This concept is common in other research either as an area per bank length per time unit (Figure 5.19 B) or as a metrical retreat per time unit (Figure 5.19 A). Another common approach to describe erosion rates is a volumetric change over a spatial area per time unit or an areal change over a cross-section per time unit (Figure 5.19 C). In contrast, the present research describes erosion rate as a length, perpendicular to the channel, over which erosion occurs per time unit, best described as a lateral erosion or retreat length (Figure 5.19 D).

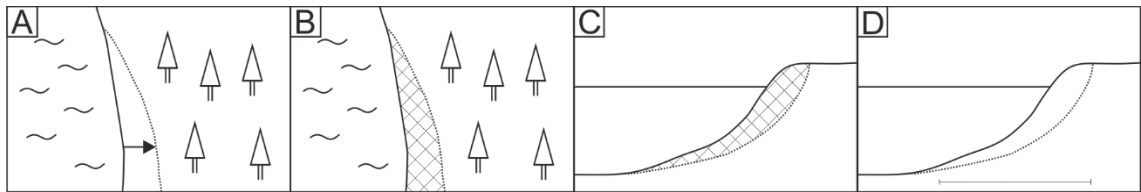


Figure 5.19: Four different approaches to quantify erosion rates, solid line indicates previous bank line, dashed line indicates new bank line. Crossed filling indicates area. A) Planform metrical erosion (bank top retreat), B) Planform areal erosion (spatial bank top retreat), C) Cross-sectional areal erosion, D) Lateral erosion length (horizontal length of section with reduced elevation), used in this research.

Planform approaches (Figure 5.19 A and B), although often straightforward to understand, are usually heavily related to the water line (boundary between land and water). In meandering systems with steep banks, the planform position of this water line is relatively stable, but in braided systems, where bars are ubiquitous, the water line is heavily dependent on the flood level and as such is not stable over time (Marra et al., 2014). Cross-sectional approaches (Figure 5.19 C and D), to the contrary, are not dependent on a waterline and determine rates of erosion regardless of water level. Of these approaches, the incorporation of vertical elevation change (Figure 5.19 C) is preferred over the more basic lateral erosion length (Figure 5.19 D) approach, in particular in order to link with sediment transport. However, this research opts for the more basic approach that allows faster and robust computation and is less sensitive to fluctuations of bank height and water depth. Additionally this avoids excessive impact of scour holes as observed in these experiments (Fernandez et al., 2021).

To reduce noise in the identification of regions of the cross-section undergoing erosion, a threshold vertical elevation change value was selected. This research applied a sensitivity analysis of different thresholds on a single map to identify the optimal threshold for the total dataset. The threshold could also be identified considering the vertical uncertainties in the elevation datasets (e.g. Wheaton et al., 2009). The final threshold (2 mm) still is distinctly larger than the median grain size (4 times) or scan error (2 times).

The decision to ignore vertical elevation change leads to several shortcomings. First, by using a constant threshold to identify erosion, there will numerically be no difference in lateral erosion length between a channel bank vertically eroding two times (Figure 5.20 A) the threshold value and a channel bank vertically eroding five times the threshold value (Figure 5.20 B). Thus, there is no consideration of net erosion volume. Similarly, an incising channel would be represented in a similar way (Figure 5.20 C) as a channel that actually migrated laterally (apart from a lack of deposition rates for the former) (Figure 5.20 B). Second, when vertical erosion perpendicular to the channel is below the threshold for a handful of pixels, the erosion is broken up and erosion width is based on only one part, thereby underestimating effective erosion (Figure 5.20 D).

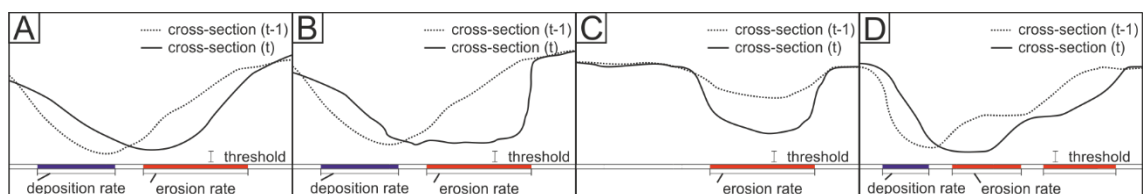


Figure 5.20: Overview of lateral erosion and deposition lengths in different hypothetical cross-sections/ scenarios. Top part of each graph shows cross-section with current elevation (solid line) and previous elevation (dashed line). Bottom part of each graph shows the application of the threshold vertical elevation change to identify regions of erosion (red) and deposition (blue) along the cross-section. Points with vertical elevation changes with a magnitude less than the threshold are neither depositional nor erosional. Scenarios include A) a channel migrating laterally to the right. B) a channel migrating laterally to the right while also expanding, C) an incising channel and D) a complex terraced channel migrating to the right.

5.4.2. Higher median lateral erosion lengths

To put this research in perspective, a conceptual modelling study on channel width introduces five different scenarios that will impact the channel width in curved, single channel, fluvial systems (Eke et al., 2014). As all these scenarios, due to similar processes, can be considered for individual braid channels, it is important how each of these would be represented by this analysis method which considers erosion width. Of these scenarios, inner migration is almost irrelevant, since channels in braided systems do not naturally migrate towards the inner bank. Further, the pair of opposite settings (both banks deposit or both banks erode) can be

subcategorized as either channel filling or incision (e.g. Figure 5.20 C), which would overestimate erosion/deposition rates, or channel narrowing/widening, which would likely underestimate lateral erosion/deposition rate as the algorithm would select one bank/bar only. For the last (and most important) quadrant, Eke et al. (2014) distinguish between bank pull (erosion > deposition) or bar push (deposition > erosion), both alternatives are represented differently by this research. In contrast to other scenarios, which reduce the occurrence of either deposition or erosion (less records), these latter scenarios both provide a similar number of records of erosion and deposition rates. However, bank pull would result in higher median lateral erosion lengths in contrast to bar push, which would result in higher median lateral deposition lengths.

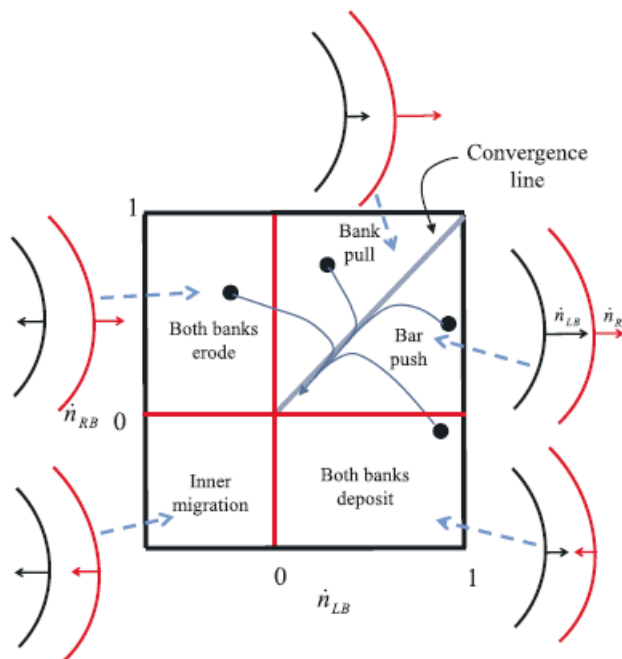


Figure 5.21: Schematic plot in phase space of bank-migration scenarios showing the different phases of channel-bank interaction. n_{LB} and n_{RB} are the migration rates of the left and right banks, respectively (Eke et al., 2014).

Therefore, the experimental channels in this research, in which median lateral deposition lengths are 26% smaller than the median lateral erosion lengths, could be experiencing bank pull and a widening of channels at a rate of 25 mm hr⁻¹ or 25-35 mm over the course of a single experiment. This hypothesis is not supported by observations during the experiments where dominant channel widening was not observed and but can have occurred near instantaneous due smaller scale of the experiment.

An alternative explanation for the difference between median lateral erosion and deposition lengths is related to the vertical erosion threshold applied and the spatial behaviour of fluvial systems. In general, erosion is localised to areas of the channel with faster flow velocities while deposition occurs at locations with slower flow velocities. As a result, deposition has the potential to occur over a larger spatial extent, which would be represented by higher median lateral deposition lengths in this research. However, this enhancement of median lateral deposition lengths is countered by the use of a threshold vertical elevation change value, because the more extensive areas of small deposition may be ignored since elevation changes are below the threshold and thus ignored in the algorithm of this research. As a consequence, this may result in relatively higher median lateral erosion lengths. Thus, it is important to only consider lateral erosion and deposition lengths from this work relative to each other when comparing them to natural rivers or other experimental research.

5.4.3. Differences between the channels

Section 5.2 indicated that the layout of the two experimental runs was similar but not identical. This dissimilarity occurred mainly in run 1 and was heavily linked to an alteration in sediment input. Whereas this has no impact on this research and the used methods, it reduces potential for other, more statistical methods.

One of these differences, the inclusion of small flood events with a limited sediment load, can be detected in the net sediment output (highest values in Figure 5.11 C). However, neither the raw sediment output (Figure 5.11 B), the global area of change (Figure 5.12) nor any of the individual probability density graphs (not shown) indicate any difference for these events nor their subsequent large flood events. Visual observations during the experiments showed no change either, at least not beyond the initial metre where the scour hole expanded due to a lack of sediment. Subsequently, this suggests the limited impact of sediment shortages in these events is related to one of three things: they were either too short to initiate a major shift in the system; they only changed the upstream part of the flume, which is ignored in the probability

density graphs due to a 1 m^2 upstream requirement; or the impact of these small shortage events was limited because the difference in sediment availability was dwarfed by the impact of preceding larger events and their sediment deposition.

5.4.4. Differences in discharge

In contrast, the change of discharge, had a major impact on the outcomes of the experiments. Apart from the raw sediment output, that was obviously also linked to a higher sediment input, large flood events also showed a consistently higher area of change over all events. Whereas this effect was larger in the vegetated events, as discussed further below, it was consistent. On top of that, two final events of run 1, with 3.5 L s^{-1} , indicate an area of change over 10 percent higher and 1.2 times larger than the regular large flood events. Despite a small dataset ($n = 2$), this indicates at least a similar increase as the increase between regular large flood events (3 L s^{-1}) and small flood events (2 L s^{-1}), despite half the increase in discharge. This outcome may reflect the nonlinearity of sediment transport (see Chapter 2) and thus morphology that also indicates the importance in understanding these processes while looking at climatic changes.

5.4.5. Surrogate vegetation

The outcomes of this experiment agree with previous experiments (chapter 3) and past research, since both erosion and deposition are reduced in experiments with vegetation. Tal and Paola (2010) observe more localized erosion and deposition patterns, something in line with reduced lateral erosion and deposition lengths in this research. Gran and Paola (2001) showed that an increased density of vegetation caused a reduction in lateral mobility whereas this research shows a reduction in lateral erosion rates as vegetation becomes older, an effect also observed in chapter 3.

A closer look at the results (Figure 5.22 A-C) indicates that the impact of vegetation on lateral erosion and deposition lengths strongly relates to the magnitude of the flood events in the experiment. Although both lateral erosion and deposition reduce consistently, the net reduction in lateral erosion is dominated by the reduction of erosion rates during small flood events.

Likewise, the net reduction in lateral deposition is dominated by the reduction of deposition rates during large flood events (in fact, deposition increases slightly during small flood events).

Vegetated experiments compared to bare experiments			Ageing of vegetation	
A All events	B Large flood	C Small flood	D Large floods	E Small floods
Erosion ↓	Erosion →	Erosion ↓	Erosion ↓	Erosion →
Deposition ↓	Deposition ↓	Deposition →	Deposition ↘	Deposition →

Figure 5.22: Overview of overall trends of lateral erosion and deposition in vegetated and non-vegetated experiments for A) all events, B) large flood events only and C) small flood events only. Overview of trends of lateral erosion and deposition in vegetated events over time for D) large flood events and E) small flood events.

Whereas the origin of these impacts is open for interpretation, two alternative explanations are offered for the above relations. First, the extra cohesion due to the added vegetation is strong enough to resist the flow and slow down erosion during small floods, resulting in reduced lateral erosion rates compared to the non-vegetated case. Consequently, during larger flood events, this vegetative strength is overcome and the likelihood of uprooting by the flow is increased, thereby only decreasing erosion rates slightly.

Alternatively, Figure 5.22 C, shows similar erosion rates alongside greatly reduced deposition rates. This setting, dominated by incising channels, has previously been observed in physical experiments with vegetated channels (Tal & Paola, 2010). Consequently, as flow reduces during smaller flood events, deposition rates can increase slightly in the aftermath of such large flood event. This latter effect highlights the interrelation between erosion rates and deposition rates. Hence, with erosion rates larger than deposition rates, channels generally increase in width. Conversely, when deposition rates are larger than erosion rates, channels are likely to reduce in width.

In the present experiments, channel widths increase in large floods and decrease in small floods. Whereas this effect is not novel (e.g. bank pull or bar push (Eke et al., 2014)), it is not the only result that could be predicted with this method.

5.4.6. Surrogate vegetation age

The introduction of vegetation age or maturity show slightly shifted trends (Figure 5.22 D-E). Notably, the effect of vegetation age is clearly seen in the large flood events of run 2 (Figure 5.18). Both erosion and deposition rates at these large flood events decrease over time (and thus age). Conversely, erosion and deposition rates during small flood events barely change as vegetation ages. Indirectly suggests that the threshold stress for uprooting of vegetation is located in the range of the discharge regime of these experiments. Furthermore, the patterns also suggest more channel narrowing during large events when vegetation becomes more mature. Gran and Paola (2001) observe this effect in physical models too. Moreover, within a common understanding of natural rivers indicates the natural shift from braided to meandering rivers often correlates with the development of vegetation (Alabyan & Chalov, 1998; Church, 2006). However, in contrast to natural rivers, where differentiation between smaller or larger flood events is less distinct, this research's smaller flood events in show no decrease in erosion/deposition rates when vegetation became more mature.

Since these variations in rates are only highlighted when comparing individual time steps in the vegetated run and not when comparing non-vegetated to vegetated runs, two different explanations are proposed in this research. First, young vegetation increases erosion rates in large flood events and deposition rates in small flood events. Second, the differences between the non-vegetated and vegetated runs are enforced by the experiments themselves. Whereas both explanations are valid, this research favours the second and links this to processes of armouring and compaction. Despite near opposites, armouring is a process in natural rivers (and other morphologic features), where the erosion resistance increases over time. In natural rivers, this occurs due the removal by wind or water of fine particles. In contrast compaction is the process where soil is compacted due the removal of water and air as well as gravity, however like armouring it enhances the initial cohesion of the surface. In a flume environment a similar process could occur over the periods of no flow in between the events or more likely over periods of no flow between experimental days. Figure 5.12 A, indicates a small trend where the

area of change decreases gradually over the course of the experiments, both for the large and the small events. A comparison with Figure 5.12 B even indicates the 5 day old vegetation has a change of similar magnitude as the first few events in the non-vegetated experiments (Figure 5.12 A). Considering that this effect is time dependent, it matches with events 9 to 13 that are a step lower than their predecessors while following a 2.5 day break instead of a 0.5 day break.

Finally, there is the question of how similar specific river systems in the experiments have been, and to what extent the comparison is validated between the different beds and experiments. For example, Figure 5.14 indicates a difference between two parallel beds, a difference that is enhanced when considering just non-vegetated experiments. However, due to the set-up of the experiment, this research is not able to separate out the impact of these variations in event order or spin-up cycle which potentially impact or invalidate the outcomes of the experiment itself. To date, no research has explored the impact of event order, event variation or even spin-up intervals to enable the exclusion of their impact.

5.5. Conclusions

This chapter utilized a set of larger scale braided river experiments to understand the impact of alfalfa vegetation on braided river evolution under changing discharge conditions. It analysed these patterns of the system in a novel approach. As such it showed that:

- Erosion/deposition rates are an alternative approach to describe system mobility in braided systems.
- The alfalfa surrogate vegetation is effective in reducing the mobility in channels in braided systems.
- The impact of alfalfa is dependent on time; older alfalfa sprouts reduce the mobility of the system more effectively, especially by reducing erosion rates.

This chapter has also helped to illuminate multiple processes that play a role in understanding how vegetation impacts experimental fluvial systems. In addition, it raises several questions that will be explored further in chapter 6.

6. Discussion

The primary aim of this thesis was to understand the impact of vegetation on fluvial systems. In order to achieve this aim, three physical modelling experiments covering different spatial-temporal scales were undertaken. First, a series of short, small scale bank erosion experiments that show the increasing impact vegetation and surrogates have on the rates of bank erosion. Second, a series of medium scale tabletop experiments that show how erosion rates can be adjusted during physical modelling experiments. And third, a set of larger scale braided river experiments that show the evolution of a braided system under evolving vegetation. (Thomas et al., 2014; Baynes et al., 2018). Vegetation, being a living organism, evolves over time, often at time scales asynchronous to the evolution of the fluvial system itself. Physical modelling provides a tool to investigate the interplay between vegetation and the fluvial system and has the potential to provide useful inputs to numerical modelling to parameterise natural processes (Thomas et al., 2014). This obviously leads back to how to scale these impacts effectively; so far physical models have used basic surrogates for vegetation. However, extended data is missing on how to properly scale these surrogates as well as how to approach surrogates when dealing with a range of different timescales. This research has undertaken a range of experiments, all executed in an attempt to get a better understanding of how to scale and use surrogates for vegetation and how these surrogates can help to represent a range of different time scales as well as the practicalities for operating these physical models. Issues that will be touched upon over the next sections.

6.1. Scaling

Chapter 2 showed that physical models span a wide variety of types and sizes and all of them require scaling to represent specific natural conditions, specific settings or areas dependent on a combination of temporal and spatial scales. As such, it is important to understand the spatial and/or temporal scales of the present untreated sediment experiments before interpreting the impact that vegetation or its surrogates have on the scaling of the experiments.

The braided river experiment of chapter 5 (B_b in Figure 6.1) is a clear example of a reach-scale analogue model that adapts itself with each sequential flood event. With the main aim to understand the relative impact of these flood events, several other scaling factors are slightly relaxed in order to represent a generic system. Initial conditions aimed to represent a braided gravel bed river, suggesting a scaling factor of 15 for fine gravel or 50 for coarse gravel. For coarse gravel bed rivers this represented a 125 m wide channel belt over a reach of 500 m. Following similar scaling factors, this suggests an initial forming discharge of $27 \text{ m}^3 \text{ s}^{-1}$, a small flood event of $35 \text{ m}^3 \text{ s}^{-1}$, and a large flood event of $53 \text{ m}^3 \text{ s}^{-1}$ (Heller, 2011). Following similar scaling principles, hourly events then scale to 7 hr natural flood events (see Table 6.1 for a range of scaling examples). For these untreated experiments, flood events applied in the experiments represent sequential events with the assumption that no morphological change occurs between flood events during periods of regular flow. This is a simplification from natural conditions where rivers remain active and often stabilise either by compaction or incision between flood events.

Table 6.1: Analogue braided river experiments placed in context by showing different Froude scaling factors based on sediment size.

Sediment size	Scaling		Geometric		Flood events $\text{m}^3 \text{ s}^{-1}$			Event time
	factor	size	width (m)	reach (m)	forming	small	large	
cobbles	250	114.5 mm	625	2500	1482	1976	2965	16
very coarse gravel	100	45.8 mm	250	1000	150	200	300	10
coarse gravel	50	22.9 mm	125	500	27	35	53	7
medium gravel	30	13.7 mm	75	300	7	10	15	5
fine gravel	15	6.9 mm	37.5	150	1.3	1.7	2.6	4
very fine gravel	8	3.6 mm	20	80	0.3	0.4	0.5	3
very coarse sand	4	1.8 mm	10	40	0.05	0.06	0.10	2
coarse sand	2	0.9 mm	5	20	0.01	0.01	0.02	1

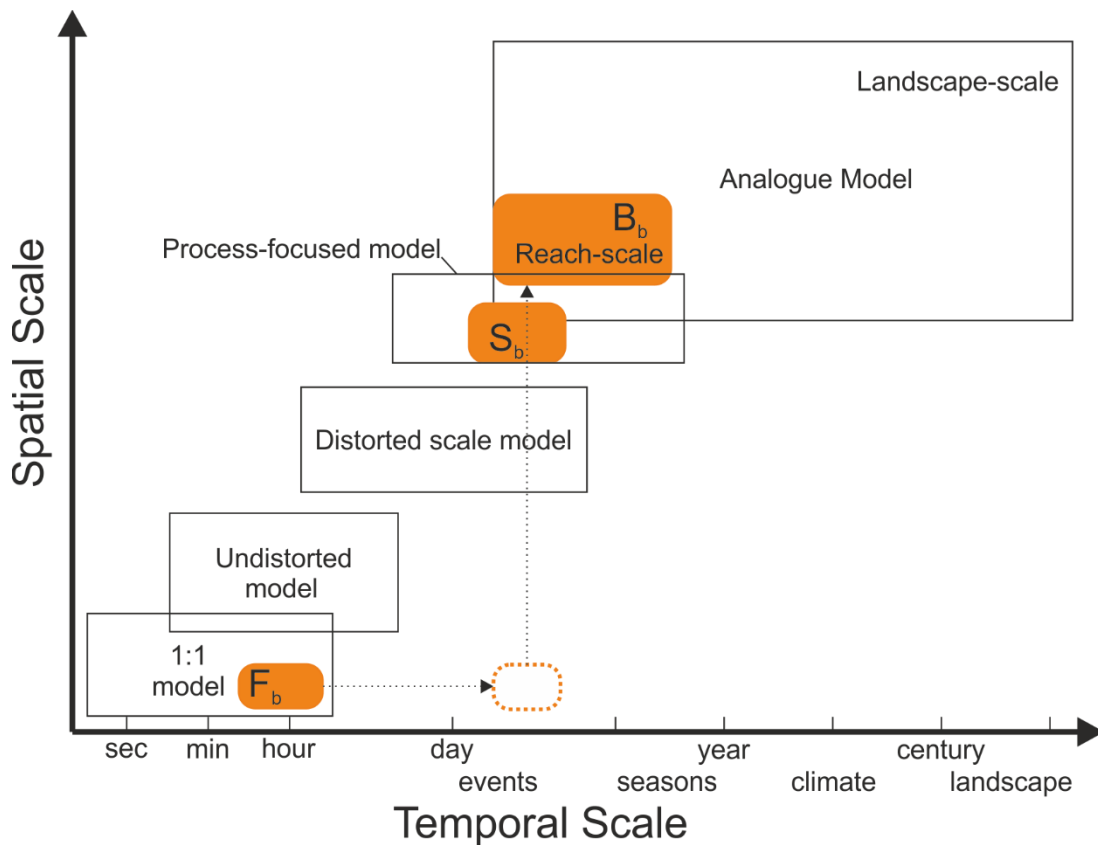


Figure 6.1: Schematic overview of different types of physical models and their placement over spatial and temporal scale. Coloured fields indicate suggested location of the present experiments highlighted in orange (bare experiments). B_b are the bare braided experiments, S_b are the bare planform river experiments and F_b are the bare bank erosion experiments (concept after Peakall et al., 1996).

The bank erosion experiments of chapter 3 (F_b in Figure 6.2) can be interpreted as representing two different scales. In the first interpretation, as coupled experiments, they were a 1:1 representation of a bank in an analogue model like the braided experiments (B_b). As conditions were not monitored in detail, the assumption was made that turbulent subcritical flow occurred in the majority of channels in analogue models and as such similar conditions would suffice as long as flows were turbulent and subcritical. Resulting flow conditions are then similar to the planform experiments and therefore represent the conditions of the analogue braided river experiments. In the second interpretation, these bank erosion experiments were standalone experiments representing a retreating riverbank. In this scenario, the model banks represent a bank of a specific (but unspecified) height, partially submerged by the flow.

6.1.1. Vegetation spatial scaling

Scaling vegetation geometrically is straightforward: a 20 mm high alfalfa sprout geometrically represents a 2-metre high tree for a scale factor of 100. However, geometric scaling is far from the complete picture when implementing vegetation (Frostick et al., 2014; Thomas et al., 2014). Introduction of mass, stresses, rigidity and other aspects of natural vegetation all contribute to the complexity of multidimensional scaling. This research ignored most of these surface processes, and as such the need to scale stems and leaves and their related aspects of rigidity, flexibility or tensile strength. Instead, this research focused on below-surface processes and the impact of the vegetation on binding the sediment. The forces acting on the banks are not directly related to the scale, instead a cubic scaling factor is required when introducing forces to Froude-scaled models (Johnson et al., 2014).

This research opted to relax spatial vegetation scaling for three distinct reasons. First, the areal density of vegetation is widely variable in natural conditions and thus it is difficult to select a specific prototype for cohesion of vegetation. Second, finding a specific, perfectly spatially scaled, type of surrogate vegetation would go beyond the setting of this research. Third, anticipated long-term vegetation assemblage change (e.g. due to climate change or fluvial evolution) would suggest that identification of specific vegetation type today will not be reflective of likely future conditions. Instead, this research focused on temporal scaling of vegetation and the global impact alterations in vegetation can have on the fluvial system.

6.1.2. Temporal scaling

Previous research has framed temporal scaling of vegetation and the issues and complexities associated with it (Baynes et al., 2018). In this section, this study will reframe that research by highlighting some principles of fluvial hydrographs (Figure 6.2) and use these to form an analogue for vegetation and climatic change. In natural systems, floods can be described by their magnitude, duration, volume and degree of symmetry (see Figure 6.2). Flood events are often linked to rainfall events (or daily snowmelt) and the impact of such events is dependent on the

shape and size of the catchment, the location and intensity of the rainfall event as well as the hydrological aspects of the subsurface and vegetation in the catchment. Flood frequency and base flow can be seen as independent external factors. In a complete natural system, frequency only depends on the sequence of rainfall events and as such has a short-term impact on the hydrograph of a system. Base flow also varies over time but it has a longer term impact as it often follows a pattern heavily linked to seasonality (e.g. snowmelt or evapotranspiration) and as such allows individual flood events to be enhanced (or suppressed) dependent on their timing. This concept avoids adding a rising trend to a base flow to represent climate change. Whereas for lowland rivers and marine or estuarine settings sea level rise is important, in the majority of gravel-bed braided rivers either the gradient or the distance to sea is too large to allow backwater effects of a higher sea level to protrude into these reaches. Simultaneously, long-term changes to temperature or precipitation associated with climate change can be described by an alteration of either the base flow or flood events.

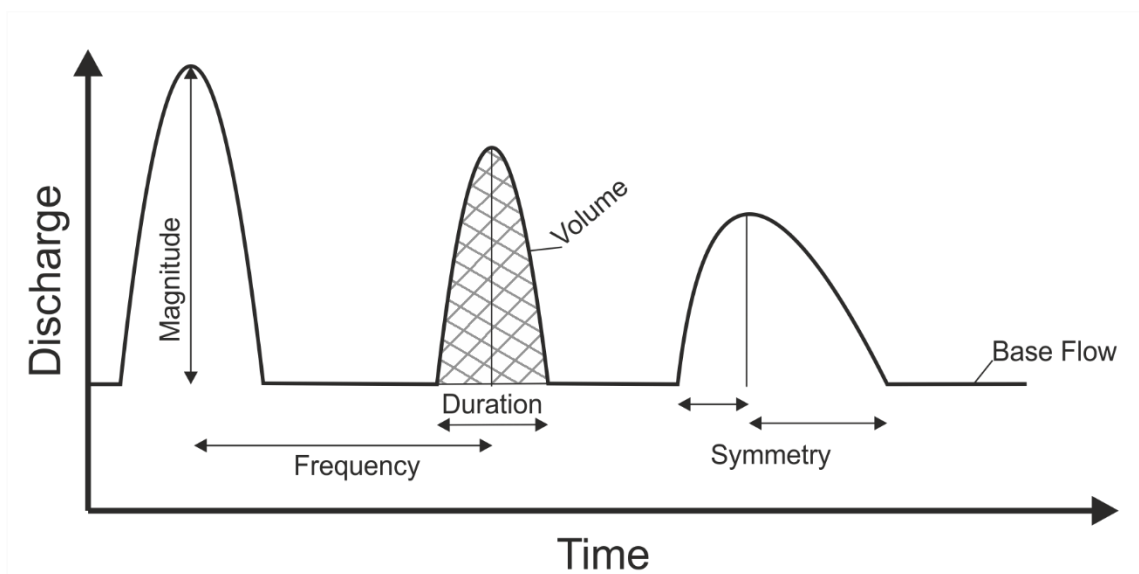


Figure 6.2: Schematic conceptual overview of features to describing characteristics of hydrographs.

When considering temporally scaling the impact of vegetation on the fluvial system it is these last two temporal factors of fluvial change, base flow and flood events, that are essential. Most processes associated with vegetation can schematically be described using three different cycles (Figure 6.3), cycles that follow similar principles of magnitude and symmetry as flood

hydrographs (Figure 6.2). Nonetheless, asymmetry is often larger within the vegetation cycles due to the relative quick initial response of vegetation following a disturbance. A first cycle for vegetation follows the life cycle for vegetation (Figure 6.3, top line), over time vegetation develops and as such is expected to increase its impact on a fluvial system. Naturally, vegetation decays of old age or external (to the fluvial system) environmental impacts. A second cycle is seasonality; this cycle is a yearly recurrent cycle that often follows a similar, identical or shifted, recurrent period as base flow in flood hydrographs (Figure 6.3, middle line). Seasonality is often a variation draped atop the life cycle of vegetation, in particular for perennial vegetation, while neglectable for annual vegetation. The third cycle, recovery, is the shortest and directly linked to flood events (Figure 6.3, bottom line). If individual plants or an area of vegetation is damaged (but not destroyed), it will attempt to recover. Normally this recovery process is more effective than regular growth in seasonal or life cycles. Hence, it can be seen as a sudden decline followed by a long inclining tail, which dependent on the damage and time frame eventually will catch up on long term evolution.

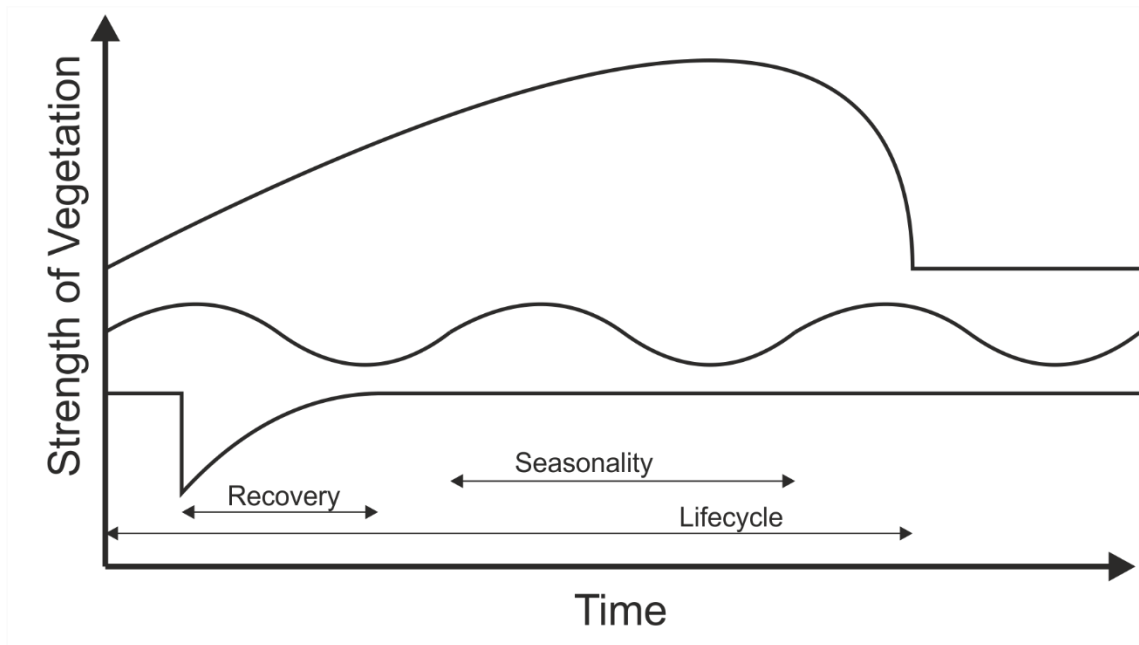


Figure 6.3: Schematic overview of three conceptual vegetation time scales indicating recovery, seasonal and life cycle. Combined (not shown), recovery and seasonality superimposed on a lifecycle it shows the conceptual strength of vegetation over time.

By projecting the proposed hydrographic time scales upon the cyclic behaviour of vegetation it becomes clear that the longest time scale for vegetation, specifically perennial vegetation like trees, is beyond hydrographic time scales and closing in on time scales often related to system shifts, thereby underlining the complexity of the use and influence of vegetation. The other two are more aligned: seasonal cyclicality of vegetation generally has a similar period as cyclicality in base flow but they may be offset. The flood recovery interval for vegetation directly relates to a flood event in such a way that the magnitude is inversely related to the magnitude or volume of the flood peak, altered by the conceptual strength of the vegetation. The length of this recovery interval is then dependent on both the position on the life and seasonality cycle. Consequently, when the reoccurrence interval (frequency) of equal (or larger) flood events (Figure 6.2) is smaller than the recovery length (Figure 6.3), systems theoretically become more inclined to degrade. This concept links with the proposed T_{veg} of Paola (2001), where higher flood frequency with limited recovery length would result in an increased T^* and thus widening of the braided system.

The braided river experiments (chapter 5) in this research aimed to capture two of the vegetation time scales to determine the impact they have on a fluvial system. The short-term impact on vegetation, the recovery time scale, was represented as the breaks between flood events and the impact of recovery interval was thus represented by the difference in vegetative health between the first similar flood event of a day and the second similar flood event on the same day. However, within the experiments there was no or very limited evidence of recovery (chapter 5, Figure 5.12) between these first and second events, in fact, in events with younger vegetation the impact of vegetation increased over the second event, thereby suggesting a reverse, stabilising, relation to flood impact.

The long-term impacts of vegetation, the combined lifecycle and seasonality, was represented in the experiments by the growth time of the alfalfa, and as such aligns with the different running days in the braided river experiments (chapter 5) or with the different vegetation settings in the bank erosion experiments (chapter 3). Hence, both experiments were effective in capturing the impact of vegetation age on a fluvial system thereby generating a dataset of erodibility of alfalfa over its own lifecycle. Here, alfalfa was used as an analogue for real vegetation, allowing each stage of alfalfa to mimic a certain stage of natural vegetation. As such, this dataset links alfalfa strength to a certain moment on a lifecycle, regardless of seasonality or flood recovery as each event in the experiments was a representation of just a single moment in time without memory.

As a result, these events with vegetation draw on multiple locations within a time and space diagram. Compared to the non-vegetated experiments they are a similar spatial scale but the temporal scale is in general larger (but can be similar) as it represents either the seasonal or life cycle of vegetation. As such, experiments with vegetation can be seen as different snapshots along the temporal axis (Figure 6.4).

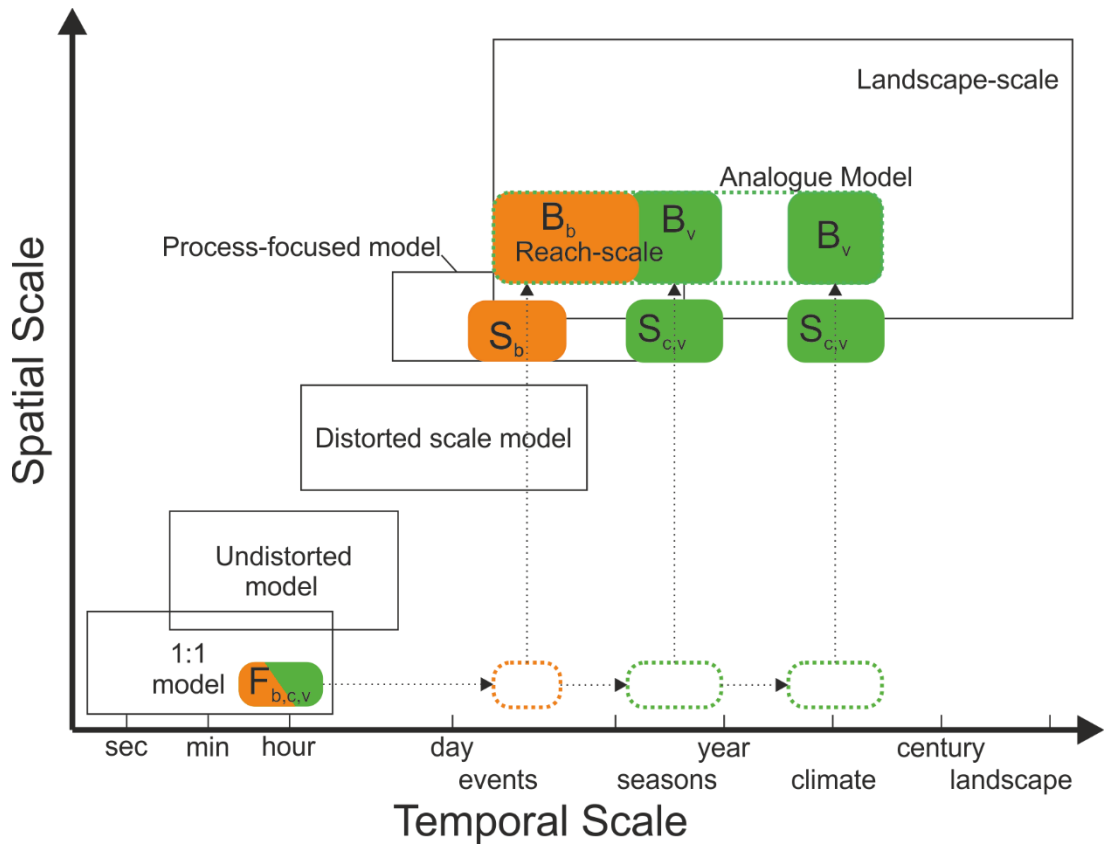


Figure 6.4: Schematic overview of different types of physical models and their placement over spatial and temporal scales. Coloured fields indicate suggestive location of the present experiments highlighted in orange (bare experiments) or green (experiments with surrogates). Uppercase B are the braided experiments, S are the planform experiments and F are the bank erosion experiments. Subscripts indicate bare settings (_b), vegetated settings (_v) or settings with surrogates (_c) (concept after Peakall et al., 1996).

6.1.3. Chemical scaling

Throughout this research, experiments used different chemicals as surrogates for vegetation. In this process, it was attempted to scale the chemical surrogates quasi 1:1 to the cohesion of alfalfa surrogate vegetation (Figure 6.5), thereby proposing scaling decisions and associated issues with how alfalfa is scaled to natural vegetation.



Figure 6.5: Schematic overview scaling choices of different used surrogates within the present sets of experiments.

Beyond the specific scaling towards prototype vegetation, the scaling of chemicals, being introduced as a grained powder, needs to obey (or at least not disagree) with scaling rules for sediment and flow. Grains of the chemicals are both much finer than the sediment and only a fraction ($1/1000^{\text{th}}$) of the mass. As such, any impact on roughness, flow and other hydrodynamics should be negligible. However, once activated, chemicals can have additional impacts such as drag reduction (Wyatt et al., 2011) but these impacts were not observed herein.

6.2. Use of surrogates in physical models

Over the past decades, several surrogates have been used to represent cohesion in physical models, e.g. clay (Smith, 1998), silica (van Dijk et al., 2012), cress-like vegetation (Gran & Paola, 2001), biofilms (Malarkey et al., 2015), and chemicals (Tolhurst et al., 2002). This thesis has focused on two of them; chemical surrogates and the cress-like vegetation alfalfa (*Medicago sativa*). While alfalfa has been used effectively in a wide range of fluvial physical models (Bertoldi et al., 2015; Gran & Paola, 2001; Tal & Paola, 2010; van de Lageweg et al., 2010), this research did not aim to explore the representability of alfalfa vegetation, instead it compared the characteristics of alfalfa with the characteristics of less commonly used chemical surrogates. Nonetheless, as environmental conditions impact alfalfa growth and development, a reflection was made on how to use alfalfa, extending the research of Clarke (2014) by focussing on experimental use and repeatability. For surrogate vegetation and corresponding chemical surrogates, a range of parameters and choices must be considered for their use in experimental physical modelling. Figure 6.6 shows an overview of which choices are needed and what options (mandatory and optional) there are to tune when using live surrogates such as alfalfa or chemicals in a physical model. The next sections will discuss and expand on this diagram.

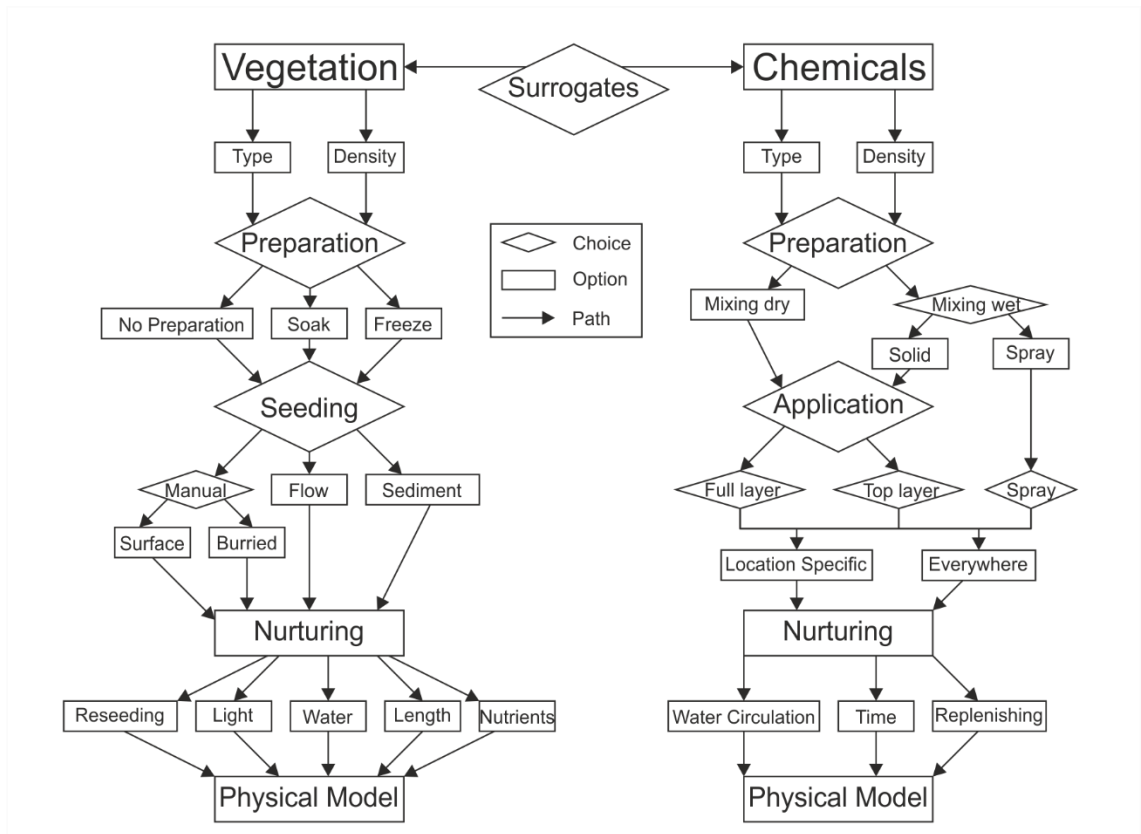


Figure 6.6: Flow-diagram of choices and options when using two surrogates to represent vegetation in a physical model. Diagram of surrogate vegetation, based on Alfalfa, on the left, diagram of surrogate chemicals, based on Xanthan Gum, Carrageenan and Sodium Alginate, on the right.

6.2.1. Live vegetation surrogates

6.2.1.1. Species selection and preparation

The first step after choosing to use a living surrogate is to select a species and a seeding density. The added cohesion of vegetation relates predominantly to the roots or root structure. However, no root structure is the same, and is different for different species or environments (e.g. Pages, 2011). Moreover, as vegetation develops over time, simultaneously root structures develop over time, just as they also can change in response to changing environmental conditions. On top of that, cohesive strength of roots may also vary seasonally. Whereas the focus of this research was on alfalfa due to its robustness and root characteristics (Clarke, 2014; van de Lageweg et al., 2010), in other settings other types of surrogate vegetation may be favourable to represent different species or processes (Lokhorst et al., 2019). Likewise, seeding density needs to be selected dependent on the overall aim. Overall, a higher seeding density

generates more erosion resistance, but results in chapter 3 show that erosion resistance does not continue to increase with seeding density. Additionally, Clarke (2014) identified the need to consider germination rates (i.e. how many seeds sprout out of those seeded), particularly when representing specific natural settings.

After selecting surrogate vegetation, the option of seed preparation needs to be considered. For all experiments reported herein, seeds were used without preparation. However, past research showed that pre-soaking seeds for several days in water or moist paper towels (Clarke, 2014; Gran & Paola, 2001) increases germination rates and reduces germination times (Clarke, 2014) and thus can reduce experimental time (at the cost of more time-intensive preparation in advance). However, pre-soaking has disadvantages experienced during the set-up of the present experiments. First, wet seeds tend to cluster, making them more difficult to distribute evenly. Seeds can be air-dried but this takes time and space which is not always readily available, in particular for larger quantities of seeds like in chapter 5. Second, pre-soaking stimulates germination to start early and as such can result in entangling of small sprouts in the paper towel or each other, making them more fragile and difficult to distribute. The additional resources (time, manpower and/or space) for pre-soaking therefore need to be balanced against the potential advantages of rapid germination.

6.2.1.2. Seeding

Experiments in the present research use a manual method to spread seeds over the surface of the sediment. The spreading of seeds was favoured over methods that bury seeds because: 1. it does not disturb existing morphology by planting, 2. it does not disturb existing morphology by sprouting, and 3. it results in less variation in germination rates. In contrast, burial of seeds can be seen as more similar to natural processes, but since it interferes with the morphology of the experiment it has not been used frequently in physical experiments (only by Clarke (2014)). One alternative approach within physical modelling is to distribute the seeds using the flow through the fluvial system. This can be done by mixing the seeds with the incoming flow and using

designated flood events to spread them out over channels, bars and floodplains (van Dijk et al., 2013b), a method that approximates natural seed distribution by the flow. A second alternative approach is a hybrid method with manual surface seeding (Gran and Paola, 2001) where seeds spread into the channels are redistributed within the channel by the flow, a method that approximates natural dispersal of seeds by wind. Flow-driven distribution methods, although representative for natural flow distribution of seeds, have the tendency to generate clusters of seeds and thus vegetation on depositional areas, potentially over enhancing erosion resistance at such locations. A third alternative method would introduce burial of seeds in an initial bed, before the existence of a distinct morphology. Although this would remove the extra seeding task, its use is debatable for larger spatial experiments due its limited control on sprouting.

6.2.1.3. Nurturing

After sowing seeds, several methods can be adopted to nurture the surrogate plants. All options can limit, enhance or even force growth in a specific direction. Although these affect the growth during both the growing period and during the effective physical experiment, the setup is in general an order of magnitude longer and thus the focus of this section. Water and lighting (or the lack thereof) are the most critical factors to control. Both exist already in the experimental setting and as such tuning them improves repeatability of experiments. Water is important for two aspects, germination and root growth. A lack of water prevents or slows down the germination rate of an alfalfa seed, which can enhance the time of an experiment, but it can also cause different growth conditions across an experiment when areas are less moist than others due to, for example, a lower water table. Experimental observations (e.g. chapter 5 and Williams et al. (2018)) suggest a fuzzy threshold for moisture to allow sprouting but evidence for this is lacking. The influence of the water table on roots is clear, since plants naturally tend to seek water. Hence, a low water table forces roots to extend vertically while a high water-table stimulates horizontal or even above-surface root growth.

Root growth is also dependent on light availability. Van de Lageweg *et al.* (2010) demonstrated that darker areas of the laboratory encouraged alfalfa plants to spend more energy on above surface biomass growth thereby increasing stem height at the cost of root length. Beyond light intensity, three other factors influence vegetation growth. First, light direction, with light coming from the side (e.g. windows) tending to force growth in a dominant direction away from the normal. Second, lighting type, which can be differentiated in three different categories; natural sunlight, either direct or indirect, which is often least favoured due its dynamic location and strength; regular room lighting, e.g. fluorescent lighting; and specific 'grow-lights' that include near-infrared light to enhance plant growth and simulate the properties of natural sunlight. Both latter sources of light are suitable but growing speeds with near-infrared light tend to be faster based on experience from chapters 3 and 5 as well as other research (Clarke, 2014; van de Lageweg *et al.*, 2010). Moreover, experiments in chapter 4 showed that different lighting types can interact with each other, so it is favourable to include experiments from multiple light sources.

Third, root length and root complexity increase over time. As such, in order to represent specific systems or conditions quantitatively it is important to select a specific stage of plant growth independently from other environmental conditions in a flume. An additional factor that can be included is reseeding, which allows new seeds to grow beyond an initial seeding cycle and allows coexistence of different stages of vegetation succession. Whereas reseeding is optional within physical models, its use could heavily expand the possibilities of the representation of natural systems, in particular those over longer time scales where different seeding could help capture a range of instances in the vegetation life cycle and thus accelerate relative time. Nonetheless, it requires similar choices as the initial seeding procedure with a strong preference for surface methods of manual seeding or flow distribution due to the destructive impact other methods have on an existing system.

The final control is the use of nutrients; within physical modelling this optional control has not been employed so far. However, in agricultural crop growing practices it is a common addition (W. K. Berg et al., 2005). Alfalfa seeds naturally have enough nutrients to grow in nutrient poor (e.g. sand used in physical experiments) environments. Nonetheless, agricultural research on alfalfa indicates growth rates of several tens of centimetres for both stem and roots with the addition of added nutrients (Undersander et al., 2011). Whereas enhanced growth would not necessarily suit analogue fluvial models, it may provide opportunities for introducing vegetation into physical models with a smaller spatial scale (e.g. undistorted models or distorted scale models). One warning should be taken into account while using alfalfa: in agricultural fields it is used as a rotational crop due to its auto toxicity (W. K. Berg et al., 2005; Undersander et al., 2011). As such, there is a theoretical potential for physical models to become infertile for alfalfa after repeated use but in practice this is unlikely because of the relatively short duration of physical models. Finally, there is unexplored potential to use nutrients to enhance growth times and reduce experimental downtime.

6.2.2. Chemical surrogates

An alternative approach to surrogate vegetation in physical models is the use of chemical surrogates. For chemical surrogates, this research lists similar choices and parameters to consider when setting-up a physical model (Figure 6.6).

6.2.2.1. *Type and concentration*

Like surrogate vegetation, chemical surrogates can vary widely and as such a selection of type and concentration is required. This research focused on a type of chemicals often grouped as EPS (extracellular polymeric substances) or polysaccharides, which are often relatively easily obtainable as powdered food additives (e.g. xanthan gum, carrageenan or sodium alginate, (chapter 3)). The selection of type and concentration are the primary factors to adapt the cohesive strength and as such a key step to understand how to represent vegetation.

6.2.2.2. Preparation

Regardless of the type of chemical, water is required to activate the cohesive effect of the chemical. This research used three different types of chemicals (xanthan gum, carrageenan and sodium alginate) and found no difference between the chemicals in response to different mixing methods (chapters 3 and 4). A first approach mixes the dry chemical powder with the dry sediment before slowly adding water. This research (chapter 3) found that a consistent mixture can be produced by adding 230 mL of water per kilogram of sediment. One alternative methods initially mixes the chemical powder in water, forming a slimy or gel-like, highly viscous mixture, before adding it to the sediment by either mixing it through (Fernandez et al., 2019) or spraying it on top the sediment surface (see chapter 5). For these wet mixing methods, consistency was harder to control, in particular as mixing with water at temperatures less than 50°C (+/- 10°C) favours flocculation (see chapter 4). As a final alternative method, van de Lageweg *et al.* (2018) spread powdered xanthan gum over the sediment before spraying it with water. Of these methods, the first approach is novel, despite its effective use in linked experiments later (Sanders, 2020; Williams, McLelland, et al., 2018) or similar proportions as used in later research on soil strength (Soldo and Miletic, 2019), and is preferred over other methods, as it allows full control of concentration and simple bed preparation. In addition, spraying methods alter conditions during an experiment, which can be advantageous or disadvantageous depending on the preferred settings of an experiment. Furthermore, the depth to which the cohesive influence extends into the substrate is unknown and remains untested.

The importance of capturing layering may be critical for deciding the application method. Hence, the depth of this cohesive layer is key. Layers that are too shallow promote bank or bar undercutting, whereas filling the entire the sediment basin with a mixture would require more time and resources. An effective middle ground, used in this research, is to only apply the mixture up to the expected channel depth. Furthermore, any type of layering has to accommodate any potential leaching of the chemical down through the sediment column (chapter 4), an effect that, if significant, is expected to reduce over time. Additionally, a choice

can be made whether to selectively add chemicals to specific areas or on specific morphologic features. This method has not been tested for longer durations (periods beyond a single day).

6.2.2.3. *Maintenance*

Once the chemical is applied and activated there are three critical behaviours of chemical surrogates that can be monitored. First, the behaviour of chemical surrogates alters as the moisture content reduces, becoming strongest (more cohesive) when the material dries out. During this research, application times were kept brief (under 15 minutes), however, there is no quantitative estimation of the rate at which the material hardens. As such, it is advisable to avoid long application times to avoid solidifying the entire bed. This limits the ability to control the behaviour of these chemicals over time, hence this research introduced an alternative approach with sodium alginate (see chapter 3). It was found that the addition of sodium bicarbonate to the fluid allowed a controlled reduction of the cohesive effect of sodium alginate. This approach requires careful monitoring of the water in a system that recirculates water in a 'closed-loop' since sediment containing chemical surrogates erodes, either releasing the chemical surrogates or dissolving them. Thus, when sodium alginate reacts with sodium bicarbonate, the concentration of sodium bicarbonate is expected to reduce due to the reaction as seen in chapters 3-4. The impact of this effect can best be monitored by measuring conductivity and best countered by using larger fluid volumes in the closed system.

6.2.3. *Is there a best approach?*

Beyond the key information on how to use chemical surrogates, how to use surrogate live vegetation and how to scale them, it is also critical to understand the advantages and disadvantages of each of the methods and in what type of models the different methods may be optimal.

Surrogate vegetation like alfalfa has already proven its functionality in physical modelling (Gran and Paola, 2001; Tal and Paola, 2007), but the present research has enhanced this understanding in two ways. First, as alfalfa becomes older and more complex, its impact on the system, e.g.

erosion rates, becomes larger despite a slightly diminished effect. Second, the complexity of alfalfa not only depends on the duration of growth but is also affected by environmental conditions in the lab (e.g. moisture and lighting), an effect which was already touched upon by Clarke (2014) but was strengthened by this research. Furthermore, although preparation and seeding approaches can slightly lower experimental downtime by days (see Clarke, 2014), alfalfa takes still several days to a week of preparation time before it has developed into a stage where it generates some impact on (and thus is representative of) fluvial systems. Unlike alfalfa, chemical surrogates can represent this complexity and thus cohesion near instantly at a timespan well within bed preparation time, a factor that becomes even more favourable when older, and more resistant, vegetation is needed which requires longer growth periods for alfalfa. Although chemical surrogates can represent the cohesive effect of all stages of alfalfa growth, in settings where different stages of vegetation follow each other in sequence (e.g. the braided river experiments (chapter 5)) the basic approach (chapter 3) with chemicals lacks the adaptability to represent *in situ* growing alfalfa. Introduction of an alternative approach using sodium alginate and water dosed with sodium bicarbonate (chapter 3) partially resolves issues with adaptability. This alteration of the fluid, achieved *in situ* by adding sodium bicarbonate, allows control of the cohesive character of the chemical surrogate. Furthermore, this approach is effective in both directions, allowing both a reduction and an increase in cohesion, thereby enhancing its potential over alfalfa that only increases in cohesion under environmental conditions (chapter 4). However, depending on the method, the use of these chemicals comes with a limitation. When sediment is dry- (or wet-) mixed with the sodium alginate, there is a limitation to apply these on existing morphology. The alternative, the use of a spray of dissolved chemicals, does not have this limitation but experiments (chapter 4) have shown that cohesive processes are different and cohesion is more difficult to control.

Another important aspect when considering experiments to represent vegetation is the ability to represent the settlement of bare areas by vegetation. Not only can alfalfa be spread or

seeded manually on either specific areas of the flume or on specific morphologic features, it, as a floating seed, also allows distribution by the flow, thereby mimicking patterns of flow-based settlement of natural vegetation. Such spatial organisation cannot be achieved by chemical surrogates.

A last aspect is sensitivity to environmental conditions. Alfalfa, as touched upon earlier, despite being one of the most robust amongst surrogate vegetation (van de Lageweg et al., 2010), is sensitive to both moisture and light conditions. On the other hand, lighting conditions do not alter chemical surrogates. Furthermore, xanthan gum is not affected by common changes in environmental conditions either, e.g. pH (REF). Nonetheless, in this research, all chemical surrogates showed a sensitivity to open air once activated with water, specifically when the sediment started to dry out or drain. This identifies two recommendations when planning these types of experiments. First, experimental setup needs to be quick and thus favours automated mixing procedures. Second, continuous (beyond small temporal breaks for data collection) experiments are favoured over experiments with overnight breaks, common in physical experiments (e.g. braided experiments in chapter 5), to keep experimental beds moist.

The above indicates that the effectiveness of either alfalfa surrogates or chemical surrogates is dependent on conditions and thus dependent on the purpose of the physical model. Evidence presented herein can help predict what type of physical models would benefit most from the use of chemical surrogates, and what type of physical models would benefit most from the use of alfalfa. Hence, it introduces a conceptual spatial scale – mobility diagram; spatial scale hereby describing the size of the experiment whereas relative mobility is an indicative channel migration rate per channel width. In this conceptual diagram (Figure 6.7), the use of chemical surrogates is recommended for small-scale and short-term experiments with a large number of repetitions (e.g. like the bank erosion experiments in chapter 3) to overcome the long growing times of surrogate vegetation. On a larger scale (e.g. process-based or analogue models similar to chapters 4 and 5), the use of chemical surrogates is still effective on spatially less dynamic

settings with low and unidirectional relative mobility (e.g. the evolution of a meander bend). Chapter 4 shows that chemical surrogates can be effective for either constant or changing cohesive conditions (e.g. seasonality or even life cycles of plants). However, for more dynamic systems with constant reworking of bars (e.g. the braided river experiments in chapter 5), the lack of reapplication of chemical surrogates would hinder the ability to present the natural behaviour of growth and regrowth of vegetation. Finally, over the largest spatial scales, chemicals have the ability to outweigh surrogate vegetation again, as here chemicals can represent geological features by using horizontal or vertical layers through the bed to look at the long-term evolution of these systems. The latter also links to a third potential axis in this diagram: time. Shorter experiments with limited temporal variation favour conditions for chemical surrogates, longer experiments with more temporal variation require the flexibility of surrogate vegetation.

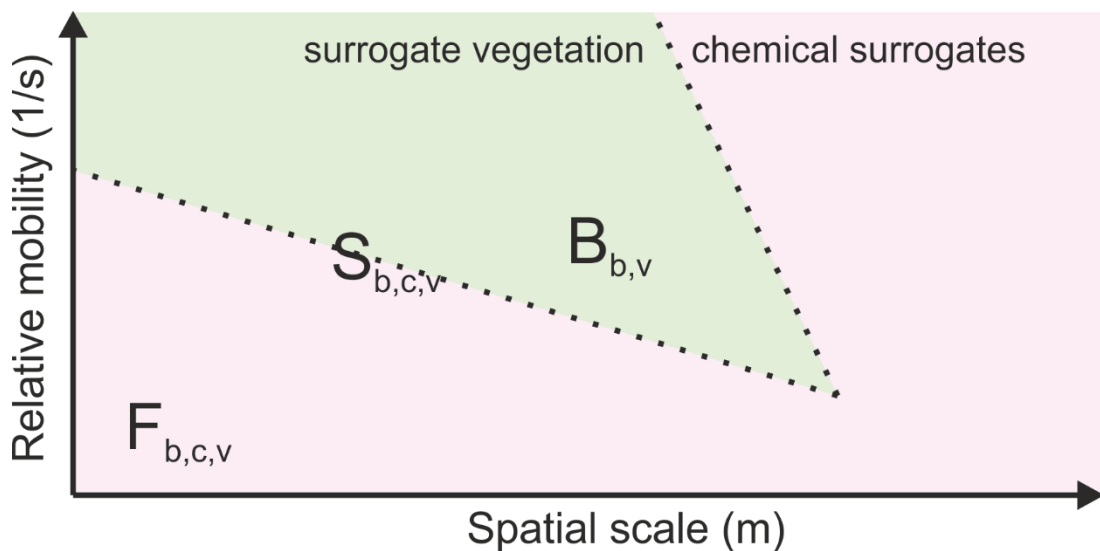


Figure 6.7: Conceptual spatial-mobility diagram with spatial scale of experiments against relative channel mobility; conceptual channel mobility described as channel movement relative to channel width ($ms^{-1}m^{-1}$). Shading indicates preference for surrogate vegetation (green) or chemical surrogates (pink). Uppercase letters indicate braided river experiments (B), planform river experiments (S) and bank erosion experiments (F).

6.3. Limitations

The above paragraphs have already suggested specific issues with the executed braided river experiments (chapter 5). As such, this section will discuss limitations in design and execution of the present braided experiments as both alter the reliability of results and should therefore be acknowledged to prevent repetition in future physical experiments.

6.3.1. Discharge

The first, and possibly largest, issue was related to the discharge, which was too high, in particular for the relatively small sediment size. Similar experiments either used a lower discharge (Bertoldi et al., 2015; Gran & Paola, 2001; Peirce et al., 2018; van de Lageweg, 2013; van Dijk, Teske, et al., 2013) or a larger grain size (Ashworth, 1996; Eaton & Church, 2004; Egozi & Ashmore, 2008, 2009; Garcia Lugo et al., 2015; Moreton et al., 2002; Peirce et al., 2018) that would limit the lateral extent of the braided system. Experiments with both a similar range of discharges and a similar sediment size either had a shorter experimental duration (Hoey & Sutherland, 1991; Young & Davies, 1991) or used aggrading basins (Ashworth et al., 2007). Moreover, both characteristic aspects of the present set of experiments, an increasing channel forming discharge and the growth of vegetation within the channel belt, could force lateral expansion of the channel belt and as such would benefit from a wider experimental bed. As such, this research would strongly suggest lower discharges that additionally reduce the impact of other boundary effects as well.

6.3.2. Experimental basin width

Previous physical modelling studies that have used alfalfa in fluvial models either started off on an already developed braided system (Gran and Paola, 2001; Tal and Paola, 2007; Bertoldi et al., 2015) or an undeveloped or single thread meandering channel (Braudrick et al., 2009; van Dijk et al., 2013b). Despite the initial differences, all experiments show the stabilizing impact of surrogate vegetation. In contrast to the present research that alternated two discharge regimes, all previous models of vegetation in braided rivers used a single discharge that allowed sediment

transport. Conversely, experiments that studied meandering used a mixture of discharge regimes and suggested that higher peak flows dominantly impact (increase) deposition rates at the floodplain (van Dijk, van de Lageweg, et al., 2013). However, discharge variability is not unique to meandering systems and previous braided river experiments without vegetation or added cohesion have varied discharge to approximate flood flows. Most of these experiments used a different discharge for different experimental runs (Ashworth, 1996; Garcia Lugo et al., 2015; Peirce et al., 2018) but others used either a stepped hydrograph (Egozi & Ashmore, 2009; Peirce et al., 2018) or a sequence of high and low flows similar to the present research (van de Lageweg, 2013).

Peirce et al. (2018) indicated that increased stream power (due to increased discharge) was linked to increased active channel width. This concept of active width is similar to the area of change discussed in chapter 5, which was also positively related to discharge. Egozi and Ashmore (2008, 2009) suggested that braiding index increased with increased discharge, both when averaged over longer periods and in response to shifts over shorter time spans (1 hr intervals). However, although these shorter hourly time spans had an identical duration as the intervals in the braided experiments of chapter 5, this relationship was not observed herein as erosion width did not change significantly with increased discharge. (van de Lageweg, 2013) used a bimodal sequence of alternating large and small discharge events with dissimilar durations (2.5 hr small vs 0.5 hr large). Like the larger stream power experiments of Peirce (2018), the experiments with variable flow (and higher peak discharge) showed larger active areas but on average smaller vertical changes due the shorter duration of peak events. Obviously, a slight increase in deposition on the floodplains occurred due banks overtopping and floodplain inundation.

These findings were not duplicated herein. Whereas previous research all suggested that the active width increased at higher discharges, a key difference with the experiments of chapter 5 exists: the width of the experimental bed herein was not wide enough to allow the braided system to stay within a channel belt and as a result, no outer bank erosion could occur after the

flow had eroded towards the edge of the bed, something that occurred within the spin-up period of this experiment. Since banks are a key source of sediment in the system (van de Lageweg, 2013), this could significantly alter the system dynamics. Therefore, it is recommended that, for the discharges employed herein, a wider experimental basin is used.

6.3.3. Boundary effects

Lateral boundary effects in the braided river experiments (chapter 5), e.g. flow aligning with the bed wall, were artificially reduced with the placement of angled groynes and high-density alfalfa vegetation, but still occurred between sets of groynes. By reducing the flow, the likelihood of occurrence of boundary effects is reduced as is the effective experimental area. Alternatively, an extra, highly cohesive strip could be introduced at the edge of the experimental bed with a similar roughness but a higher shear strength to avoid both erosion and flow sticking to the 'wall'. In the second (vegetated) run of the braided river experiment (chapter 5), extra seeds were sown at the edge of the experimental bed to increase flow resistance. Run 8 of the planform river experiments (chapter 4) introduced an alternative by adding sodium alginate to a strip of sediment to increase the resistance to the flow. Of these two, the alginate-sediment mixture has an identical roughness as the regular sediment but sediment starvation is more likely to occur downstream because it provides limited sediment. In contrast, surrogate vegetation, like alfalfa, would slightly alter the roughness for otherwise bare experiments, but partly prevents sediment starvation downstream.

A third consideration in these experiments are the inlet conditions. In the present experiments (chapter 5) sediment was dropped in the flow as a static point source. Over time, this caused heavy sedimentation in the central upstream part of the bed that favoured channel splitting towards the lateral edges of experimental bed and away from the central area of interest. Whereas sediment input was in range of the transport capacity of the flow (Bertoldi et al., 2009a), the point source application on an expanding but initial 0.20 m wide channel would

stimulate an oversupply at the centre of the channel that promotes deposition. Hence, three alternative approaches are suggested to negate the impact of these processes:

- Mix sediment and water before entering the experimental bed. This can be achieved either by mixing the sediment and flow using an expanded pump (e.g. peristaltic pump) or by using an extended inlet that allows sediment to be mixed with the flow. The latter could be created with use of a sediment-coated material (Mao, 2012) or, as chapter 5 has shown, by creating a channel with a high concentration of chemicals;
- Use a moving inlet that moves laterally over time, making outflow less static and additionally forcing a long term dynamic system (van Dijk, van de Lageweg, et al., 2013);
- Change the point source into a curtain that spreads more evenly over the flow. Chapter 4 shows that this effect can be enhanced by using the principle of a quincunx that encourages spreading over the width of the channel.

6.3.4. Temporal effects

The braided experiments in this research use a flood duration of an hour. This hour long interval is long enough to capture changes in behaviour (Egozi and Ashmore, 2009). However, for local effects of channel progression, an hourly interval of data collection is too long in dynamic systems where channels migrate multidirectionally. As such, the present research underestimates channel migration rates as channels move back and forth within the measurement interval. Peirce et al. (2018) estimated that an interval of 15 minutes was sufficient to capture morphologic changes without losing information on local movement. However, as Peirce et al. (2018) showed, this ideal interval is dependent on stream power, with a larger stream power implying shorter time intervals. As the stream power of the present research was high ($0.35 - 0.55 \text{ W m}^{-1}$), a shorter interval would have reduced the underestimation of channel migration rates. Alternatively, potential exist to use T^* (Paola, 2001) to determine the discharge where the system's equilibrium would not be larger than the existing

experimental bed width. Adding cohesion (e.g. vegetation) at later stages in experiments then only make this width smaller (and the allowed discharge larger).

As discussed above, the present braided river experiments consisted of both small and large flood events. In the experimental set-up (section 5.2), a third type of flood event was introduced. However, this extra small flood event with a sediment deficit was not successful. Not only is the data set of events with a sediment deficit limited (2 per bed per run), the events themselves also have the potential to alter the morphology prior to subsequent events. Furthermore, the sediment shortage at the inlet was not observed in the sediment output, and thus can only have induced shifts in the braided system itself that were not monitored (e.g. channel gradient).

A similar limitation exists in Run 2 with vegetation. Here, the number of flood events within each vegetative stage was both limited and variable. This caused some experimental sets to start an experimental day with a large flood event (event 8) in contrast to the more common low events (event 1, 5 and 11) in other vegetative stages. However, due the limited number of events (1 or 2) per vegetation stage, this impact cannot be distinguished. Future research would benefit from regular and structured hydrographs with a high number of repetitions. Repetitions in a range of 30-40 have been suggested for braided experiments on bed load (Redolfi, 2018, pers. comm.) but are obviously out of range for experiments with growing surrogate vegetation. As such, future experiments need to find a balance between repetition and consistency when using surrogate vegetation. This was in part overcome in the present research by using an analysis method (chapter 5) that due to its local nature (and thus high number of replicates) is less sensitive to the limited number of replicated events.

6.4. Impact of vegetation

Beyond the structural limitations of the experiments, there is also a debate on of the extent to which live surrogate vegetation is representative of natural vegetation in rivers. As suggested previously, the flood discharges of this experiment were too large, an effect that excluded any outer bank processes from the experiment. In natural braided systems, there is a clear

distinction between outer bank processes (e.g. expansion of the braid belt) and inner belt processes. Often the outer bank is densely vegetated with a well-established soil that makes the outer bank relatively erosion resistant. However, when outer bank erosion continues in an incising or contained system, undercutting can occur below soil that is reinforced by roots of growing vegetation (e.g. Figure 6.8 A). This will eventually cause cantilever mass failures that allow erosion to follow a more irregular pattern due to the interaction between shear strength and transport capacity on a block of sediment (Figure 6.8 B). In addition, over relatively short timescales, outer bank erosion is an irreversible process because outer bank deposition has a larger time scale that is beyond the scope of this research and links to channel belt wide avulsive processes that are less common in braided systems.

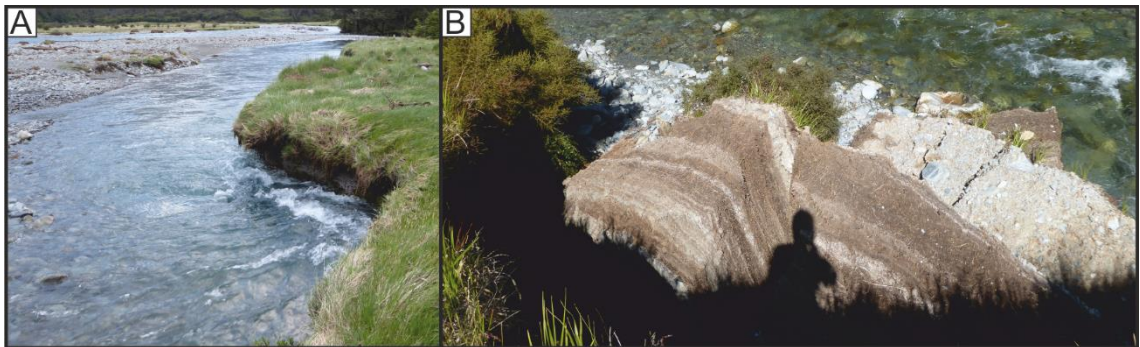


Figure 6.8: Examples of bank erosion; A) Potential for undercutting of a grassy bank at Waiau river (NZ). B) Result of an undercut bank as compact blocks of soil in a small braided river (Dingle Burn (NZ)). Pictures by the author (2020)

Inner channel belt erosive processes are more common as the shear strength of the non-cohesive and/or unconsolidated sediment is often less than that of the outer bank. One reason for this is that in active braided systems vegetation does not have enough time to develop into full-grown trees and as such structurally provides less strength to the surrounding sediment. However, within the channel belt, vegetation often follows a progressive succession, linked to how long it has been without stress since a last flood event (Figure 6.9 A). As such, the duration of each successional stage depends on the climate, soil/sediment type as well as the regular flood regime of the system. Although vegetation assemblages vary, successional stages are consistent in gravel rivers (e.g. Corenblit et al., 2007; Gurnell, 2014). Hence, a first stage relates

to mosses and small pioneering species that develop sheltered between sediment clasts (Figure 6.9 B). This is succeeded by scattered, small herbaceous plants (Figure 6.9 C) and eventually grass cover (Figure 6.9 D). These herbaceous plants slowly create a stable substrate on which shrubs and eventually trees can establish. However, the above stages are less consistent in finer grained systems, where the different stages are more intertwined (e.g. Simon et al., 2006).

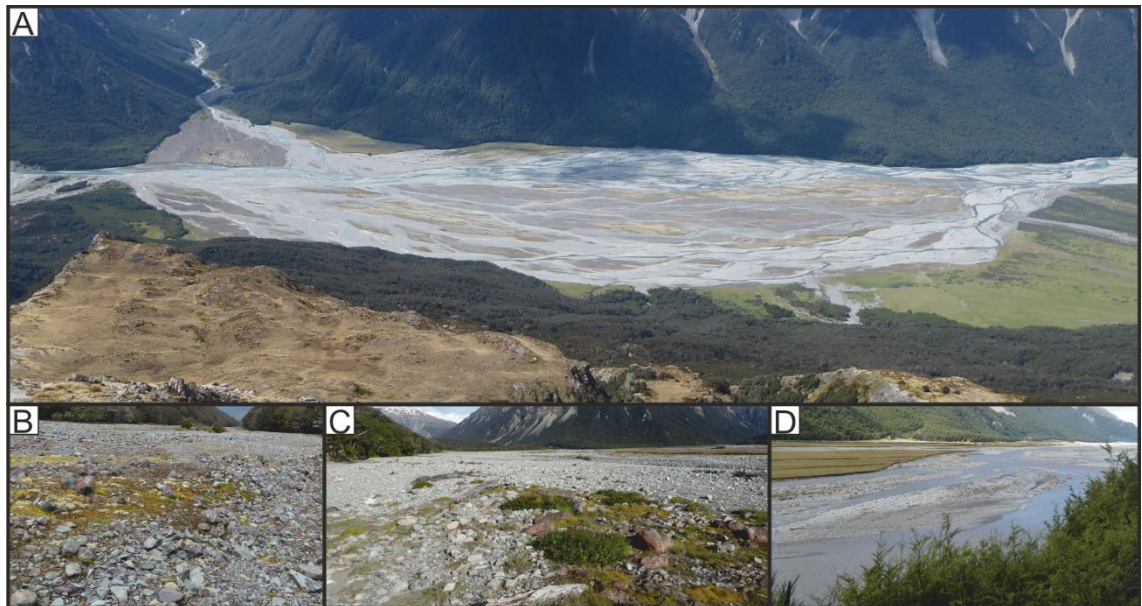


Figure 6.9: Overview of different stages of vegetation succession in active braided systems in New Zealand. Colours in A highlight the different stages of succession occurring simultaneously in the channel belt of the Upper Waimakariri- grey = base sediment, yellows = mosses, light green = grasses, dark green = trees. B mosses at Steele Creek, C small herbaceous vegetation at Waimakariri river and D grasses at Hopkins river. Pictures by the author (2020).

Within physical modelling, it is expected that the cohesion due to vegetation increases along each progressive stage. However, there is limited evidence of a linear relation (Edmaier et al., 2014) in particular due the interplay of above-surface drag forces and below-surface root structures whose impact depends on both flow depth and bank height. As such, physical modelling studies can improve by understanding the specific impact of these different stages on cohesion which can be identified in the field from aerial imagery and at ground level (see Figure 6.9) and thus specified at the local scale. Additionally, there is an opportunity to use sedimentary records of erosion in physical models (see Figure 6.10 and van de Lageweg (2013a)) and align these to colour patterns in aerial imagery of braided rivers (e.g. similar to Figure 6.9 A).

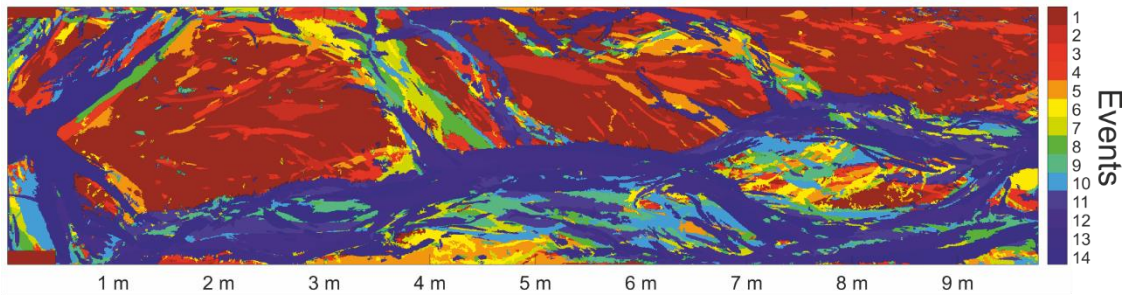


Figure 6.10: Map of bed 1 after the final event (14) of Run 2 that indicates the last event that erosion (> 2 mm) occurred for each cell. These types of maps can be used to capture the temporal evolution of the spatial distribution of the channels over the bed and linked to the potential age of vegetation.

7. Conclusion

The introduction of vegetation in physical models is not straightforward. Some researchers have used similar methods (e.g. alfalfa (Bertoldi et al., 2015; Braudrick et al., 2009; Tal & Paola, 2007)), others designed methods that fitted a specific purpose (e.g. Coulthard, 2005) and yet others used vegetation as a tool (e.g. to increase cohesion (Gran & Paola, 2001)). As such, to represent vegetation in flumes it is key to understand what factors or processes any model vegetation needs to simulate. There has been significant growth of research on vegetation, ranging from catchment scale research on deforestation or land use change (Twine et al., 2004), through reach scale impacts of riparian vegetation (Steiger et al., 2003) to morphologic unit scale impacts on pioneering bar growth (Crouzy et al., 2013). Furthermore, there has been research on individual plants for either through flow (Boothroyd, 2017), bank resistance (Pollen, 2007) or sediment trapping (Gurnell, 2014) but also case specific research on wood deposits (Welber et al., 2013) or flood management protection by vegetation (Iacob et al., 2014). Like the variety of the research and vegetation types, it comes as no surprise that there is no single representation method as of yet and it is likely this variety is too large for such to happen in the near future, making it fruitful to aim for overarching areas and the processes involving them, e.g. cohesion, flow resistance, flow retention, and sedimentation. Therefore, this thesis touched upon one aspect, i.e. cohesion, and explored the possibilities to represent this in physical modelling.

The present research has shown that the cohesive effect of vegetation cannot be neglected. Added vegetation in the experiments reduces erosion rates, an impact that increases as vegetation grows more mature (and complex). This research introduced erosion width as a different approach to qualify channel mobility and showed that local effects of erosion by vegetation propagate into a reduction in channel mobility, in particular for smaller floods. Vegetation age is also important for channel mobility but its impact is mainly observed in a reduction of channel mobility during large floods.

Beyond capturing the overall impact of vegetation on fluvial systems, this research put effort in understanding how to represent vegetation within physical models. Hence, it showed that the cohesive effect of vegetation can be represented by using live vegetation or chemical surrogates. Chemical surrogates have the benefit of near instant application for most required conditions and thus provide a reduction in experimental time for temporally uniform conditions. Live surrogate vegetation allows cohesion to evolve and become stronger over time as root structures develop. Straightforward application of chemical surrogates does not provide this benefit. However, this research showed that the use of a different fluid medium allows control over the cohesive effect of the chemical surrogate. This expands the potential of this chemical surrogate to most fluvial settings with lateral migration.

References

- Alabyan, A. M., & Chalov, R. S. (1998). Types of river channel patterns and their natural controls. *Earth Surface Processes and Landforms*, 23(5), 467–474. [https://doi.org/10.1002/\(SICI\)1096-9837\(199805\)23:5<467::AID-ESP861>3.0.CO;2-T](https://doi.org/10.1002/(SICI)1096-9837(199805)23:5<467::AID-ESP861>3.0.CO;2-T)
- An, H., Chen, S., Chan, H., & Hsu, Y. (2013). Dimension and frequency of bar formation in a braided river. *International Journal of Sediment Research*, 28(3), 358–367. [https://doi.org/10.1016/S1001-6279\(13\)60046-3](https://doi.org/10.1016/S1001-6279(13)60046-3)
- Ashmore, P. (1982). Laboratory modelling of gravel braided stream morphology. *Earth Surface Processes and Landforms*, 7(3), 201–225. <https://doi.org/10.1002/esp.3290070301>
- Ashmore, P. (1991a). Channel Morphology and Bed Load Pulses in Braided, Gravel-Bed Streams. *Geografiska Annaler*, 73(1), 37–52. <https://doi.org/10.2307/521212>
- Ashmore, P. (1991b). How do gravel-bed rivers braid? *Canadian Journal of Earth Sciences*, 28, 326–341. <https://doi.org/10.1139/e91-030>
- Ashworth, P. J. (1996). Mid-channel bar growth and its relationship to local flow strength and direction. *Earth Surface Processes and Landforms*, 21(2), 103–123. [https://doi.org/10.1002/\(SICI\)1096-9837\(199602\)21:2<103::AID-ESP569>3.0.CO;2-O](https://doi.org/10.1002/(SICI)1096-9837(199602)21:2<103::AID-ESP569>3.0.CO;2-O)
- Ashworth, P. J., Best, J. L., & Jones, M. (2004). Relationship between sediment supply and avulsion frequency in braided rivers. *Geology*, 32(1), 21–24. <https://doi.org/10.1130/G19919.1>
- Ashworth, P. J., Best, J. L., & Jones, M. A. (2007). The relationship between channel avulsion, flow occupancy and aggradation in braided rivers: Insights from an experimental model. *Sedimentology*, 54(3), 497–513. <https://doi.org/10.1111/j.1365-3091.2006.00845.x>
- Ashworth, P. J., Ferguson, R. I., & Powell, M. D. (1991). Bedload Transport and Sorting in Braided Channels. In P. Billi, R. D. Hey, C. R. Thorne, & P. Tacconi (Eds.), *Dynamics of Gravel-bed Rivers* (Issue July, pp. 497–515). Chichester, UK; John Wiley & Sons Ltd.
- Bankhead, N. L., Thomas, R. E., & Simon, A. (2016). A combined field, laboratory and numerical study of the forces applied to, and the potential for removal of, bar top vegetation in a braided river. *Earth Surface Processes and Landforms*, 42(3), 439–459. <https://doi.org/10.1002/esp.3997>
- Baynes, E. R. C., Attal, M., Niedermann, S., Kirstein, L. A., Dugmore, A. J., & Naylor, M. (2015). Erosion during extreme flood events dominates Holocene canyon evolution in northeast Iceland. *Proceedings of the National Academy of Sciences*, 112(8), 2355–2360. <https://doi.org/10.1073/pnas.1415443112>
- Baynes, E. R. C., van de Lageweg, W. I., McLelland, S. J., Parsons, D. R., Aberle, J., Dijkstra, J., Henry, P. Y., Rice, S. P., Thom, M., & Moulin, F. (2018). Beyond equilibrium: Re-evaluating physical modelling of fluvial systems to represent climate changes. *Earth-Science Reviews*, 181(February 2017), 82–97. <https://doi.org/10.1016/j.earscirev.2018.04.007>
- Bendix, J., & Stella, J. C. (2013). Riparian Vegetation and the Fluvial Environment: A Biogeographic Perspective. In J. Shroder, D. R. Buller, & C. R. Hupp (Eds.), *Treatise on Geomorphology*: (Vol. 12, pp. 53–74). San Diego; Elsevier. <https://doi.org/10.1016/B978-0-12-374739-6.00322-5>

- Berg, W. K., Cunningham, S. M., Brouder, S. M., Joern, B. C., Johnson, K. D., Santini, J., & Volenec, J. J. (2005). Influence of phosphorus and potassium on alfalfa yield and yield components. *Crop Science*, *45*(1), 297–304. <https://doi.org/10.2135/cropsci2005.0297>
- Bertoldi, W., Ashmore, P., & Tubino, M. (2009). A method for estimating the mean bed load flux in braided rivers. *Geomorphology*, *103*(3), 330–340. <https://doi.org/10.1016/j.geomorph.2008.06.014>
- Bertoldi, W., & Tubino, M. (2005). Bed and bank evolution of bifurcating channels. *Water Resources Research*, *41*(7), 1–12. <https://doi.org/10.1029/2004WR003333>
- Bertoldi, W., Welber, M., Gurnell, A. M., Mao, L., Comiti, F., & Tal, M. (2015). Physical modelling of the combined effect of vegetation and wood on river morphology. *Geomorphology*, *246*(July), 178–187. <https://doi.org/10.1016/j.geomorph.2015.05.038>
- Bertoldi, W., Welber, M., Mao, L., Zanella, S., & Comiti, F. (2014). A flume experiment on wood storage and remobilization in braided river systems. *Earth Surface Processes and Landforms*, *39*(6), 804–813. <https://doi.org/10.1002/esp.3537>
- Bertoldi, W., Zanoni, L., & Tubino, M. (2009). Planform dynamics of braided streams. *Earth Surface Processes and Landforms*, *34*, 547–557. <https://doi.org/10.1002/esp.1755>
- Bolla Pittaluga, M., Repetto, R., & Tubino, M. (2003). Channel bifurcation in braided rivers: Equilibrium configurations and stability. *Water Resources Research*, *39*(3), 1046. <https://doi.org/10.1029/2001WR001112>
- Boothroyd, R. J. (2017). *Flow-vegetation interactions at the plant-scale: the importance of volumetric canopy morphology on flow field dynamics* [PhD, Durham University]. http://etheses.dur.ac.uk/12363/1/Richard_Boothroyd_2017.pdf?DDD14
- Braudrick, C. A., Dietrich, W. E., Leverich, G. T., & Sklar, L. S. (2009). Experimental evidence for the conditions necessary to sustain meandering in coarse-bedded rivers. *Proceedings of the National Academy of Sciences*, *106*(40), 16936–16941. <https://doi.org/10.1073/pnas.0909417106>
- Camporeale, C., Perona, P., Porporato, A., & Ridolfi, L. (2005). On the long-term behavior of meandering rivers. *Water Resources Research*, *41*(12), 1–13. <https://doi.org/10.1029/2005WR004109>
- Cannon, W. A. (1949). A Tentative Classification of Root Systems. *Ecology*, *30*, 452–458.
- Carson, M. A., & Kirkby, M. J. (1972). Hillslope Form and Process. In M. A. Carson (Ed.), *Cambridge Geographical Studies* (Vol. 10, Issue 8). Cambridge; Cambridge University Press.
- Casagli, N., Rinaldi, M., Gargini, A., & Curini, A. (1999). Pore water pressure and streambank stability: Results from a monitoring site on the Sieve River, Italy. *Earth Surface Processes and Landforms*, *24*(12), 1095–1114. [https://doi.org/10.1002/\(SICI\)1096-9837\(199911\)24:12<1095::AID-ESP37>3.0.CO;2-F](https://doi.org/10.1002/(SICI)1096-9837(199911)24:12<1095::AID-ESP37>3.0.CO;2-F)
- Cazanacli, D., Paola, C., & Parker, G. (2002). Experimental Steep, Braided Flow: Application to Flooding Risk on Fans. *Journal of Hydraulic Engineering*, *128*(3), 322–330.
- Chang, I., Im, J., Prasadhi, A. K., & Cho, G. C. (2015). Effects of Xanthan gum biopolymer on soil strengthening. *Construction and Building Materials*, *74*(x), 65–72. <https://doi.org/10.1016/j.conbuildmat.2014.10.026>

- Chen, C., Wu, L., Perdjon, M., Huang, X., & Peng, Y. (2019). The drying effect on xanthan gum biopolymer treated sandy soil shear strength. *Construction and Building Materials*, *197*, 271–279. <https://doi.org/10.1016/j.conbuildmat.2018.11.120>
- Church, M. (2006). Bed Material Transport and the Morphology of Alluvial River Channels. *Annual Review of Earth and Planetary Sciences*, *34*(1), 325–354. <https://doi.org/10.1146/annurev.earth.33.092203.122721>
- Clarke, L. E. (2014). The use of live vegetation in geomorphological experiments: How to create optimal growing conditions. *Earth Surface Processes and Landforms*, *39*(5), 705–710. <https://doi.org/10.1002/esp.3534>
- Corenblit, D., Tabacchi, E., Steiger, J., & Gurnell, A. M. (2007). Reciprocal interactions and adjustments between fluvial landforms and vegetation dynamics in river corridors: A review of complementary approaches. *Earth-Science Reviews*, *84*(1–2), 56–86. <https://doi.org/10.1016/j.earscirev.2007.05.004>
- Coulthard, T. J. (2005). Effects of vegetation on braided stream pattern and dynamics. *Water Resources Research*, *41*(4), 1–9. <https://doi.org/10.1029/2004WR003201>
- Crouzy, B., Edmaier, K., Pasquale, N., & Perona, P. (2013). Impact of floods on the statistical distribution of riverbed vegetation. *Geomorphology*, *202*, 51–58. <https://doi.org/10.1016/j.geomorph.2012.09.013>
- Darby, S. E., & Thorne, C. R. (1994). Prediction of tension crack location and riverbank erosion hazards along destabilized channels. *Earth Surface Processes and Landforms*, *19*(3), 233–245. <https://doi.org/10.1002/esp.3290190304>
- Decho, A. W. (2000). Microbial biofilms in intertidal systems: An overview. *Continental Shelf Research*, *20*(10–11), 1257–1273. [https://doi.org/10.1016/S0278-4343\(00\)00022-4](https://doi.org/10.1016/S0278-4343(00)00022-4)
- Dick, B. M., Hey, R., Peralta, P., Jewell, I., Simon, P., & Peszlen, I. (2014). Estimating annual riverbank erosion rates - a dendrogeomorphic method. *River Research and Applications*, *30*, 845–856. <https://doi.org/10.1002/rra.2682>
- Eaton, B. C. (2006). Bank stability analysis for regime models of vegetated gravel bed rivers. *Earth Surface Processes and Landforms*, *31*(1), 1438–1444. <https://doi.org/10.1002/esp.1364>
- Eaton, B. C., & Church, M. (2004). A graded stream response relation for bed load-dominated streams. *Journal of Geophysical Research*, *109*(F3), 1–18. <https://doi.org/10.1029/2003JF000062>
- Edmaier, K., Crouzy, B., Ennos, R., Burlando, P., & Perona, P. (2014). Influence of root characteristics and soil variables on the uprooting mechanics of *Avena sativa* and *Medicago sativa* seedlings. *Earth Surface Processes and Landforms*, *39*(10), 1354–1364. <https://doi.org/10.1002/esp.3587>
- Egozi, R., & Ashmore, P. (2008). Defining and measuring braiding intensity. *Earth Surface Processes and Landforms*, *33*, 2121–2138. <https://doi.org/10.1002/esp.1658>
- Egozi, R., & Ashmore, P. (2009). Experimental analysis of braided channel pattern response to increased discharge. *Journal of Geophysical Research: Earth Surface*, *114*(2), 1–15. <https://doi.org/10.1029/2008JF001099>

- Eke, E., Parker, G., & Shimizu, Y. (2014). Numerical modeling of erosional and depositional bank processes in migrating river bends with self-formed width: Morphodynamics of bar push and bank pull. *Journal of Geophysical Research: Earth Surface*, *119*, 1455–1483. <https://doi.org/10.1002/2013JF003020>
- Federal Interagency Stream Restoration Working Group (U.S.). (1998). *Stream corridor restoration: principles, processes, and practices*.
- Ferguson, R. I. (1987). Hydraulic and sedimentary controls of channel pattern. In K. S. Richards (Ed.), *River channels: environment and processes* (pp. 129–158). Oxford; Blackwell.
- Fernandez, R. L., McLelland, S., Parsons, D. R., & Bodewes, B. (2021). Riparian vegetation life stages control the impact of flood sequencing in a laboratory braided river. *Earth Surface Processes and Landforms*, *46*(11), 2315–2329.
- Fernandez, R. L., Thom, M., & Dijkstra, J. (2019). *Protocols for scaling biogeomorphology in time*. Deliverable D8.5. Report submitted to the European Union under the EC 8th Framework Programme Contract no. 654110, Hydralab+. Deltares: Delft. Available online: https://hydralab.eu/private/Modules/Tools/EUProject/documents/330/D08-5_Protocols_scaling_biogeomorphology_in_time.pdf [Accessed 5/12/2020]
- Fredlund, D. G., & Rahardjo, H. (1993). Soil Mechanics for Unsaturated Soils. In *Soil Mechanics for Unsaturated Soils* (Vol. 1, pp. 1–517). New York; John Wiley & Sons, Inc. <https://doi.org/10.1002/9780470172759>
- Friedkin, J. F. (1945). A laboratory study of the meandering of alluvial rivers. In *War Department; Corps of Engineers, U.S. Army; Mississippi River commission* (Issue May 1945). Vicksburg.
- Frostick, L. E., Thomas, R. E., Johnson, M. F., Rise, S. P., & McLelland, S. J. (2014). *Users Guide to Ecohydraulic Modelling and Experimentation: Experience of the Ecohydraulic Research Team (PISCES) of the HYDRALAB Network* (1st ed.). Leiden, The Netherlands; CRC Press/Balkema. <https://doi.org/10.1201/b16630>
- Ganti, V., Chadwick, A. J., Hassenruck-Gudipati, H. J., Fuller, B. M., & Lamb, M. P. (2016). Experimental river delta size set by multiple floods and backwater hydrodynamics. *Science Advances*, *2*(5), 1–11. <https://doi.org/10.1126/sciadv.1501768>
- Garcia Lugo, G. A., Bertoldi, W., Henshaw, A. J., & Gurnell, A. M. (2015). The effect of lateral confinement on gravel bed river morphology. *Water Resources Research*, *51*, 4923–4947. <https://doi.org/10.1002/2015WR017081>
- Gardner, J. T., & Ashmore, P. E. (2011). Geometry and grain-size characteristics of the basal surface of a braided river deposit. *Geology*, *39*(3), 247–250. <https://doi.org/10.1130/G31639.1>
- Garssen, A. G., Baattrup-Pedersen, A., Voeselek, L. A. C. J., Verhoeven, J. T. A., & Soons, M. B. (2015). Riparian plant community responses to increased flooding: A meta-analysis. *Global Change Biology*, *21*(8), 2881–2890. <https://doi.org/10.1111/gcb.12921>
- Garssen, A. G., Verhoeven, J. T. A., & Soons, M. B. (2014). Effects of climate-induced increases in summer drought on riparian plant species: A meta-analysis. *Freshwater Biology*, *59*(5), 1052–1063. <https://doi.org/10.1111/fwb.12328>
- Germanoski, D., & Schumm, S. A. (1993). Changes in Braided River Morphology Resulting from Aggradation and Degradation. *The Journal of Geology*, *101*, 451–466.

- Gran, K., & Paola, C. (2001). Riparian vegetation controls on braided stream dynamics. *Water Resources Research*, 37(12), 3275–3283. <https://doi.org/10.1029/2000WR000203>
- Gurnell, A. M. (2014). Plants as river system engineers: Further comments. *Earth Surface Processes and Landforms*, 40(1), 135–137. <https://doi.org/10.1002/esp.3671>
- Gurnell, A. M., Holloway, J. V., Liffen, T., Serlet, A. J., & Zolezzi, G. (2019). Plant root and rhizome strength: are there differences between and within species and rivers? *Earth Surface Processes and Landforms*, 44, 389–392. <https://doi.org/10.1002/esp.4499>
- Gurnell, A. M., Rinaldi, M., Belletti, B., Bizzi, S., Blamauer, B., Braca, G., Buijse, A. D., Bussetini, M., Camenen, B., Comiti, F., Demarchi, L., García de Jalón, D., González del Tánago, M., Grabowski, R. C., Gunn, I. D. M., Habersack, H., Hendriks, D., Henshaw, A. J., Klösch, M., Lastoria, B., Latapie, A., Marcinkowski, P., Martínez-Fernández, V., Mosselman, E., Mountford, J. O., Nardi, L., Okruszko, T., O'Hare, M. T., Palma, M., Percopo, C., Surian, N., van de Bund, W., Weissteiner, C., & Ziliani, L. (2016). A multi-scale hierarchical framework for developing understanding of river behaviour to support river management. *Aquatic Sciences*, 78(1), 1–16. <https://doi.org/10.1007/s00027-015-0424-5>
- Hagerty, D. J., Spoor, M. F., & Parola, A. C. (1995). Near-Bank Impacts of River Stage Control. *Journal of Hydraulic Engineering*, 121(2), 196–207. [https://doi.org/10.1061/\(ASCE\)0733-9429\(1995\)121:2\(196\)](https://doi.org/10.1061/(ASCE)0733-9429(1995)121:2(196))
- Hanson, G. J., & Simon, A. (2001). Erodibility of cohesive streambeds in the loess area of the Midwestern USA. *Hydrological Processes*, 15(1), 23–38. <https://doi.org/10.1002/hyp.149>
- Heller, V. (2011). Scale effects in physical hydraulic engineering models. *Journal of Hydraulic Research*, 49(3), 293–306. <https://doi.org/10.1080/00221686.2011.578914>
- Hicks, D. M., Duncan, M. J., Lane, S. N., Tal, M., & Westaway, R. (2007). 21 Contemporary morphological change in braided gravel-bed rivers: new developments from field and laboratory studies, with particular reference to the influence of riparian vegetation. *Developments in Earth Surface Processes*, 11, 557–584. [https://doi.org/10.1016/S0928-2025\(07\)11143-3](https://doi.org/10.1016/S0928-2025(07)11143-3)
- Hoey, T. B., & Sutherland, A. J. (1991). Channel morphology and bedload pulses in braided rivers: a laboratory study. *Earth Surface Processes and Landforms*, 16(5), 447–462. <https://doi.org/10.1002/esp.3290160506>
- Hong, L. B., & Davies, T. R. H. (1979). A study of stream braiding. *Geological Society of America Bulletin*, 90(11), 1839–1859. <https://doi.org/10.1130/GSAB-P2-90-1839>
- Hundey, E. J., & Ashmore, P. E. (2009). Length scale of braided river morphology. *Water Resources Research*, 45(8), 1–9. <https://doi.org/10.1029/2008WR007521>
- Iacob, O., Rowan, J. S., Brown, I., & Ellis, C. (2014). Evaluating wider benefits of natural flood management strategies: An ecosystem-based adaptation perspective. *Hydrology Research*, 45(6), 774–787. <https://doi.org/10.2166/nh.2014.184>
- IPCC. (2014). Climate Change 2014: Synthesis Report. In Intergovernmental Panel on Climate Change (Ed.), *Climate Change 2014: Synthesis Report. Contribution of Working Groups I, II and III to the Fifth Assessment Report of the Intergovernmental Panel on Climate Change*. Geneva; Cambridge University Press. <https://doi.org/10.1017/CBO9781107415324>

- Javernick, L. A. (2013). *Modeling flood-induced processes causing Russell lupin mortality in the braided Ahuriri River, New Zealand* [PhD, University of Canterbury]. <https://doi.org/10.26021/2273>
- Jiang, Z., Perona, P., Francis, R., Molnar, P., & Burlando, P. (2009). An experimental comparison of silica gel and quartz sand grains as sediment media for growing vegetation at the laboratory scale. *Aquatic Sciences*, *71*(3), 350–355. <https://doi.org/10.1007/s00027-009-9207-1>
- Kasprak, A., Wheaton, J. M., Ashmore, P. E., Hensleigh, J. W., & Peirce, S. (2015). The relationship between particle travel distance and channel morphology: Results from physical models of braided rivers. *Journal of Geophysical Research: Earth Surface*, *120*(1), 55–74. <https://doi.org/10.1002/2014JF003310>
- Kean, J. W., & Smith, J. D. (2006). Form drag in rivers due to small-scale natural topographic features: 1. Regular sequences. *Journal of Geophysical Research: Earth Surface*, *111*(4). <https://doi.org/10.1029/2006JF000467>
- Kellerhals, R., Bray, D. I., & Church, M. (1976). Classification and Analysis of River Processes. *Journal of Hydraulic Divisions*, *102*(7), 813–829.
- Kellerhals, R., & Church, M. (1989). The morphology of large rivers: Characterization and management. In D. P. Dodge (Ed.), *Proceedings of the International Large River Symposium* (Vol. 106, pp. 31–48). Ottawa; Canadian Special Publication Fisheries and Aquatic Sciences.
- Kelly, W. E., & Gularte, R. C. (1981). Erosion Resistance of Cohesive Soils. *Journal of the Hydraulics Division*, *107*(10), 1211–1224. <https://doi.org/10.1061/JYCEAJ.0005743>
- Kleinhans, M. G. (2005). Flow discharge and sediment transport models for estimating a minimum timescale of hydrological activity and channel and delta formation on Mars. *Journal of Geophysical Research E: Planets*, *110*(12), 1–23. <https://doi.org/10.1029/2005JE002521>
- Kleinhans, M. G. (2010a). A tale of two planets: geomorphology applied to Mars' surface, fluvio-deltaic processes and landforms. *Earth Surface Processes and Landforms*, *35*, 102–117. <https://doi.org/10.1002/esp.1895>
- Kleinhans, M. G. (2010b). Sorting out river channel patterns. *Progress in Physical Geography*, *34*(3), 287–326. <https://doi.org/10.1177/0309133310365300>
- Kleinhans, M. G., Braudrick, C., van Dijk, W. M., van de Lageweg, W. I., Teske, R., & Van Oorschot, M. (2015). Swiftiness of biomorphodynamics in Lilliput- to Giant-sized rivers and deltas. *Geomorphology*, *244*, 56–73. <https://doi.org/10.1016/j.geomorph.2015.04.022>
- Kleinhans, M. G., Ferguson, R. I., Lane, S. N., & Hardy, R. J. (2013). Splitting rivers at their seams: Bifurcations and avulsion. *Earth Surface Processes and Landforms*, *38*, 47–61. <https://doi.org/10.1002/esp.3268>
- Kleinhans, M. G., & van den Berg, J. H. (2011). River channel and bar patterns explained and predicted by an empirical and a physics-based method. *Earth Surface Processes and Landforms*, *36*(6), 721–738. <https://doi.org/10.1002/esp.2090>
- Kleinhans, M. G., van Dijk, W. M., van de Lageweg, W. I., Hoyal, D. C. J. D., Markies, H., van Maarseveen, M., Roosendaal, C., van Weesep, W., van Breemen, D., Hoendervoogt, R., & Cheshier, N. (2014). Quantifiable effectiveness of experimental scaling of river- and delta

- morphodynamics and stratigraphy. *Earth-Science Reviews*, 133, 43–61. <https://doi.org/10.1016/j.earscirev.2014.03.001>
- Knighton, D. (1998). *Fluvial Forms and Processes; A New Perspective* (2nd ed.). London; Routledge. <https://doi.org/10.4324/9780203784662>
- Langendoen, E. J., & Simon, A. (2008). Modeling the evolution of incised streams. II: Streambank erosion. *Journal of Hydraulic Engineering*, 134(7), 905–915. [https://doi.org/10.1061/\(ASCE\)0733-9429\(2008\)134:7\(905\)](https://doi.org/10.1061/(ASCE)0733-9429(2008)134:7(905))
- Leddy, J. O., Ashworth, P. J., & Best, J. L. (1993). Mechanisms of anabranch avulsion within gravel-bed braided rivers: observations from a scaled physical model. *Geological Society, London, Special Publications*, 75(1), 119–127. <https://doi.org/10.1144/GSL.SP.1993.075.01.07>
- Leduc, P., Ashmore, P., & Gardner, J. T. (2015). Grain sorting in the morphological active layer of a braided river physical model. *Earth Surface Dynamics*, 3(4), 577–585. <https://doi.org/10.5194/esurf-3-577-2015>
- Leduc, P., Peirce, S., & Ashmore, P. (2019). Short communication: Challenges and applications of structure-from-motion photogrammetry in a physical model of a braided river. *Earth Surface Dynamics*, 7(1), 97–106. <https://doi.org/10.5194/esurf-7-97-2019>
- Lee, K. Y., & Mooney, D. J. (2012). Alginate: Properties and biomedical applications. *Progress in Polymer Science (Oxford)*, 37(1), 106–126. <https://doi.org/10.1016/j.progpolymsci.2011.06.003>
- Leopold, L. B., & Wolman, M. G. (1957). River Channel Patterns: Braided, Meandering and Straight. In *United States Geological Survey Professional Paper 282-B*. Washington DC; US Government Printing Office. <https://doi.org/10.3133/pp282B>
- Leopold, L. B., Wolman, M. G., & Millar, J. P. (1964). *Fluvial Processes in Geomorphology* (1st ed.). San Francisco; Freeman.
- Lokhorst, I. R., de Lange, S. I., van Buiten, G., Selaković, S., & Kleinhans, M. G. (2019). Species selection and assessment of eco-engineering effects of seedlings for biogeomorphological landscape experiments. *Earth Surface Processes and Landforms*, 44(14), 2922–2935. <https://doi.org/10.1002/esp.4702>
- Malarkey, J., Baas, J. H., Hope, J. a, Aspden, R. J., Parsons, D. R., Peakall, J., Paterson, D. M., Schindler, R. J., Ye, L., Lichtman, I. D., Bass, S. J., Davies, A. G., Manning, A. J., & Thorne, P. D. (2015). The pervasive role of biological cohesion in bedform development. *Nature Communications*, 6, 6257. <https://doi.org/10.1038/ncomms7257>
- Mao, L. (2012). The effect of hydrographs on bed load transport and bed sediment spatial arrangement. *Journal of Geophysical Research: Earth Surface*, 117(3), 1–16. <https://doi.org/10.1029/2012JF002428>
- Marra, W. A., Kleinhans, M. G., & Addink, E. A. (2014). Network concepts to describe channel importance and change in multichannel systems: Test results for the Jamuna River, Bangladesh. *Earth Surface Processes and Landforms*, 39(6), 766–778. <https://doi.org/10.1002/esp.3482>
- Marshak, S. (2008). *Earth, portrait of a planet* (J. Repcheck & T. Foley, Eds.; third). New York; Norton & Company Inc.

- Martinez, F., Blum, L., Rider, S., Cardenas, A., & Piovesan, D. (2017). Re-calibration of camera space manipulation techniques accounting for fisheye lens radial distortion. *2017 IEEE Signal Processing in Medicine and Biology Symposium (SPMB)*, 1–2. <https://doi.org/10.1109/SPMB.2017.8257048>
- McBride, M., Hession, W. C., Rizzo, D. M., & Thompson, D. M. (2007). The influence of riparian vegetation on near-bank turbulence: a flume experiment. *Earth Surface Processes and Landforms*, 32, 2019–2037. <https://doi.org/10.1002/esp.1513>
- Mehta, A. J. (1991). Review notes on cohesive sediment erosion. In N. C. Kraus, K. J. Gingerich, & D. L. Kriebel (Eds.), *Coastal Sediments 1991: Proceedings of a Specialty Conference on Quantitative Approaches to Coastal Sediment Processes* (pp. 40–53). ASCE.
- Métivier, F., Lajeunesse, E., & Devauchelle, O. (2017). Laboratory rivers: Lacey’s law, threshold theory, and channel stability. *Earth Surface Dynamics*, 5(1), 187–198. <https://doi.org/10.5194/esurf-5-187-2017>
- Metivier, F., & Meunier, P. (2003). Input and output mass flux correlations in an experimental braided stream. Implications on the dynamics of bed load transport. *Journal of Hydrology*, 271(1–4), 22–38. [https://doi.org/10.1016/S0022-1694\(02\)00312-8](https://doi.org/10.1016/S0022-1694(02)00312-8)
- Micheli, E. R., & Kirchner, J. W. (2002). Effects of wet meadow riparian vegetation on streambank erosion. 1. Remote sensing measurements of streambank migration and erodibility. *Earth Surface Processes and Landforms*, 27(6), 627–639. <https://doi.org/10.1002/esp.338>
- Moreton, D. J., Ashworth, P. J., & Best, J. L. (2002). The physical scale modelling of braided alluvial architecture and estimation of subsurface permeability. *Basin Research*, 14(3), 265–285. <https://doi.org/10.1046/j.1365-2117.2002.00189.x>
- Munns, R., Schmidt, S., & Beveridge, C. (2010). *Plants in Action, 2nd Edition* (R. Munns, S. Schmidt, & C. Beveridge, Eds.; 2nd ed.). <http://plantsinaction.science.uq.edu.au/content/about>
- Murray, A. B., & Paola, C. (1997). Properties of a cellular braided-stream model. *Earth Surface Processes and Landforms*, 22(11), 1001–1025. [https://doi.org/10.1002/\(sici\)1096-9837\(199711\)22:11<1001::aid-esp798>3.0.co;2-o](https://doi.org/10.1002/(sici)1096-9837(199711)22:11<1001::aid-esp798>3.0.co;2-o)
- Nanson, R. A., Nanson, G. C., & Huang, H. Q. (2010). The hydraulic geometry of narrow and deep channels; evidence for flow optimisation and controlled peatland growth. *Geomorphology*, 117(1–2), 143–154. <https://doi.org/10.1016/J.GEOMORPH.2009.11.021>
- Osman, A. M., & Thorne, C. R. (1988). Riverbank Stability Analysis. I: Theory. *Journal of Hydraulic Engineering*, 114(2), 134–150. [https://doi.org/10.1061/\(asce\)0733-9429\(1988\)114:2\(134\)](https://doi.org/10.1061/(asce)0733-9429(1988)114:2(134))
- Pagès, L. (2011). Root System Architecture: Analysis from Root Systems to Individual Roots. In J. Gliński, J. Horabik, & J. Lipiec (Eds.), *Encyclopedia of Earth Sciences Series* (Encycloped). Springer, Dordrecht. <https://doi.org/10.1007/978-90-481-3585-1>
- Paola, C. (2001). Modelling stream braiding over a range of scales. In M. P. Mosley (Ed.), *Gravel Bed Rivers V* (A; pp. 11–46). Wellington; New Zealand Hydrological Society.
- Paola, C., Straub, K., Mohrig, D., & Reinhardt, L. (2009). The “unreasonable effectiveness” of stratigraphic and geomorphic experiments. *Earth-Science Reviews*, 97(1–4), 1–43. <https://doi.org/10.1016/j.earscirev.2009.05.003>

- Parker, G., Wilcock, P. R., Paola, C., Dietrich, W. E., & Pitlick, J. (2007). Physical basis for quasi-universal relations describing bankfull hydraulic geometry of single-thread gravel bed rivers. *Journal of Geophysical Research: Earth Surface*, 112(4). <https://doi.org/10.1029/2006JF000549>
- Parsons, D. R., Schindler, R. J., Hope, J. A., Malarkey, J., Baas, J. H., Peakall, J., Manning, A. J., Ye, L., Simmons, S., Paterson, D. M., Aspden, R. J., Bass, S. J., Davies, A. G., Lichtman, I. D., & Thorne, P. D. (2016). The role of biophysical cohesion on subaqueous bed form size. *Geophysical Research Letters*, 43(4), 1566–1573. <https://doi.org/10.1002/2016GL067667>
- Partheniades, E. (1965). Erosion and Deposition of Cohesive Soils. *Journal of the Hydraulics Division*, 91(1), 105–139. <https://doi.org/10.1061/JYCEAJ.0001165>
- Peakall, J., Ashworth, P., & Best, J. (1996). Physical Modelling in Fluvial Geomorphology: Principles, Applications and Unresolved Issues. *The Scientific Nature of Geomorphology: Proceedings of the 27th Binghamton Symposium on Geomorphology*, 221–253.
- Peakall, J., Ashworth, P. J., & Best, J. L. (2007). Meander-Bend Evolution, Alluvial Architecture, and the Role of Cohesion in Sinuous River Channels: A Flume Study. *Journal of Sedimentary Research*, 77(3), 197–212. <https://doi.org/10.2110/jsr.2007.017>
- Peirce, S., Ashmore, P., & Leduc, P. (2018). The variability in the morphological active width: Results from physical models of gravel-bed braided rivers. *Earth Surface Processes and Landforms*, 43(11), 2371–2383. <https://doi.org/10.1002/esp.4400>
- Peirce, S., Ashmore, P., & Leduc, P. (2019). Evolution of grain size distributions and bed mobility during hydrographs in gravel-bed braided rivers. *Earth Surface Processes and Landforms*, 44(1), 304–316. <https://doi.org/10.1002/esp.4511>
- Pérez-Harguindeguy, N., Díaz, S., Garnier, E., Lavorel, S., Poorter, H., Jaureguiberry, P., Bret-Harte, M. S., Cornwell, W. K., Craine, J. M., Gurvich, D. E., Urcelay, C., Veneklaas, E. J., Reich, P. B., Poorter, L., Wright, I. J., Ray, P., Enrico, L., Pausas, J. G., de Vos, A. C., Buchmann, N., Funes, G., Quétier, F., Hodgson, J. G., Thompson, K., Morgan, H. D., ter Steege, H., van der Heijden, M. G. A., Sack, L., Blonder, B., Poschlod, P., Vaieretti, M. V., Conti, G., Staver, A. C., Aquino, S., & Cornelissen, J. H. C. (2013). New handbook for standardised measurement of plant functional traits worldwide. *Australian Journal of Botany*, 61(3), 167–234. <https://doi.org/10.1071/BT12225>
- Perona, P., Crouzy, B., McLelland, S., Molnar, P., & Camporeale, C. (2014). Ecomorphodynamics of rivers with converging boundaries. *Earth Surface Processes and Landforms*, 39(12), 1651–1662. <https://doi.org/10.1002/esp.3614>
- Perona, P., Molnar, P., Crouzy, B., Perucca, E., Jiang, Z., McLelland, S., Wüthrich, D., Edmaier, K., Francis, R., Camporeale, C., & Gurnell, A. (2012). Biomass selection by floods and related timescales: Part 1. Experimental observations. *Advances in Water Resources*, 39, 85–96. <https://doi.org/10.1016/j.advwatres.2011.09.016>
- Pollen, N. (2007). Temporal and spatial variability in root reinforcement of streambanks: Accounting for soil shear strength and moisture. *Catena*, 69(3), 197–205. <https://doi.org/10.1016/j.catena.2006.05.004>
- Pollen-Bankhead, N., & Simon, A. (2008). Enhanced application of root-reinforcement algorithms for bank-stability modeling. *Earth Surface Processes and Landforms*, 34(1), 471–480. <https://doi.org/10.1002/esp.1690>

- Pollen-Bankhead, N., Simon, A., & Thomas, R. E. (2013). 12.8 The Reinforcement of Soil by Roots: Recent Advances and Directions for Future Research. In *Treatise on Geomorphology* (Vol. 12, pp. 107–124). Elsevier. <https://doi.org/10.1016/B978-0-12-374739-6.00325-0>
- Puijalon, S., Bornette, G., & Sagnes, P. (2005). Adaptations to increasing hydraulic stress: Morphology, hydrodynamics and fitness of two higher aquatic plant species. *Journal of Experimental Botany*, *56*(412), 777–786. <https://doi.org/10.1093/jxb/eri063>
- Rahardjo, H., & Fredlund, D. G. (1995). Experimental verification of the theory of consolidation for unsaturated soils. *Canadian Geotechnical Journal*, *32*(5), 749–766.
- Rasband, W. (2019). *ImageJ* (1.52d). Bethesda; National Institutes of Health, USA. <https://imagej.nih.gov/ij/>
- Redolfi, M., Bertoldi, W., Tubino, M., & Welber, M. (2018). Bed Load Variability and Morphology of Gravel Bed Rivers Subject to Unsteady Flow: A Laboratory Investigation. *Water Resources Research*, *54*(2), 842–862. <https://doi.org/10.1002/2017WR021143>
- Reitz, M. D., Jerolmack, D. J., Lajeunesse, E., Limare, A., Devauchelle, O., & Métivier, F. (2014). Diffusive evolution of experimental braided rivers. *Physical Review E - Statistical, Nonlinear, and Soft Matter Physics*, *89*(5), 1–6. <https://doi.org/10.1103/PhysRevE.89.052809>
- Rinaldi, M., & Darby, S. E. (2007). 9 Modelling river-bank-erosion processes and mass failure mechanisms: progress towards fully coupled simulations. In H. Habersack, H. Plegay, & M. Rinaldi (Eds.), *Gravel-Bed Rivers VI: From Process Understanding to River Restoration* (Vol. 11, pp. 213–239). Elsevier. [https://doi.org/10.1016/S0928-2025\(07\)11126-3](https://doi.org/10.1016/S0928-2025(07)11126-3)
- Rosatti, G. (2002). Validation of the physical modeling approach for braided rivers. *Water Resources Research*, *38*(12), 31-1-31–38. <https://doi.org/10.1029/2001WR000433>
- Rowntree, K. M., & Dollar, E. S. J. (1999). Vegetation controls on channel stability in the Bell River, Eastern Cape, South Africa. *Earth Surface Processes and Landforms*, *24*(2), 127–134. [https://doi.org/10.1002/\(SICI\)1096-9837\(199902\)24:2<127::AID-ESP944>3.0.CO;2-3](https://doi.org/10.1002/(SICI)1096-9837(199902)24:2<127::AID-ESP944>3.0.CO;2-3)
- Sanders, H. (2020). *Biotic and abiotic controls of burrowing by signal crayfish (Pacifastacus leniusculus) and the implications for sediment recruitment to rivers* [PhD, Loughborough University]. <https://doi.org/10.26174/thesis.lboro.13718128.v1>.
- Sapozhnikov, V. B., & Foufoula-Georgiou, E. (1997). Experimental evidence of dynamic scaling and indications of self-organized criticality in braided rivers. *Water Resources Research*, *33*(8), 1983–1991.
- Sapozhnikov, V. B., & Foufoula-Georgiou, E. (1999). Horizontal and vertical self-organization of braided rivers toward a critical state. *Water Resources Research*, *35*(3), 843–851. <https://doi.org/10.1029/98WR02744>
- Schumm, S. A. (1985). Patterns of Alluvial Rivers. *Annual Review of Earth and Planetary Science*, *13*, 5–27.
- Schumm, S. A., & Khan, H. R. (1972). Experimental Study of Channel Patterns. *Geological Society of America Bulletin*, *83*, 1755–1770.
- Schumm, S. A., & Lichty, R. W. (1965). Time, space, and causality in geomorphology. *American Journal of Science*, *263*(2), 110–119. <https://doi.org/10.2475/ajs.263.2.110>

- Schumm, S. A., Mosley, M. P., & Weaver, W. E. (1987). *Experimental fluvial geomorphology*. New York; John Wiley & Sons.
- Schwanghart, W., & Scherler, D. (2014). Short Communication: TopoToolbox 2 - MATLAB-based software for topographic analysis and modeling in Earth surface sciences. *Earth Surface Dynamics*, 2(1), 1–7. <https://doi.org/10.5194/esurf-2-1-2014>
- Schwarz, M., Cohen, D., & Or, D. (2010). Root-soil mechanical interactions during pullout and failure of root bundles. *Journal of Geophysical Research*, 115(F4), F04035. <https://doi.org/10.1029/2009JF001603>
- Selby, M. J. (1982). Rock mass strength and the form of some inselbergs in the central namib desert. *Earth Surface Processes and Landforms*, 7(5), 489–497. <https://doi.org/10.1002/esp.3290070509>
- Sheets, B. A., Hickson, T. A., & Paola, C. (2002). Assembling the stratigraphic record: Depositional patterns and time-scales in an experimental alluvial basin. *Basin Research*, 14(3), 287–301. <https://doi.org/10.1046/j.1365-2117.2002.00185.x>
- Shields, A. (1936). *Application of similarity principles and turbulence research to bed-load movement* [PhD]. California Institute of Technology.
- Simon, A., & Collison, A. J. C. (2002). Quantifying the mechanical and hydrologic effects of riparian vegetation on streambank stability. *Earth Surface Processes and Landforms*, 27(5), 527–546. <https://doi.org/10.1002/esp.325>
- Simon, A., Curini, A., Darby, S. E., & Langendoen, E. J. (2000). Bank and near-bank processes in an incised channel. *Geomorphology*, 35(3–4), 193–217. [https://doi.org/10.1016/S0169-555X\(00\)00036-2](https://doi.org/10.1016/S0169-555X(00)00036-2)
- Simon, A., & Darby, S. E. (1997). Process-form interactions in unstable sand-bed river channels: A numerical modeling approach. *Geomorphology*, 21, 85–106.
- Simon, A., Pollen, N., & Langendoen, E. (2006). Influence of two woody riparian species on critical conditions for streambank stability: upper Truckee river, California. *Journal of the American Water Resources Association*, 42(1), 99–113. <https://doi.org/10.1111/j.1752-1688.2006.tb03826.x>
- Smith, C. E. (1998). Modeling high sinuosity meanders in a small flume. *Geomorphology*, 25(1–2), 19–30. [https://doi.org/10.1016/S0169-555X\(98\)00029-4](https://doi.org/10.1016/S0169-555X(98)00029-4)
- Steiger, J., Gurnell, A. M., & Goodson, J. M. (2003). Quantifying and characterizing contemporary riparian sedimentation. *River Research and Applications*, 19(4), 335–352. <https://doi.org/10.1002/rra.708>
- Stromberg, J. C. (2013). Root patterns and hydrogeomorphic niches of riparian plants in the American Southwest. *Journal of Arid Environments*, 94, 1–9. <https://doi.org/10.1016/j.jaridenv.2013.02.004>
- Tal, M., Gran, K., Murray, A. B., Paola, C., & Hicks, D. M. (2004). Riparian vegetation as a primary control on channel characteristics in multi-thread rivers. In S. J. Bennett & A. Simon (Eds.), *Riparian Vegetation and Fluvial Geomorphology* (Vol. 8, pp. 43–58). <https://doi.org/10.1029/008WSA04>
- Tal, M., & Paola, C. (2007). Dynamic single-thread channels maintained by the interaction of flow and vegetation. *Geology*, 35(4), 347–350. <https://doi.org/10.1130/G23260A.1>

- Tal, M., & Paola, C. (2010). Effects of vegetation on channel morphodynamics: Results and insights from laboratory experiments. *Earth Surface Processes and Landforms*, 35(9), 1014–1028. <https://doi.org/10.1002/esp.1908>
- Taylor, D. W. (1948). *Fundamentals of Soil Mechanics*. New York; John Wiley & Sons, Inc.
- Thieme, C. (2000). Sodium Carbonates. In *Ullmann's Encyclopedia of Industrial Chemistry* (7th (1999-)). New York, NY; Wiley. https://doi.org/10.1002/14356007.a24_299
- Thomas, R. E., Johnson, M. F., Frostick, L. E., Parsons, D. R., Bouma, T. J., Dijkstra, J. T., Eiff, O., Gobert, S., Henry, P. Y., Kemp, P., McLelland, S. J., Moulin, F. Y., Myrhaug, D., Neyts, A., Paul, M., Penning, W. E., Puijalón, S., Rice, S. P., Stanica, A., Tagliapietra, D., Tal, M., Tørum, A., & Vousdoukas, M. I. (2014). Physical modelling of water, fauna and flora: Knowledge gaps, avenues for future research and infrastructural needs. *Journal of Hydraulic Research*, 52(3), 311–325. <https://doi.org/10.1080/00221686.2013.876453>
- Thomas, R. E., & Pollen-Bankhead, N. (2010). Modeling root-reinforcement with a fiber-bundle model and Monte Carlo simulation. *Ecological Engineering*, 36(1), 47–61. <https://doi.org/10.1016/j.ecoleng.2009.09.008>
- Thorne, C. R. (1978). *PROCESSES OF BANK EROSION IN RIVER CHANNELS* [PhD]. University of East Anglia.
- Thorne, C. R. (1982). Processes and mechanisms of river bank erosion. In R. D. Hey, J. C. Bathurst, & C. R. Thorne (Eds.), *Gravel-Bed Rivers: Fluvial processes, Engineering and Management* (pp. 227–271). Chichester; John Wiley & Sons.
- Thorne, C. R. (1990). Effects of vegetation on riverbank erosion and stability. In J. B. Thornes (Ed.), *Vegetation and Erosion* (pp. 125–144). Chichester; Wiley.
- Thorne, C. R. (1992). Bend scour and bank erosion on the meandering Red River, Louisiana. In M. A. Carling & G. E. Petts (Eds.), *Lowland Floodplain Rivers: Geomorphological Perspectives* (pp. 125–144). Chichester; Wiley.
- Thorne, C. R. (1997). Channel Types and Morphological Classification. In C. R. Thorne, R. D. Hey, & M. D. Newson (Eds.), *Applied Fluvial Geomorphology for River Engineering and Management* (pp. 175–221). John Wiley & Sons Ltd.
- Thorne, C. R., & Tovey, N. K. (1981). Stability of composite river banks. *Earth Surface Processes and Landforms*, 6(5), 469–484. <https://doi.org/10.1002/esp.3290060507>
- Tolhurst, T. J., Gust, G., & Paterson, D. M. (2002). The influence of an extracellular polymeric substance (EPS) on cohesive sediment stability. *Proceedings in Marine Science*, 5(C), 409–425.
- Tron, S., Perona, P., Gorla, L., Schwarz, M., Laio, F., & Ridolfi, L. (2015). The signature of randomness in riparian plant root distributions. *Geophysical Research Letters*, 42(17), 7098–7106. <https://doi.org/10.1002/2015GL064857>
- Twine, T. E., Kucharik, C. J., & Foley, J. A. (2004). Effects of land cover change on the energy and water balance of the Mississippi River basin. *Journal of Hydrometeorology*, 5(4), 640–655. [https://doi.org/10.1175/1525-7541\(2004\)005<0640:EOLCCO>2.0.CO;2](https://doi.org/10.1175/1525-7541(2004)005<0640:EOLCCO>2.0.CO;2)
- Undersander, D., Hall, M. H., Vassalotti, P., & Cosgrove, D. (2011). Alfalfa germination and growth. In *University of Wisconsin Extension* (Issue A3681). Madison. www.alfalfa.org

- van de Lageweg, W. I. (2013). *Morphodynamics and sedimentary architecture of meandering rivers* [PhD]. Utrecht University.
- van de Lageweg, W. I., McLelland, S. J., & Parsons, D. R. (2018). Quantifying biostabilisation effects of biofilm-secreted and extracted extracellular polymeric substances (EPSs) on sandy substrate. *Earth Surface Dynamics*, 6(1), 203–215. <https://doi.org/10.5194/esurf-6-203-2018>
- van de Lageweg, W. I., van Dijk, W. M., Hoendervoogt, R., & Kleinhans, M. G. (2010). Effects of riparian vegetation on experimental channel dynamics. *Riverflow 2010, Volume 2*, 1331–1338. <https://doi.org/10.1002/2013WR013574.F>
- van de Lageweg, W. I., van Dijk, W. M., & Kleinhans, M. G. (2013a). Channel belt architecture formed by a meandering river. *Sedimentology*, 60(3), 840–859. <https://doi.org/10.1111/j.1365-3091.2012.01365.x>
- van de Lageweg, W. I., van Dijk, W. M., & Kleinhans, M. G. (2013b). Morphological and Stratigraphical Signature of Floods In A Braided Gravel-Bed River Revealed From Flume Experiments. *Journal of Sedimentary Research*, 83(11), 1032–1045. <https://doi.org/10.2110/jsr.2013.70>
- van den Berg, J. H. (1995). Prediction of alluvial channel pattern of perennial rivers. *Geomorphology*, 12(4), 259–279. [https://doi.org/10.1016/0169-555X\(95\)00014-V](https://doi.org/10.1016/0169-555X(95)00014-V)
- van der Meer, F. D., & de Jong, S. M. (2006). *Imaging Spectrometry* (F. D. van der Meer & S. M. de Jong, Eds.; Vol. 4). Dordrecht; Springer.
- van Dijk, W. M., Teske, R., van de Lageweg, W. I., & Kleinhans, M. G. (2013). Effects of vegetation distribution on experimental river channel dynamics. *Water Resources Research*, 49(11), 7558–7574. <https://doi.org/10.1002/2013WR013574>
- van Dijk, W. M., van de Lageweg, W. I., & Kleinhans, M. G. (2012). Experimental meandering river with chute cutoffs. *Journal of Geophysical Research: Earth Surface*, 117(3), 1–18. <https://doi.org/10.1029/2011JF002314>
- van Dijk, W. M., van de Lageweg, W. I., & Kleinhans, M. G. (2013). Formation of a cohesive floodplain in a dynamic experimental meandering river. *Earth Surface Processes and Landforms*, 38(13), 1550–1565. <https://doi.org/10.1002/esp.3400>
- van Oorschot, M., Kleinhans, M., Geerling, G., & Middelkoop, H. (2016). Distinct patterns of interaction between vegetation and morphodynamics. *Earth Surface Processes and Landforms*, 41(6), 791–808. <https://doi.org/10.1002/esp.3864>
- van Rijn, L. C. (1993). *Principles of sediment transport in rivers, estuaries and coastal seas*. Amsterdam; Aqua Publications.
- Warburton, J., & Davies, T. (1994). Variability of Bedload Transport and Channel Morphology in a Braided River Hydraulic Model. *Earth Surface Processes and Landforms*, 19, 403–421. <https://doi.org/10.1002/esp.3290190503>
- Welber, M., Bertoldi, W., & Tubino, M. (2013). Wood dispersal in braided streams: Results from physical modeling. *Water Resources Research*, 49(11), 7388–7400. <https://doi.org/10.1002/2013WR014046>

- Wheaton, J. M., Brasington, J., Darby, S. E., & Sear, D. A. (2009). Accounting for uncertainty in DEMs from repeat topographic survey: improved sediment budgets. *Earth Surface Processes and Landforms*, 35, 135–156.
- Williams, H., Houseago, R., McLelland, S., van de Lageweg, W., Grasso, F., Henry, P.-Y., & Thom, M. (2018). *Sediment-Biota Interactions (Experimental Protocols)* (Issue 9). Deliverable D9.3. Report submitted to the European Union under the EC 8th Framework Programme Contract no. 654110, Hydralab+. Deltares: Delft. Available online: https://hydralab.eu/private/Modules/Tools/EUProject/documents/327/D9.3_Protocols_Sediment-Biota_Interactions_v2.0.pdf [Accessed 18/11/2020]
- Williams, H., McLelland, S., Murphy, B., Baartman, J., van der Ploeg, M., & Parsons, D. (2018). Experimental modelling Natural Flood Management interventions at the catchment scale. *20th EGU General Assembly, EGU2018*, 14411.
- Wohl, E., Lane, S. N., & Wilcox, A. C. (2015). The science and practice of river restoration. *Water Resources Research*, 51(8), 5974–5997. <https://doi.org/10.1002/2014WR016874>
- Wolman, M. G., & Brush, L. M. (1961). Factors Controlling the Size and Shape of Stream Channels in Coarse Noncohesive Sands. In *Geological Survey Professional Paper* (Issues 282-G). Washington. <https://doi.org/10.3133/pp282G>
- Wu, X. (2017). *Wave-induced ripple development in mixed clay-sand substrates* [PhD]. University of Hull.
- Wyatt, N. B., Gunther, C. M., & Liberatore, M. W. (2011). Drag reduction effectiveness of dilute and entangled xanthan in turbulent pipe flow. *Journal of Non-Newtonian Fluid Mechanics*, 166(1–2), 25–31. <https://doi.org/10.1016/j.jnnfm.2010.10.002>
- Wyatt, N. B., & Liberatore, M. W. (2009). Rheology and viscosity scaling of the polyelectrolyte xanthan gum. *Journal of Applied Polymer Science*, 114(6), 4076–4084. <https://doi.org/10.1002/app.31093>
- Xavier, P., Stephen, S. E. A., Grace, C., & Bhavisha, J. J. (2019). Optimizing the Making Conditions of Gluten Free Bread Based On Xanthan Gum, Potato Starch and Sorbitol. *International Journal of Engineering and Advanced Technology*, 8(5), 149–153.
- Young, W. J., & Davies, T. R. H. (1991). Bedload Transport Processes in a Braided Gravel-Bed River Model. *Earth Surface Processes and Landforms*, 16, 499–511.